MASTERARBEIT | MASTER'S THESIS

Titel | Title

Synthesis of Epitope-Tagged Venom Peptide Probes Targeting NaV1.7

verfasst von | submitted by

Julius Valentin Pauly B.Sc.

angestrebter akademischer Grad | in partial fulfilment of the requirements for the degree of

Master of Science (MSc)

Wien | Vienna, 2024

Studienkennzahl lt. Studienblatt | Degree programme code as it appears on the student record sheet:	UA 066 862
Studienrichtung lt. Studienblatt | Degree programme as it appears on the student record sheet:	Masterstudium Chemie
Betreut von | Supervisor:	Univ.-Prof. Dr. Christian Friedrich Wilhelm Becker

Preface

This thesis was completed as part of the Master's program in Chemistry at the University of Vienna. The practical work was conducted between April and June 2023 in the Sensory Neuropharmacology Group, under the supervision of Prof. Irina Vetter, at the Institute for Molecular Bioscience, University of Queensland, Brisbane, Australia. The research then continued from September 2023 to January 2024 at the Institute for Biological Chemistry, University of Vienna, under the supervision of Univ.-Prof. Dr. Christian Friedrich Wilhelm Becker and Assoc. Prof. Dipl.-Ing. Markus Muttenthaler, PhD.

1 Acknowledgement

First and foremost, I would like to thank Professor Irina Vetter from the Institute for Molecular Bioscience at the University of Queensland. She made it possible for me to begin my Master's thesis in Brisbane. The experiences I gained during this time in Australia enriched me both personally and academically. I would also like to thank Dr. Hue Tran and Tabea Klasfauseweh: Hue supported me in my practical work in Brisbane, while Tabea conducted the electrophysiological measurements and prepared and provided the cells. I am grateful to the entire research group of Professor Vetter for the pleasant atmosphere and the warm welcome to the *Monday Cake Club*.

My sincere thanks go to Professor Christian Becker from the Institute for Biological Chemistry at the University of Vienna for his supervision, evaluation, and ongoing support throughout my work. I would also like to thank Professor Markus Muttenthaler for the opportunity to continue my Master's thesis in his research group in Vienna and for his expert guidance in the fields of venom peptides and synthesis. A special thanks goes to Dr. Predrag Kalaba for his supervision, practical support, proofreading of my Master's thesis, valuable feedback, and the good times at the institute.

I would also like to thank the entire Institute for Biological Chemistry in Vienna for the pleasant working atmosphere and their always helpful support with practical problems and academic questions.

Lastly, I would like to thank my entire family and friends for their constant support and encouragement. My thanks also go to Franjo Weber, M.Sc., for his helpful assistance. I would like to express my special gratitude to my grandparents, Erna and Erwin, without whose generous support my stay in Australia and my Master's studies in this form would not have been possible.

2 Danksagung

An erster Stelle möchte ich mich bei Professorin Irina Vetter vom Institute for Molecular Bioscience der University of Queensland bedanken. Sie hat es mir ermöglicht, meine Masterarbeit in Brisbane zu beginnen. Die Erfahrungen, die ich während dieser Zeit in Australien gesammelt habe, haben mich sowohl persönlich als auch akademisch bereichert. Ebenfalls danke ich Dr. Hue Tran und Tabea Klasfauseweh: Hue unterstützte mich bei meiner praktischen Arbeit in Brisbane, während Tabea die elektrophysiologischen Messungen durchführte sowie Zellen vorbereitete und zur Verfügung stellte. Der gesamten Arbeitsgruppe von Professorin Vetter möchte ich für die angenehme Atmosphäre und die herzliche Aufnahme in den wöchentlichen *Cake Club* danken.

Mein aufrichtiger Dank gilt Professor Christian Becker vom Institut für Biologische Chemie an der Universität Wien für seine Betreuung, Bewertung und kontinuierliche Unterstützung während meiner Arbeit. Außerdem möchte ich Professor Markus Muttenthaler dafür danken, dass er mir die Möglichkeit gegeben hat, meine Masterarbeit in seiner Forschungsgruppe in Wien fortzusetzen, sowie für seine fachkundige Anleitung in den Bereichen Gift-Peptide und Synthese.

Ein besonderer Dank geht an Dr. Predrag Kalaba für seine Betreuung, die praktische Unterstützung, das Korrekturlesen meiner Masterarbeit, das wertvolle Feedback und die schöne Zeit am Institut.

Dem gesamten Institut für Biologische Chemie in Wien danke ich für die angenehme Arbeitsatmosphäre und die stets hilfsbereite Unterstützung bei praktischen Problemen und fachlichen Fragen.

Zu guter Letzt danke ich meiner gesamten Familie und meinen Freunden für die ständige Unterstützung und den Zuspruch. Mein Dank gilt auch Franjo Weber, M.Sc., für seine hilfreiche Unterstützung. Besonders möchte ich mich bei meinen Großeltern, Erna und Erwin, bedanken: Ohne ihre großzügige Unterstützung wäre mein Aufenthalt in Australien und mein Masterstudium in dieser Form nicht möglich gewesen.

3 Table of Contents

4 List of Abbreviations

aa	Amino acid(s)
A, Ala	L-Alanine
ACN	Acetonitrile
Boc	tert-Butyloxycarbonyl
C, Cys	L-Cysteine
C-terminus	Carboxy-Terminus
Cu	Copper
CuAAC	Cu(I)-catalysed azide–alkyne cycloaddition
D	Domain
D, Asp	L-Aspartic Acid
Da	Dalton
DCC	N,N'-Dicyclohexylcarbodiimide
DCM	Dichloromethane
ddH_2O	Ultrapure water
DIC	N,N'-Diisopropylcarbodiimide
DMF	Dimethylformamide
DODT	3,6-Dioxa-1,8-octanedithiol, 2,2′-(Ethylenedioxy)diethanethiol
E, Glu	L-Glutamic Acid
EC_{50}	Half maximal effective concentration
ESI	Electrospray ionisation
F, Phe	L-Phenylalanine
FLAG	Peptide tag (Sequence DYKDDDDK)
Fmoc	N-(9-Fluorenylmethoxycarbonyl)
G, Gly	L-Glycine
Gn	Guanidine
GSH	Glutathione (Sequence γ-ECG)
GSSG	Glutathione disulfide
H, His	L-Histidine
HA	Hemagglutinin peptide tag (Sequence YPYDVPDYA)
HATU	1-[Bis(dimethylamino)methylene]-1H-1,2,3-triazolo[4,5-b]pyridinium 3-oxide hexafluorophosphate
HBTU	2-(1H-Benzotriazole-1-yl)-1,1,3,3-tetramethyluronium hexafluorophosphate
HCTU	2-(7-Aza-1H-benzotriazole-1-yl)-1,1,3,3-tetramethyluronium hexafluorophosphate
HEK293	Human embryonic kidney 293 cell line
His-tag	(Sequence HHHHHH)
HOBt	N-hydroxybenzotriazole
HPLC	High Performance Liquid Chromatography
I	Current
I, Ile	L-Isoleucine
IC_{50}	Half maximal inhibitory concentration
K, Lys	L-Lysine
kDa	Kilodalton

l	Liter
L/D	*latin*: laevus/dexter (Stereodescriptors)
LD$_{50}$	Dose lethal to 50% of a test population
L, Leu	L-Leucine
LC	Liquid Chromatography
M, Met	L-Methionine
[M]	Molarity [mol·l^{-1}]
MS	Mass spectrometry
N, Asn	L-Asparagine
Na$_V$	Voltage gated sodium channel
n.d.	Not determined
N$_3$K	6-Azido-L-lysine
NMR	Nuclear Magnetic Resonance
N-terminus	Amino-Terminus
Mpe	3-methylpentan-3-yl
Oxyma	Ethyl cyano(hydroxyimino)acetate
P, Pro	L-Proline
Pbf	2,2,4,6,7-pentamethyldihydrobenzofuran-5-sulfonyl
PDB	Protein Data Bank
Pra	Propargylglycine
PS	Polystyrene
Q, Gln	L-Glutamine
R, Arg	L-Arginine
RP	Reverse Phase
S, Ser	L-Serine
SPPS	Solid-Phase Peptide Synthesis
T, Thr	L-Threonine
-*t*Bu	*tert*-Butyl
TFA	Trifluoroacetic acid
Th	Thomson
THPTA	Tris[(1-hydroxypropyl-1H-1,2,3-triazol-4yl)methyl] amine
TIMS	Trapped Ion Mobility Spectrometry
TIPS	Triisopropyl silane
TM	Transmembrane
TOF	Time-of -Flight
V	Voltage
V, Val	L-Valine
VGSC	Voltage-gated sodium channel
VSD	Voltage-sensing domain
W, Trp	L-Tryptophan
Y, Tyr	L-Tyrosine

Abstract

Na$_V$1.7, one of nine subtypes of voltage-gated sodium channels (Na$_V$), is a critical target in pain management. Despite extensive research, developing Na$_V$1.7-targeting analgesics has proven challenging due to limited preclinical success and the difficulty of achieving selectivity, given the high sequence similarity among different Na$_V$ subtypes. Selective detection of Na$_V$1.7 is crucial for advancing research and ultimately developing new pain medications, particularly for addressing chronic pain in light of the ongoing opioid crisis.

Venom peptides that potently inhibit Na$_V$ subtypes have been invaluable in advancing our structural and functional understanding of these channels. In the scope of this work, it is proposed that the selective visualization of Na$_V$1.7 can be achieved by using modified venom peptides as probes instead of primary antibodies in a Proximity Ligation Assay (PLA).

The primary objective was to design and synthesize probes that preserve the high affinity and selectivity of the original venom peptides. The designed probes were derived from the disulfide-rich µ-conotoxin KIIIA and µ-Theraphotoxin-Pn3a[D8N].

Linear precursors of KIIIA and Pn3a[D8N], modified with a spacer sequence and an azide moiety, were assembled using solid-phase peptide synthesis (SPPS) and thermodynamically folded. Alkyne-functionalized epitope tags were synthesized and ligated to the venom peptides *via* bioorthogonal *CuAAC* ligation, resulting in a series of KIIIA- and Pn3a-based epitope-tagged probes. These probes were then electrophysiologically tested on Na$_V$1.7. The HA-tagged KIIIA probes exhibited a loss of inhibitory potency, while the FLAG-tagged Pn3a[D8N] demonstrated an 17.7-fold decrease in potency. These initial results guided the design of additional probes and Pn3a derivatives, which are yet to be tested. The probe designs and syntheses were critically evaluated, and next steps, and a research outlook for further Na$_V$1.7 probe development based on Pn3a, is presented.

Zusammenfassung

Na$_\mathrm{V}$1.7, einer von neun Subtypen der spannungsabhängigen Natriumkanäle (Na$_\mathrm{V}$), ist ein essentielles Target in der Schmerztherapie. Trotz umfangreicher Forschung ist die Entwicklung von Na$_\mathrm{V}$1.7-zielgerichteten Analgetika aufgrund begrenzter präklinischer Erfolge und der Herausforderung, eine hohe Selektivität zu erreichen, schwierig. Eine sensitive und selektive Methode zur Detektion von Na$_\mathrm{V}$1.7 spielt daher eine entscheidende Rolle in der Forschung und Entwicklung neuer Schmerzmedikamente. Insbesondere angesichts der anhaltenden Opioid-Krise ist die Entwicklung neuer Medikamente für die Behandlung chronischer Schmerzen von großer Bedeutung.

Der Einsatz von Giftpeptiden, die verschiedene Na$_\mathrm{V}$-Subtypen potent inhibieren, hat zum Verständnis der strukturellen und funktionellen Eigenschaften dieser Ionenkanäle beigetragen. Im Zuge dieser Arbeit wird vorgeschlagen, dass die selektive Visualisierung von Na$_\mathrm{V}$1.7 durch den Einsatz modifizierter Giftpeptide als Sonden anstelle von Primärantikörpern in einem Proximity Ligation Assay (PLA) erreicht werden kann. Das Design der Sonden basierte auf den disulfidreichen Giftpeptiden µ-conotoxin KIIIA und µ-Theraphotoxin-Pn3a[D8N].

Lineare Vorstufen von KIIIA und Pn3a[D8N], modifiziert mit einer Spacer-Sequenz und einer Azid-Gruppe, wurden mittels Festphasenpeptidsynthese (SPPS) hergestellt und anschließend thermodynamisch gefaltet. Alkin-funktionalisierte Epitope-Tags wurden synthetisiert und über bioorthogonale CuAAC-Ligation an die Giftpeptide gekoppelt, wodurch eine Reihe von KIIIA- sowie Pn3a-basierten, Epitop-markierten Sonden erhalten wurde. Diese Sonden wurden anschließend elektrophysiologisch an Na$_\mathrm{V}$1.7 getestet. Die mit HA-Tag versehenen KIIIA-Sonden zeigten einen Verlust der Na$_\mathrm{V}$1.7 hemmenden Potenz, während die mit FLAG-Tag markierten Pn3a[D8N]-Sonden eine 17.7-fache Verringerung der Potenz aufwiesen. Diese ersten Ergebnisse dienten als Grundlage für das Design weiterer auf Pn3a[D8N] basierender Sonden und Derivate, deren Testung noch aussteht. Das Design und die Synthese der Sonden wurden im Zuge dieser Arbeit kritisch bewertet, und es wird ein Forschungsausblick einschließlich einer alternativen Strategie für die weitere Entwicklung von Na$_\mathrm{V}$1.7-Sonden auf der Grundlage von Pn3a vorgestellt.

1 Introduction

1.1 Venom peptides – Valuable tools for (pain) research

Venoms are specialized secretions that adversely affect the viability of envenomated organisms. The biological effects of venoms are as diverse as their chemical components. Typically, venoms function in predation or defence, either by immobilizing or killing prey, or by deterring predators through the infliction of pain. The key distinction between venoms and other toxin classes, such as poisons, lies in their mode of delivery. Poisons are ingested or absorbed, while venoms are injected directly into the internal tissues of organisms *via* a wound (Avalo et al., 2022; Casewell et al., 2013; Fry et al., 2015, 2009; Nelsen et al., 2014). Among the most lethal venoms for mammals is that of *Oxyuranus microlepidotus* (Inland taipan), which exhibits an LD_{50} value of 0.0225 mg/kg in murine models, demonstrating the venom's potent lethality even at minimal doses (Barber et al., 2014). The effects of venom can also vary with dosage, as demonstrated by *Synanceia trachynis* (stonefish) venom, which induces an initial decrease in blood pressure at low doses, followed by an increase at higher doses (Church and Hodgson, 2000).

Venoms contain at least one or more toxin and other biomolecules and consist of a mixture of minerals, small molecules, nucleic acids, and proteins or peptides (Jackson and Parks, 1989; Kuhn-Nentwig et al., 2011; Rash and Hodgson, 2002). Numerous organisms across different phyla and taxa have independently evolved to be venomous, highlighting the evolutionary success of venoms and indicating the molecular evolution the toxic constituents of venoms have undergone (Schendel et al., 2019).

Venom components have proven valuable in drug development. Among the plethora of biologically active molecules found in animal venoms, pharmaceuticals such as Captopril (ACE inhibitor), Exenatide (GLP-1 analogue), and Ziconotide (analgesic) have been developed (Bordon et al., 2020; Ferreira, 1965; Furman, 2012; Smith and Deer, 2009). Additionally, venom-derived substances have been instrumental in chemical biology, particularly for studying the function and structure of ion channels (Dutertre and Lewis, 2010; Kalia et al., 2015; MacKinnon and Miller, 1988).

Especially the venoms of arthropods (e.g., centipedes, scorpions, spiders) and molluscs (e.g., cone snails) are a rich source of neuropharmacological compounds, often small, disulfide-rich peptides, specifically targeting ion channels (Armishaw and Alewood, 2005; Hakim et al., 2015; Herzig, 2019; Klint et al., 2012; Langenegger et al., 2019; Possani et al., 1999; Saez et al., 2010; Terlau and Olivera, 2004). These natural neurotoxins have been successfully used to study the physiology and pharmacology of voltage-gated sodium channels, prominent pain targets, by selectively inhibiting, modulating, or arresting the channels in specific conformations or aiding in structural elucidation of these channels, for example, by identifying and mapping binding sites (Dutertre and Lewis, 2010; Jiang et al., 2021; Kalia et al., 2015; Minassian et al., 2013; Mueller et al., 2020; Osteen et al., 2016).

A brief introduction is provided to help readers understand peptide toxin nomenclature in the following chapters. The name should convey information about the pharmacological target, biological origin, and relation to similar toxins. As can be seen in **Figure 1**, the name starts with a Greek letter descriptor (following International Union of Basic and Clinical Pharmacology-recommended nomenclature for channels/receptors) that gives information about the target (receptor or channel) and optionally subtype specificity (Alexander et al., 2007). The family and species of origin are then specified by a generic name and a code of upper- and lowercase letters. A numeral and lowercase letter are added to

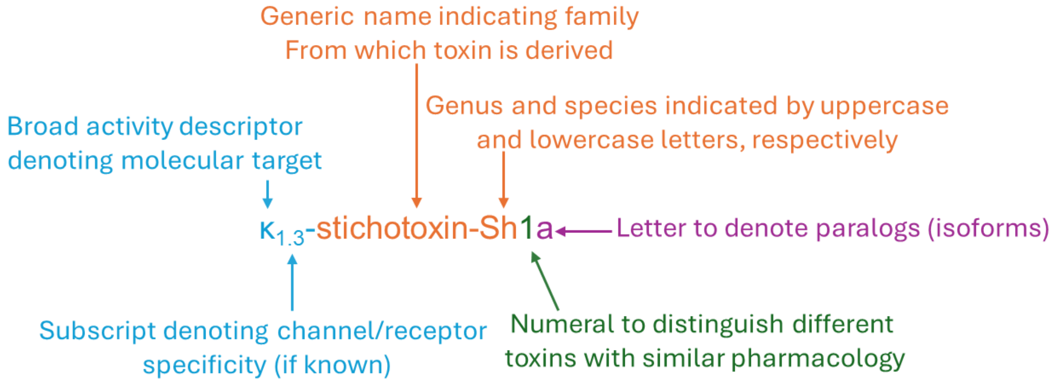

Figure 1. Illustration of the system for naming peptide toxins. The name consists of three segments: a Greek letter (descriptor) for the toxin's activity (light blue), its biological source (orange), and its relation to other toxins (green/purple). Figure is redrawn from (King et al., 2008).

distinguish between similar and paralogous peptide toxins. In this figure, a sea anemone toxin (ShK) that targets the 1.3 subtype of voltage-gated potassium channels (K$_V$) is used as an example. This nomenclature was proposed in 2008 by King *et al*. (King et al., 2008b).

1.2 Voltage-Gated Sodium Channels

Ions do not passively diffuse across cell membranes and require specialized transport proteins. Voltage-gated sodium channels (VGSCs or Na$_V$ channels) are transmembrane proteins that facilitate Na$^+$ influx, depolarizing excitable cell membranes and generating action potentials (Catterall et al., 2005; Chahine, 2018; Hodgkin and Huxley, 1952). Their voltage-dependent activation is determined by the membrane potential sensed by a voltage-sensing domain (Chahine, 2018; Israel et al., 2017). Thus far, nine subtypes of eukaryotic VGSCs, Na$_V$1.1 – Na$_V$1.9, encoded by the *SCN1A* – *SCN5A* and *SCN8A* – *SCN11A* genes, have been discovered, with more than 50% sequence identity (Catterall et al., 2005; Goldin, 2001). Na$_V$ subtypes can be classified by their sensitivity to Tetrodotoxin (TTX), a small-molecule neurotoxin from the puffer fish. Na$_V$1.1–Na$_V$1.4, Na$_V$1.6, and Na$_V$1.7 are TTX-sensitive, blocked by low nanomolar concentrations. Na$_V$1.5, Na$_V$1.8, and Na$_V$1.9 are TTX-resistant, requiring high micromolar concentrations for inhibition (Catterall et al., 2005; de Lera Ruiz and Kraus, 2015; Narahashi, 1974; Waxman et al., 1999).

The expression of Na$_V$ α-subunits is tissue-specific, with Na$_V$1.1 - Na$_V$1.3 being predominantly found in the central nervous system (CNS). Nav1.4 is found in skeletal muscles, and Na$_V$1.5 is prevalent in heart tissue, responsible for cardiac function. NaV1.6 is present in both the peripheral and central nervous systems, while Na$_V$1.7 - Na$_V$1.9 see preferential expression in nociceptive neurons (Chahine, 2018; Israel et al., 2017; Yang et al., 2018). These Na$_V$ channels are crucial for generating Na$^+$ currents that initiate and propagate action potentials in nerves and muscle fibres (Chahine, 2018; Israel et al., 2017). The Na$_V$ channel tissue distribution and associated channelopathies are displayed in **Figure 2**. The structural composition of Na$_V$ channels is depicted in **Figure 3**. Eukaryotic NaV channels consist of an α-subunit (~260 kDa), forming the pore, often associated with one or two smaller β-subunits (~30–40 kDa) (Catterall et al., 2005). The α-subunit has four homologous domains (DI to DIV), each containing six transmembrane helices (S1 to S6) (Numa and Noda, 1986). Segments S1 to S4 form the voltage-sensing domains (VSD), with the S4 segment being crucial for sensing membrane polarisation changes. The structural composition of Na$_V$ channels is depicted in **Figure 3**. The pore and ion-selectivity filter is formed by the fifth and sixth transmembrane segments from each domain and the connecting P-loops. Sodium channel inactivation is facilitated by the "inactivation gate," located between S6 of domain III and S1 of domain IV. The extracellular loop between S3 and S4 in domain II binds various gating modifier toxins. The voltage-sensing

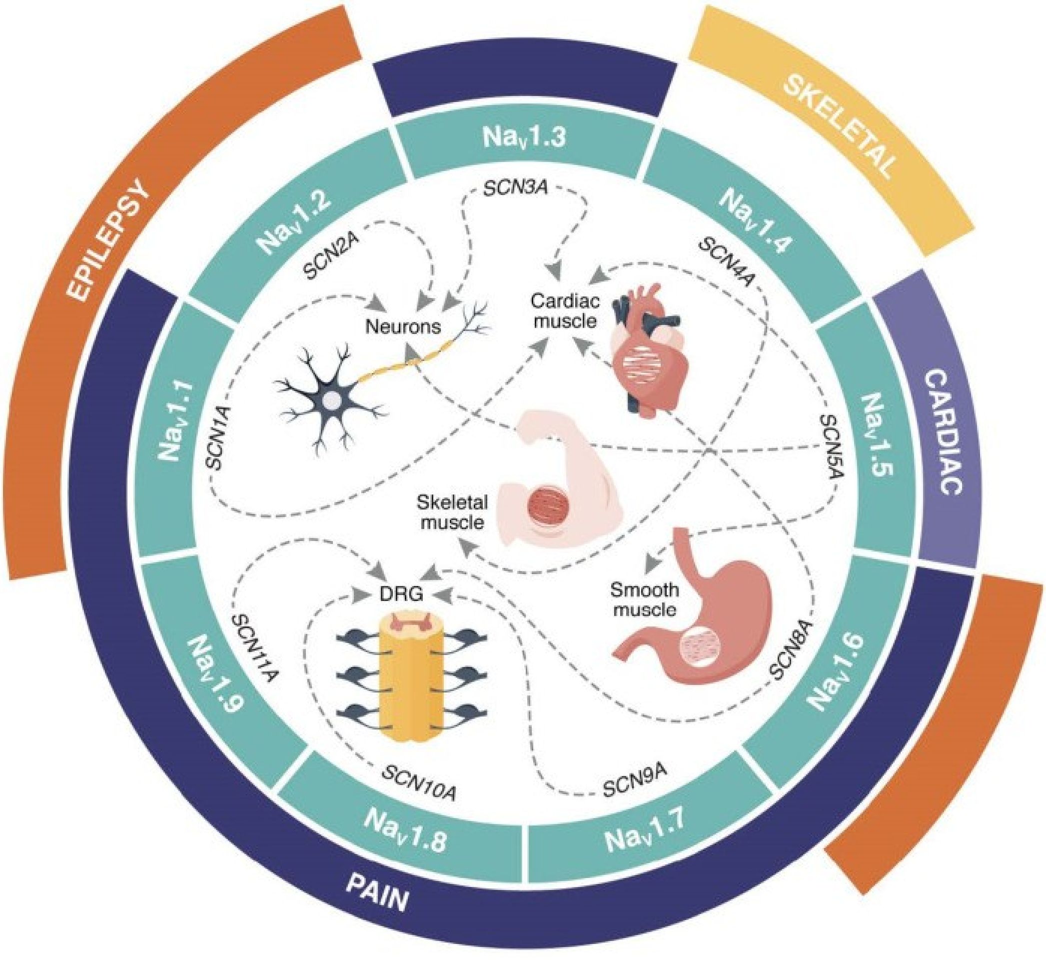

Figure 2. Tissue distribution of human Na$_V$ channels and associated channelopathies. The nine Na$_V$ channel subtypes (Na$_V$1.1–1.9, indicated by circle segments in teal) are encoded by specific SCNxA genes (where x represents 1–5 and 8–11). The tissues primarily expressing these various Na$_V$ subtypes are connected with dotted arrows. The outer segments illustrate the channelopathies associated with Na$_V$ channel mutations: pain (dark blue), cardiac disorders (purple), epilepsy (orange), and skeletal muscle disorders (yellow). DRG stands for dorsal root ganglia. Figure taken and description adapted from (McMahon et al., 2024).

domain (S1–S4) regulates channel opening during membrane depolarisation, driven by the movement of positively charged residues in the S4 helix. Upon depolarisation, S4 segments move outward, opening the channel pore. Inactivation occurs as the inactivation gate folds into the pore, and repolarisation resets the

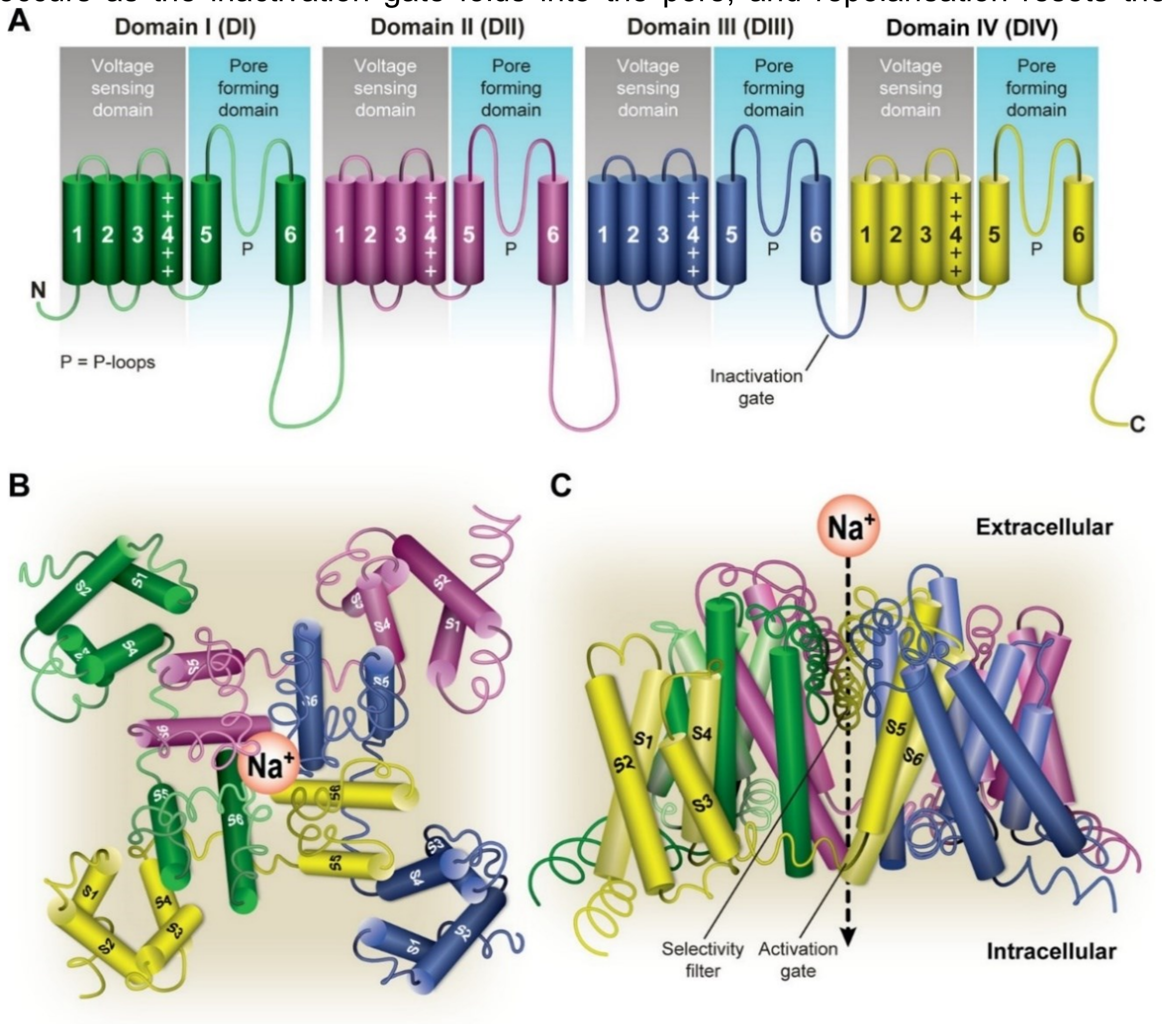

Figure 3. Structural composition of Na$_V$ channels. (A) The pore-forming α- subunit comprises a single polypeptide chain and forms four homologous domains (DI – DIV). Each domain comprises six transmembrane (TM) helices (1 – 6), connected *via* intra- or extracellular loops. The pore and the ion-selectivity filter are formed by the fifth and sixth TM segments from each domain and the connecting re-entrant loops (P). Segments S1 to S4 in each domain constitute the voltage-sensing domains (VSD), with the arginine-rich, positively charged TM segment four being crucial for detecting changes in membrane polarisation. Sodium channel inactivation is facilitated by a short hydrophobic sequence, known as the "inactivation gate", located in the intracellular between S6 of domains III and S1 of domain IV. The extracellular loop between segments S3 and S4 in domain II (red) is the binding site for various gating modifier toxins, and the loops between S5 and S6 constitute the pore (P-loop). **(B)** Top view from the extracellular side of the open-channel structure of Na$_V$Ms from *Magnetococcus sp*., with four identical domains colour-coded to emphasise parallels to the human Na$_V$ structure **(C)** Side perspective of the crystal structure of the open Na$_V$Ms channel. Originating from *Magnetococcus sp*. The selectivity filter (SF) is situated at the middle of the channel pore, and the activation gate is found at the intracellular section of the pore - figure taken from source (de Lera Ruiz and Kraus, 2015).

channels to their resting state. The pore domain features a narrow channel with an ion selectivity filter that selects only hydrated sodium ions. Key amino acid residues aspartate, glutamate, lysine and alanine in the selectivity filter determine ion selectivity and permeability (Catterall, 2000; Chahine, 2018; Israel et al., 2017).

While the α-subunit can manage voltage-dependent ion gating, its function is regulated by auxiliary β-subunits (30–40 kDa), as shown in the cryo-electron microscopy structure of human Na$_V$1.7 in **Figure 5** (Shen et al., 2019). The β1- and β3-subtypes bind to the α-subunit through noncovalent interactions, whereas the β2- and β4-subtypes are linked to the α-subunit via disulfides. (Chahine and O’Leary, 2011) These β-subunits modulate the channel's kinetics and surface expression (Isom, 2002, 2000; Israel et al., 2017; Noda et al., 1986).

Na$_V$ channels have three primary states: closed (resting), open (conducting), and inactivated (nonconducting). The mechanism of gating is depicted and described in **Figure 4** (Israel et al., 2017). After opening, these channels quickly move to a nonconducting state, causing the sodium currents to diminish rapidly. Prolonged depolarisation leads to slow inactivation, which impacts the excitability of nerve and muscle cells. Additionally, specific VGSC subtypes can produce persistent sodium currents, such as Nav1.9 in sensory neurons, and resurgent currents during the repolarisation phase, both of which play a role in maintaining continuous neuronal activity (Catterall, 2000; Chahine, 2018).

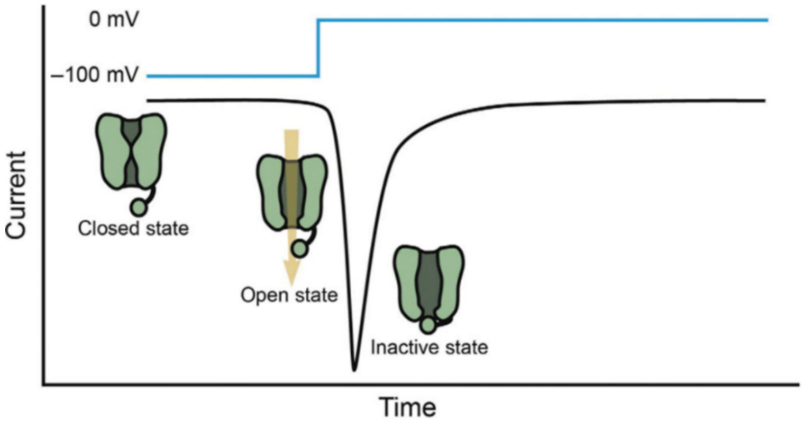

Figure 4. Na$_V$ channel gating mechanism and conductive properties. During a depolarizing voltage step, NaV channels transition from a closed (resting) state to an open state, allowing Na$^+$ ions to permeate through the channel pore. This is followed by fast inactivation, where the channel is closed by the inactivation particle blocking the pore. The channel then returns to the closed state as the membrane potential returns to resting levels. Figure taken and description adapted from (Israel et al., 2017).

Nine neurotoxin binding sites on Na$_V$ channels have been proposed, situated at different locations on the α-subunit (Israel et al., 2017). Inhibitory toxins are designated with the descriptor 'μ'. μ-Conotoxins and theraphotoxins, found in the venoms of cone snails and tarantulas, respectively, primarily target sites 1, 3, and 4. By binding to site 1, conotoxins block the pore. Theraphotoxins act as gating modifiers at sites 3 and 4, keeping the channel in a closed state or altering its activation by shifting voltage dependence (Israel et al., 2017; King et al., 2008b). The mode of action and two examples, μ-conotoxin KIIIA and μ-theraphotoxin Pn3a, will be further detailed in sections 1.5 and 1.6.

Given the critical roles VGSCs play in cellular processes, they are also implicated in various diseases. VGSC mutations underlie numerous neurological disorders known as channelopathies. Examples include certain types of epilepsy (Na$_V$1.1, Na$_V$1.2), autism (Na$_V$1.2), migraine (Na$_V$1.1), and cognitive impairment (Na$_V$1.2), as displayed in **Figure 2** (Dichgans et al., 2005; Dravet, 2011; Mantegazza et al., 2010; Rauch et al., 2012; Sanders et al., 2018). Especially Na$_V$1.7 has been linked to pain disorders and neuropathies, which will be further highlighted in section 1.3 (Cox et al., 2006; Fertleman et al., 2006).

1.3 Na$_V$1.7

Na$_V$1.7 significantly influences pain perception by regulating the excitability of peripheral sensory neurons (Black et al., 2012; Chahine, 2018; Dib-Hajj et al., 2007; Vetter et al., 2017; Yang et al., 2018). It is abundantly found in sensory neurons, including those in the dorsal root ganglia (DRG), as well as sympathetic and trigeminal ganglia. This channel is distributed throughout the central and peripheral branches of these neurons, including axons and nerve endings in the skin, named nociceptors (Black et al., 2012; Dubin and Patapoutian, 2010; Toledo-Aral et al., 1997; Vetter et al., 2017). Nociceptive pain is a sensory experience triggered by harmful chemical, thermal, or mechanical stimuli. Nociceptors detect these noxious stimuli and transfer pain signals *via* the spinal cord to the brain, where the signals are processed and eventually perceived to serve the essential function of prompting a rapid response to injury or avoidance of harm, thereby promoting survival (Dib-

Hajj et al., 2007; Dubin and Patapoutian, 2010; Eagles et al., 2022; Raja et al., 2020; Yam et al., 2018).

Na$_V$1.7's distinctive gating properties, such as its slower recovery from inactivation and delayed onset of closed-state inactivation, enable it to generate significant ramp currents during slow, small depolarisations. This makes Na$_V$1.7 pivotal in amplifying generator potentials and setting the action potential firing threshold in pain-sensing neurons (Black et al., 2012; Cummins et al., 1998; Rush et al., 2007; Vetter et al., 2017). The role of Na$_V$1.7 in action potential generation and its association with pain disorders make this channel a high-potential therapeutic target (Bennett et al., 2019; Dib-Hajj et al., 2007; Eijkelkamp et al., 2012; Mulcahy et al., 2019; Yang et al.,

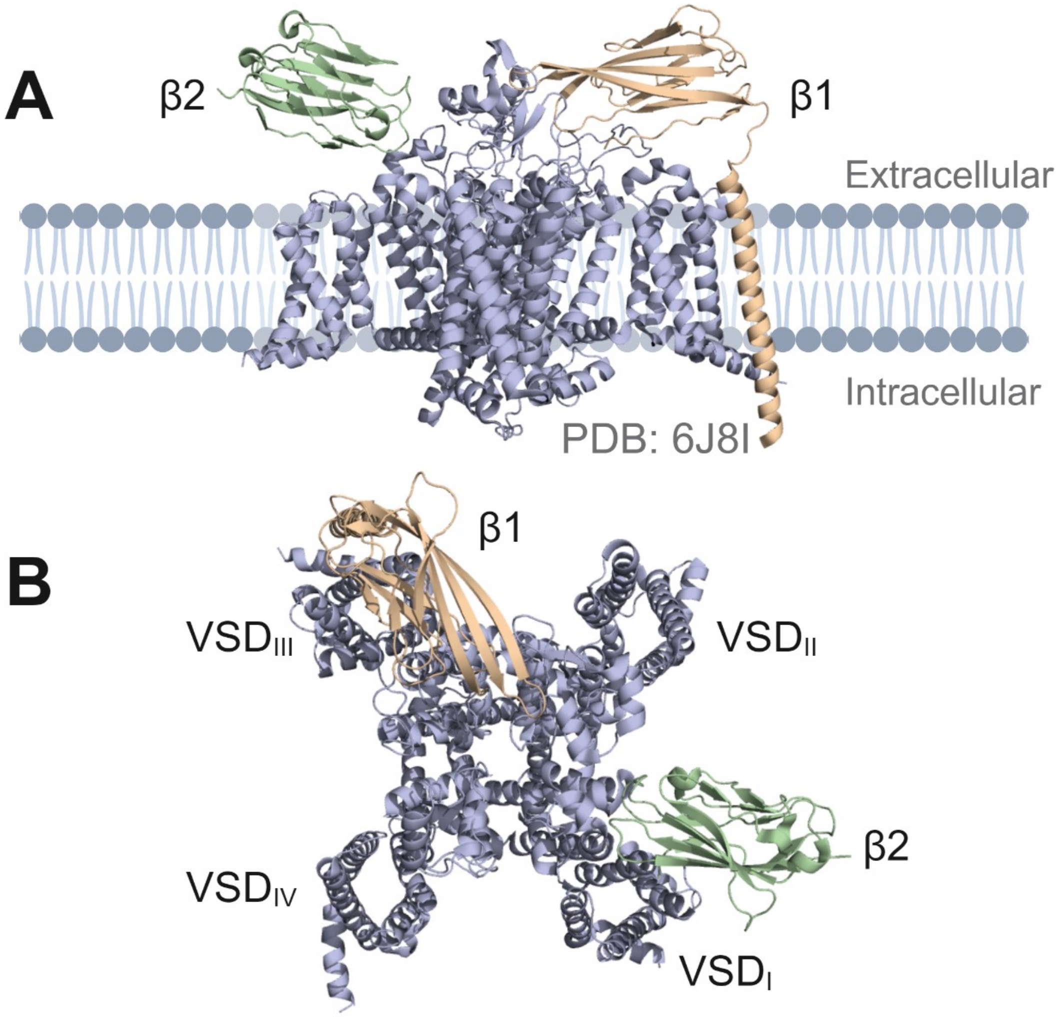

Figure 5. Cryo-electron microscopy structure of hNa$_V$1.7 including β-subunits from two perspectives. **(A)** Sideview of human Na$_V$1.7 embedded in the cellular membrane. Besides the pore-forming α -subunit, β1 and β2 subunits are shown. **(B)** Top view of the channel with annotated voltage-sensing domains (VSDI-IV). Structure determined by Shen et al., 2019, and rendered with PyMol (Protein Data Bank code: 6J8G). Figure created with BioRender.

2018). Mutations in the *SCN9A* gene, which encodes NaV1.7, are linked to different pain syndromes. Loss-of-function mutations *SCN9A*, the gene that codes for the α-subunit of NaV1.7, cause congenital insensitivity to pain (CIP), a rare condition defined by the absence of physical pain, as well as anosmia, loss of sense of smell (Cox et al., 2006; Weiss et al., 2011). In contrast, gain-of-function mutations result in conditions like inherited erythromelalgia (IEM) and paroxysmal extreme pain disorder (PEPD) (Dib-Hajj et al., 2005; Estacion et al., 2008; Fertleman et al., 2006). Individuals with diabetic and chemotherapy-induced pain disorders show an upregulation of NaV1.7 expression in the dorsal root ganglia (Chang et al., 2018; Chattopadhyay et al., 2008).Given that chronic pain affects an estimated 20-25% of the population and places a significant burden on patients and society, developing effective analgesics targeting NaV1.7 is highly desirable (Eagles et al., 2022; Gaskin and Richard, 2012; Gold and Gebhart, 2010; Hay et al., 2017; Holmes et al., 2013).

Modulators of NaV1.7 can be categorised by their mode of binding into pore blockers that occlude the channel's ion-conductive pore and block Na$^+$ permeation, such as TTX, the non-subtype selective analgesic Lidocaine or µ-conotoxins, peptides from the venom of cone snails (Golzari et al., 2014; Hui et al., 2002; Pan et al., 2019; Shen et al., 2018). Gating modifier toxins (GMT), either as activators or inhibitors, bind to voltage-sensing domains (VSDs) and arrest the channel in a specific conformation. Activators lock the channels in the open state, whereas inhibitors shift the voltage-dependence for activation (Dongol et al., 2019; Klint et al., 2012; Shen et al., 2018). There are six known neurotoxin receptor sites (Sites 1–6) on NaV channels. Pore-blockers bind to site 1, whereas neurotoxins at sites 2–6 modify the channel's gating mechanisms (Dongol et al., 2019). In human NaV channels, venom peptides specifically target the four receptor sites 1 (e.g., µ-conotoxins), 3 (e.g., scorpion α-toxins, sea anemone toxins, spider toxins), 4 (e.g., scorpion β-toxins, spider toxins), and 6 (e.g., δ-conotoxins) (Cardoso and Lewis, 2019; Dongol et al., 2019; Kozlov, 2018; Stevens et al., 2011). The mode of action of µ-cono- and spider toxins will be discussed in sections 1.5 - 1.6.1.

Despite extensive research efforts, NaV1.7-specific inhibitors have not been able to suppress NaV1.7-mediated pain to a degree observed in patients with congenital insensitivity to pain (Eagles et al., 2022). Certain peptides found in venoms, such as the spider toxin Pn3a have shown to be potent inhibitors with efficacy in animal models, especially when co-administered with opioids, but these findings could hitherto not be translated into clinical use (Deuis et al., 2017; Eagles et al., 2022; Mueller et al., 2019). Key issues of peptide-based Na$_V$1.7 inhibitors include poor tissue permeability, the inability to be administered orally, rapid clearance and the risk of triggering an immune response (Eagles et al., 2022; Recio et al., 2017). Further, animal models used in preclinical studies often do not represent the pathophysiology of human chronic pain, leading to a failure of pharmaceutical development programs in the clinical phase (Eagles et al., 2022; Hill, 2000; Mogil, 2009). Other challenges could include not accounting for β-subunits' influence (Eagles et al., 2022). Research is ongoing to determine the proportion of Na$_V$1.7 that must be targeted to achieve effective analgesia and to identify the optimal target locations within the nervous system, whether central or peripheral (Goodwin and McMahon, 2021; Vetter et al., 2017).

Further elucidating the interactome of Na$_V$1.7 may reveal new druggable targets involved in the channels' regulation. Dustrude et al., Moutal et al., and Loya-López et al. discovered that CRMP2 SUMOylation regulates peripheral Na$_V$1.7 channels in a cell-specific manner, influencing chronic neuropathic pain without affecting physiological pain responses (Dustrude et al., 2013; Loya-López et al., 2022; Moutal et al., 2020). The identification of this cell-specific regulation by CRMP2 encouraged further research into non-opioid protein-protein inhibitors targeting Na$_V$1.7 regulation as a therapeutic strategy against neuropathic pain (Cai et al., 2021; Loya-López et al., 2022).

Understanding the precise cellular and molecular involvement of Na$_V$1.7 in pain pathways could aid in developing treatments for chronic pain and pain disorders, resulting in more effective and safer medications. Given the widespread incidence of opioid abuse, the development of novel non-addictive therapeutics, e.g. ones targeting peripheral nociceptors, is of significant value (Eagles et al., 2022; Manchikanti et al., 2012; Paulozzi et al., 2011). However, high amino acid sequence homology among Na$_V$ subtypes complicates the development of subtype-specific ligands, for example, the unintended activation of Na$_V$1.9 channels by Na$_V$1.7 inhibitors which could obscure an analgesic effect (Catterall et al., 2005; Eagles et al., 2022; Zhou et al., 2020). Low molecular weight inhibitors, such as TTX, lack selectivity, whereas venom peptides exhibit excellent selectivity and high potency, making them promising candidates for pharmaceutical and probe development (Eagles et al., 2022; Peigneur and Tytgat, 2018; Safavi-Hemami et al., 2019; Shen et al., 2018; Thakur et al., 2022; Xu et al., 2024). Further developments have led to, e.g., sulfonamide-based small organic inhibitors targeting the Na$_V$1.7 channel, aiming to improve selectivity by binding outside the pore domain and stabilizing the inactivated state (Ahuja et al., 2015; Sun et al., 2014). PF-05089771, an aryl sulfonamide, failed in a Phase II trial for diabetic neuropathy, while acyl sulfonamides GX-201 and GX-585 showed better preclinical efficacy but may be limited by high plasma protein binding (Alexandrou et al., 2016; Bankar et al., 2018; Eagles et al., 2022; Focken et al., 2016; McDonnell et al., 2018). Xen402, a benzodioxol inhibitor, also failed in a Phase II trial for post-herpetic neuralgia (Eagles et al., 2022; Goldberg et al., 2012; Price et al., 2017). CNV1014802, a pyrrolidine-based inhibitor, displayed low Na$_V$ subtype-selectivity and mixed results in trigeminal neuralgia trials and continues in development (Eagles et al., 2022; Kotecha et al., 2020; Zakrzewska et al., 2017).

In particular, venoms containing the Inhibitory Cystine Knot (ICK) domain, such as the pore-blocker KIIIA and the gating modifier toxin Pn3a, are potent modulators of the Na$_V$1.7 channel (Mueller et al., 2019; Wilson et al., 2011). However, peptide drug development faces numerous challenges, including rapid renal clearance, immunogenicity, poor oral bioavailability, and degradation before achieving the desired pharmacological effect (Muttenthaler et al., 2021; Wang et al., 2022). While intrathecal administration, as seen with ziconotide, can bypass these issues, it imposes a significant burden on patients (Smith and Deer, 2009). Therefore, developing an ideally orally available peptide drug is highly desirable but challenging, as it requires specific modifications and specialized formulations (G. Chen et al., 2022; Nugrahadi et al., 2023).

1.4 Knottins and the Inhibitory Cystine Knot (ICK) motif

Peptide toxins exhibit significant structural diversity, yet many share the common feature of disulfide bonds, which play a crucial role in stabilising their unique and biologically active three-dimensional structures (Lavergne et al., 2015). In venom peptides, the most common structural motif is the Inhibitor Cystine Knot (ICK) (Undheim et al., 2016). Disulfide bonds are covalent linkages between two thiol side-chains of the amino acid cysteine to form a sulfur-sulfur-bond (cystine). The structural description of the Potato Carboxypeptidase A Inhibitor (PCI) in 1982 was the first mention of a peptide with three disulfides that displayed a distinct knotted topology (Rees and Lipscomb, 1980). In 1993, the structure of three knotted cystine was first described in an animal toxin, the ω-conotoxin GVIA, a voltage-gated calcium channel antagonist found in the venom of *Conus geographus* (Davis et al., 1993; Olivera et al., 1984).

Following these discoveries, in the 1990s, the term “Knottin” was established to describe the arrangement of three interwoven (“knotted”) cystines. However, based on the inhibitory activity that many peptides with this particularly knotted cysteine topology display, the term “Inhibitor Cystine Knot” was proposed. Both terms are often used synonymously, even though ICK also implies an inhibitory function (Craik et al., 2001; Galochkina and Gelly, 2022). According to the KNOTTIN database, the term knottin is used more generally and comprises of different families of knotted disulfide rich peptides, cyclic cystine knots, growth factor cystine knots and inhibitor cystine knots, each of them describing a structurally unique subgroup (Daly and Craik, 2011; Postic et al., 2018).

The general structure of the ICK motif and the three-dimensional structure of an example ICK peptide are shown in **Figure 6 A-D** (Craik et al., 2001; Galochkina and Gelly, 2022). ICKs are between 30 – 50 amino acids and have at least three disulfide bonds (Postic et al., 2018). Two of the three disulfides form a macrocyclic ring with the peptide backbone, and a third disulfide threads through this ring (Galochkina and Gelly, 2022; Postic et al., 2018). This intramolecular knot is accompanied by antiparallel β-strands, an integral feature of ICKs (**Figure 6 C**) (Pallaghy et al., 1994). ICK peptides all share the characteristic cysteine connectivity **I-IV**, **II-V** and **III-VI** (**Figure 6 B**, **C**) with the **III-VI** disulfide bond threading through the loop (**Figure *6* A**). This pattern distinguishes ICK peptides from other cystine knot peptides, which may have different connectivity, such as growth factor cystine-knots, a different cystine penetrating the macrocycle, or additional structural features such as backbone cyclisation seen in plant-derived cyclotides (Craik et al., 1999;

Galochkina and Gelly, 2022; Postic et al., 2018). ICK peptides further share the cysteine framework $CX_{3–7}CX_{3–8}CX_{0–7}CX_{1–4}CX_{4–13}C$ (X can be any amino acid) (Craik et al., 2001). This further specification implies that certain conotoxins, despite exhibiting the ICK connectivity, would be distinguished by their cysteine framework, sequence length, or lack of β-strands. Further, the connectivity alone is not sufficient to form a knot, as the loop space also impacts the peptide structure (Craik et al., 2001). A more detailed description of conotoxins can be found in section 1.5. The Nuclear Magnetic Resonance (NMR) structure in **Figure 6 D** belongs to the conotoxin GS that displays an ICK motif (Hill et al., 1997).

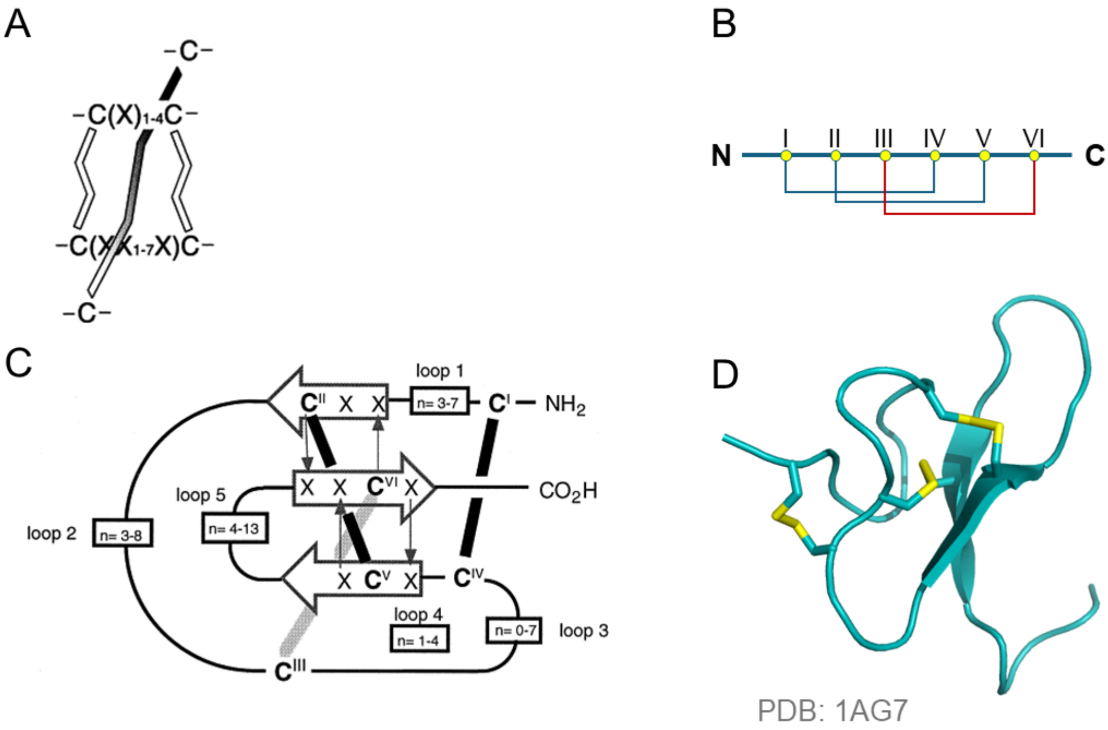

Figure 6. Schematic depiction of the structural arrangement and consensus features of the Inhibitory Cystine Knot (ICK) motif. **(A)** A molecular knot is formed by two cystines that form a loop with the peptide backbone a third cystine threads through the loop, creating the impression of a knot. Figure taken from (Craik et al., 2001). **(B)** A one-dimensional schematic representation of cysteine connectivity with the threading cystine in red. The six cysteines (yellow dots) involved in forming the three cystines of the motif are enumerated in Roman numerals. N- and C-terminus are designated as N and C. Figure redrawn from (Galochkina and Gelly, 2022). **(C)** β-strands are depicted as arrows, with cysteine (C) and other variable residues (X) indicated. Cysteine residues are numbered I to VI, while loops are identified as 1 to 5; the count of residues between cysteines in each loop is displayed in boxed numerals. Hydrogen bonds are represented by arrows pointing from the amide proton to the carbonyl oxygen. Figure taken from (Craik et al., 2001). **(D)** Three-dimensional NMR structure of conotoxin GS from *Conus geographus*, exemplifying the topology of the ICK domain (Hill et al., 1997). The disulfides are shown in yellow. Image rendered with PyMol (PDB: 1A7G)

Disulfide-rich peptide toxins usually show excellent stability towards proteolytic, thermal or chemical degradation (Colgrave and Craik, 2004; Roesler and Rao, 2000). Further, the disulfide scaffold restricts and rigidises the structure. Despite the rigidity, the disulfide framework allows for high variability in the inter-cystine loops (King, 2015). The presence of the knottin motif throughout many different phyla and taxa highlights the evolutionary success due to the inherent stability and the pharmacological potency, selectivity and specificity (Saez et al., 2010; Schendel et al., 2019; Undheim et al., 2016; Zhu et al., 2003). As of July 2024, the UniProt database hosts 12157 entries with both keywords "knottin" and "toxin", 2242 of which are reviewed entries (The UniProt Consortium, 2023).

1.5 Conotoxins (CTX) – Components of *Conus* venoms

Cone snails are venomous marine gastropods belonging to the *Conidae* family, comprising 500-700 species within the *Conus* genus. They are renowned for their predatory behaviour (Dutertre et al., 2014; Puillandre et al., 2015; Röckel et al., 1995). To immobilise prey, cone snail venoms contain various disulfide-rich peptides, so-called conotoxins, that potently act on a variety of receptors (e.g., G protein-coupled receptors), ion channels and enzymes (Akondi et al., 2014; Terlau et al., 1996; Vetter and Lewis, 2012). Single venoms can contain over 1000 different peptides, and the existence of hundreds of thousands of conotoxins is estimated (Biass et al., 2009; Davis et al., 2009; Dutertre and Lewis, 2011). Conotoxins are classified by their pharmacological target and structural features, and can be further classified by their gene superfamily, which is determined by the sequence of their precursors (Akondi et al., 2014; Kaas et al., 2010). Conotoxin sequences can span 11 - 50 amino acids and contain between 2-5 disulfides, and some larger conotoxins form dimers (Jin et al., 2019). In **Table 1**, cysteine patterns, disulfides, and pharmacological families of the different frameworks are listed to give an overview of the structural diversity.

Loop structures in between the stabilising disulfide frameworks of conotoxins display short secondary-structure motifs, such as α-helices, β-turns, and β-sheets. These structural features contribute to their high potency, receptor selectivity, and protease resistance. Even within the same cysteine framework, conotoxins show a wide range of structural diversity. Disulfide bond connectivity, loop region size, and sequence can lead to varied three-dimensional structures and distinct pharmacological effects (Akondi et al., 2014; Jin et al., 2019).

Their structural stability, small size, target specificity and synthetical availability make conotoxins valuable for neurological research and drug development; Conotoxins are excellent molecular probes for validating targets and discovering peptide drug candidates. Pain-related conotoxin research that focused on identifying novel ion channel modulators has led to the development of Ziconotide (Prialt, synthetic ω-MVIIA), an FDA-approved drug derived from *Conus magus*, which blocks N-type calcium channels to treat severe chronic pain (Akondi et al., 2014; Jin et al., 2019; Norton, 2010; Safavi-Hemami et al., 2019; Smith and Deer, 2009; Vetter and Lewis, 2012; Wilson et al., 2011).

Table 1. Cysteine Frameworks and Corresponding Pharmacological Families in Conotoxins. Framework III is highlighted in bold letters. X indicates any amino acid; O represents hydroxyproline; ND means not determined at the molecular level; α refers to nicotinic acetylcholine receptors; γ pertains to neuronal pacemaker cation currents (inward cation current); δ denotes VGSCs (agonist, delays inactivation); ε indicates presynaptic calcium channels or G protein-coupled presynaptic receptors; ι refers to VGSCs (agonist, no delayed inactivation); κ denotes voltage-gated K channels (blocker); μ represents VGSCs (antagonist, blocker); ρ refers to α1-adrenoceptors; σ denotes serotonin-gated ion channels 5-HT3; τ indicates somatostatin receptor; χ represents neuronal noradrenaline transporter; ω refers to voltage-gated calcium channels (blocker); and φ indicates granulin activity. Table from source (Jin et al., 2019).

Framework	Cysteine Pattern	Disulfides	Pharmacol. Family
I	CC−C−C	2	α, ρ
II	CCC−C−C−C	3	α
III	**CC−C−C−CC**	**3**	**α, ι, κ, μ**
IV	CC−C−C−C−C	3	α, κ, μ
V	CC−CC	2	ε, μ, τ
VI/VII	C−C−CC−C−C	3	δ, γ, κ, μ, ω
VIII	C−C−C−C−C−C−C−C−C−C	5	α, σ
IX	C−C−C−C−C−C	3	ND
X	CC−CXOC	2	χ
XI	C−C−CC−CC−C−C	4	ι, κ
XII	C−C−C−C−CC−C−C	4	ND
XIII	C−C−C−CC−C−C−C	4	ND
XIV	C−C−C−C	4	α, κ
XV	C−C−CC−C−C−C−C	4	ND
XVI	C−C−CC	4	ND

XVII	C−C−CC−C−CC-C	4	ND
XVIII	C−C−CC−CC	3	ND
XIX	C−C−C−CCC−C−C−C−C	5	ND
XX	C−CC−C−CC−C−C−C−C	5	α
XXI	CC−C−C−C−CC−C−C−C	5	ND
XXII	C−C−C−C−C−C−C−C	4	ND
XXIII	C−C−C−CC-C	3	ND
XXIV	C−CC−C	2	α
XXV	C−C−C−C−CC	3	ND
XXVI	C−C−C−C−CC−CC	4	ω
XXVII	C−C−C−CCC−C−C	4	φ
XXVIII	C−CC−C−C−C	3	δ/κ

Five classes of conotoxins target Na$_V$ channels: μ-, μO-, μO-S-, δ-, and ι-conotoxins. Each class has unique structural features and distinct pharmacological effects. μ-Conotoxins are Na$_V$ channel inhibitors that bind to site 1 near the ion-conducting pore, thus blocking it (Cestèle and Catterall, 2000). They have been extensively studied for their therapeutic potential, particularly in pain management. However, their off-target activity at Na$_V$1.4, which led to paralysis and death of model organisms, has limited their development. Efforts are ongoing to engineer μ-conotoxins to target therapeutically relevant Na$_V$ isoforms selectively (Chen et al., 2018; Jin et al., 2019).

In contrast, μO-conotoxins inhibit Na$_V$ channels by interacting with the voltage sensor in domain II, restricting channel opening without blocking the pore. They are less studied due to synthesis challenges. δ-Conotoxins activate Na$_V$ channels by delaying inactivation, causing persistent neuronal firing, and interacting with hydrophobic residues in the S3/S4 linker of domain IV. ι-Conotoxins also activate Na$_V$ channels but through different mechanisms compared to δ-conotoxins. The general effects of different classes of conotoxins on Na$_V$ channels is illustrated in **Figure 7** by showing alterations in current-time diagrams after depolarisation and venom treatment as well as current-voltage diagrams that show the voltage dependence of sodium permeation (Israel et al., 2017).

Despite the varied mechanisms of these conotoxin classes, μ-conotoxins remain a key focus due to their potential applications and ongoing efforts to refine their selectivity and minimise side effects.

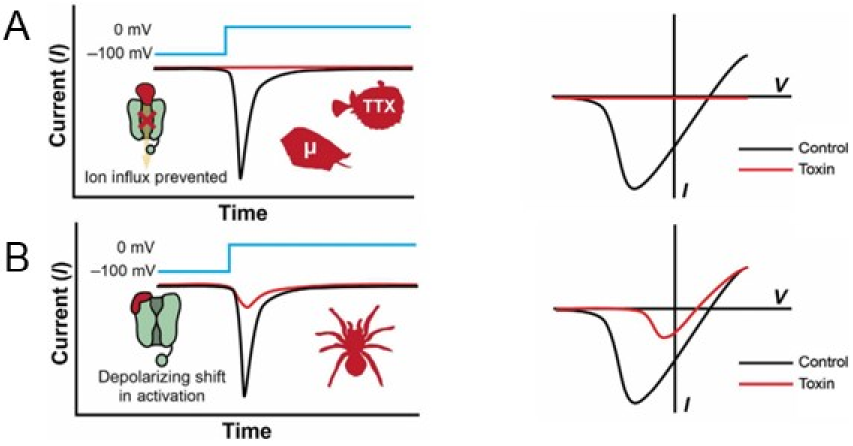

Figure 7. Current-time and current-voltage diagrams illustrating the effects of inhibitory conotoxins and spider venom peptides on VGSCs. **(A)** Pore-blocker toxins, such as TTX or μ-conotoxin KIIIA, occlude the sodium ion conductive pore of VGSCs. **(B)** Gating modifier toxins, such as μ-Theraphotoxin Pn3a, alter the voltage dependence of $Na_V1.7$ by shifting it to more depolarised potentials (Deuis et al., 2017). The effects of the toxins are indicative of an IC_{100} concentration. Figure taken and adapted from (Israel et al., 2017).

1.5.1 μ-Conotoxin-KIIIA

KIIIA is a 16 amino acid *μ*-conotoxin from *Conus kinoshitai* and is the shortest *μ*-conotoxin discovered hitherto (Bulaj et al., 2005; Khoo et al., 2009). The peptide is amidated at the C-terminus and contains six cysteine residues in the CC−C−C−CC pattern, thus being categorised as framework III (Bulaj et al., 2005). A structural depiction of KIIIA is provided in **Figure 8**. *μ*-conotoxins natively display I-IV, II-V and III-VI connectivity. Noticeably, for synthetic KIIIA folded thermodynamically, two isomers with different connectivity are obtained: Isomer 1 (I-V, II-IV, III-VI) and Isomer 2 (I-VI, II-IV, III-V) (Jin et al., 2019; Kaas et al., 2010; Khoo et al., 2012).

As a pore-blocker toxin, KIIIA occludes the Na^+-permeable pore of VGSCs. ***Figure 9*** shows the cryo-electron microscopy structure of KIIIA bound to the pore region of human $Na_V1.2$ and the β2-subunit from two perspectives. The positively charged Lys^7 resides in the Na^+ entry site of the pore and interacts with the critical Glu residue of $Na_V1.2$, preventing the influx of Na^+ cations (Pan et al., 2019). Other important residues determined via an alanine mutation experiments are Trp^8, Arg^{10}, Asp^{11}, His^{12}, all located within the α-helical sequence and Arg^{14}, located at the C-terminus (Zhang et al., 2007).

The inhibitory activity of KIIIA (isomer 1) on NaVs is reported in the literature with the following decreasing order on rat NaVs (rNa$_V$1.X): 2 > 4 > 6 > 1 ≈ 7 > 3 > 5, which display over 95% sequence identity with human NaVs (Goldin et al., 2000; Wilson et al., 2011; Zhang et al., 2007). A comparative study evaluated the activity of the three isomers on the pain targets Na$_V$1.7 and Na$_V$1.2, as well as Na$_V$1.4, which is associated with adverse off-target effects. Isomer 1 demonstrated the activity shown in **Table 2** and selectivity as follows: Na$_V$1.4 > Na$_V$1.2 > Na$_V$1.7; the native isomer exhibited a preference for Na$_V$1.4 > Na$_V$1.7 ≈ Na$_V$1.2; and Isomer 2 showed nearly equal potency at Na$_V$1.4 and Na$_V$1.2, with reduced effectiveness at Na$_V$1.7. (Tran et al., 2022)

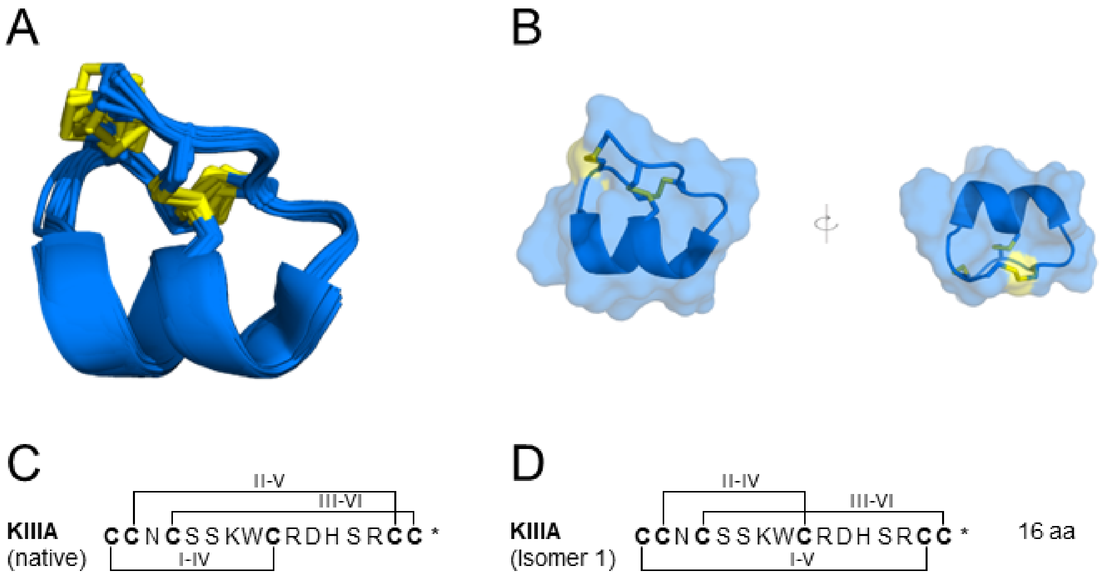

Figure 8. Three-dimensional structure and amino acid sequence of KIIIA. (A) Overlay of 20 NMR solution structures of the KIIIA backbone (blue) displaying the native fold. Disulfides are shown in yellow. **(B)** Backbone and surface (transparent) structures are shown from two different perspectives. **(C)** Sequence and connectivity of the 16 amino acid conotoxin KIIIA in the native fold. **(D)** Sequence and connectivity of KIIIA Isomer 1. Structures rendered with PyMol (PDB: 7SAV).

Table 2. Activity of different disulfide-isomers of KIIIA on hNaV1.2, hNaV1.4, and hNaV1.7 determined using automated electrophysiology. Data presented as mean (± SD), with n = 5 cells per data point. Table taken from (Tran et al., 2022).

Sodium Channel Subtypes	**IC$_{50}$ [nM]**		
	Isomer 1	**Isomer 2**	**Native KIIIA**
hNaV1.2	124 ± 34	1371 ± 403	875 ± 129
hNaV1.4	65 ± 15	2051 ± 482	472 ± 94
hNaV1.7	413 ± 71	5388 ± 547	887 ± 295

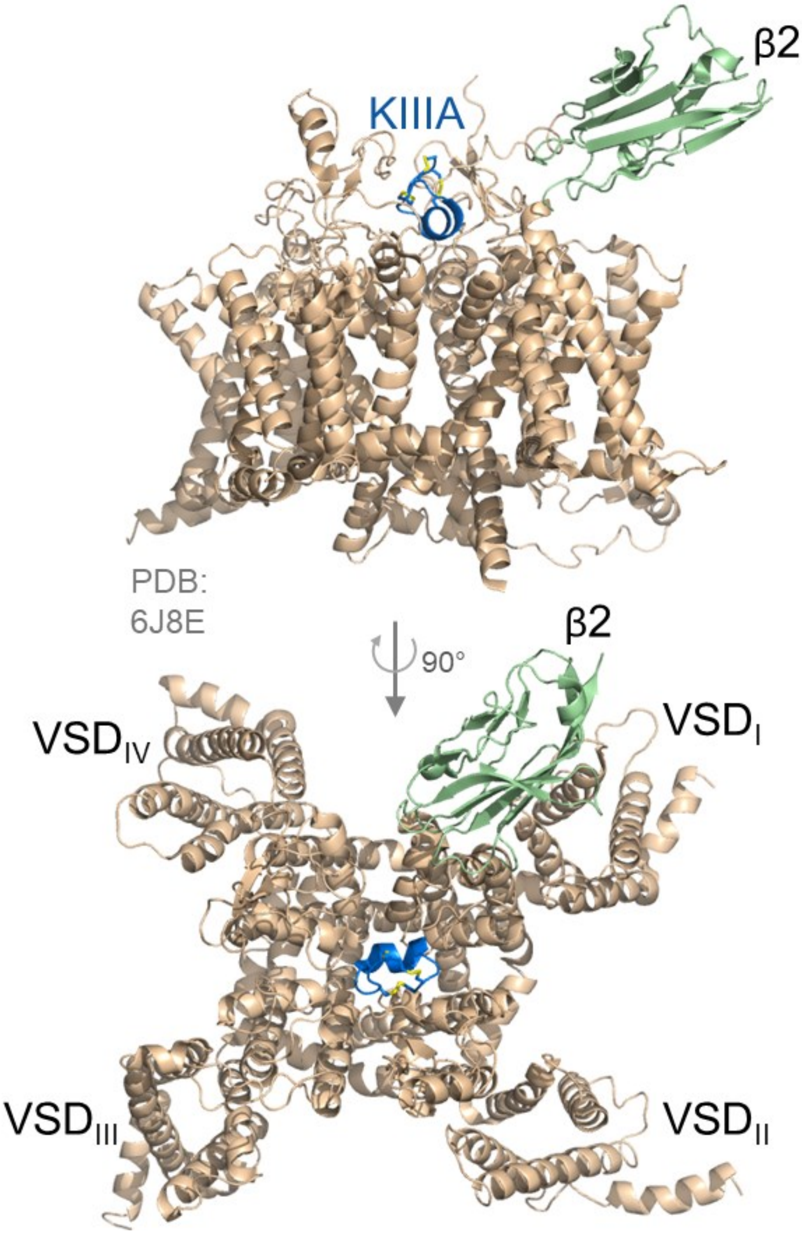

Figure 9. Structure of human $Na_V1.2$ with β2-subunit bound to KIIIA. The upper image shows a side perspective of $Na_V1.2$-pore-blockage by KIIIA. A top perspective is provided in the lower image. The β2-subunit is shown in green, KIIIA in blue and disulfides are highlighted in yellow. (Pan et al., 2019) Structures were rendered in PyMol (PDB: 6J8E).

1.6 Spider venom peptides

Spiders rank second only to insects and thus represent one of the largest groups of land-dwelling organisms. They evolved around 300 million years ago and inhabit many ecological niches (Kuhn-Nentwig et al., 2011; Wang et al., 2018). Spiders are known for their diverse and successful predatory abilities on land, boasting a vast number of over 52192 identified species (spread over 4391 genera) and possibly

>150,000 species worldwide (Guo et al., 2024; “NMBE - World Spider Catalog,” 2024). Their venoms contain specialised peptides for immobilising or killing prey or for self-defence, giving spiders an evolutionary advantage (Guo et al., 2024; Morgenstern and King, 2013). These compounds can affect mammals by interacting with receptor sites that are structurally conserved, as vertebrate and insect receptors—the primary prey of spiders—can have around 60% sequence identity (Dongol et al., 2019; Gordon et al., 1996; King, 2015; King et al., 2008a; Loughney et al., 1989; Nyffeler, 1999; Nyffeler and Birkhofer, 2017). Venom-gland transcriptomics and the application of proteomics have significantly impacted the study and discovery of spider venoms and their inherent diversity; the promising pharmaceutical properties of these venoms were soon recognised (Chen et al., 2008; Escoubas et al., 2006; Haney et al., 2014; King, 2011). With estimated over ten million peptides ranging from 2-8 kDa in size, spider venoms contain an immense library of pharmacologically interesting natural compounds (Escoubas et al., 2006; King, 2015, 2011).

Spider venoms comprise a chemically diverse cocktail of salts, organic molecules, peptides and proteins with and without enzymatic activity (Jackson and Parks, 1989; King and Hardy, 2013; Rash and Hodgson, 2002; Senji Laxme et al., 2019). Especially disulfide-rich peptide stand out as the active ingredients (Lüddecke et al., 2022; Pineda et al., 2020). Most disulfide-rich spider toxins are fewer than 40 amino acids long and adopt the ICK motif (King, 2015; Shaikh and Sunagar, 2023). These ICK toxins are potent modulators of ion channels, with the majority targeting NaVs (Dongol et al., 2019). Based on their sequence characteristics and cysteine framework, these toxins are categorized as NaSpTxs (“Nav-targeting spider toxins”) in twelve families (NaSpTx 1-12) (Klint et al., 2012). Spider toxins mainly bind at two allosteric binding sites in VGSCs, the extracellular side of VSDII (Site 4) and VSDIV (Site 3). These binding sites and their mode of NaV-modulation categorises them as gating modifier toxins (GMTs) (Catterall et al., 2007). Modulation of VGSC by GMT leads to peak-current inhibition by two different modes, either by arresting the VSD in the closed state or altering the voltage-dependence by shifting it to more depolarised potentials, as shown in **Figure 7 (B)** (Israel et al., 2017). GMTs also show affinity for and interact with lipids of the membrane (Henriques et al., 2016; Jung et al., 2010; Milescu et al., 2007). The surface of GMTs features a hydrophobic area encircled by positively charged amino acid residues that interact with conserved hydrophobic and negatively charged residues on the different VGSC sites. The positively charged Lys as well as Trp, and Tyr play an important role in the process of lipid interaction (Agwa et al., 2017). The concept of a "trimolecular relationship" has emerged, where the lipid membrane facilitates the interaction with VGSC by anchoring and positioning the GMT optimally (Agwa et al., 2017; Henriques et al., 2016; Lau et al., 2016).

A comparison of three GMT of different NaSpTxs between 30 and 35 amino acids targeting Na$_V$1.7 at site 4 will be given to exemplify the mode of action and Na$_V$ modulation. The theraphotoxin (TRTX) HwTx-IV (Huwentoxin-IV, μ-TRTX-Hh2a) is a member of NaSpTx family I and inhibits Na$_V$1.7 (IC$_{50}$ ~30 nM) by trapping VSD$_{II}$ (Neff and Wickenden, 2021; Peng et al., 2002; Xiao et al., 2008). Pn3a (μ-TRTX-Pn3a), which belongs to NaSpTx family II and will be further highlighted in the following section, inhibits Na$_V$1.7 (IC$_{50}$ 0.8 nM) with a high selectivity (40 fold) over other subtypes (Deuis et al., 2017; Mueller et al., 2020; Neff and Wickenden, 2021). The NaSpTx family III member ProTx-II (β/ω-TRTX-Tp2a) is one of the most potent and selective NaV$_{1.7}$ inhibitors (IC$_{50}$ 0.3 nM) with high selectivity over other subtypes (~100 fold) (Schmalhofer et al., 2008; Xiao et al., 2010; Xu et al., 2019). The sequences of these three GMT and their respective IC$_{50}$ are provided in **Figure *10*** (Neff and Wickenden, 2021).

In lieu of a full structure of Pn3a bound to Na$_V$1.7, a crystal structure for ProTx-II, a GMT with a similar pharmacological profile at Na$_V$1.7 and sharing a binding site analogous to Pn3a, shifts the voltage dependence of Na$_V$1.7 activation to more

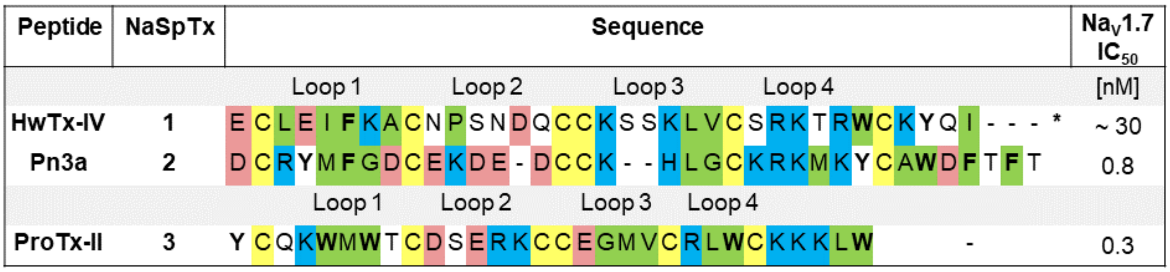

Peptide	**NaSpTx**	**Sequence**	**Na$_V$1.7 IC$_{50}$**
		Loop 1 Loop 2 Loop 3 Loop 4	[nM]
HwTx-IV	1	ECLEI**F**KACNPSNDQCCKSSKLVCSRKTR**W**CK**Y**QI - - - *	~ 30
Pn3a	2	DCR**Y**M**F**GDCEKDE - DCCK - - HLGCKRKMK**Y**CA**W**D**F**T**F**T	0.8
		Loop 1 Loop 2 Loop 3 Loop 4	
ProTx-II	3	**Y**CQK**W**M**W**TCDSERKCCEGMVCRL**W**CKKKL**W** -	0.3

Figure 10. Sequence alignment of spider toxins HwTx-IV, Pn3a and ProTx-II. These knottins belong to three different NaSpTx families and target site 4 of Na$_V$1.7. IC$_{50}$ values are taken from sources specified in the text. Yellow highlights indicate conserved cysteines, blue marks positively charged residues, red represents negatively charged residues, green shows hydrophobic residues, and bold letters show aromatic residues. The asterisk (*) denotes an amidated C-terminus. Loop regions between cysteines are indicated. Figure adapted from (Dongol et al., 2019).

depolarised (positive) potentials (see **Figure 7 (B)**), as shown in **Figure 11** (Deuis et al., 2017; Mueller et al., 2020; Xu et al., 2019). As displayed in the crystal structure, the peptide toxins resides on the outside of the VSDs of the channel (**Figure 11 (A-C)**). In this model, a bacterial Na$_{V}$Ab has been engineered by transferring hNa$_{V}$1.7 VSD$_{II}$s onto the bacterial channel. ProTx-II allosterically binds to the S3-S4 loop region of VSD$_{II}$ of Na$_{V}$1.7 to arrest the channel in active and inactive (closed) states, even though the affinity for closed Na$_{V}$1.7 channel conformation is higher. The mode of VSD$_{II}$ modulation is electrostatic and relies on opposing charges on the surface of the peptide as well as the channel's VSD. ProTx-II also interacts with the membrane during VSD binding (Xu et al., 2019). Despite the promising *in vitro* properties of ProTx-II, the high affinity and selectivity for Na$_{V}$1.7 failed to translate into *in-vivo* analgesia in animal models (Schmalhofer et al., 2008). In contrast, HwTx-IV relieved acute inflammatory and chronic neuropathic pain in animal models. However, neuromuscular side effects due to low

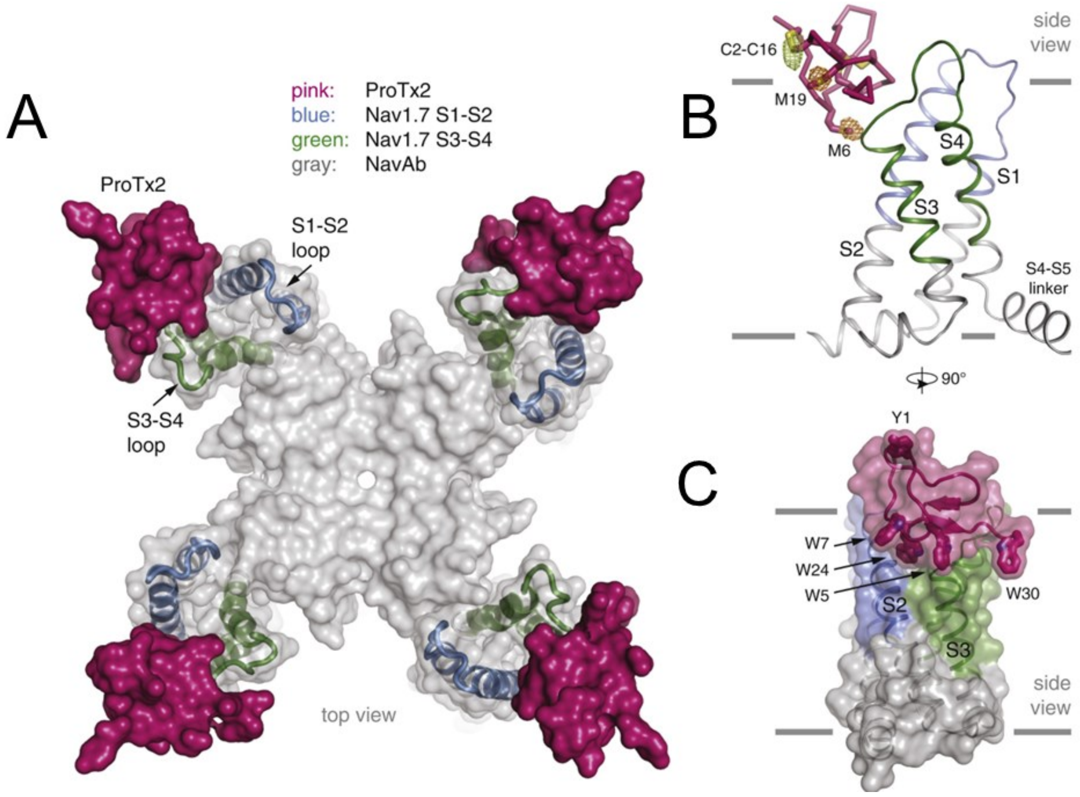

Figure 11. The crystal structure of the ProTx-II-VSD$_{II}$-NavAb channel. (A) The complex between VSD$_{II}$-NavAb and ProTx-II-viewed from the top, with the human Nav1.7 VSD$_{II}$ segment displayed in blue (S1–S2) and green (S3–S4). **(B)** A membrane view of the backbones of ProTx-II and the VSD$_{II}$. ProTx-II resides on the VSDs outer face and within the membrane. Yellow and orange mesh from SeCys2-SeCys16 for anomalous difference peaks of SeMet-ProTx-II derivatives at M6 and M19, respectively. Another membrane view spotlighting Y1, W5, W7, W24, and W30 on ProTx-II. Figure modified from (Xu et al., 2019).

subtype-selectivity challenged making use of the antinociceptive efficacy of this spider venom peptide (Liu et al., 2014; Rahnama et al., 2017). Pn3a, on the other hand, has shown promising antinociceptive properties, which will be discussed in the following section (Deuis et al., 2017; Mueller, 2020; Mueller et al., 2019).

1.6.1 μ-Theraphotoxin Pn3a

Theraphotoxins are the bioactive, disulfide-rich peptides found in the venoms of spiders of the *Theraphosidae* family (King et al., 2008b; Klint et al., 2012). This family of spiders consists of 168 genera and 1109 species ("NMBE - World Spider Catalog," 2024). Pn3a is a 35-residue spider venom peptide that was isolated from the venom of the South American tarantula *Pamphobeteus nigricolor*. It displays typical ICK structure and, as briefly described in previous sections, acts as a GMT and inhibits VGSC with a high selectivity for $Na_V1.7$. A structural depiction of Pn3a, as well as the amino acid sequence, is provided in **Figure 12** (Deuis et al., 2017).

As a GMT, Pn3a binds the neurotoxin binding site 4 of Na_Vs. The general mode of action is similar to ProTx-II described in the previous section. It involves Pn3a interacting with the S3-S4 linkers in VSD_{II} and VSD_{IV} of $Na_V1.7$, ultimately leading to a shift in voltage-dependence of the activation to more depolarised potentials, as shown (See **Figure 7 (B)**) (Deuis et al., 2017; Israel et al., 2017).

Since its first pharmacological characterisation and structural elucidation in 2017, Pn3a has been regarded as a very potent and one of the most selective inhibitors of $Na_V1.7$, a valuable tool to probe the channel and possesses an analgesic potential (Deuis et al., 2017; Mueller, 2020; Mueller et al., 2019). Syntheses have been published showing that Pn3a can be accessed *via* Solid Phase Peptide Synthesis (SPPS) (see 3.1.2 and 3.1.3) and thermodynamic folding of a linear precursor (see 3.1.6) (Deuis et al., 2017; Mueller, 2020; Tran et al., 2023a). Pn3a has also been successfully recombinantly expressed from *E. coli* (rPn3a) which has, for example, allowed isotopic labelling of the peptide for binding studies (Sharma et al., 2020). Structure-activity-relationship (SAR) investigations have found that mutating the negatively charged aspartic acid to charge-neutral asparagine (D8N mutation) results in enhanced activity on $Na_V1.7$ and analgesic effects *in vivo* after systemic administration in a $Na_V1.7$ mouse model. *In vitro*, Pn3a[D8N] most potently inhibited $Na_V1.7$ (IC_{50} 0.21 nM), with >40-fold to >1000-fold selectivity over other subtypes (Mueller et al., 2020). A comparison of wild-type Pn3a and Pn3a[D8N]

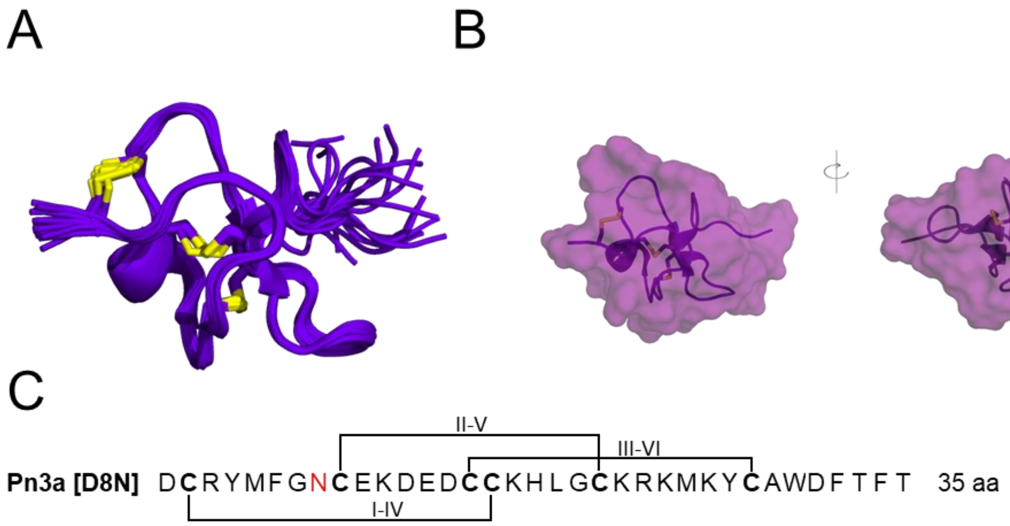

Figure 12. Three-dimensional structure and amino acid sequence of wild-type Pn3a. (A) 20 lowest energy NMR structures are superimposed in deep purple. Disulfides are shown in yellow. **(B)** Transparent surface plot with backbone of two perspectives of one selected state of the peptide. **(C)** The sequence and cysteine connectivity of the [D8N] mutant is shown with the mutation highlighted in red - structures rendered with PyMol (PDB: 5T4R).

selectivity and IC_{50} for several Na$_V$ subtypes is provided in **Table 3** with values taken from (Deuis et al., 2017; Mueller et al., 2020). Systemic co-administration of subtherapeutic doses of opioid receptor agonists and Pn3a in different mouse models of pain produced analgesia and antiallodynic effects in a synergistic manner (Deuis et al., 2017; Mueller et al., 2019). However, no analgesic efficacy

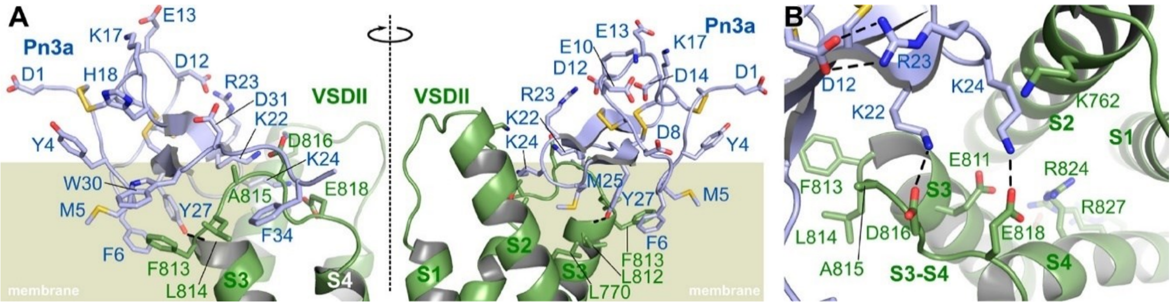

Figure 13. A molecular model depicting the interaction between wild-type Pn3a and the Nav1.7 VSD$_{II}$ (down state). (A) The model features side-view perspectives, rotated by 180°, illustrating the interaction between Na$_V$1.7's VSD$_{II}$ (green) and Pn3a (light blue) with the membrane marked in olive green. The VSD$_{II}$ comprises four α-helical segments S1–S4. **(B)** Zoom-perspective to highlight the electrostatic interactions of positively charged residues Lys^{22} and Lys^{24} with the negatively charged Asp^{816} and Glu^{818} in the S3–S4 segment (Relevant side-chains shown as sticks, hydrogen bonds as dashed lines). The molecular models are based on homology modelling with the cryo-EM structure of the hNa$_V$1.7 VSD$_{II}$-Na$_V$Ab chimera bound to ProTx-II (PDB 6N4R), the cryo-EM structure of hNav1.7 (PDB 6J8H), and the NMR solution structure of Pn3a (PDB 5T4R) as templates. Figure taken from (Mueller et al., 2020).

was observed against formalin, carrageenan, or Freud's complete adjuvant-induced pain after intraplantar injection in mice (Deuis et al., 2017).

Table 3. Potency of Pn3a[D8N] and wild-type Pn3a at Nav-subtypes and their fold selectivity relative to Nav1.7. Data is presented as mean IC_{50} assessed by whole-cell patch–clamp experiments. Pn3a and Pn3a[D8N] subtype-selectivity is independently determined as the ratio of the IC_{50} value obtained for each respective isoform relative to $Na_V1.7$, calculated by $IC_{50}(Na_V1.X)/IC_{50}(Na_V1.7)$. Table adopted from (Deuis et al., 2017; Mueller et al., 2020).

	Pn3a[D8N]		Pn3a	
Na_V subtype 1.X	IC_{50} [nM]	$Na_V1.7$ selectivity	IC_{50} [nM]	$Na_V1.7$ selectivity
1	14	67	37	41
2	9	43	124	138
3	48	229	210	233
4	97	462	144	160
5	343	1633	800	889
6	25	119	129	143
7	0.21	1	0.9	1
8	>1000	>4762	>1000	>1111

Most interestingly, Pn3a's off target activities on other subtypes are low at efficacious concentrations at $Na_V1.7$ and other ion channels such as voltage-gated potassium or calcium channels, nicotinic acetylcholine receptors were not affected by Pn3a at concentrations higher than required to inhibit $Na_V1.7$ inward current (Deuis et al., 2017). It is unclear how these findings would translate into clinical use against chronic pain states, as animal models do not ideally represent humans. Additionally, the almost complete inhibition of $Na_V1.7$ channels required to achieve pain-free states is not achieved with Pn3a (Eagles et al., 2022). Nevertheless, Pn3a remains an interesting platform for the development of therapeutic strategies targeting $Na_V1.7$, as well as a valuable probe for studying the channel's involvement in pain (Deuis et al., 2017).

1.7 Proximity Ligation Assay

The Proximity Ligation Assay (PLA) is a molecular biological technique for visualising and quantifying proteins, protein interactions, modifications, and presence within a cell. It combines the specificity of antibodies with the sensitivity of DNA amplification (Bagchi et al., 2015; Söderberg et al., 2006). The method was first described in 2002 and showed high sensitivity, enabling the detection of zeptomole (40 × 10−21 mol) of the cytokine platelet-derived growth factor (Fredriksson et al., 2002). In the classic set-up, PLA leverages the principle that two antibodies, each conjugated to a unique oligonucleotide, can bind to their respective target epitopes on (interacting) proteins. When these antibodies are in close proximity (typically within 40 nanometers), the attached oligonucleotides serve as templates for a DNA amplification reaction (Bagchi et al., 2015; Cane et al., 2017; Söderberg et al., 2006).

The procedure is illustrated in **Figure 14** and begins with the incubation of a sample that contains potentially interacting proteins of interest with primary antibodies. The antibodies recognise different epitopes of the proteins and are raised in different species to ensure specificity and reduce cross-reactivity. Secondary antibodies conjugated with complementary oligonucleotides (PLA probes, plus and minus) are then added. If the target proteins are in close proximity and the primary antibodies successfully bind, the oligonucleotides on the PLA probes can hybridise into a connector oligonucleotide, allowing the ligation of the two PLA probes' oligonucleotides into a circular DNA molecule (Bagchi et al., 2015; Cane et al., 2017).

This circular DNA serves as a template for rolling circle amplification (RCA), a process that generates a long single-stranded DNA product, which remains tethered to the site of the interaction. The RCA product can then be detected using fluorescently labelled complementary oligonucleotide probes, enabling the visualisation of protein interactions as fluorescent spots under a fluorescence microscope. Each fluorescent spot corresponds to a single protein interaction event, allowing for quantitative analysis (Bagchi et al., 2015; Cane et al., 2017).

PLA offers several advantages, including high sensitivity and specificity, the ability to detect low-abundance proteins, and the capability to study protein interactions *in situ* within fixed cells or tissue sections. The PLA can be valuable for understanding protein interactions and modifications, elucidating cellular mechanisms and disease pathways. Its compatibility with standard immunofluorescence microscopy infrastructure and commercial availability of PLA reagents also enhances its accessibility (Bagchi et al., 2015; Cane et al., 2017). For example, in NaV1.7 research, the PLA was employed to visualize NaV1.7-protein interactions, leading

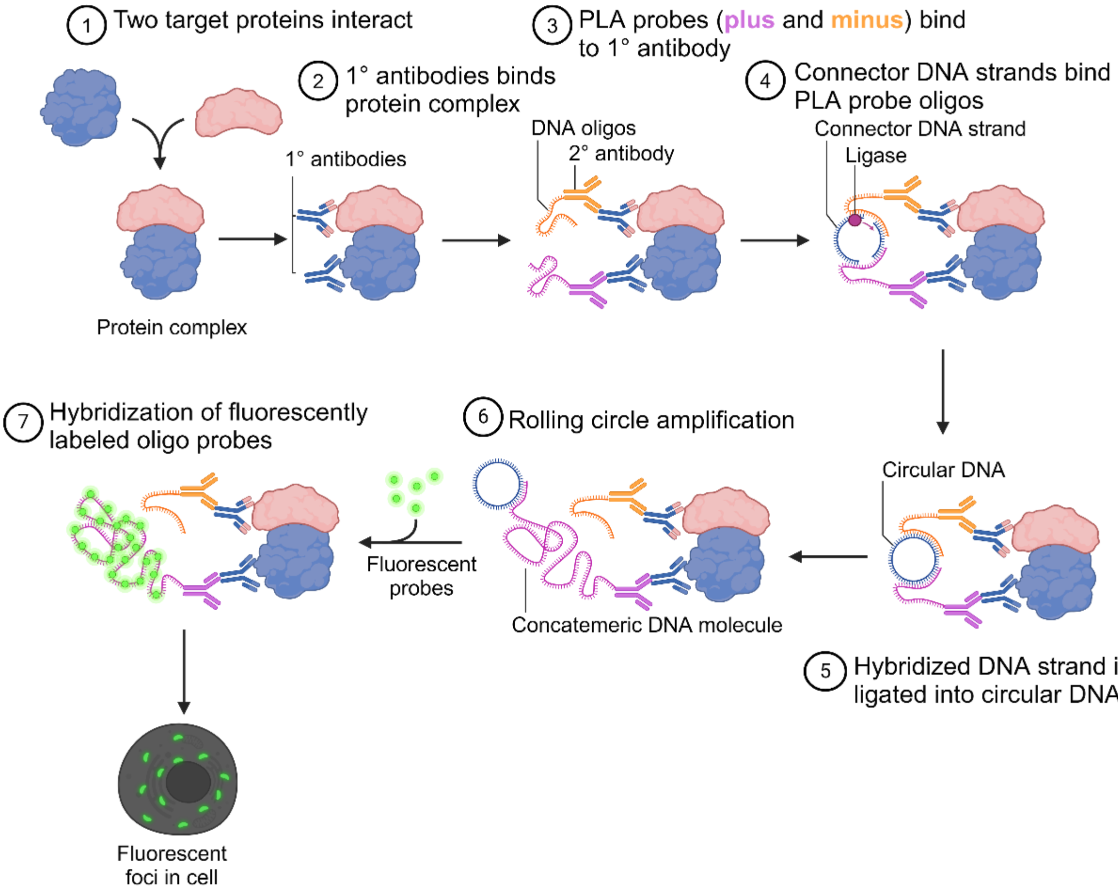

Figure 14. Proximity Ligation Assay (PLA). An illustration of the PLA, starting with the interaction of two target proteins and ending with the detection of fluorescent signals *in cellulo*. The steps include **(1)** the interaction of two target proteins, **(2)** the binding of primary antibodies to different epitopes of the protein complex, **(3)** the subsequent binding of PLA probes to the primary antibodies, **(4)** the ligation of connector DNA strands that bind the PLA probe oligos, **(5)** the ligation of hybridised DNA strands into circular DNA, **(6)** the rolling circle amplification (RCA) producing concatemeric DNA, and **(7)** the hybridisation of fluorescently labelled oligo probes resulting in visible fluorescent signals that indicate the protein-protein interaction - figure created with BioRender.

to the elucidation of the CRMP2 SUMOylation mechanism in Na$_V$1.7 regulation. This discovery has paved the way for the potential use of protein-protein inhibitors targeting antiallodynic nociception in pain models (Cai et al., 2021; Loya-López et al., 2022; Moutal et al., 2020).

2 Research Aim

Investigating $Na_V1.7$, along with its regulation and interactome, is crucial for advancing our understanding of its role in disease and supporting drug development. The PLA is a highly sensitive and selective antibody-based imaging technology, capable of visualizing $Na_V1.7$ *in situ*, offering insights into its molecular mechanisms.

Venom peptides, known for their selective binding to ion channels, have significantly advanced our understanding of Na_Vs through structural and functional studies. We aim to develop a modified PLA for $Na_V1.7$ visualization by utilizing the high target affinity and selectivity of venom peptides. This novel approach involves replacing primary antibodies with venom peptide-based probes.

The focus of this work is on designing probes based on two selective venom peptides, each tagged with a specific epitope sequence. These tags will enable the probes to be recognized by antibodies raised against them. The aims of this work are to:

I. Design venom peptides-based probes for $Na_V1.7$ and explore the synthetic feasibility

II. Biologically test synthesized probes against $Na_V1.7$

III. Evaluate the feasibility of developing a venom peptide-based PLA based on the outcomes of the synthesis (**II**) and testing (**III**).

3 Research Methodology

3.1 Peptide Synthesis: Historical Overview and Methodologies

Peptide chemistry has evolved significantly since its inception in the late 19th century, driven by advances in synthetic techniques, structural elucidation methods, and therapeutic applications. The field's early milestones include Theodor Curtius's 1882 synthesis of N-protected benzoylglycylglycine and the 1902 creation of the free dipeptide glycylglycine by Ernest Fourneau and Emil Fischer, who also introduced the term “peptide” (Babu, 2001; Curtius, 1882; Fischer and Fourneau, 1901). A significant advancement occurred in 1932 when Max Bergmann introduced the carbobenzoxy (Cbz) protecting group for amine protection three decades after Fischer’s initial peptide synthesis (Bergmann and Zervas, 1932). This development laid the foundation for protection group chemistry, which has become a crucial aspect of peptide synthesis. The 1950s brought significant advancements in peptide chemistry when Vincent du Vigneaud synthesised the octapeptide oxytocin (CYIQNCPLG-NH_2) in 1953, earning the Nobel Prize for his contributions in 1955. Additionally, the decade saw the introduction of another vital protecting group, the Boc group (tert-butyloxycarbonyl), by Albertson and McKay in 1957, further enriching the peptide chemist’s arsenal (McKay and Albertson, 1957; “The Nobel Prize in Chemistry 1955,” 2024; Vigneaud et al., 1953).

Especially the introduction of Solid Phase Peptide Synthesis in 1963 by Bruce Merrifield has had an everlasting impact in the field, for which he was awarded the Nobel Price in Chemistry in 1984 (“The Nobel Prize in Chemistry 1984,” 2024). For the synthesis of a tetrapeptide (LFKV) Merrifield utilised an insoluble polymer that bears the growing peptide chain. The respective cycles of N-deprotection, washing, and coupling are carried out while the peptide is covalently bound to the polymer resin. The liquid phase, containing unreacted material, cycle-specific reagents, and side- and cleavage products can be easily removed. Thus, compared to solution phase chemistry, SPPS has drastically simplified peptide synthesis, as purification and characterisation are not required after each synthetic step (Jaradat, 2018; Merrifield, 1963). This was exemplified in the synthesis of bovine insulin by Merrifield in 1966, which previously took other researches months using classical methods but could now be completed with higher yields within days (Marglin and Merrifield, 1966). In 1965, Merrifield described the first automated device to carry out SPPS, laying the foundation for modern, fully automated, and parallelised SPPS (Merrifield, 1965).

In 1970, Han and Carpino developed the base labile Fmoc (9-fluorenylmethyloxycarbonyl) group protecting strategy, providing an alternative to Boc protection, orthogonal to many other protecting groups and still commonly used up to date in peptide synthesis (Carpino and Han, 1970).

Refinement of the established methods, novel solid phase polymers, linkers, immobilisation strategies and the expansion of the repertoire of coupling reagents have refined peptide chemistry over the decades, allowing for the synthesis of more complex and challenging sequences (Jaradat, 2018). Advances in recombinant biology as well as the development of chemical and enzymatical ligation strategies for peptides, such as Native Chemical Ligation (NCL), the α-Ketoacid hydroxylamine (KAHA) ligation, Cu(I)-catalysed azide–alkyne cycloaddition (*CuAAC*), and enzyme-mediated ligations have paved the way for innovation in biomolecular synthesis (Ajingi et al., n.d.; Jaradat, 2018; Li, 2011; Schmidt et al., 2017).

Many decades of advances have led to the discovery and synthesis of a plethora of novel or nature-inspired peptides, particularly therapeutic peptides used to combat a variety of ailments such as diabetes, chronic pain, gut disorders, and infectious diseases. This progress eventually culminated in around 40 peptide-based drugs being approved by 2022 and more undergoing clinical trials (Wang et al., 2022).

3.1.1 Peptide bond formation

A peptide bond forms when the amine group of one amino acid condenses with the carboxylic acid group of another amino acid. The amine acts as a nucleophile, attacking the electrophilic carbonyl carbon. However, in the absence of enzymes (as in living organisms) or auxiliary chemicals, exposing a free N-terminus to an acid leads to salt formation due to the basicity of the amine and the acidic nature of its counterpart. In this situation, no peptide bond can form because protonation of the amine and deprotonation of the acid reduce the nucleophilicity of the amine and significantly decrease the electrophilicity of the carbonyl group. To form a peptide bond between two amino acids under laboratory conditions, activation of the carboxylic acid is necessary (**Figure 15**). Coupling agents such as HATU, DIC, and Oxyma can assist in this process and are thus valuable tools widely used in peptide chemistry.

A selection of different coupling agents is depicted in **Figure 16**, featuring HOBt (N-hydroxybenzotriazole), the aminium salts HATU (1-((dimethylamino)(dimethyliminio)methyl)-1H-[1,2,3]triazolo[4,5-b]pyridine 3-oxide hexafluorophosphate), HBTU (2-(1-H-benzotriazole-1-yl)-1,1,3,3-tetramethylaminium hexafluorophosphate) and HCTU (2-(6-Chloro-1-H-benzotriazole-1-yl)-1,1,3,3-tetramethylaminium hexafluorophosphate), the carbodiimides DIC (Diisopropylcarbodiimide) and DCC (Dicyclohexylcarbodiimide) as well as Oxyma (Ethyl cyanohydroxyiminoacetate). The latter was found to be an excellent and non-explosive alternative for HOBt used in carbodiimide-mediated coupling reactions (See **Figure 21**) (Subirós-Funosas et al., 2009). The choice of the coupling reagents can have a significant impact on the end product in terms of coupling efficiency, racemisation, and practical aspects (Jaradat, 2018).

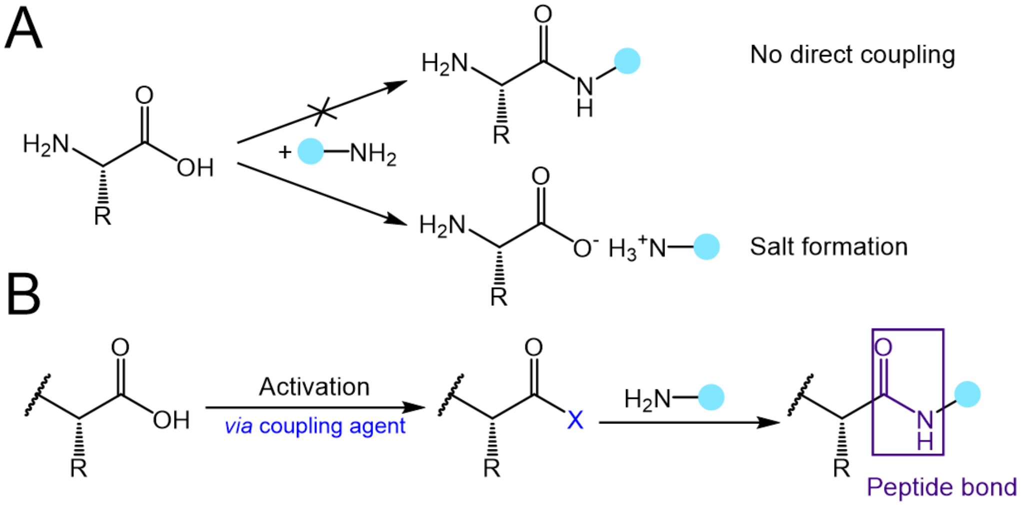

Figure 15. Peptide bond formation. (A) Peptide bond formation does not spontaneously occur when two amino acids are exposed. Instead, the amine group and the carboxylic acid undergo salt formation in an acid-base reaction. **(B)** Peptide bond formation thus requires auxiliary chemicals (coupling agents) to activate the carboxylic acid, making it susceptible to a nucleophilic attack by the amine, resulting in the condensation of both groups to form a peptide bond.

DCC and DIC were introduced as coupling reagents in 1955 and 1961, respectively, and have been in use ever since (Sheehan et al., 1961; Sheehan and Hess, 1955). The carbodiimides react with the carboxylic acid of the peptide or amino acid, a reactive O-acylisourea is formed and then undergoes aminolysis by the amine function of another amino acid to yield a peptide bond.(Jaradat, 2018) The formation of the DIC is to be preferred over DCC in solid phase reactions due to the better solubility of the urea byproduct that simplifies separation. In 1970, HOBt was introduced as a coupling agent, and HOBt is often used in combination with DIC as the addition of HOBt suppresses racemisation compared to a solely carbodiimide-mediated coupling (Jaradat, 2018; König and Geiger, 1970). The mechanism proceeds *via* the formation of an O-acylisourea derivative as described for the carbodiimide mediated peptide coupling. HOBt then reacts with the O-acylisourea to form a reactive active ester with the C-terminus. A nucleophilic attack by the amine group releases the HOBt and results in peptide bond formation (Jaradat, 2018; König and Geiger, 1970).

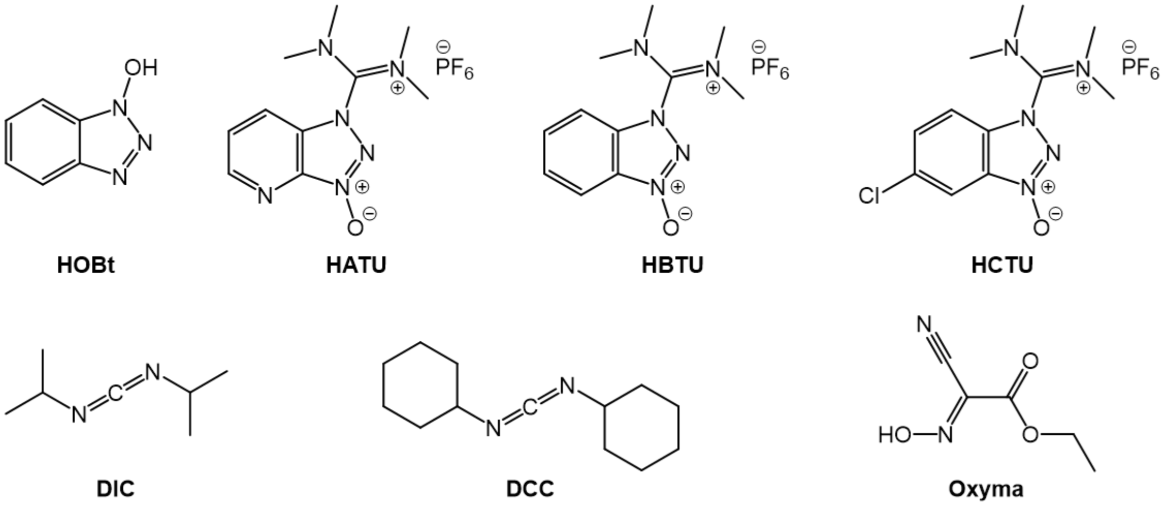

Figure 16. Structures of selected coupling agents used for peptide bond formation. From top left to bottom right, HOBt (N-hydroxybenzotriazole), HATU (1-((dimethylamino)(di-methyliminio)methyl)-1H-[1,2,3]triazolo-[4,5-b]pyridine 3-oxide hexafluorophos-phate), HBTU (2-(1-H-benzotriazole-1-yl)-1,1,3,3-tetramethylaminium hexafluoro-phosphate), HCTU (2-(6-Chloro-1-H-benzotriazole-1-yl)-1,1,3,3-tetramethyl-aminium hexafluoro-phosphate), DIC (Diisopropylcarbodiimide), DCC (Dicyclohexylcarbodiimide) and Oxyma (Ethyl cyanohydroxy-imino acetate).

Further coupling agent development saw the introduction of aminium salts HBTU. HATU and HCTU in 1978, 1993 and 2002, respectively (Carpino, 1993; Dourtoglou et al., 1978; Marder et al., 2003). All bear a positive charge at the N-guanidinium moiety and work follow the same mechanistic principle. Compared to the other aminium salts mentioned, HATU displays better coupling yields and lower susceptibility towards enantiomerisation, making it favourable in many applications (Jaradat, 2018). The HATU-mediated peptide bond formation is shown in ***Figure 17***. First, the sterically hindered trialkyl amine base DIPEA deprotonates the carboxylic acid of the amino acid, followed by a nucleophilic attack of the electrophilic aminium carbon by the carboxylate. The ester of the intermediate is then displaced by the 1-hydroxybenzotriazolate, forming an active ester that is susceptible to aminolysis (nucleophilic substitution by the free amino group of the coupling partner), yielding an amide bond. It has to be pointed out that the carboxy component and the aminium salt are reacted first before the amine group is introduced to prevent guanidinylation of the amine (Jaradat, 2018).

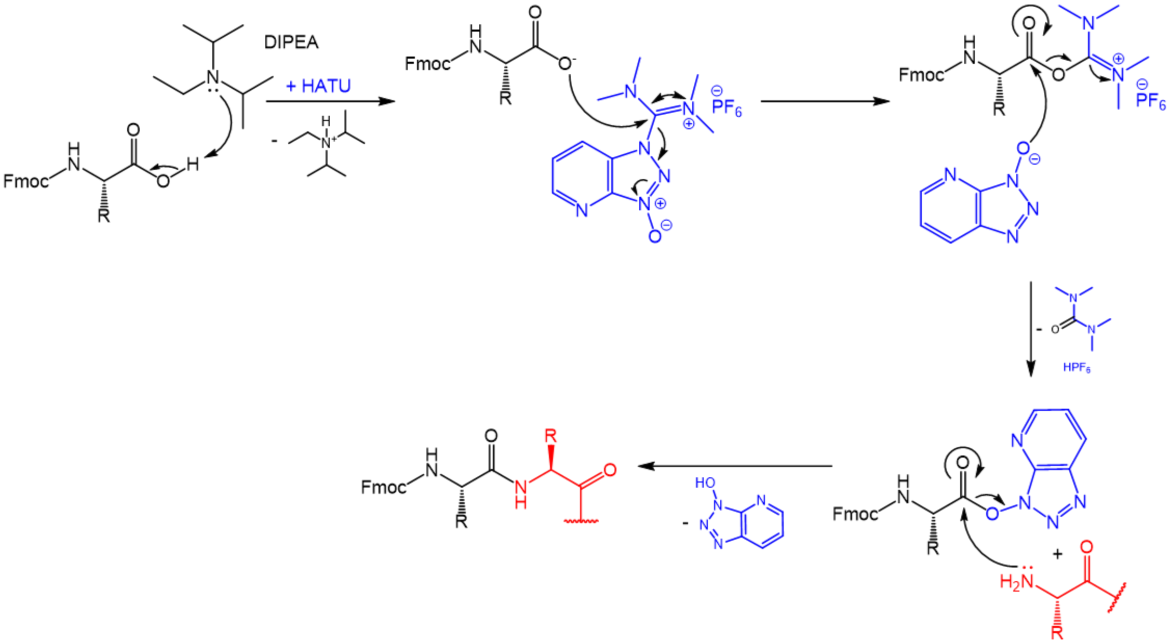

Figure 17. HATU mediated coupling reaction of two amino acids. In the first step, the C-terminus is deprotonated by a base (DIPEA). The resulting carboxylate then acts as a nucleophile on the iminium moiety of HATU. The intermediate ester is then displaced by the 1-hydroxybenzotriazole, releasing tetramethylurea. This reaction yields a reactive ester, which can undergo aminolysis by the amino group of another amino acid.

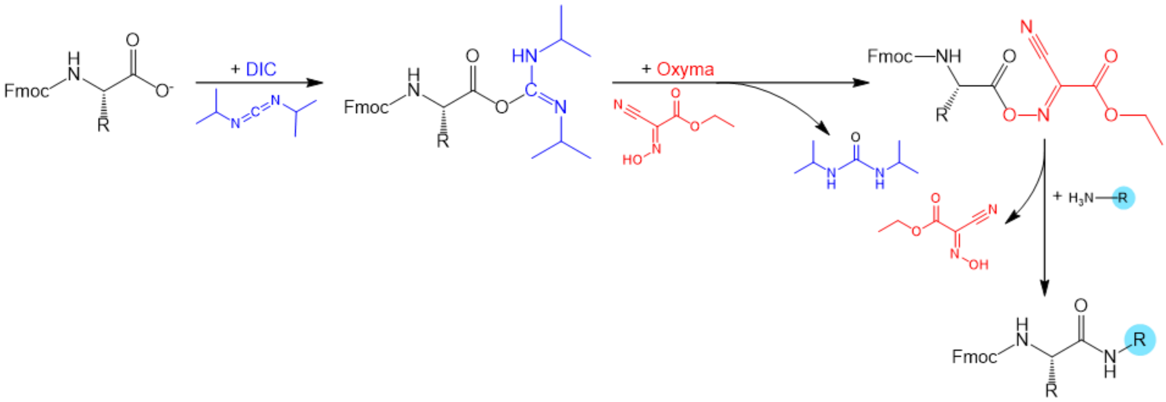

Figure 18. Mechanistic depiction of the DIC/Oxyma-mediated coupling reaction between a carboxylic acid and an amine. In the first step of the reaction, O-acylisourea is formed and reacts with the oxime group of Oxyma. The resulting oxime ester undergoes aminolysis to yield the final product with an amide bond.

Generally, racemisation reactions during coupling are of concern, and reaction conditions to minimize or suppress racemisation must be chosen. For example, base catalysed and carbodiimide-mediated coupling may lead to the formation of a racemic mixture of amino acids (L- and D-isomers), e.g., *via* oxazolone formation (El-Faham and Albericio, 2011; Goodman and Stueben, 2002; Tulla-Puche et al., 2015).

In microwave-assisted automated solid phase peptide synthesis (See 3.1.3), the DIC/Oxyma mediated coupling is commonly used. **Figure 18** gives an overview of this coupling reaction. First, the C-terminus of the amino acid reacts with the carbodiimide to form the reactive O-acylisourea intermediate. The nucleophilic attack of the oxime displaces the urea and the intermediate oxime ester can undergo aminolysis with the amine group of another amino acid, resulting in peptide bond formation (Jaradat, 2018; Manne et al., 2022). Oxyma was found to be an excellent and non-explosive alternative for HOBt (Subirós-Funosas et al., 2009).

3.1.2 Solid Phase Peptides Synthesis using the Fmoc strategy

Solid Phase Peptide Synthesis, invented by Robert Bruce Merrifield in 1963, enables researchers to assemble long sequences in a short amount of time (Marglin and Merrifield, 1966; Merrifield, 1963). The principle of SPPS is based on repeating cycles of deprotection and coupling reactions, supported by the solid phase, an insoluble polymer modified with linker regions that bear the nascent peptide chains (“resin”).

For SPPS, two common protecting strategies exist, the Fmoc/tBu (9-fluorenylmethoxycarbonyl/tert-butyl) and Boc/Bzl (tert-butyloxycarbonyl/benzyl) strategy, that determine the conditions and reagents that can be used. Here, the Fmoc strategy will be highlighted. **Figure 19** displays a Fmoc- and side-chain protected peptide linked to a solid support. The temporary Fmoc protecting group is base labile and is removed before each coupling step. In contrast, the orthogonally acid-labile side-chain protection and the linker region are cleaved in one final step after chain assembly.

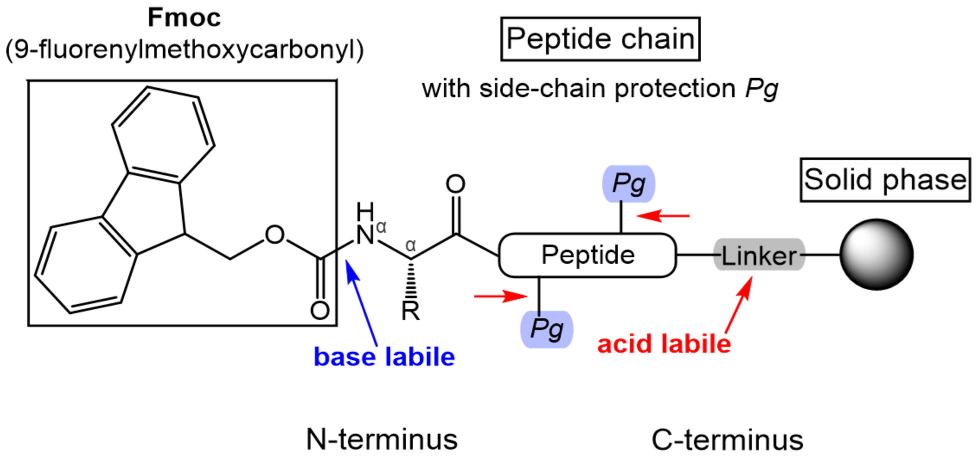

Figure 19. Immobilised peptide during Fmoc-SPPS. The peptide chain is N-protected with the base-labile Fmoc (9-fluorenylmethoxycarbonyl) group. Reactive side-chains are protected by acid-labile groups (*Pg*). The C-terminus of the peptide is covalently attached to the solid phase via a linker region. Orthogonal to the base-labile Fmoc group, the linker, and side-chain protecting groups can be cleaved off under acidic conditions.

The workflow of the SPPS is shown in **Figure 20**. The first (C-terminal) amino acid of the desired sequence is activated and chemically attached to the solid phase *via* a linker region. Before each coupling, the temporary N-terminal Fmoc-protection needs to be removed using a base. The mechanism of base-mediated Fmoc deprotection is displayed in **Figure 23** (See 3.1.4).

After deprotection of the N-terminus, the next activated and protected amino acid is added, and a peptide bond is formed between the two amino acids. During the whole procedure, reactive amino acid side-chains stay protected with respective protecting groups to minimize undesired reactions. Washing steps to rid the reaction mixture of reagents that may interfere are carried out after each reaction step. When the desired sequence is assembled after multiple cycles, the linear peptide chain is globally deprotected and cleaved off the resin in a one-step reaction, yielding the crude peptide. For Fmoc-SPPS, cleavage is performed under acidic conditions by treating the peptidyl resin with a strong acid such as trifluoro acetic acid (TFA).

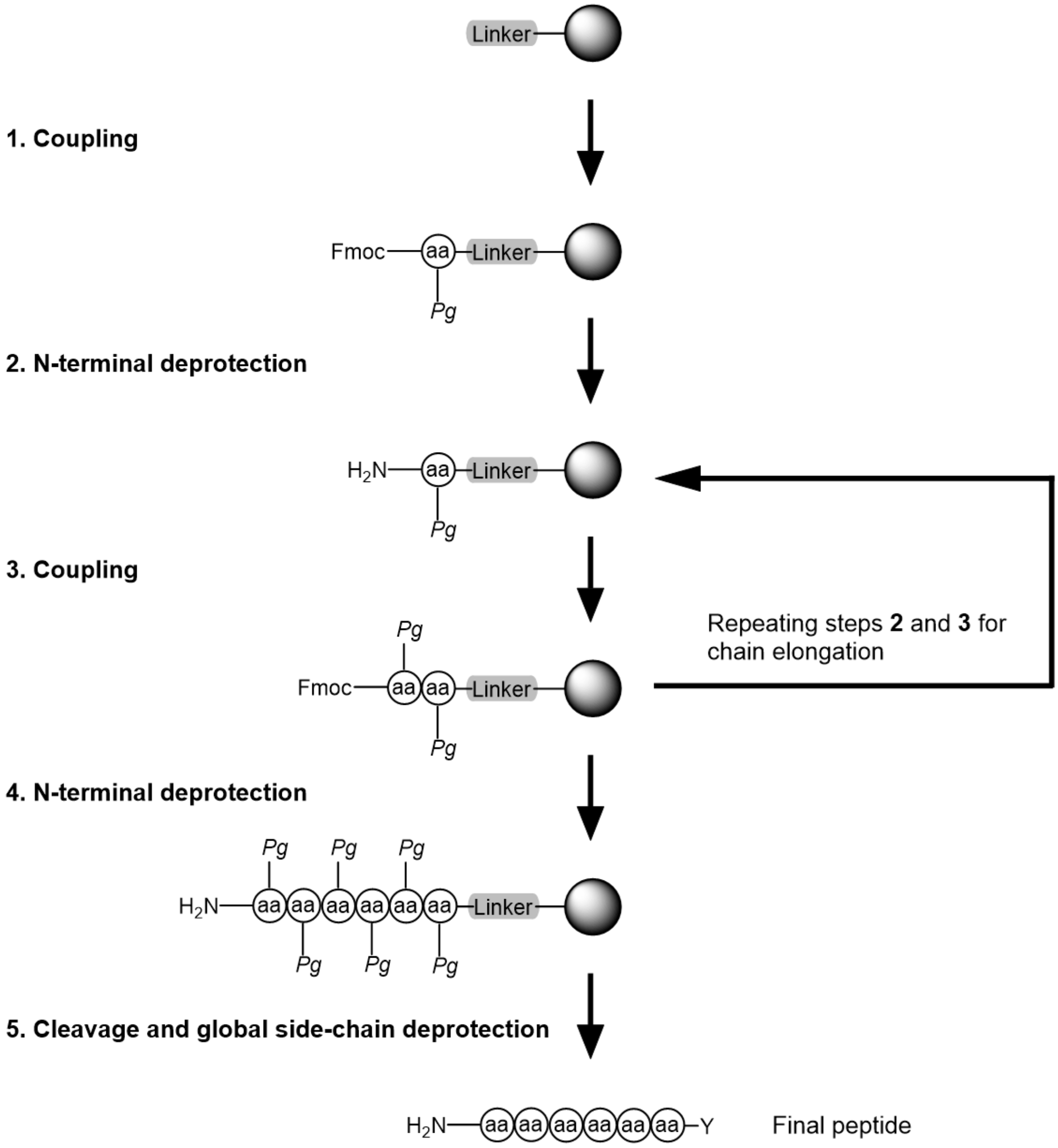

Figure 20. Scheme of the SPPS reaction. (1) The first amino acid is activated and attached to the resin, **(2)** N-deprotected, **(3)** and coupled to the C-terminus of the second activated amino acid. **(4)** The side-chains of the Fmoc-amino acids (aa) are temporarily protected with protecting groups (*Pg*). Repeating the steps with the respective amino acids yields the final sequence. **(5)** After a final N-deprotection, the side-chain protecting groups are globally removed, and the peptide is cleaved off the solid support, yielding the crude peptide. The choice of resin determines whether a free carboxy terminus (Y=OH) or an amide (Y=NH2) is obtained after cleavage.

Natural limitations of the SPPS method exist. Even though various coupling reagents and optimised protocols with good efficiencies have been established, a growing number of cycles (=long amino acid sequence) drastically reduces the yield of the final product. A peptide chain of 40 amino acids with 99% coupling efficiency would have a theoretical yield of 0.99^{40}= 66.9%, and 95% coupling efficiency would imply only 12.85% theoretical yield. Further, difficult sequences prone to aggregation, can reduce the yield as well. For longer peptides, special reagents (N^{α}-alkylated Fmoc-Tmob-Gly-OH or “Pseudoprolines”) that disrupt aggregation or different strategies, such as ligation of shorter chains, can be considered (Coin et al., 2007; Jaradat, 2018; Johnson et al., 1995; Toniolo et al., 1981).

3.1.3 Automated microwave-assisted Solid Phase Peptide Synthesis

The use of microwave irradiation for peptide synthesis was first reported in 1992 (Yu et al., 1992). A decade later, in 2003, the corporation CEM pioneered the first dedicated automated microwave-assisted peptide synthesizer (Jonathan et al., 2003). Automated microwave-assisted solid phase peptide synthesis (MW-SPPS) devices enhance the peptide assembly process of SPPS by integrating microwave irradiation into the procedure, which accelerates both coupling and deprotection reactions. The advantages of faster reaction times, better efficiencies, and higher crude product purities are attributed to the kinetic effects of heating the mixture (Bacsa et al., 2008; Yu et al., 1992). The automation component of these synthesizers allows for programmable sequences of amino acids, automated delivery of reagents from reservoirs, and control over reaction times and temperatures.

Typically, MW-SPPS is performed at temperatures ranging from 45°C to 80°C, with coupling and Fmoc-deprotection reactions completed within 5-6 minutes and 3-4 minutes, respectively (Murray et al., 2011; Vanier, 2013). However, exact conditions can vary depending on the sequence, exact temperature, and reagents used. As elevated temperatures can promote side reactions, the formation of aspartimides and amino acid racemisation need to be considered when choosing reaction conditions, and measures may be necessary to assess the occurrence of such reactions (Vanier, 2013).

For automated microwave-assisted solid phase peptide synthesis, coupling with DIC/Oxyma is commonly used. As a non-explosive alternative to HOBt with high coupling efficiency and low racemisation, Oxyma is highly favorable (Subirós-Funosas et al., 2009). The reaction equation for DIC/Oxyma mediated coupling in MW-SPPS is illustrated in **Figure 21**.

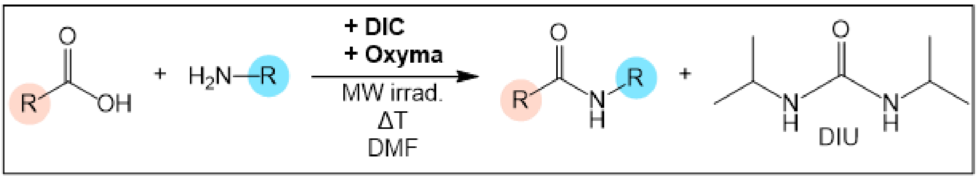

Figure 21. Reaction equation for DIC and Oxyma mediated coupling in microwave (MW) assisted SPPS.

3.1.4 Protecting groups

The emergence of protecting groups has had an revolutionary impact on peptide chemistry. Various protecting groups exist that allow for different approaches and strategies. In 1932, the first removable N^{α} protecting group was described by Bergmann and Zervas (Bergmann and Zervas, 1932). This carbobenzoxy group, (Cbz or simply “Z”) pioneered the field of temporary N^{α}-protection and laid the foundation for the development of the still relevant N^{α}-protecting groups Boc (tert-butyloxycarbonyl), an acid labile ester, in 1957 and Fmoc (9-

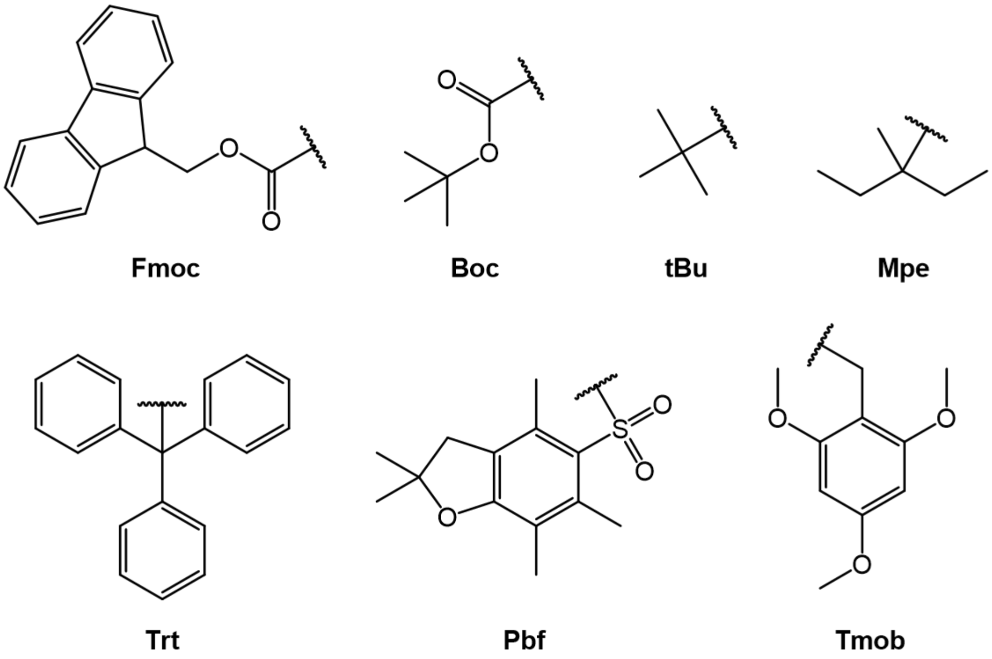

Figure 22. A selection of protecting groups for Nα and side-chain protection of peptides during SPPS. From top left to bottom right, Fmoc (9-fluorenylmethoxycarbonyl), Boc (tert-butyloxycarbonyl), tBu (tert-butyl), Mpe (3-methyl-pent-3-yl), Trt (trityl), Pbf (2,2,4,6,7-Pentamethyldihydrobenzofuran-5-sulfonyl) and Tmob (2,4,6-Trimethoxybenzyl).

fluorenylmethoxycarbonyl), a base labile ester, in 1970 (Carpino and Han, 1970; McKay and Albertson, 1957).

In **Figure 22**, structures of a selection of N^{α}- (Fmoc and Boc) and side-chain protecting groups (Boc, tBu, Mpe, Trt, Pbf, Tmob) are shown. Fmoc and Boc are classical protecting groups for the N-terminus of peptides with different implications of the synthetic route, and both are still in use with their respective orthogonal side-chain protection strategy, Fmoc/tBu and Boc/Bzl. As the latter required the use of corrosive and toxic hydrogen fluoride (HF) for side-chain deprotection, the Fmoc strategy is more commonly used (Jaradat, 2018; Tulla-Puche et al., 2015). Here, the use of Fmoc will be highlighted.

The Fmoc strategy employs side-chain protection groups that are stable to bases but can be cleaved under acidic conditions. Fmoc deprotection requires a base, such as piperidine (Carpino and Han, 1970; Jaradat, 2018; Tulla-Puche et al., 2015). The mechanism of piperidine-mediated Fmoc deprotection is depicted in **Figure 23**. The proton in position 9 of the fluorene system is acidic enough to be abstracted by the amine base. The carbanion undergoes an elimination reaction (E1cb) that releases the 9-methylene-fluorene, which can further react in additional reactions (O’Ferrall and Slae, 1970). Decarboxylation then gives the free amine.

In contrast, Boc-N^{α} protection is commonly cleaved by trifluoroacetic acid (TFA). However, Boc can also be used to protect side-chain amines, such as in lysine (N^{ε}), making it a suitable and Fmoc-orthogonal side-chain protecting group. Due to the unreactive nature of their side-chains, Ala, Gly, Ile, Leu, Met, Phe, Pro, and Val do not require a protecting group. In contrast, Arg, Asp, Cys, Glu, Lys, Ser, Thr, Tyr require the protection of reactive side-chain moieties and Asn, Gln, His, Trp protection is recommended as well (Jaradat, 2018). Common side-chain protecting groups are tBu (tert-butyl) for Asp, Glu, Ser, Thr and Tyr, Trt (trityl) for Asn, Gln and Cys, Boc for Lys and Trp and Pbf (2,2,4,6,7-Pentamethyldihydrobenzofuran-5-sulfonyl) for Arg (Jaradat, 2018; Tulla-Puche et al., 2015). The Mpe (3-methyl-pent-3-yl) group can be useful for Asp protection as it effectively protects against aspartimide formation (Karlström and Undén, 1996). Another very common Cys protection group is the Acm (acetamidomethyl) group (Jaradat, 2018; Tulla-Puche et al., 2015).

The methoxybenzyl analogues Hmb (2-hydroxy-4-methoxybenzyl), Dmb (2,4-dimethoxybenzyl) and Tmob (2,4,6-Trimethoxybenzyl) have found application as cysteine protecting groups, however, attached to the amino terminus these groups do not serve as a classical N$^{\alpha}$ protecting group, but can in suppressing backbone hydrogen bonding and thus “protect” the nascent peptide chain from aggregation, useful for difficult sequences (Isidro-Llobet et al., 2009; Johnson et al., 1993; Munson et al., 1992; Society, 1998; Spears et al., 2021; Zoukimian et al., 2022).

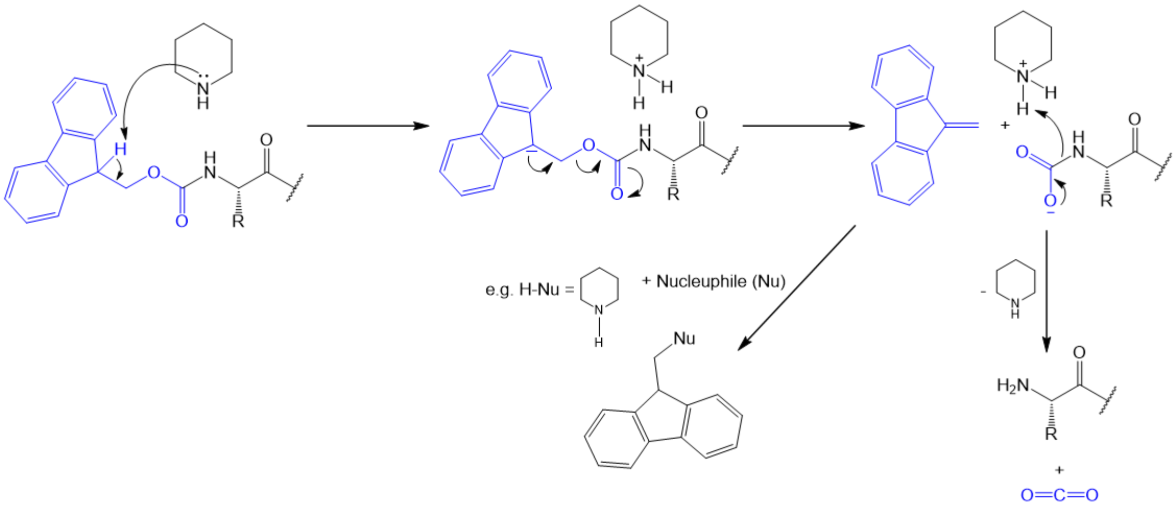

Figure 23. Fmoc N-terminal deprotection reaction with piperidine. The Fmoc group (blue) is deprotected by the base piperidine and undergoes elimination (E_{1c}b), resulting in the formation of 9-methylene-fluorene and CO_2 after decarboxylation, yielding the free amine. The 9-methylene-fluorene can subsequently react with nucleophiles present, such as piperidine.

Global deprotection of the peptide is usually performed in a one-step reaction together with the cleavage of the peptidyl resin under acidic conditions using a strong acid; a common choice is the volatile TFA (Kremsmayr and Muttenthaler, 2022; Tulla-Puche et al., 2015). Scavengers, such as trisiopropylsilane (TIPS) and (DODT) are added to the TFA to suppress side reactions of and unwanted modification by the released protecting groups (Pearson et al., 1989; Teixeira et al., 2002).

3.1.5 Resins for SPPS – Solid support and linkers

SPPS follows the principle of immobilizing the first amino acid on an insoluble resin and conducting step-wise chain elongation until the desired sequence is obtained. The resin consists of polymer beads functionalised with linkers that provide attachment sites for the growing peptide chain and quantitatively enable eventual cleavage (Jaradat, 2018). A common material choice is divinylbenzene-crosslinked (1-2%) polystyrene (PS) (Blackburn, 1998). To ensure compatibility with the synthesis conditions, both the polymeric support and the linker must be mechanically, chemically, and thermally stable (Tulla-Puche et al., 2015). The nature of the resin, especially the linker, determines the synthetic route and compatibility with certain protection strategies and further influences the chemical nature of the final product. Usually, the peptide is immobilised on the solid phase via the C-terminus (Jaradat, 2018; Merrifield, 1963). A selection of different structures of resins is depicted in **Figure 24**. For the hydroxy-type Wang and 2-chlorotrityl resin, an ester linkage with the peptide is established, yielding a carboxylic acid after cleavage (Barlos et al., 1991; Jaradat, 2018; Wang, 1973). Rink-amide (Benzhydrylamine), and Sieber-amide (Xanthenylamine) resins form an amide bond with the amino group and the C-terminus of the peptide and yield an amidated peptide after cleavage (Jaradat, 2018; Rink, 1987; Sieber, 1987). The resins depicted in **Figure 24** are cleavable by TFA acidolysis.

The substitution value characterizes the amount of peptide (mmol) that can be loaded onto a given amount of resin, expressed in [mmol/g]. For longer or challenging sequences, lower substitution values can be favourable.(Kent, 1988) As most of the reactions take place within the polymeric network of the solid phase

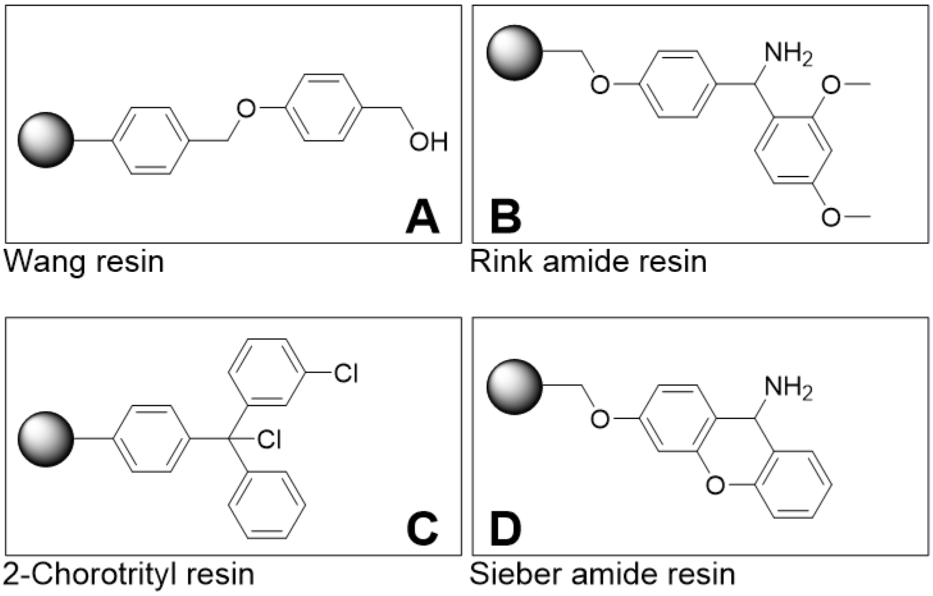

Figure 24. A selection of different resins used in SPPS. The depicted linkers are attached to the polymer and bear reactive groups that allow coupling of amino acids. Beads of the linker-functionalised polymer are referred to as “resin”. **(A)** The Wang resin consists of a linker attached to a polystyrene. **(B)** The Rink-amide resin consists of, **(C)** 2-chlorotrityl resin and **(D)** Sieber-amide resin, respectively.

and are controlled by diffusion, proper swelling of the resin with the respective solvent, for example DMF, DCM, or THF, is crucial to ensure accessibility of all reactive sites (Hudson, 1999; Kent, 1988; Tulla-Puche et al., 2015).

3.1.6 Oxidative folding of peptides

The three-dimensional structure of a disulfide-rich peptide is highly dependent on the correct disulfide bond formation (Price-Carter et al., 1998). One or more disulfide bonds within a peptide restrict the peptide structurally into a certain biologically active conformation by positioning pharmacophoric amino acid side-chains to optimize interactions with molecular targets and further provide its stability towards degradation by proteases (Colgrave and Craik, 2004; King, 2015; Kolmar, 2008; Roesler and Rao, 2000). Multiple cysteines imply the possibility of many different isomers being formed. For example, a peptide with three disulfide bonds consisting of six cysteines 15 different isomers would be possible, following Equation (1) (Kauzmann, 1959).

$$P(n) = \frac{(2n)!}{2^n\, n!} \qquad (1)$$

Hence, for the synthesis of disulfide-rich peptides, it is crucial to select a synthetic strategy that ensures the formation of the desired folding. Utilizing orthogonal protecting groups allows for sequential deprotection and the directed formation of sulfur-sulfur bonds in cysteine side-chains, facilitating the production of specific folds in peptides with multiple disulfide linkages (Postma and Albericio, 2014).

A different approach for peptide folding is air-oxidation, often supported by a redox buffer of glutathione (GSH) and glutathione disulfide (GSSG) in an aqueous medium (X.-T. Chen et al., 2022; Deuis et al., 2017; Park et al., 2014; Wu et al., 2013). As a one-step, global cysteine oxidation method, air oxidation is less labour-intensive than elaborated, multi-step protection schemes (Kam et al., 2024). The linear peptide is diluted in a buffer with specific salt composition and ionic strength to prevent aggregation. Diluting the peptide to high levels minimizes the formation of intermolecular disulfide bonds. When exposed to air, oxygen promotes the formation of disulfide bonds between cysteine side-chains. The buffer's slightly alkaline pH causes partial deprotonation of sulfhydryl groups, which increases the nucleophilicity of the resulting thiolate. This facilitates nucleophilic substitution reactions, including scrambling reactions and mixed disulfide bond formation between the peptide and glutathione species (Kam et al., 2024). As *in vivo*, the glutathione redox system, comprising reduced glutathione (GSH) and its oxidised form (GSSG), plays a crucial role in peptide folding. GSSG acts as an oxidant to form correct disulfide bonds, while GSH serves as a reducing agent to cleave improperly formed disulfide bonds, supporting the peptides in achieving their thermodynamically stable conformation (Okumura et al., 2011).

Although air oxidation can be time-consuming (hours to days) and may produce mixtures of correctly, incorrectly, and unfolded peptides, at the expense of the yield, the reagents are inexpensive and non-toxic (Kam et al., 2024; Wong et al., 2011).

3.1.7 Cu(I)-catalysed azide–alkyne cycloaddition (CuAAC)

The cycloaddition reactions of terminal alkynes with azides, catalysed by Cu(I) species, are known as *CuAAC* (Copper-Catalysed Azide-Alkyne Cycloaddition) reactions. The reaction was first described by Barry Sharpless and Morten Meldal in 2001 (Rostovtsev et al., 2002; Tornøe et al., 2002). The *CuAAC* reaction is an archetypal 'click reaction'. Click reactions are designed to be conducted under mild conditions, ensuring robustness to variations in concentration or environmental factors. They should exhibit tolerance towards water and common functional groups while yielding only the desired product, enabling the rapid synthesis of complex molecules (Kolb et al., 2001; Kolb and Sharpless, 2003). In 2022, the Nobel Prize in Chemistry was awarded to Carolyn R. Bertozzi, Morten Meldal, and K. Barry Sharpless "for the development of click chemistry and bioorthogonal chemistry", crediting the impact of the discovery and implementation of click reactions like the *CuAAC* reaction ("The Nobel Prize in Chemistry 2022," 2024).

With the introduction of Cu(I) as a catalyst to the azide-alkyne reaction, the selective formation of 1,4-disubstituted 1,2,3-triazoles in aqueous media and at ambient temperatures from terminal alkynes is made possible. The *CuAAC* reaction requires only sub-stoichiometric amounts of copper salts like $CuSO_4$ in the presence of a reducing agent (e.g., sodium ascorbate) to generate the active copper(I) species *in situ* (Rostovtsev et al., 2002).

An overview of the reaction is shown in **Figure 25**. Additionally, a more detailed mechanistic cycle is depicted below. The mechanism of the *CuAAC* proceeds through the formation of a copper(I)-acetylide complex, which subsequently reacts with an organic azide. This process involves the coordination of another π-bound copper(I) ion to the copper acetylide, forming a dinuclear intermediate. The copper(I)-acetylide intermediate is reversibly coordinated by the azide and then undergoes nucleophilic attack, forming a six-membered metallacycle. The cycloaddition is completed by reductive elimination, producing the 1,4-disubstituted 1,2,3-triazole and regenerating the copper(I) catalyst (Héron and Balcells, 2022; Worrell et al., 2013).

The use of this reaction in peptide chemistry allows the ligation already deprotected and folded peptides, evading interference with the synthesis, under non-denaturing conditions. The azide and alkyne can be introduced into the respective peptide

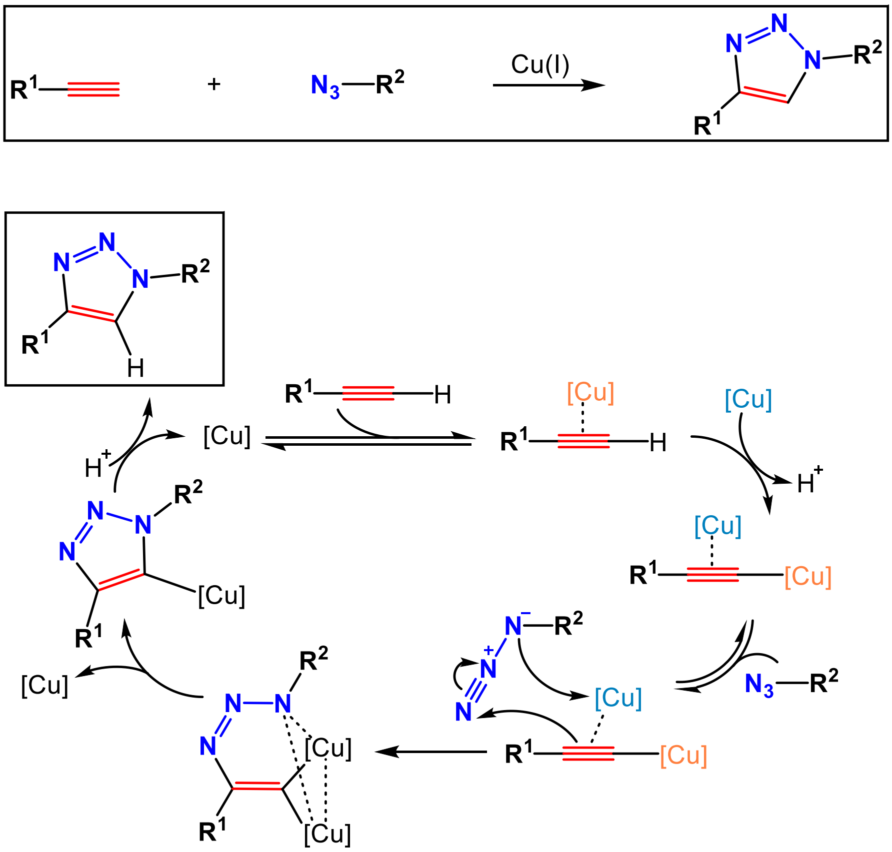

Figure 25. The mechanism of the *CuAAC* reaction. Reaction equation and mechanistic depiction (below) of the Copper-Catalysed Azide-Alkyne Cycloaddition (*CuAAC*) reaction, illustrating the formation of 1,4-disubstituted 1,2,3-triazoles from terminal alkynes and azides through the catalytic action of copper(I) species.

sequences on-resin as amino acid analogues, for instance 6-azido lysine or propargyl glycine. The chemically stable 1,2,3-triazole possesses similar properties to the amide bond and has bee used as a bio isosteric replacement (Brik et al., 2005; Bonandi et al., 2017; Kumari et al., 2020).

Auxiliaries, such as the water-soluble multidentate ligands TBTA (tris-(benzyltriazolylmethyl)amine) and THPTA (tris(3-hydroxypropyltriazolylmethyl)-amine) stabilize the copper(I), especially in aqueous condition and oxygen exposure against oxidation and further aid the catalytic transformation (Chan et al., 2004; Donnelly et al., 2008).

3.2 Peptide Analysis and Purification Methods

3.2.1 Reverse-Phase High-Performance Liquid Chromatography

The physicochemical properties of proteins and peptides are highly variable, influenced by their size, amino acid sequence, and structure. These characteristics can be utilised to separate and purify analytes from heterogeneous samples of different molecules. Common separation approaches for peptides in solution involve chromatographical techniques, such as High Performance Liquid Chromatography (HPLC) (Tulla-Puche et al., 2015). In HPLC, peptides are separated based on their competing interaction with mobile and stationary phases (Aguilar, 2003; Kurreck et al., 2022). The mobile phase can consist of one or more solvents in a defined composition that flows through the system and carries the dissolved samples from the injection port through the separatory column to the detector. For the separation of peptides and proteins, water and acetonitrile, acidified with trifluoroacetic acid (TFA), are common choices (Aguilar, 2003). The TFA protonates basic functional groups of the peptides and serves as an ion pairing agent that shields positive charges and enhances the separation (Åsberg et al., 2017; Mant and Hodges, 2019; Mirza and Chait, 1994).

The composition of the mobile phase can be fixed (isocratic) or change throughout the separation (gradient). The separation is achieved when the analytes pass the separatory column and the column material (stationary phase) interacts with the molecules (Aguilar, 2003; Kurreck et al., 2022).

In Reverse Phase HPLC (RP-HPLC), the mobile phase is more polar than the stationary phase that consists of silica spheres surface-functionalised with non-polar side-chains such as butyl (C4), suited for larger peptides and proteins, or octadecyl (C18), suited for smaller molecules. Hydrophobic parts of peptides adsorb to the surface of the stationary phase until the solvent gradient reaches a polarity that results in the elution of the analyte. Thus, the compound's retention depends on the hydrophobicity determined by the amount of charged, polar and hydrophobic side-chains. In a setup where the mobile phase gets increasingly non-polar, more hydrophobic molecules elute later as they are retained to a higher degree than polar, hydrophilic molecules (Kurreck et al., 2022; Mant and Hodges, 2019).

Figure 26 displays a scheme of a general HPLC set-up. The mobile phase is taken from solvent reservoirs and a high-pressure pump provides an even flowrate. HPLC systems are operated at elevated pressure to reduce the overall time of separation. The samples, previously prepared in vials, are stored in a tray within the instrument. An autosampler automatically draws and injects a defined sample volume into the HPLC system, ensuring consistent and precise sample introduction. The sample is injected in an injection port, usually via a six way valve, where it is loaded into a sample loop, that can either be bypassed or directed to the column or waste, respectively.

Before the separatory column, a smaller guard column can be placed to trap particles and pollutants. After being retained and separated on the main column, the analytes pass a detector that monitors the elution. As peptide bonds absorb at 214 nm and aromatic amino acid side-chains at 280 nm, UV detectors are a well-suited choice (Kurreck et al., 2022). The absorbance signal at the specific time the analyte molecules reach the detector (retention time) is used to characterize the analyte later. Below the schematic set-up, **Figure 26** shows an example chromatogram with the absorbance plotted against the retention time and peaks corresponding to the eluting analytes and impurities, respectively.

The fractioned analytes can be collected after passing the detector instead of being directed to waste, allowing the recovery of the sample molecules. Further, in preparative HPLC, larger columns with higher capacity enable the purification of greater amounts of material.

3.2.2 Electrospray ionisation (ESI) Mass Spectrometry (MS)

Electrospray Ionisation Mass Spectrometry (ESI-MS) is an analytical technique extensively used for peptide analysis that combines electrospray ionisation with mass spectrometry to determine the mass-to-charge (m/z; whereas m = mass and z = charge) ratio of ions. Mass spectrometry has proven invaluable for peptide chemists due to the speed of analysis, its versatility and especially sensitivity while accurately measuring molecular masses (Fenn et al., 1989; Kurreck et al., 2022; McCullagh and Oldham, 2019; Zhang et al., 2014). The analyte sample is dissolved, usually in either water and acetonitrile or a mixture, and acidified with a small amount of acid (formic acid) that facilitates ionisation. Combined LC-MS systems

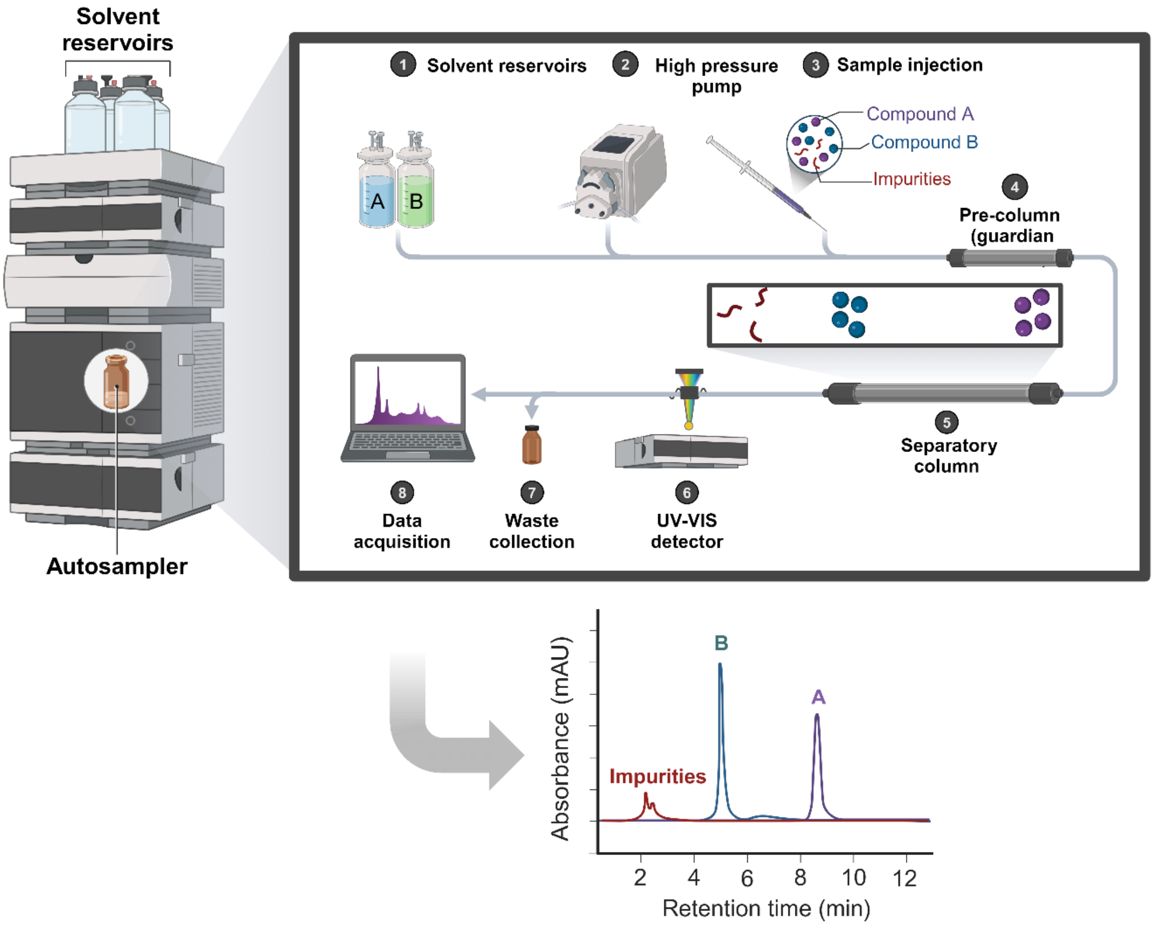

Figure 26. Schematic overview of a High-Performance Liquid Chromatography (HPLC) set-up. The system comprises reservoir of solvents (A, B), a high pressure pump, a sample injection port, a precolumn (guardian column), a separatory column (e.g. C18 stationary phase), a photometric detector (UV/VIS), and a data acquisition system. The solvent reservoir supplies the mobile phase, which is constantly delivered at high pressure by the pump. The injector introduces the dissolved sample into the mobile phase stream, which then flows through the precolumn and eventually reaches the separatory column, where separation occurs. The detector measures the absorbance of the eluting compounds, and the data acquisition system correlates elution time and signal. Figure created with BioRender.

are often used to separate the components of the samples before introducing them into the MS system (McCullagh and Oldham, 2019). Besides, in direct injection mode no preceding separation is performed. The sample is reaches the ESI source through a fine spraying nozzle (**Figure 27** C). A high voltage (3-4 kV) is applied between the needle and the mass spectrometer inlet. The resulting electric field charges the surface of the liquid, leading to the generation of charged droplets

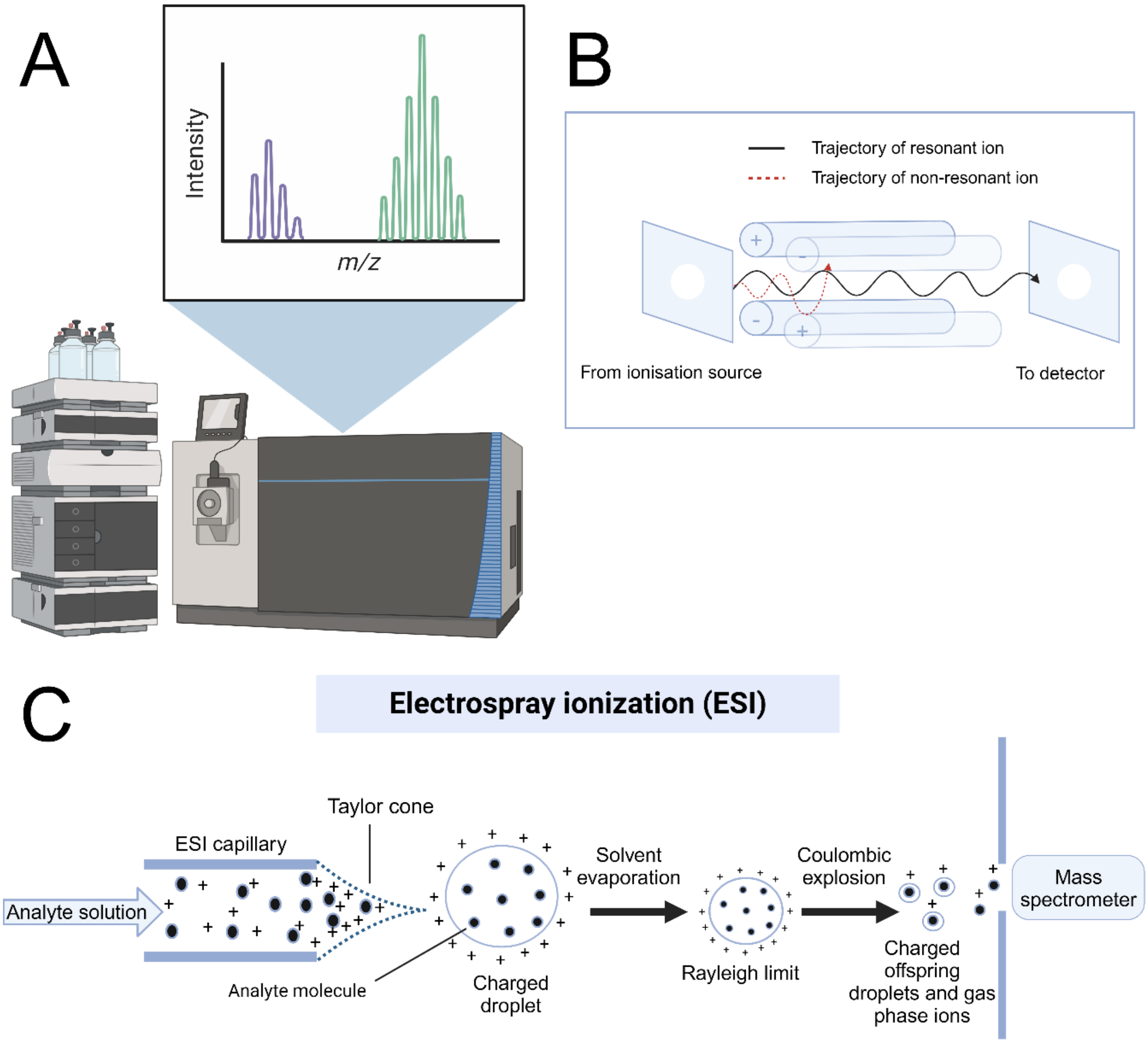

Figure 27. (A) Illustration of a mass spectrometer coupled with an exemplary mass spectrum, showing the plot of mass-to-charge ratios (m/z) against the detected intensity. **(B)** Schematic representation of the basic components of a quadrupole detector, detailing the arrangement of the four parallel rods and their function in filtering ions based on their m/z ratio by varying the radio frequency and direct current voltages applied to the rods. **(C)** Diagram of an Electrospray Ionisation (ESI) source, depicting the process by which ions are generated from a liquid sample through the application of a high voltage to create a fine aerosol, subsequently leading to ion desolvation and transfer into the mass spectrometer for analysis - figure created with BioRender.

(Kurreck et al., 2022; McCullagh and Oldham, 2019). The dispersion of charged droplets travels through a drying gas (usually dinitrogen) that facilitates solvent evaporation and increases the charge density on the droplets' surface, eventually leading to Coulombic repulsion that causes the droplets to fission into smaller droplets. This process continues until desolvation results in the formation of gas-phase ions. These gas-phase ions are then directed into the mass spectrometer’s vacuum system through ion optics that guide and focus the ions (Kurreck et al., 2022; McCullagh and Oldham, 2019).

The mass analyser separates the ions based on their mass-to-charge ratio by using one of several types of mass analysers, such as quadrupole, Orbitrap, or time-of-flight (TOF) analysers. These analysers rely on different mechanisms to filter or measure the ions by their m/z ratio. For example, a quadrupole (**Figure 27** B) creates an oscillating electric field where only particular m/z ratios have a stable trajectory and can travel towards the detector. TOF analysers measure the time it takes for ions to travel a fixed distance and the Orbitrap traps ions in an electrostatic field and measures the frequency of their oscillations (Kurreck et al., 2022; McCullagh and Oldham, 2019).

Once separated, the ions are detected by an ion detector that converts the ion signal into an electrical signal. This data is then processed to generate a mass spectrum, displaying the intensity of detected ions as a function of their m/z ratio (**Figure 27 A**). For peptide analysis, the mass spectrum provides critical information about the molecular weight of the peptides. Further sequencing can be achieved using tandem mass spectrometry (MS/MS), where selected precursor ions are fragmented in a collision cell, and the resulting fragment ions are analysed to deduce the amino acid sequence (Kurreck et al., 2022; McCullagh and Oldham, 2019).

3.3 Patch Clamp Electrophysiology

Cellular membranes function as physical and osmotic barriers, separating the exterior and interior of a cell or its organelles from their environment. This barrier limits the transport of substances, compartmentalizes the cell, and creates concentration and voltage gradients. The latter is particularly important for the excitability of cells (e.g. in neurons, muscle and cardiac cells), such as neurons. Proteins embedded in the cell membrane, like ion channels, help to overcome and modulate this barrier by facilitating the passage of molecules or ions in a well regulated way, usually as a response to certain stimuli, for example signal molecules (ligands), mechanical stress, variations in temperature or a change in the membrane potential (voltage).

Electrophysiology is the study of the electrical properties of biological cells and tissues. It involves measuring and analysing the electrical activity of cells. Techniques such as patch clamping allow the study of the currents that pass through cell membranes, providing insights into how cells communicate and process information and stimuli response. Hence, this scientific discipline is crucial in understanding normal cellular functions and diagnosing and treating diseases related to electrical activity in the body (Hill and Stephens, 2021).

Patch clamping was developed in the late 1970s by Erwin Neher and Bert Sakmann, for which they were awarded the Nobel Prize in Physiology or Medicine in 1991 (Neher et al., 1978; Neher and Sakmann, 1976; “The Nobel Prize in Physiology or Medicine 1991,” 2024). The core principle of patch clamping involves the use of a glass micropipette with a very fine tip to isolate a small patch of the cell membrane. A high-resistance seal (gigaohm seal) is formed between the pipette and the membrane that allows measuring the electrical currents that flow through ion channels within that patch (Molleman, 2003).

There are several configurations of the patch clamp technique, each suited to different types of studies. In Cell-Attached mode, the pipette is attached to the cell membrane without disrupting it. This allows for the measurement of ion channel activity in a relatively undisturbed cellular environment. In contrast there is the Whole-Cell mode, where after forming a seal, the membrane patch within the pipette is ruptured, allowing the interior of the pipette to become continuous with the cell’s cytoplasm. This enables the measurement of the overall ionic currents of the entire cell and allows control over the intracellular environment. The Inside-Out and Outside-Out Patch modes are used to study the properties of individual ion channels. In the inside-out mode, the pipette is retracted to expose the intracellular side of the membrane to the external solution, which is helpful in studying the effects of intracellular molecules. In the outside-out mode, the membrane patch reseals with the extracellular side facing outwards, which is ideal for studying the effects of extracellular substances (Molleman, 2003).

Patch clamping has been extensively used to study the mechanisms of action for various ion channels as well as their roles in cellular (patho-)physiology. It has enabled the discovery of how specific ion channels contribute to generating and propagating electrical signals in excitable cells. Additionally, this technique is vital in drug development and pharmacology for testing the effects of drugs on ion channels (Py et al., 2011).

3.3.1 Automated patch clamp

Advanced automated systems, like the QPatch by Sophion Bioscience, have accelerated the patch clamping process, enabling larger-scale studies and high-throughput screening, especially valuable for drug discovery. The QPatch system automates many aspects of the patch clamp process, such as cell sample preparation, sealing and recording, reducing the manual effort required significantly. The system requires the use of a single-use biochip that features a planar array of chambers with microfluidic flow channels for the measured compound. Measuring and reference electrodes are incorporated into the chip and extra- and intracellular fluid are stored (Dunlop et al., 2008; Mathes, 2006; Obergrussberger et al., 2021). This set up allows for the parallel recording from multiple cells, each being one biological replicate, enhancing the efficiency of experiments. Automated whole-cell patch-clamp electrophysiology has been applied to study and characterize venom peptides (Deuis et al., 2017; Robinson et al., 2024; Tilley et al., 2014).

3.4 Dot Blot

Immunoblotting techniques utilize the specificity of antibodies to bind membrane-bound proteins or peptides of interest, allowing for their visual detection and identification. Among these techniques, the Dot Blot stands out as a rapid, separation-free method (Stott, 1989). Proteins or peptides of interest are directly spotted onto a membrane, such as nitrocellulose or PVDF (Stott, 1989). Excess material is thoroughly washed away, and the membrane undergoes a blocking step to prevent nonspecific antibody binding (Masoodi et al., 2021; Mishra, 2022). Next, the membrane is treated with a primary antibody solution to specifically bind the target proteins or peptides. To enhance detection sensitivity, a secondary antibody against the primary antibody is then applied. This secondary antibody may be conjugated with a fluorescent dye or an enzyme that facilitates a chemiluminescent reaction, providing a visual means to detect and analyse the binding events (Heinicke et al., 1992; Qi et al., 2018). Alternatively, Ponceau S staining enables reversible colorimetric detection of membrane-bound proteins (Goldman et al., 2016; Stott, 1989).

The dot blot offers high-throughput capabilities and allows for the relative quantification of samples. However, a key limitation of this method is that it provides no information on the size or molecular weight of the proteins (Mishra, 2022; Qi et al., 2018; Rupprecht et al., 2010; Stott, 1989).

For research tasks where the sample has been pre-characterized, and the objective is to assess the presence of a specific antigen or to evaluate antibody binding, the dot blot technique offers an efficient approach. This method allows for rapid and detection of antigen presence or antibody interactions, making it suitable when detailed protein characterization or size differentiation is not required.

4 Results

4.1 Venom peptide-based probe design

We propose developing two venom peptide-based probes for use in a modified Proximity Ligation Assay (PLA) for the selective detection of $Na_V1.7$. (**Figure 28**). As described in the introductory section 1.5.1 and 1.6.1, conotoxin KIIIA and the theraphosid toxin Pn3a are potent and selective inhibitors of $Na_V1.7$ that have been researched for their analgesic potential and bind the channel on two different allosteric sites. For detection *via* PLA, both peptide-based probes must bind the channel simultaneously to enable close proximity between the secondary antibodies. Therefore, the VSD_{II} binding Pn3a and the pore-blocker KIIIA were chosen as the parent peptide platform for probe design.

The [D8N] mutation of Pn3a selected for this work shows improved potency (IC_{50} = 0.2 nM at $hNa_V1.7$) and enhanced selectivity compared to wild-type Pn3a,

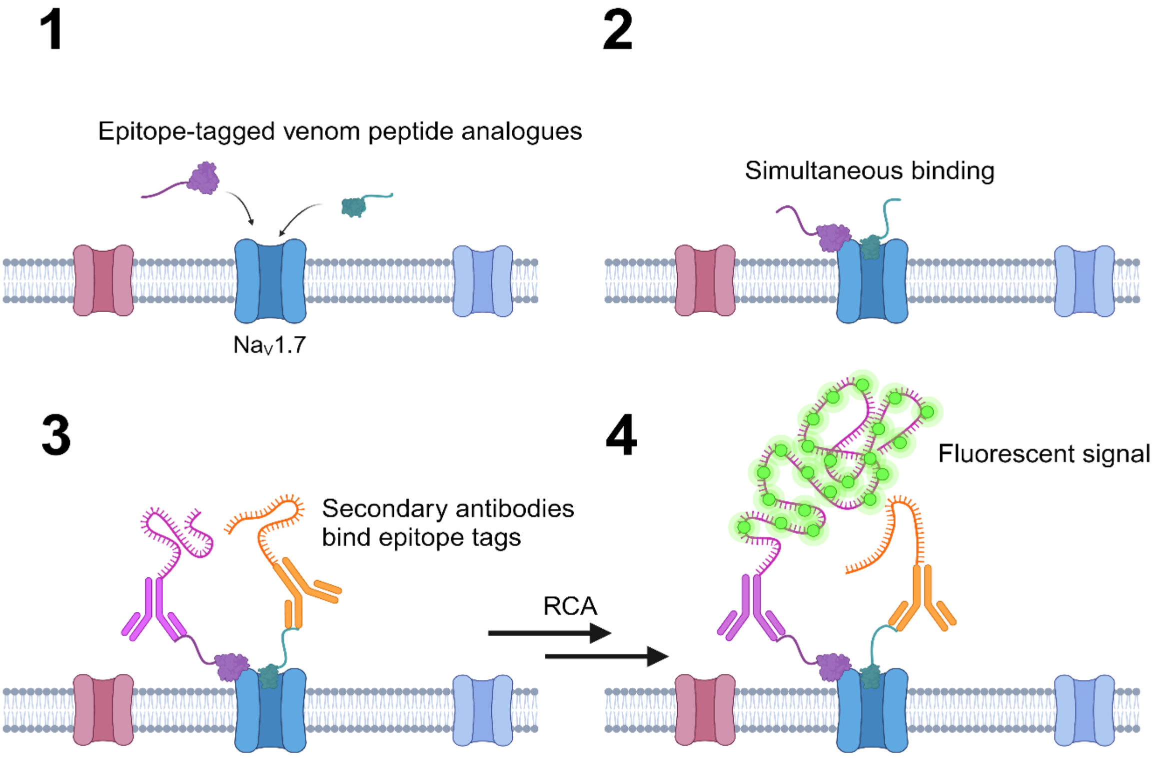

Figure 28. Proposed modification of the Proximity Ligation Assay. Two epitope-tagged venom peptide analogues **(1)** with different $Na_V1.7$ binding sites selectively bind the channel over other subtypes, e.g. in a tissue sample **(2)**. Secondary antibodies with oligo-DNA tags selectively recognize the epitope tags and bind them, respectively **(3)**. After ligation and RCA, as described in section 1.7, fluorescent probes hybridize the amplification product and produce a signal that corresponds to the presence of $Na_V1.7$ **(4)**.

with a 43-fold increase over $Na_V1.2$ and greater than a 4762-fold increase over $Na_V1.8$. (Mueller et al., 2020)

Both peptides require antibody recognition sites for the secondary antibody to bind. The general design for the peptide probes is shown in **Figure 29**. In this design, each venom peptide is N-terminally modified with a spacer sequence and ligated to an epitope tag via *CuAAC*. C-terminal modification was not considered because, for KIIIA, the native and amidated C-terminus is crucial for potency, and any C-terminal modification negatively affects potency. (Coelho et al., 2014; Hashimoto et al., 1985; Tran et al., 2020) The C-terminal residues of Pn3a are important for interaction with VSD_{II}, with multiple hydrophobic residues embedded in the cellular membrane during channel interaction. (Mueller et al., 2020; Sharma et al., 2020) Modification

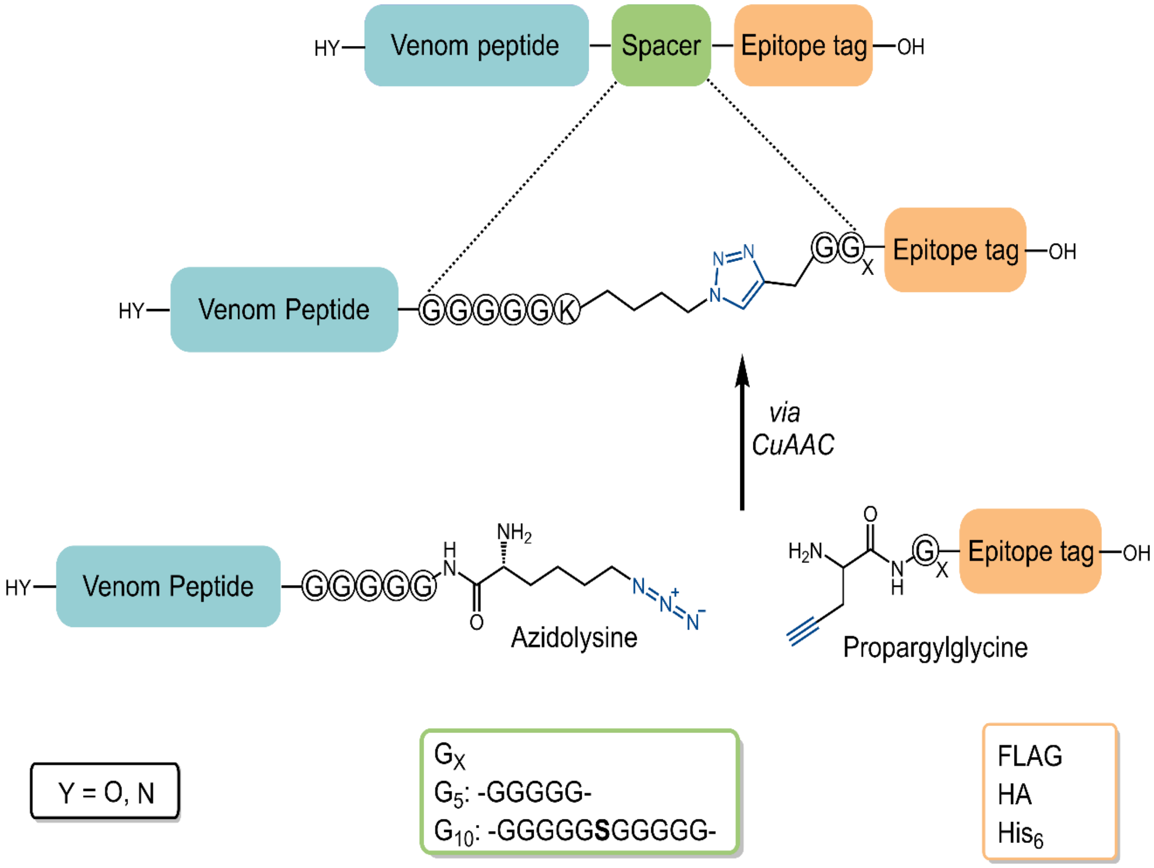

Figure 29. General design of the PLA compatible venom peptide analogues. The respective venom peptide is modified with a spacer and the antibody recognition site (epitope). The modified amino acids azidolysine and propargylglycine enable click chemistry (*CuAAC*) while maintaining a native peptide backbone. The resulting triazole is supposed to be isosteric to a peptide bond. For the conotoxin KIIIA that is amidated at the C-terminus, Y = N and for Pn3a[D8N], Y = O.

of the C-terminus of Pn3a has been shown to decrease potency compared to N-terminal sequence modifications. (Tran et al., 2023b) The N-terminal extension of conotoxin KIIIA with glycine spacer sequences has been previously investigated, revealing that short glycine repeats are well tolerated. (Tran et al., 2020, 2023b) Similarly, a strategy involving the N-to-N ligation of Pn3a with KIIIA via CuAAC, using pentaglycine spacers to develop heterobivalent toxins, has demonstrated that the bivalent construct maintains potency comparable to the modified monovalent Pn3a. (Tran et al., 2023b) Consequently, glycine repeats were selected as spacers due to their lack of interfering charges, preservation of native peptide bonds, and demonstrated ability to conserve potency at the target. In this work, spacer lengths of ten and sixteen amino acids were chosen, two probes per venom peptide and epitope tag were initially designed to assess the potential influence of the respective spacer length on potency against $Na_V1.7$. Each venom peptide analogue is N-terminally modified with five glycine residues (G_5) and one side-chain-modified amino acid for biorthogonal ligation. The variable spacer length (G_x) consists of five (G_5) and ten (G_{10}) glycine residues on the side of the epitope sequences; the latter includes one serine residue in between to prevent secondary structure formation. (Ohnishi et al., 2006)

For antibody recognition, the commonly used epitope sequences FLAG, HA, and His_6 were selected, as the sequences are short and antibodies against these epitopes are commercially available.

Rather than assembling each probe as a single sequence, a synthesis route was chosen in which the venom peptide is ligated to the epitope tag *via CuAAC*. Specifically, the venom peptides were modified with azidolysine ((N_3)K) and the epitope tags with propargylglycine (Pra). The ligation approach was chosen to avoid interference with peptide folding, e.g., formation of inactive isomers or requiring novel folding protocols due to heavily modified venom peptide sequences. Short modifications of few amino acids at the N-terminus of KIIIA, PaurTx3, another spider venom peptide, and Pn3a were tolerated during the folding process. (Tran et al., 2020, 2023b) The CuAAC ligation is fast, straight forward, and the 1,4-disubstituted 1,2,3-triazole formed during ligation can be considered isosteric to a peptide bond. (Agouram et al., 2021; Bonandi et al., 2017; Brik et al., 2005). Azidolysine and propargylglycine are commercially available and can be easily incorporated into peptide sequences using standard coupling protocols. Additionally, the azide and alkyne building blocks are chemically stable under conditions used for cleavage after solid-phase peptide synthesis (SPPS) and thermodynamic folding, making the *CuAAC* ligation strategy well-suited for the intended application. Furthermore, the ligation strategy also allows for modularity. Click-active peptides can be synthesised and subsequently tagged with any epitope sequence, requiring only a single batch of venom peptides and one protocol for assembly and folding across different probes.

Conclusively, the modular nature of this approach allows for an adaptable probe design, enabling the easy incorporation of various epitope tags without compromising peptide folding or solid-phase synthesis. The CuAAC ligation strategy was chosen not only for its efficiency but also for its seamless integration into the overall design of our probes. The amino acid sequences of all ligation peptides and Pn3a[D8N] derivatives are shown in **Table 4**.

Table 4. Amino acid sequences of venom peptides analogues and epitope-tag peptides.

Peptide	Sequence
Pra-G$_5$His$_6$	Pra-GGGGGHHHHHH
Pra-G$_{10}$His$_6$	Pra-GGGGGSGGGGGHHHHHH
Pra-G$_5$HA	Pra-GGGGGYPYDVPDYA
Pra-G$_{10}$HA	Pra-GGGGGSGGGGGHHHHHHYPYDVPDYA
Pra-G$_5$FLAG	Pra-GGGGGDYKDDDDK
Pra-G$_{10}$FLAG	Pra-GGGGGSGGGGGDYKDDDDK
(N_3)K-G$_5$KIIIA	(N_3)K-GGGGGCCNCSSKWCRDHSRCC*
Pn3a[D8N]	DCRYMFGNCEKDEDCCKHLGCKRKMKYCAWDFTFT
AcG$_5$Pn3a[D8N]	AcGGGGGDCRYMFGNCEKDEDCCKHLGCKRKMKYCAWDFTFT
G$_5$Pn3a[D8N]	GGGGGDCRYMFGNCEKDEDCCKHLGCKRKMKYCAWDFTFT
(N_3)K-G$_5$Pn3a[D8N]	(N_3)K-GGGGGDCRYMFGNCEKDEDCCKHLGCKRKMKYCAWDFTFT

(N_3)K: ε-azido-L-lysine, Pra: L-Propargylglycine, Ac: Acetyl, * amidated C-terminus

4.2 Synthesis of KIIIA and Pn3a[D8N] Derived Probes

From the designs based on KIIIA and Pn3a[D8N], a total of five probes were successfully synthesized: HA-G$_6$-*Ta*-G$_5$KIIIA, HA-G$_{11}$-*Ta*-G$_5$KIIIA, FLAG-G$_5$-*Ta*-G$_5$Pn3a[D8N], FLAG-G$_{10}$-*Ta*-G$_5$Pn3a[D8N] and His$_6$-G$_5$-*Ta*-G$_5$Pn3a[D8N].[1] The conceptualization, synthesis, and electrophysiological testing of HA-G$_5$-*Ta*-G$_5$KIIIA, HA-G$_{10}$-*Ta*-G$_5$KIIIA, FLAG-G$_5$-*Ta*-G$_5$Pn3a[D8N], and FLAG-G$_{10}$-*Ta*-G$_5$Pn3a[D8N] was conducted at the Institute for Molecular Biosciences at the University of Queensland, Australia, in the Sensory Neuropharmacology Lab of Professor Irina Vetter.

Later on, Pn3a[D8N] derivatives and His$_6$-G$_5$-*Ta*-G$_5$-Pn3a[D8N] were synthesized and characterized at the Institute of Biological Chemistry in Vienna, Austria, based on the results of the electrophysiological testing. The derivatives G$_5$Pn3a[D8N] and AcG$_5$Pn3a[D8N] were intended to be tested to examine the influence of an N-terminal G$_5$ extension and charge; however, due to the lack of facilities, electrophysiological testing of these derivatives as well as His$_6$-G$_5$-*Ta*-G$_5$-Pn3a[D8N] could not be performed.

Due to the division of the synthesis work between two laboratories, Brisbane and Vienna, different instruments (analytical HPLC, mass spectrometers) were utilized. In the laboratory in Brisbane, mass spectra could not be exported; instead, only the relevant product peaks were noted. Technical failures or, in some cases, the unavailability of instruments in the Vienna laboratory necessitated the use of alternative systems, leading to inconsistencies in the type and presentation of the data. For instance, an LC-MS spectrum could not be obtained for every product; in some cases, analytical chromatography was combined with direct injection ESI-MS for characterization, or a different LC-MS system was used. High-resolution mass spectra could only be recorded for the final characterization of the products synthesized at the Institute of Biological Chemistry, Vienna.

---

[1] To avoid confusion with one-letter amino acid codes, atoms and abbreviations are written in italics (N_3 azide, *Ta* 1,4-disubstituted 1,2,3-triazole).

4.2.1 Synthesis of Epitope tags

The alkyne functionalised epitope tags Pra-G$_{[5/10]}$-[HA/FLAG] were assembled using automated microwave-assisted SPPS on a Liberty Prime automated Peptide synthesizer. After manual coupling of the amino acid L-propargylgylcine to the N-terminus, peptides were cleaved, globally deprotected and characterized. **Figure *30*** provides an overview of the synthetic scheme.

The yields and observed masses of the products are provided in **Table 6**. High-resolution mass spectra corresponding to the masses listed in **Table 6** are shown in the supplementary figures (**Figure 48** - **Figure 54**). Chromatographic data of the epitope-tag products is provided in **Figure 31**. The FLAG tag constructs were not further purified by preparative HPLC, as their purity was determined to be >85% *via*

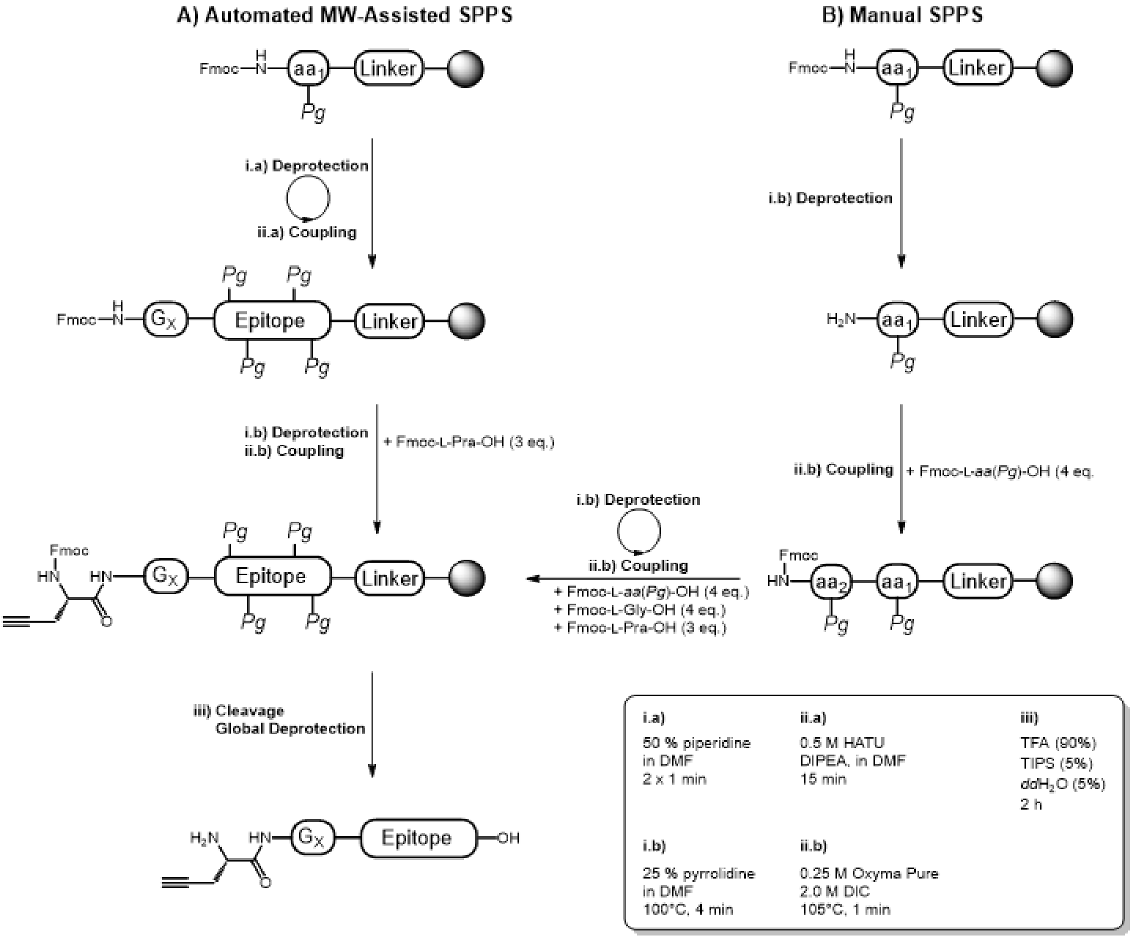

i.a)	ii.a)	iii)
50 % piperidine in DMF 2 x 1 min	0.5 M HATU DIPEA, in DMF 15 min	TFA (90%) TIPS (5%) *dd*H$_2$O (5%) 2 h
i.b)	**ii.b)**	
25 % pyrrolidine in DMF 100°C, 4 min	0.25 M Oxyma Pure 2.0 M DIC 105°C, 1 min	

Figure 30. Assembly of epitope tags and attachment of propargylglycine (Pra) onto immobilized epitope tag *via* SPPS. FLAG-G$_X$ and HA-G$_X$ tags were assembled *via* automated microwave-assisted SPPS **(A)**. G$_X$ indicates variable linker lengths of either G$_{5/6}$ or G$_{10/11}$. The His$_6$-G$_5$ and HA-G$_5$ tags were assembled manually **(B)**. In both cases, Fmoc-L-Pra-OH was coupled by manual SPPS. Tags were obtained after cleavage and global deprotection. Reaction conditions for the respective steps are displayed in the table (bottom right).

analytical RP-HPLC (per peak surface area) and deemed sufficient for the ligation

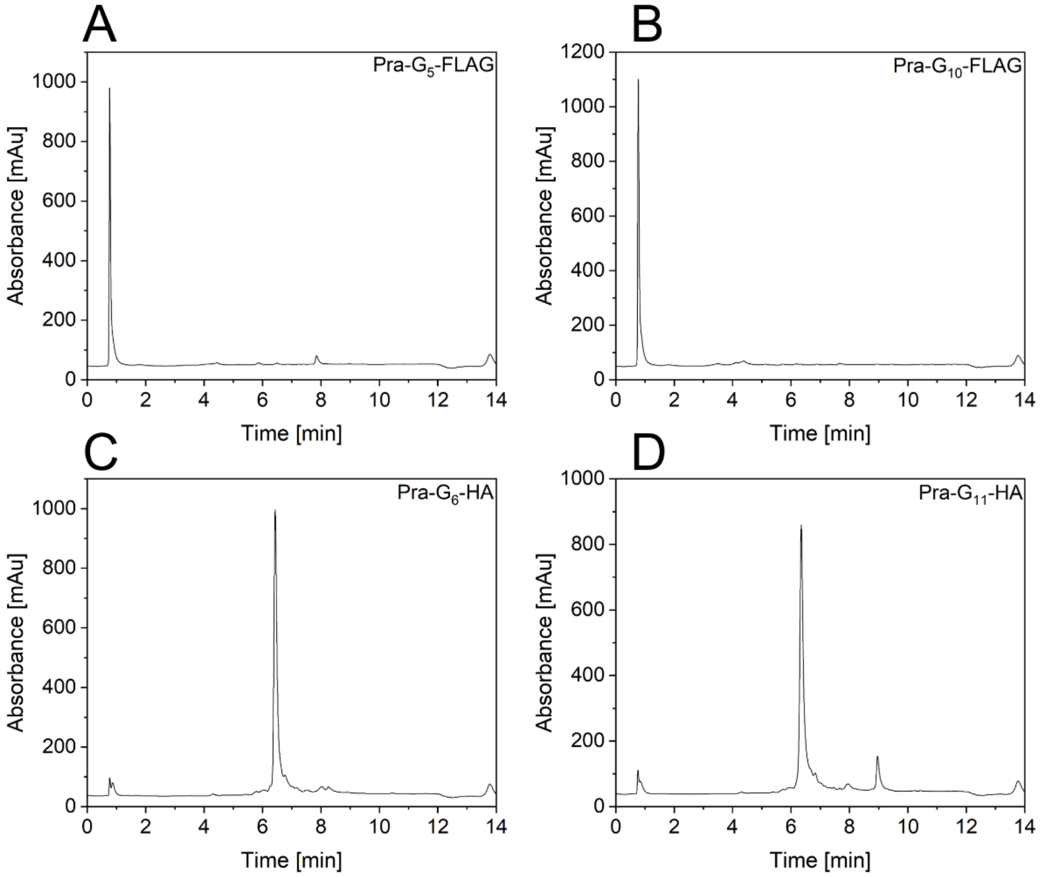

Figure 31. Analytical RP-HPLC traces of epitope tags. Elution profiles of Pra-G_6-FLAG **(A)**, Pra-G_{11}-FLAG **(B)**, Pra-G_6-HA **(C)** and Pra-G_{10}-HA **(D)**, absorbance measured at 214 nm. Analytical RP-HPLC was carried out on Shimadzu LC-20AT system with an SPD-20A Prominence UV/VIS detector and an SIL-20AHT auto-injector. Solvent gradient was 5-55% solvent B (ACN +0.05 % TFA) in solvent A (*dd*H2O + 0.5 % TFA) over 14 min (separation time) on a Hypersil GOLD C18 column (3µm particle size, 2.1 x 100 mm, 175 Å pore size, 0.7 mL/min flow rate) .

reaction. The crude HA tags were purified *via* preparative HPLC, and the collected fractions were analysed by Direct Injection ESI-MS to identify the product fractions. Pra-G_5-HA (observed mass: 1540.6 Da, calculated molecular weight: 1481.61 Da) was obtained with a yield of 61 % after purification, synthesis of Pra-G_{10}-HA (observed mass: 1913.6 Da, calculated molecular weight: 1854.86 Da) yielded 46 % product, the synthesis of Pra-G_5-FLAG (observed mass: 1393.3 Da, calculated molecular weight: 1393.34 Da) yielded 102 % without purification, and Pra-G_{10}-FLAG (observed mass: 1765.8 Da, calculated molecular weight: 1765.68 Da) was obtained with 92 % yield without purification. Noticeably, the detected most abundant mass for Pra-G_5-HA differs from the expected mass by ≈59 Da, which was initially not noticed. It was suspected that accidentally a wrong sequence with six glycine residues (calculated molecular weight for Pra-G_5-HA 1539.58 Da) was typed into the Synthesizer, which was then confirmed. Similarly, due to an observed mass difference of ≈56.97 Da, Pra-G_{10}-HA was also suspected to contain an additional glycine (calculated molecular weight for Pra-G_{11}-HA 1911.92 Da). Nevertheless, it was decided to continue with the G_6 and G_{11} tags.

4.2.2 Venom Peptide Synthesis

The linear precursors of the azide-venom-peptide derivatives of KIIIA and Pn3a[D8N] were assembled *via* automated microwave-assisted SPPS on a Liberty Prime peptide Synthesizer. All peptides were cleaved from the resins and side-chain deprotected, purified by preparative RP-HPLC, and characterized by Direct Injection ESI-MS and analytical RP-HPLC. The crude fractions were purified by preparative RP-HPLC, and ESI-MS spectra were recorded to identify the product. The linear peptides were folded by glutathione-assisted thermodynamic folding, and the correctly folded isomers were isolated by preparative RP-HPLC and characterized by analytical HPLC and Direct Injection ESI-MS. A single chromatographic peak was obtained for linear (N_3)K-G_5KIIIA (observed mass: 2329.5 Da, calculated molecular weight: 2330.62 Da, purified yield 16 %) and the major folded isomer (N_3)K-G_5KIIIA (observed mass: 2324.0 Da, calculated molecular weight: 2324.57 Da, purified yield 9 %). The conditions for oxidative folding of all Pn3a[D8N] derivatives and the modified KIIIA are depicted in **Figure 32**. Yields and observed masses of the peptides are provided in **Table 6**. For purified linear (N_3)K-

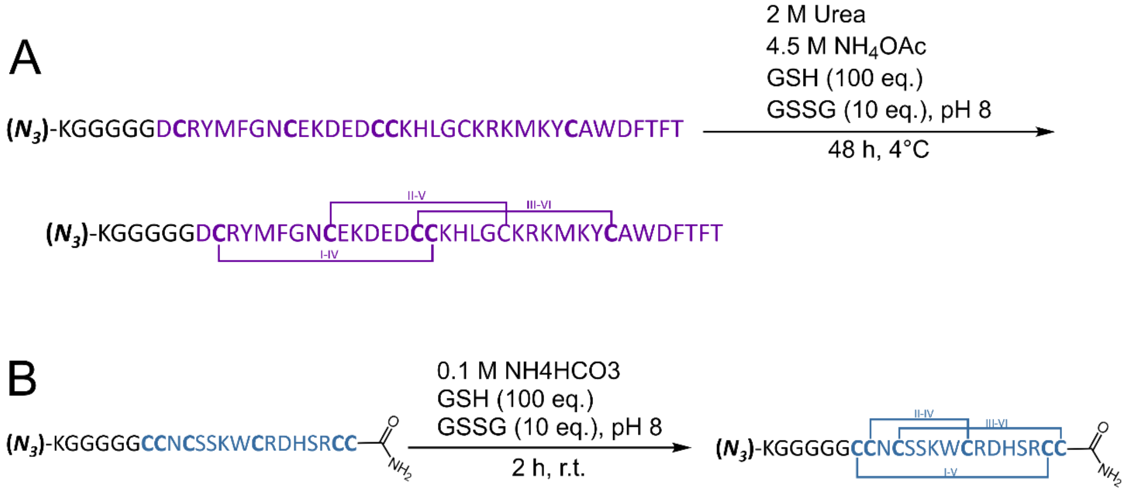

Figure 32. Thermodynamic folding of linear venom peptide precursors. Amino acid sequence, folding conditions and cysteine connectivity (in roman numerals) of the active isomers for the thermodynamic folding of (N_3)K-G_5Pn3a[D8N] **(A)** and (N_3)K-G_5KIIIA **(B)**. All Pn3a[D8N] derivatives were folded accordingly.

G_5Pn3a[D8N] a single peak was detected (observed mass: 4717.6 Da, calculated molecular weight: 4716.40 Da, purified yield 25 %) and for folded (*N_3*)K-G_5Pn3a[D8N] a characteristic double could be observed (observed mass: 4710.8 Da, calculated molecular weight: 4710.35 Da, purified yield 13 %). Chromatographic data for linear precursors and folded peptides of (*N_3*)K-G_5KIIIA and (*N_3*)K-G_5Pn3a[D8N], respectively, are depicted in **Figure 33** and **Figure 34**.

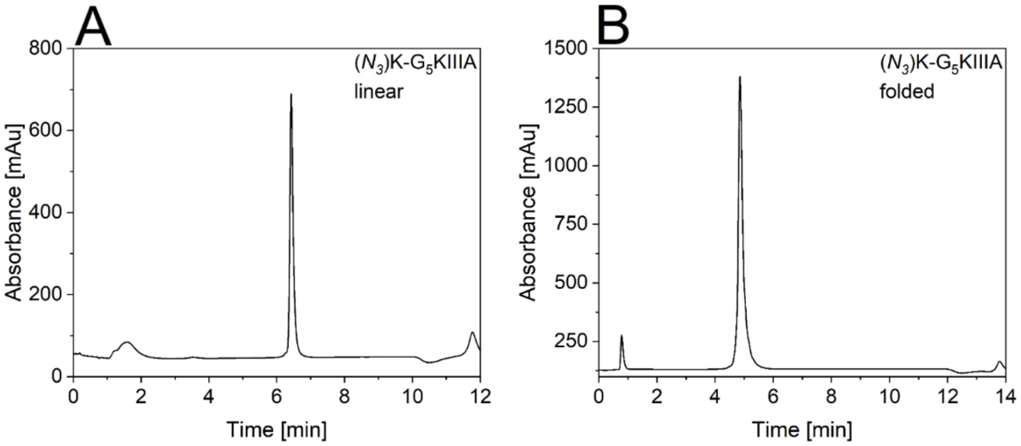

Figure 33. Analytical RP-HPLC traces of (*N_3*)K-G_5KIIIA. Elution profiles of unfolded (*N_3*)K-G_5KIIIA **(A)** and folded (*N_3*)K-G_5KIIIA **(B)**. Absorbance was measured at 214 nm. Analytical RP-HPLC was carried out on Shimadzu LC-20AT system with an SPD-20A Prominence UV/VIS detector and an SIL-20AHT auto-injector. Solvent gradient was 5-55% solvent B (ACN +0.05 % TFA) in solvent A (*dd*H2O + 0.5 % TFA) over 14 min (separation time) on a Hypersil GOLD C18 column (3µm particle size, 2.1 x 100 mm, 175 Å pore size, 0.7 mL/min flow rate).

4.2.3 Ligation of KIIIA and Pn3a[D8N] Derivatives with Epitope Tags

The click reactive (*N_3*)K-G_5KIIIA and (*N_3*)K-G_5Pn3a[D8N] were linked N- to N-terminus with HA- and FLAG-tags, respectively. The *CuAAC* ligation conditions for KIIIA and Pn3a[D8N] derived probes, as well as chromatographic, data are shown in **Figure 35** and **Figure 36 A** and **C**, respectively. For both reactions, the peaks of the initial starting material shifted to earlier retention times, indicating product formation. The yields of this ligation reaction, and observed masses are provided in **Table 6**. The final products purified *via* semipreparative RP-HPLC were characterised by analytical RP-HPLC and Direct Injection ESI-MS. For HA-G_6-*Ta*-G_5KIIIA (observed mass: 3864.8 Da, calculated molecular weight: 3864.15 Da, purified yield 8 %) and HA-G_{11}-*Ta*-G_5KIIIA (observed mass: 4236.5 Da, calculated molecular weight: 4236.48 Da, purified yield 3 %), respectively, single chromatographic peaks were obtained, as shown in **Figure 35 B** and **D**. The epitope-tagged Pn3a[D8N] derived probes FLAG-G_5-*Ta*-G_5Pn3a[D8N] (observed mass: 6104.6 Da, calculated molecular weight: 6103.69 Da, purified yield 2 %) and FLAG-G_{10}-*Ta*-G_5Pn3a[D8N] (observed mass: 6476.4 Da, calculated molecular weight: 6476.03 Da, purified yield 2 %) each yielded a characteristic double peak shown in **Figure 36 B** and **D**.

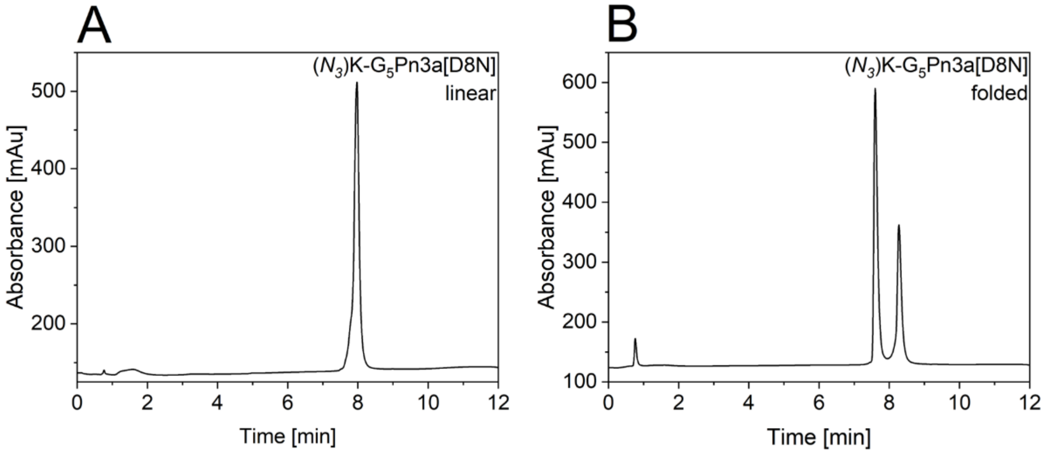

Figure 34. Analytical RP-HPLC traces of (*N_3*)K-G_5Pn3a[D8N]. Elution profiles of unfolded (*N_3*)K-G_5Pn3a[D8N] **(A)** and folded (*N_3*)K-G_5Pn3a[D8N] **(B)** with the absorbance measured at 214 nm. Analytical RP-HPLC was carried out on Shimadzu LC-20AT system with an SPD-20A Prominence UV/VIS detector and an SIL-20AHT auto-injector. Solvent gradient was 5-55% solvent B (ACN +0.05 % TFA) in solvent A (*dd*H2O + 0.5 % TFA) over 14 min (separation time) on a Hypersil GOLD C18 column (3µm particle size, 2.1 x 100 mm, 175 Å pore size, 0.7 mL/min flow rate).

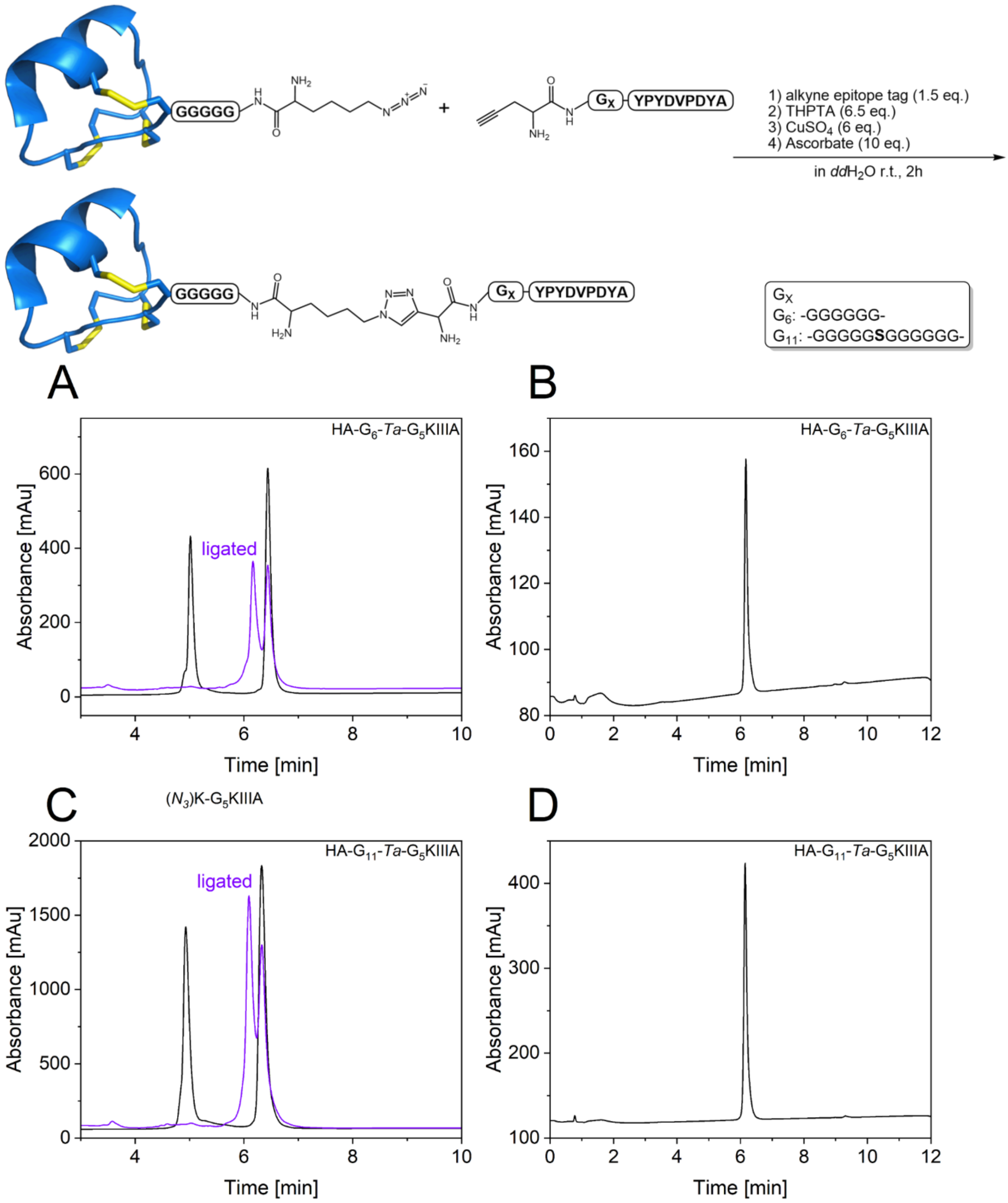

Figure 35. Analytical RP-HPLC traces of the ligation of (*N*$_3$)K-G$_5$KIIIA with Pra-G$_{6/11}$-HA *via CuAAC.* A comparison of the RP-HPLC traces at the start of the reaction and when the formation of HA-G$_6$-*Ta*-G$_5$-KIIIA was complete **(A)**. The analytical RP-HPLC trace shows the product after purification *via* semipreparative RP-HPLC **(B)**. The formation of HA-G$_{11}$-*Ta*-G$_5$-KIIIA was monitored **(C)** similarly and the product isolated *via* semipreparative RP-HPLC **(D)**. The absorbance was measured at 214 nm. Analytical RP-HPLC was carried out on Shimadzu LC-20AT system with an SPD-20A Prominence UV/VIS detector and an SIL-20AHT auto-injector. Solvent gradient was 5-55% solvent B (ACN +0.05 % TFA) in solvent A (*dd*H2O + 0.5 % TFA) over 14 min (separation time) on a Hypersil GOLD C18 column (3µm particle size, 2.1 x 100 mm, 175 Å pore size, 0.7 mL/min flow rate).

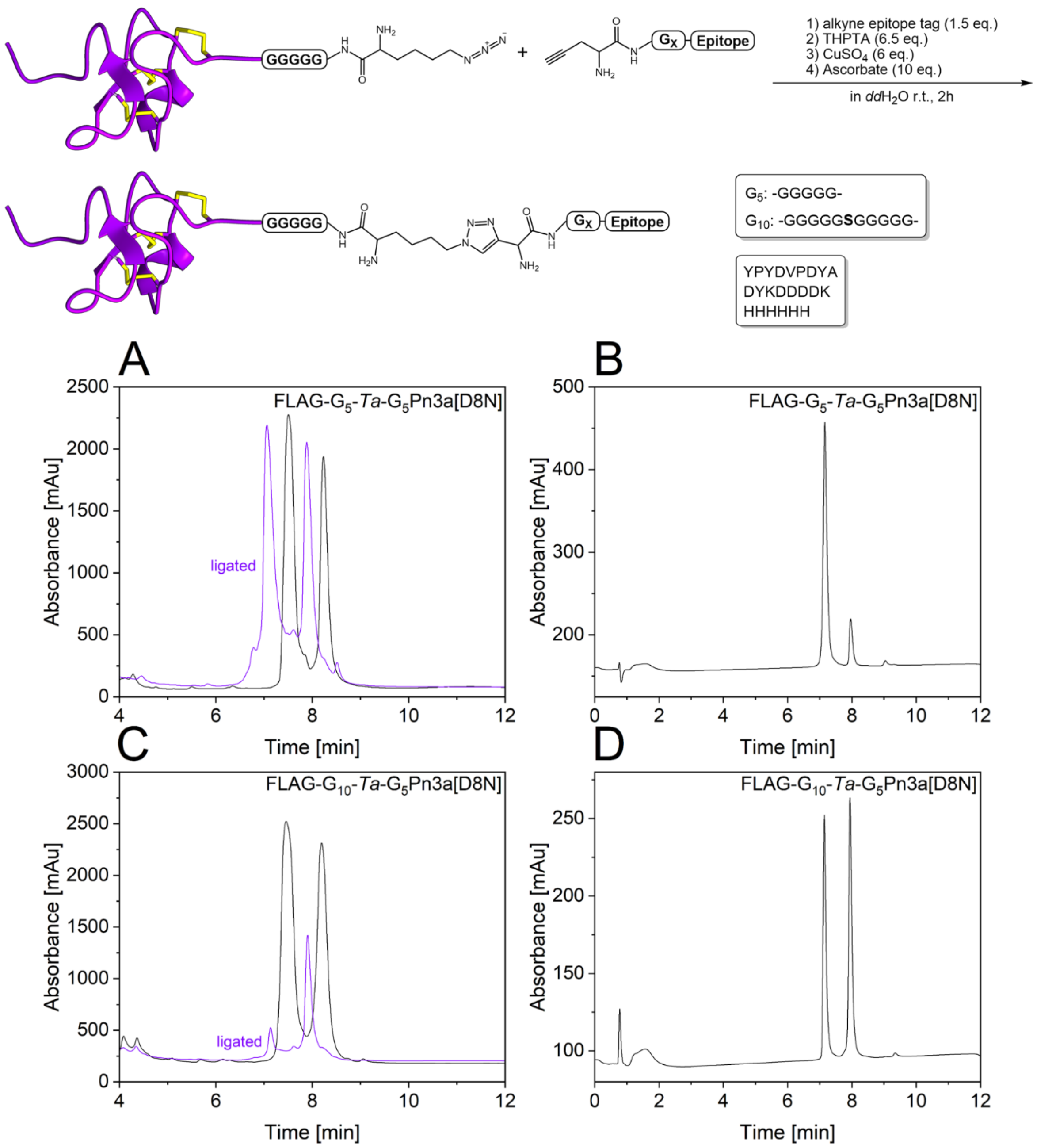

Figure 36. Analytical RP-HPLC traces of the ligation of (*N_3*)K-G_5Pn3a[D8N] with Pra-G_5-HA *via CuAAC*. A comparison of the RP-HPLC traces at the start of the reaction and when the formation of FLAG-G_5-*Ta*-G_5-Pn3a[D8N] was complete **(A)**. The analytical RP-HPLC trace shows the product after purification *via* semipreparative RP-HPLC **(B)**. The formation of FLAG-G_{10}-*Ta*-G_5-Pn3a[D8N] was monitored **(C)** similarly and the isolated product after semipreparative RP-HPLC **(D)**. The absorbance was measured at 214 nm. Analytical RP-HPLC was carried out on Shimadzu LC-20AT system with an SPD-20A Prominence UV/VIS detector and an SIL-20AHT auto-injector. Solvent gradient was 5-55% solvent B (ACN +0.05 % TFA) in solvent A (*dd*H2O + 0.5 % TFA) over 14 min (separation time) on a Hypersil GOLD C18 column (3µm particle size, 2.1 x 100 mm, 175 Å pore size, 0.7 mL/min flow rate).

4.3 Electrophysiological Testing of KIIIA- and Pn3a[D8N]-derived Probes at hNa$_V$1.7

The inhibitory potency of HA-G$_{6/10}$-tagged KIIIA and FLAG-G$_{5/10}$-tagged Pn3a[D8N] at hNa$_V$1.7 was determined by automated whole-cell patch-clamp electrophysiology. The pIC$_{50}$ values are listed in **Table 5,** and concentration-response curves are depicted in **Figure 37 A** and **C**. For comparison, Pn3a[D8N], as well as the KIIIA isomers 1 and 2 were included as internal references.

The HA-G$_{6/11}$-tagged KIIIA probes displayed low potency of inhibition at Na$_V$1.7 compared to KIIIA isomer 1, with concentrations required for IC$_{50}$ determination that are out of range of the available concentrations of this experiment, appearing even lower than KIIIA isomer 2 (**Figure 37 C**). The FLAG-G$_{5/10}$-tagged Pn3a[D8N] probes inhibited Na$_V$1.7 equally with a pIC$_{50}$ of ≈ 6.70 with a 17.7-fold decrease compared to Pn3a[D8N] (pIC$_{50}$ = 7.944 ± 0.044 nM, n = 7). A depiction of different pIC$_{50}$ values is provided in **Figure 37 B**, indicating a significant difference between both FLAG-tagged Pn3a[D8N]-based probes and Pn3a[D8N] ($P \leq 0.0001$), determined by one-way ANOVA. The internal references Pn3a[D8N] and KIIIA Isomer 1 and 2 were previously synthesized and provided by Dr. Hue Tran, following the protocol presented in this work.

Table 5. Inhibitory potency of KIIIA and Pn3a[D8N] derived epitope-tagged probes at hNa$_V$1.7 *via* automated whole-cell patch-clamp electrophysiology on HEK293 cells. Each cell tested represents one replicate (n).

Peptide	pIC$_{50}$	n
HA-G$_6$-*Ta*-G$_5$-KIIIA	n.d.	2
HA-G$_{11}$-*Ta*-G$_5$-KIIIA	n.d.	1
FLAG-G$_5$-*Ta*-G$_5$-Pn3a [D8N]	6.697 ± 0.114	2
FLAG-G$_{10}$-*Ta*-G$_5$-Pn3a [D8N]	6.698 ± 0.149	3

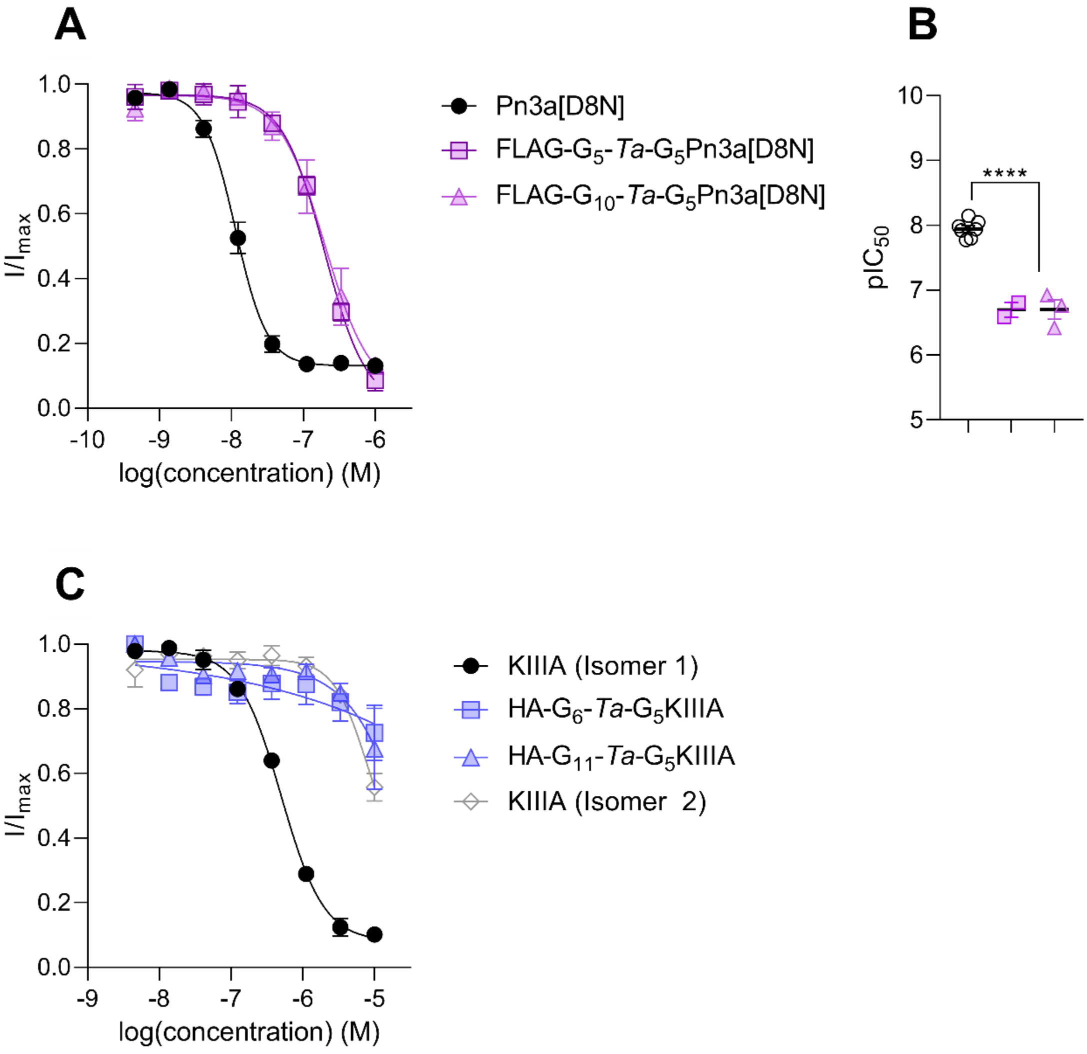

Figure 37. Inhibition of epitope tagged KIIIA and Pn3a[D8N] probes at Na$_V$1.7. Concentration-response curves of normalized Na$_V$1.7 current against the ligand concentration for FLAG-G$_5$-*Ta*-G$_5$Pn3a[D8N] (n=2) and FLAG-G$_{10}$-*Ta*-G$_5$Pn3a[D8N] (n=3) probes **(A)** and visualized pIC$_{50}$ values **(B)**, with Pn3a[D8N] included as a reference. Statistical significance was determined by one-way ANOVA, **** $P \leq 0.0001$. The respective concentration-response curves for HA-G$_6$-*Ta*-G$_5$KIIIA (n=2) and HA-G$_{11}$-*Ta*-G$_5$KIIIA (n=1) **(C)** together with the active disulfide isomer 1 and inactive isomer 2 of KIIIA as references.

4.4 Second iteration of Synthesis – Focus on Pn3a[D8N]

4.4.1 Synthesis of Epitope Tags for ligation with Pn3a[D8N]

With the results from electrophysiological testing, it was decided to focus on Pn3a[D8N] probe development and prepare Pn3a[D8N] tagged with the HA- and

His$_6$-tag as well as G$_5$Pn3a[D8N] and AcG$_5$Pn3a[D8N].This time, epitope tags with only five glycine spacers were synthesized.

Pra-G$_5$-HA and Pra-G$_5$-His$_6$ were assembled manually *via* SPPS. The principal workflow is shown in **Figure 30**. After cleavage, the epitope tags were purified by preparative RP-HPLC, and product fractions were identified *via* Direct Injection ESI-MS **Figure 38 B** and **D**. The analytical RP-HPLC traces are depicted in **Figure 38 A** and **C**. Pra-G$_5$-HA and Pra-G$_5$-His$_6$ were obtained with high purity and characterized with high-resolution mass spectrometry (Pra-G$_5$-HA observed monoisotopic mass: 1481.61 Da, exact mass: 1481.61 Da, reaction yield 53 %; Pra-G$_5$-His$_6$ observed monoisotopic mass: 1220.51 Da, exact mass: 1220.51 Da,

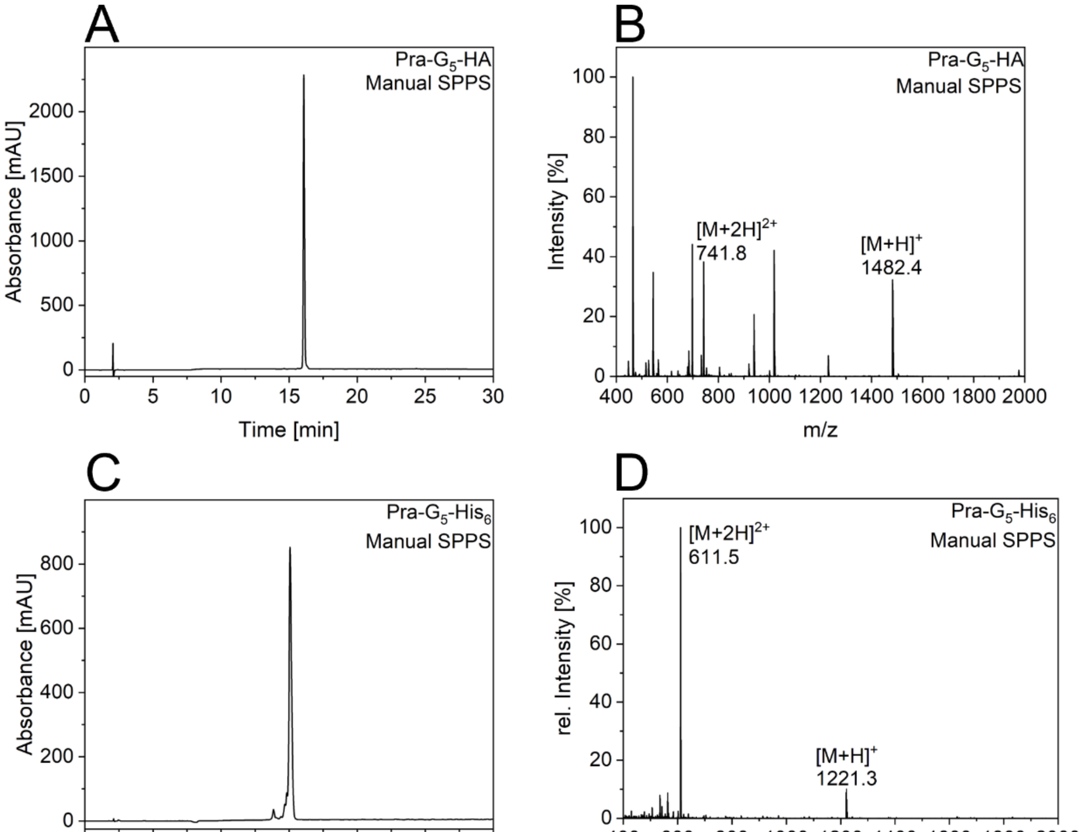

Figure 38. Analytical RP-HPLC trace and MS profile of Pra-G$_5$-HA and Pra-G$_5$-His$_6$. Analytical RP-HPLC trace of Pra-G$_5$-HA after purification *via* preparative RP-HPLC **(A)** and a Direct Injection ESI-MS spectrum **(B)**. identifying the product as Pra-G$_5$-HA. Analytical RP-HPLC trace of Pra-G$_5$-His$_6$ after purification *via* preparative RP-HPLC **(C)** and a Direct Injection ESI-MS spectrum **(D)** identifying the product as Pra-G$_5$-His$_6$. Analytical RP-HPLC was performed using a Kromasil C18 column (300-5-C18, 150 x 4.6 mm, 5 µm particle size, 300 Å pore size). Separation was performed over 30 min with a gradient of 0-20 % solvent B (ACN +0.08 % TFA) in solvent A (*dd*H2O + 0.1 % TFA) with a flow rate of 1 mL/min and the absorbance was measured at 214 nm wavelength. Direct Injection ESI-MS was performed on a Waters LC-MS system with an SQ2 mass detector.

reaction yield 67 %). An overview of yields of the epitope tags and a comparison of calculated and experimentally observed masses is shown in **Table 6**.

4.4.2 Synthesis of Pn3a[D8N] and derivatives

Pn3a[D8N] was assembled *via* automated MW-assisted SPPS on a Liberty Prime automated Synthesizer and the linear precursor was obtained after preparative RP-HPLC of the crude peptide. The product was identified and characterized by LC-MS (observed mass: 4276.8 Da, calculated molecular weight: 4276.97 Da, purified yield 11 %) and analytical RP-HPLC (**Figure 39**). The linear precursor was folded, as depicted in **Figure 36**. The characteristic peak shape identified the correctly folded isomer . The LC-MS spectra for product characterisation and the analytical RP-

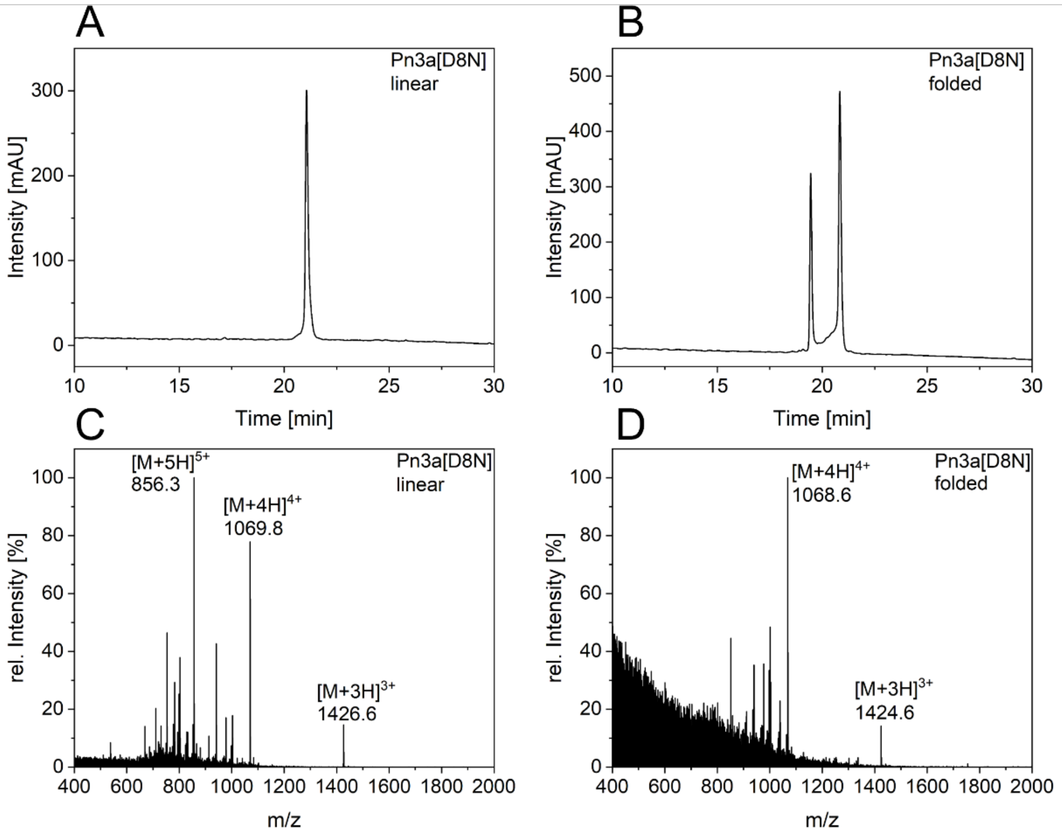

Figure 39. Analytical RP-HPLC trace and MS profile of the linear precursor and folded-Pn3a[D8N]. Analytical RP-HPLC trace of linear Pn3a[D8N] after purification *via* preparative RP-HPLC **(A)** and an ESI-MS spectrum **(C)**, identifying the product as linear Pn3a[D8N]. Analytical RP-HPLC trace of folded Pn3a[D8N] after purification *via* preparative RP-HPLC displaying the characteristic double peak **(B)** and an ESI-MS spectrum **(D)**. Analytical RP-HPLC was performed using a Kromasil C18 column (300-5-C18, 150 x 4.6 mm, 5 µm particle size, 300 Å pore size). Separation was performed over 30 min with a gradient of 5–65 % solvent B (ACN +0.08 % TFA) in solvent A (*dd*H2O + 0.1 % TFA) with a flow rate of 1 mL/min and the absorbance was measured at 214 nm wavelength. ESI-MS was performed *via* LC-MS on a Thermo LC-MS system with Thermo MSQ Plus Mass Detector and a XSelect® CSH C18 reverse phase column (3 x 75 mm, particle size of 2.5 µm, 130 Å pore size).

HPLC chromatograms are provided **Figure 39 B** and **D**. The folded product was finally characterised by high-resolution mass spectrometry (observed mass: 4267.74 Da, calculated exact mass: 4267.74 Da, purified yield 9 %). The yield of SPPS, thermodynamic folding, and observed masses are listed in **Table 6**.

G_5Pn3a[D8N] was prepared as described for Pn3a[D8N]. For AcG_5Pn3a[D8N], the free N-terminus of G_5Pn3a[D8N] was acetylated while protected and on resin. Azido lysine was coupled manually to G_5Pn3a[D8N] to obtain (N_3)K-G_5Pn3a[D8N]. Linear G_5Pn3a[D8N] (observed monoisotopic mass: 4560.9 Da, calculated molecular weight: 4562.23 Da) was obtained with a 6 % yield, AcG_5Pn3a[D8N] (observed monoisotopic mass: 4603.9 Da, calculated molecular weight: 4604.26 Da) with a

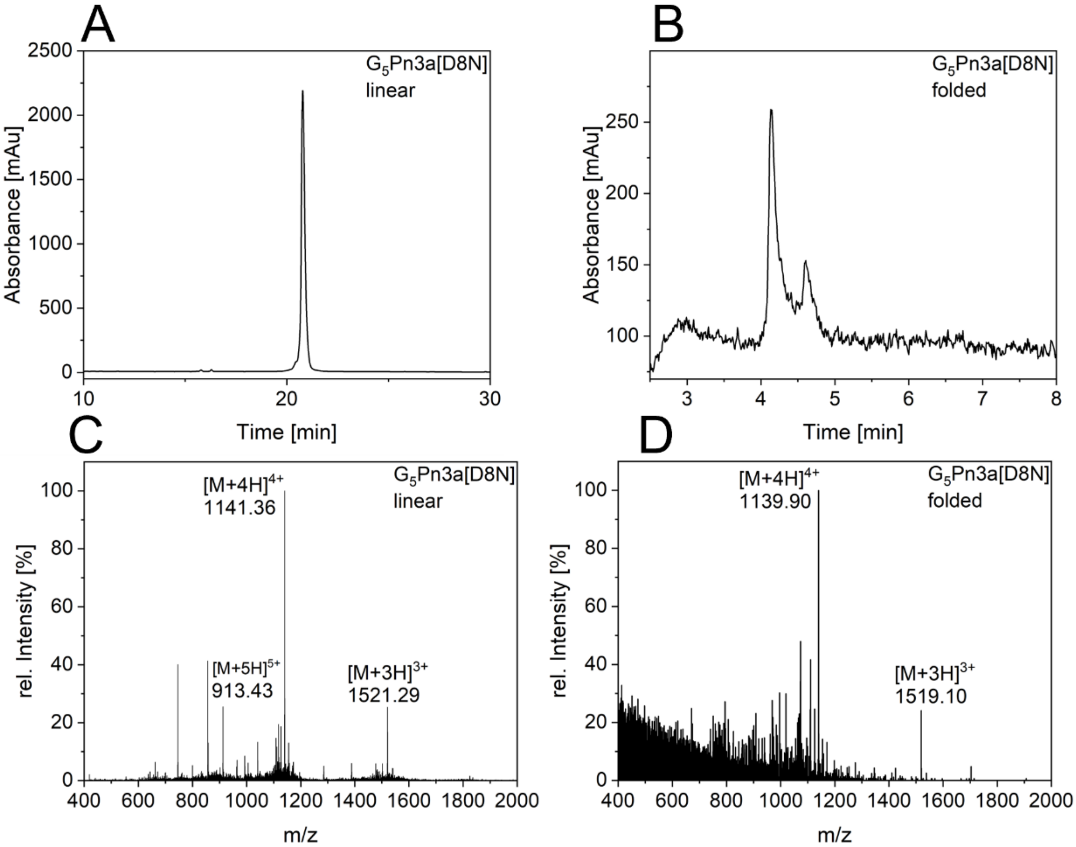

Figure 40. Analytical RP-HPLC trace and MS profile of the linear precursor and folded-G_5Pn3a[D8N]. Analytical RP-HPLC trace of linear G_5-Pn3a[D8N] after purification *via* preparative RP-HPLC **(A)** and an Direct Injection ESI-MS spectrum **(C)**, identifying the product as linear G_5-Pn3a[D8N]. Analytical RP-HPLC trace of folded G_5-Pn3a[D8N] after purification *via* preparative RP-HPLC displaying the characteristic double peak **(B)** and an Direct Injection ESI-MS spectrum **(D)**. Analytical RP-HPLC was performed using a Kromasil C18 column (300-5-C18, 150 x 4.6 mm, 5 µm particle size, 300 Å pore size). Separation was performed over 30 min with a gradient of 5–65 % solvent B (ACN +0.08 % TFA) in solvent A (*dd*H2O + 0.1 % TFA) with a flow rate of 1 mL/min and the absorbance was measured at 214 nm wavelength. Direct Injection ESI-MS was performed on a Waters LC-MS system with an SQ2 mass detector.

21 % yield and (N_3)K- G$_5$Pn3a[D8N] (observed monoisotopic mass: 4716.2 Da, calculated molecular weight: 4716.40 Da) with a 15 % yield, respectively. Folding, product identification, and characterisation were carried out as described for Pn3a[D8N]. Each derivative produced a characteristic double peak after folding. For comparison, yields and observed masses of the unfolded precursors and the final products are listed in **Table 6**. High-resolution mass spectra of the final products were recorded for final product characterisation for folded G$_5$Pn3a[D8N] (observed monoisotopic mass: 4552.85 Da, exact mass: 4552.85 Da, 16 % yield), folded AcG$_5$Pn3a[D8N] (observed monoisotopic mass: 4594.86 Da, exact mass: 4594.86

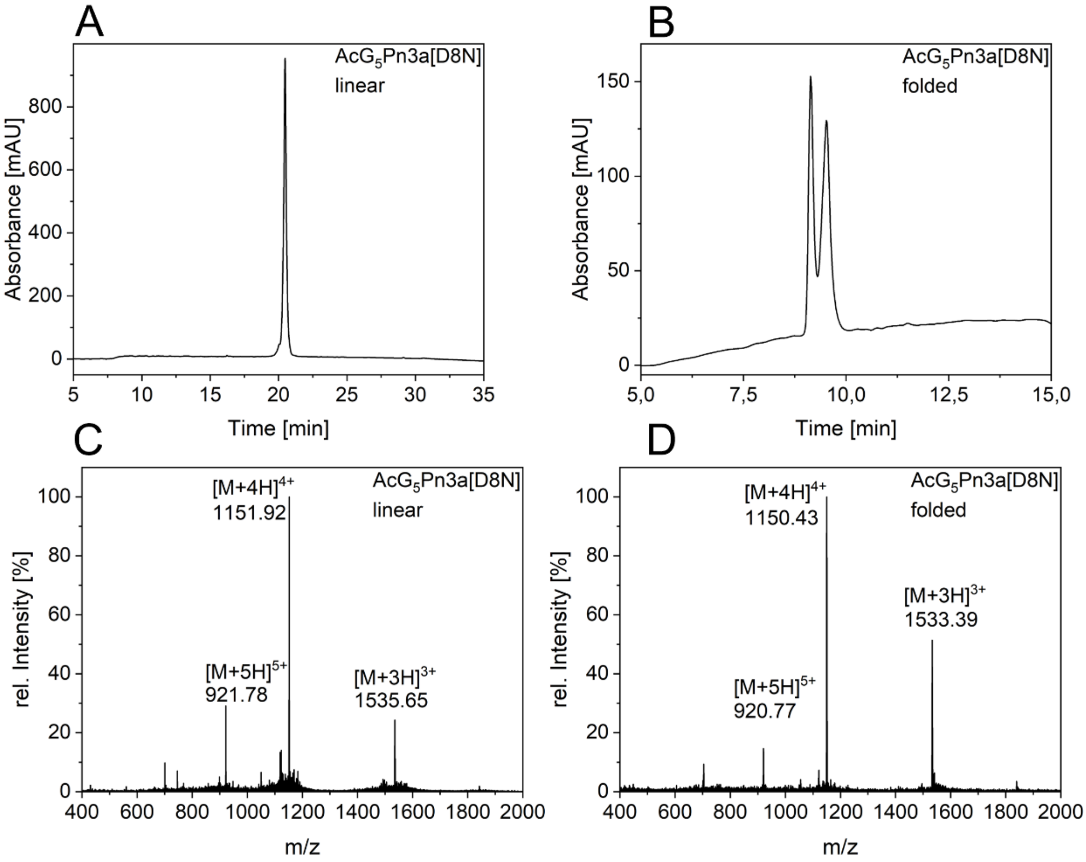

Figure 41. Analytical RP-HPLC trace and MS profile of the linear precursor and folded-AcG$_5$Pn3a[D8N]. Analytical RP-HPLC trace of linear G$_5$-Pn3a[D8N] after purification *via* preparative RP-HPLC **(A)** and an Direct Injection ESI-MS spectrum **(C)**, identifying the product as linear G$_5$-Pn3a[D8N]. Analytical RP-HPLC trace of folded G$_5$-Pn3a[D8N] after purification *via* preparative RP-HPLC displaying the characteristic double peak **(B)** and an Direct Injection ESI-MS spectrum **(D)**. Analytical RP-HPLC was performed using a Kromasil C18 column (300-5-C18, 150 x 4.6 mm, 5 µm particle size, 300 Å pore size). Separation was performed over 30 min with a gradient of 5–65 % solvent B (ACN +0.08 % TFA) in solvent A (*dd*H2O + 0.1 % TFA) with a flow rate of 1 mL/min and the absorbance was measured at 214 nm wavelength. Direct Injection ESI-MS was performed on a Waters LC-MS system with an SQ2 mass detector.

Da, 2 % yield), and folded (N_3)K-G$_5$Pn3a[D8N] (observed monoisotopic mass: 4706.93 Da, exact mass: 4706.93 Da, 9 % yield).

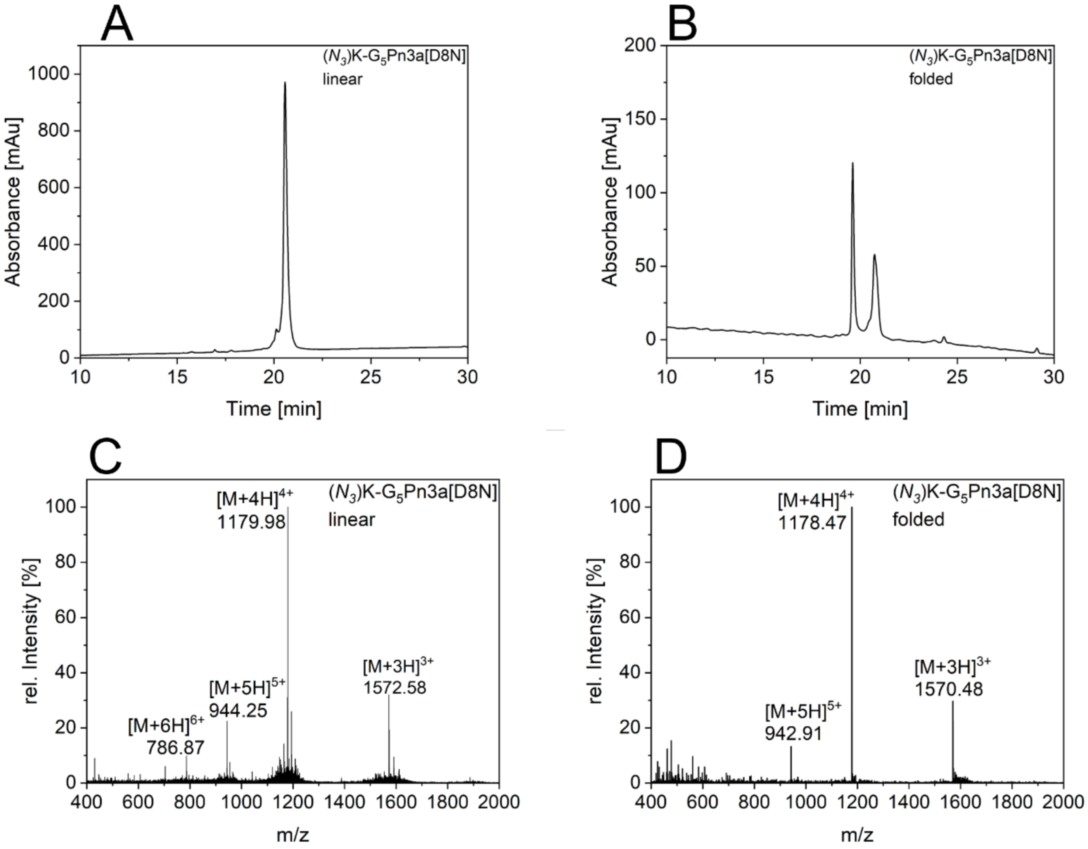

Figure 42. Analytical RP-HPLC trace and MS profile of the linear precursor and folded (*N_3*)K-G$_5$Pn3a[D8N]. Analytical RP-HPLC trace of linear (N_3)K-G$_5$-Pn3a[D8N] after purification *via* preparative RP-HPLC **(A)** and an Direct Injection ESI-MS spectrum **(C)**, identifying the product as linear (N_3)K-G$_5$-Pn3a[D8N]. Analytical RP-HPLC trace of folded (N_3)K-G$_5$-Pn3a[D8N] after purification *via* preparative RP-HPLC displaying the characteristic double peak **(B)** and an Direct Injection ESI-MS spectrum **(D)**. Analytical RP-HPLC was performed using a Kromasil C18 column (300-5-C18, 150 x 4.6 mm, 5 µm particle size, 300 Å pore size). Separation was performed over 30 min with a gradient of 5–65 % solvent B (ACN +0.08 % TFA) in solvent A (*dd*H2O + 0.1 % TFA) with a flow rate of 1 mL/min and the absorbance was measured at 214 nm wavelength. Direct Injection ESI-MS was performed on a Waters LC-MS system with an SQ2 mass detector.

4.4.3 Ligation of Pn3a[D8N] Derivatives with Epitope Tags

The *CuAAC* ligation was performed as depicted in **Figure 36**. Samples were taken initially at the start of the reaction when reactants were combined and throughout the reaction. LC-MS spectra were recorded to monitor the reaction progress and identify reaction components, such as product and starting material. For His$_6$-G$_5$-*Ta*-G$_5$Pn3a[D8N], the reaction progress, chromatograms, and mass spectra for three different timepoints are depicted (t$_0$ after mixing, t$_4$ after 1 h and t$_5$ over night). The characteristic double peak of Pn3a[D8N]-species is shown in **Figure 43 A** with the corresponding mass spectrum identifying the component as (*N*$_3$)K-G$_5$Pn3a[D8N] (**Figure 43 B**). After 1 h (t$_4$), the maximum intensity of the characteristic peak is reduced **(C)**. The mass spectrum confirms the presence of the ligation product **(D)** (observed mass: 5929.89 Da, calculated molecular weight: 5931.58 Da). Since the reaction did not progress as expected, another equivalent of copper sulphate and ascorbic acid was added after 40 min. A precipitate started to form as the reaction progressed. After an hour (t$_4$), an additional equivalent of copper sulphate, ascorbic acid, THPTA as well as Pra-G$_5$-His$_6$ (3 eq. in total) were added. After 16 hours (t$_5$), all starting material was depleted, and no peak could be detected in the liquid phase. The reaction solution was centrifuged and analytical RP-HPLC of both, the solid an liquid phase, were recorded. As shown in **Supplementary Figure 47**, the product was suspected to be present in the solid phase ("pellet" after centrifugation). After preparative RP-HPLC, pure fractions were pooled, and a final analytical RP-HPLC spectrum was recorded (**Figure 43 F**). Due to the minimal amount of product obtained, a sample was submitted to the Mass Spectrometry Centre to record a high-resolution mass spectrum for identification. The amount of product could not be unambiguously measured by gravimetrical analysis, and thus, a UV/VIS concentration determination was performed using a Nanodrop Microvolume Spectrophotometer. From the determined concentration, the amount of product was calculated. His$_6$-G$_5$-*Ta*-G$_5$Pn3a[D8N] (observed monoisotopic mass: 5927.43 Da, exact mass: 5927.44 Da) was obtained with a 25 % yield (**Table 6**). The recorded high-resolution mass spectrum is shown in **Supplementary Figure 54**.

For HA-G$_5$-*Ta*-G$_5$Pn3a[D8N], the ligation was performed as described above. The monitoring of the reaction progress is depicted in **Figure 44**. Initially, after mixing, a sample (t$_0$) was taken. The LC trace (**Figure 44 A**) shows a characteristic double peak, which was identified as (*N*$_3$)K-G$_5$Pn3a[D8N] *via* the corresponding mass spectrum (**Figure 44 B**). After taking the initial sample, another equivalent of copper sulphate and ascorbic acid was added, and the reaction was allowed to complete overnight. After 15 hours (t$_1$), the reaction was deemed almost complete (**Figure 44 C**). No precipitate formation was observed. The corresponding mass spectrum allowed the identification of residual starting material but no distinct peak that can be unambiguously assigned to the product (**Figure 44 D**) (observed mass: 6103.70

Da, calculated molecular weight: Da). The reaction was continued and subsequently subjected to semipreparative RP-HPLC the next day, however, no product fractions could be recovered and thus no further characterisation or specification of reaction yield could be made.

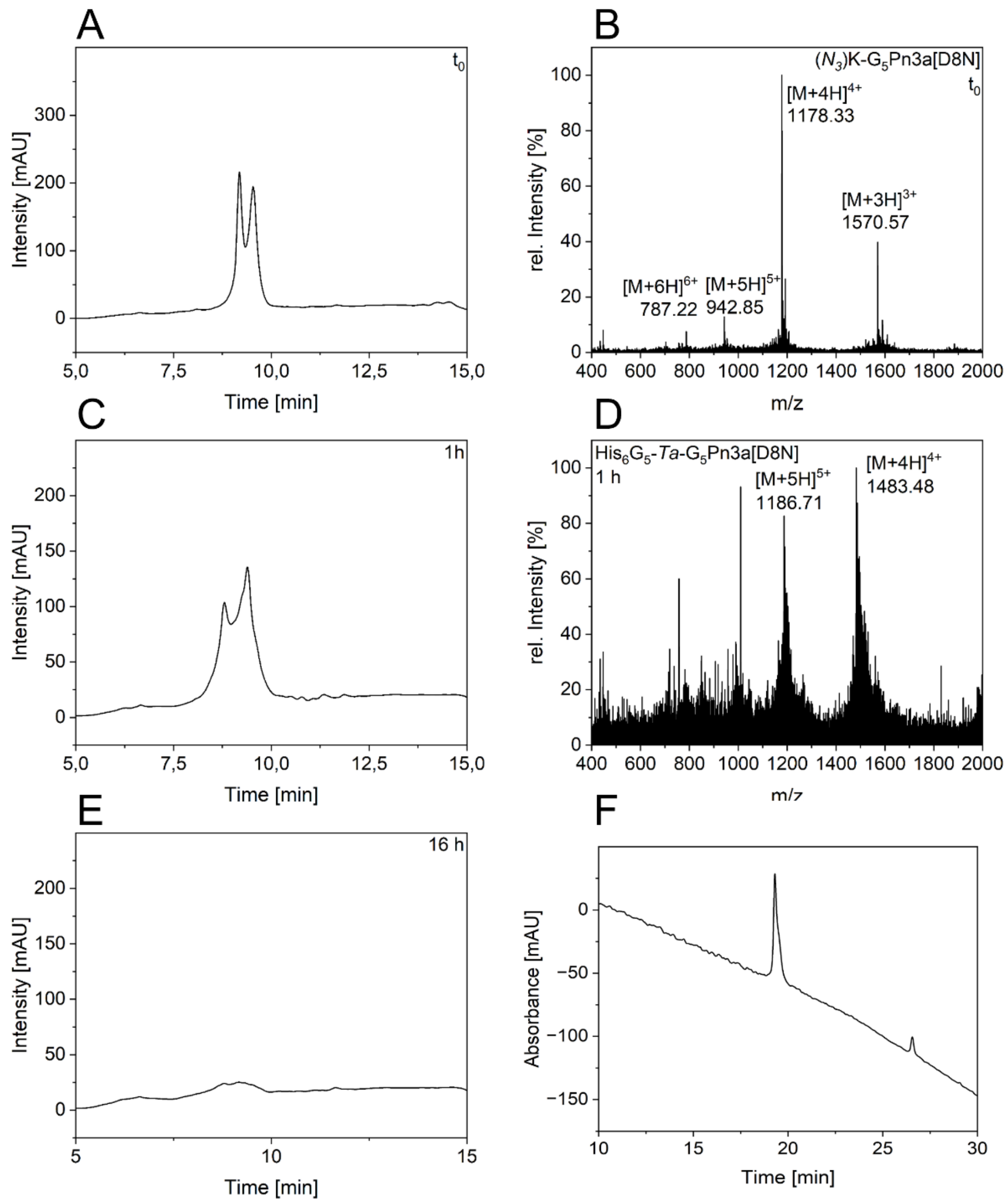

Figure 43. LC-MS and Analytical RP-HPLC and MS profile of the *CuAAC* ligation of Pra-G_5-His6 with (*N_3*)K-G_5Pn3a[D8N] at different timepoints throughout the reactions(t_0, 1 h and 16 h). LC trace **(A)** with the corresponding mass spectrum **(B)** of a sample taken at the beginning of the ligation reaction, identifying the constituent of the double peak as folded (*N_3*)K-G_5Pn3a[D8N]. Peak profile of the sample taken at 1 h (t_4) **(C)** with masses indicating the presence of the ligation product **(D)**. The final sampling shows the absence of previously observed peaks after approximately 16 h (t_5) **(E)**. Analytical RP-HPLC trace of the isolated product displays the characteristic double peak of Pn3a **(F)**. LC-MS was carried out on a Waters LC-MS system with an SQ2 mass detector, a Kromasil C18 column (300-5-C18, 50 x 4.6 mm, 5 µm particle size, 100 Å pore size) with a gradient of solvent B (ACN +0.05 % TFA) in solvent A (ddH2O + 0.05 % TFA) over 30 min (separation time) with a flow rate of 1 mL/min, measing the absorbance at 214 nm wavelength. Analytical RP-HPLC was carried out on a Kromasil C18 column (300-5-C18, 150 x 4.6 mm, 5 µm particle size, 300 Å pore size) using a Thermo Scientific UltiMate 3000 HPLC system with a 5–65 % gradient of solvent B (ACN +0.08 % TFA) in solvent A (*dd*H2O + 0.1 % TFA) over 30 min (separation time) with a flow rate of 1 mL/min. Absorbance was measured at 214 nm.

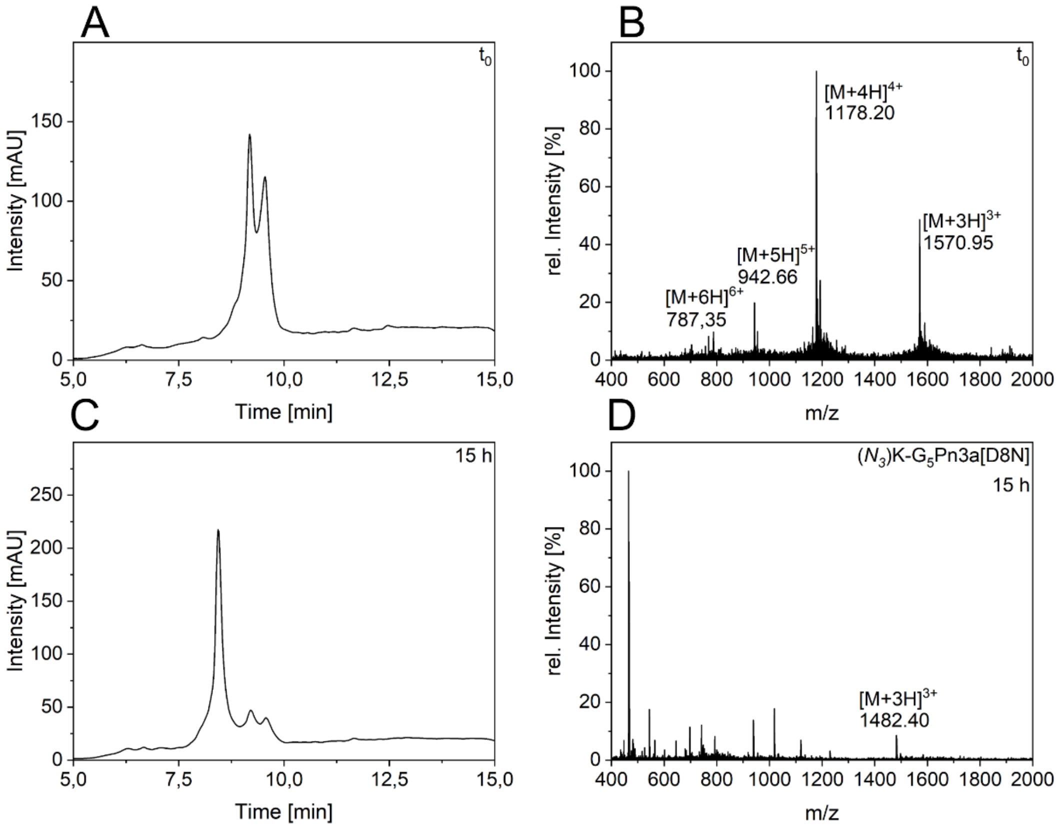

Figure 44. LC-MS and Analytical RP-HPLC and MS profile of the *CuAAC* ligation of Pra-G_5-HA with (*N_3*)K-G_5Pn3a[D8N] at different timepoints throughout the reactions(t_0 and 15 h). LC trace of a sample taken at the beginning of the reaction (t_0) **(A)** with the corresponding mass spectrum **(B)**, identifying the constituent of the double peak as folded (*N_3*)K-G_5Pn3a[D8N]. Peak profile of the sample taken after 15 h (t_1) **(C)**. Peaks of the corresponding mass spectrum of t_1 are assigned to product and starting material (purple) **(D)**. LC-MS was carried out on a Waters LC-MS system with an SQ2 mass detector, a Kromasil C18 column (300-5-C18, 50 x 4.6 mm, 5 µm particle size, 100 Å pore size) with a gradient of solvent B (ACN +0.05 % TFA) in solvent A (*dd*H2O + 0.05 % TFA) over 30 min (separation time) with a flow rate of 1 mL/min, measuring the absorbance at 214 nm wavelength.

Table 6. Observed masses in ESI-MS and high resolution timsTOF mass spectra of each product and reaction yields.

Peptide	$m_{observ.}$ [Da]		% yield	
Pra-G$_6$-HA	1540.6		61	
Pra-G$_{10}$-HA	1913.6		46	
Pra-G$_5$-FLAG	1393.3		102	
Pra-G$_{10}$-FLAG	1765.8		92	
Pra-G$_5$-HA (manual SPPS)	1481.61[a]		53	
Pra-G$_5$-His$_6$ (manual SPPS)	1220.51[a]		67	
	Linear	Folded	Linear	Folded
(*N$_3$*)K-G$_5$KIIIA	2329.5	2324.0	16	9
(*N$_3$*)K-G$_5$Pn3a[D8N][b]	4717.6	4710.8	25	13
(*N$_3$*)K-G$_5$Pn3a[D8N][c]	4716.2	4706.93[a]	15	9
Pn3a[D8N]	4276.8	4267.74[a]	11	9
AcG$_5$Pn3a[D8N]	4603.9	4594.86[a]	21	2
G$_5$Pn3a[D8N]	4560.9	4552.85[a]	6	16
HA-G$_6$-*Ta*-G$_5$KIIIA	3864.8		8	
HA-G$_{11}$-*Ta*-G$_5$KIIIA	4236.5		3	
FLAG-G$_5$-*Ta*-G$_5$Pn3a[D8N]	6104.6		2	
FLAG-G$_{10}$-*Ta*-G$_5$Pn3a[D8N]	6476.4		2	
His$_6$-G$_5$-*Ta*-G$_5$Pn3a[D8N]	5927.43[a]		25	

[a] HR-MS, calculated from the monoisotopic peak, [b] first synthesis [c] second synthesis

4.5 Dot Blot

A Dot Blot was conducted to determine whether the His-tagged Pn3a[D8N] analogue could be detected by an anti-His primary antibody. His_6-G_5-Ta-G_5Pn3a[D8N] was used as the test compound, while Pn3a[D8N], along with its analogues G_5Pn3a[D8N] and AcG_5Pn3a[D8N], served as negative controls. The Pra-$G_5$$His_6$-tag was used as a positive control for the His-Probe H15 primary antibody. Peptides were spotted in duplicate onto a PVDF membrane, and a chemiluminescent image, shown in **Figure 45**, was captured.

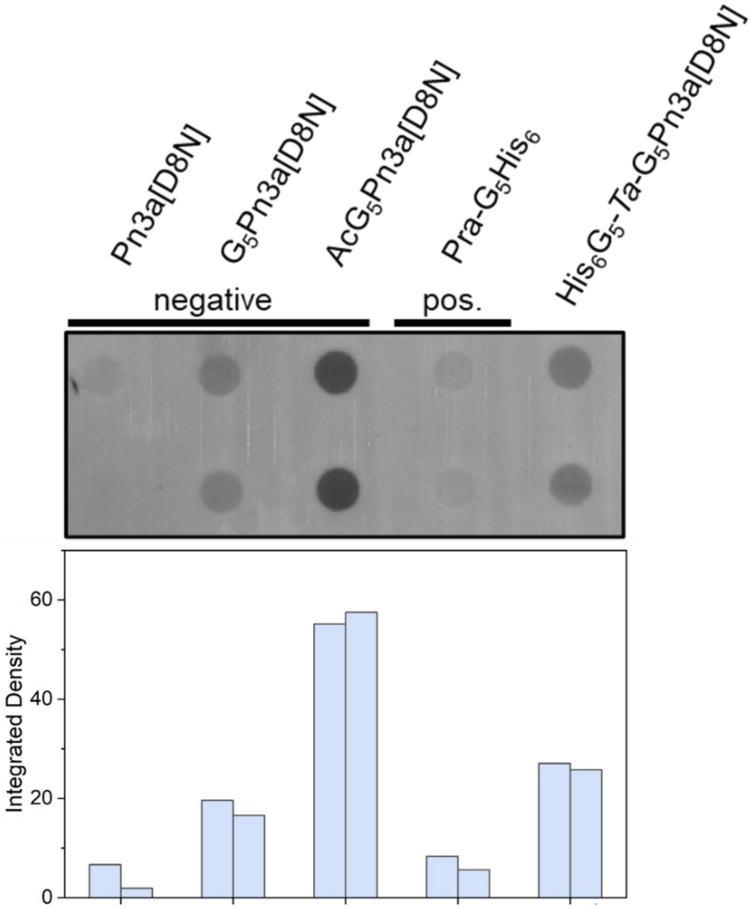

Figure 45. Dot Blot Chemiluminescence Detection of Peptide Variants on PVDF Membrane with Intensity Analysis. Chemiluminescence image of peptides blotted onto a PVDF membrane, stained with a His-Probe H15 (Rabbit, polyclonal) primary antibody and an HRP-tagged anti-Rabbit secondary antibody (Donkey, polyclonal). The peptides, spotted in duplicates, include (from left to right): Pn3a[D8N], the pentaglycine derivative G_5Pn3a[D8N], the acetylated derivative AcG_5Pn3a[D8N] (all without epitope functionalization as negative controls), the alkyne-His_6-tag as a positive control, and the His_6-tagged Pn3a[D8N] analogue. Chemiluminescence was developed using Clarity Max Western ECL Substrate (Bio-Rad) and imaged with a ChemiDoc MP System (Bio-Rad). The bar graph below represents the integrated density of the respective spots after background subtraction. Image analysis was performed using ImageJ software, and the graph was plotted using Origin.

The accompanying bar graph represents the integrated density of the blots, providing a relative quantification of the intensity levels.

A trend can be observed within the negative controls from Pn3a[D8N] to AcG5Pn3a[D8N], starting with a barely recognizable spot for Pn3a[D8N], followed by a low integrated density for G_5Pn3a[D8N], and two intense spots for AcG_5Pn3a[D8N]. The positive control, Pra-G_5-His_6, exhibits only weak integrated density, slightly more intense than Pn3a[D8N]. The His-tagged Pn3a[D8N] analogue demonstrates moderately weak antibody binding, with integrated densities higher than G_5Pn3a[D8N] but lower than AcG_5Pn3a[D8N].

5 Discussion

This work focused on the design, synthesis, and electrophysiological testing of conotoxin KIIIA and theraphosid toxin Pn3a[D8N]-based probes. The aim was to develop these probes for eventual use in a modified PLA for Na$_V$1.7. This would establish a foundation for the selective detection of Na$_V$1.7 using venom peptide-based probes instead of primary antibodies. Although the modified PLA was only conceptualized at this stage, the primary effort focused on exploring the synthetic feasibility. The probes were synthesized and subjected to electrophysiological testing at hNa$_V$1.7 to assess their functionality, a crucial step for further assay development.

5.1 Design of Venom-based Probes

The conceptualized PLA is depicted in **Figure 28**, using two venom peptide-based probes against Na$_V$1.7 to allow the selective and sensitive detection of the channel. The design of the probes is based on the well-characterised and potent inhibitors of Na$_V$1.7, KIIIA, and Pn3a. Visual identification of Na$_V$1.7 is a critical tool in the process of understanding its regulation, localisation, and interactions, especially in disease mechanisms, basic research, and drug development. Synthetic peptides offer several advantages over monoclonal antibodies that would be used in a classic PLA setup. In contrast to monoclonal antibodies, synthetic peptides can be synthesized using SPPS, offering time- and cost-efficiency. Moreover, peptide sequences can be easily modified and adapted as needed. Synthetic peptides also demonstrate high shelf stability and ensure consistent quality across batches, eliminating the variability associated with antibody production.

In this approach, Pn3a[D8N] serves as the primary driver of selectivity. At the same time, KIIIA primarily functions as the necessary second anchor, providing a binding platform for the other oligonucleic acid-tagged secondary antibody. As shown before, the intended strategies for assembly, folding, and bioorthogonal ligation of the venom peptide-based probes have been demonstrated to be compatible with both KIIIA and Pn3a (Tran et al., 2023b). This modular probe design enables the synthesis and folding of venom peptides using established protocols (Deuis et al., 2017; Jian et al., 2023; Mueller et al., 2020, 2019; Zhao et al., 2023). Various epitope-tagged probes can be synthesized, ligated, and exchanged as needed. If the modified PLA proves effective, probes based on venom peptides with different targets could be created, enabling the development of probes for the selective detection of other VGSC subtypes or even different ion channels. In principle, a broad molecular toolbox for selective and highly sensitive channel detection could be created. However, since no working assay has been established, the feasibility of the PLA modification has yet to be determined.

Moreover, the fundamental design of the assay raises concerns about its viability. Even if two probes with high affinity for $Na_V1.7$ could be developed, there is limited evidence to support the simultaneous binding of a pore-blocker and a GMT. Given that GMT binding alters the conformation of $Na_V1.7$, this could impair the binding of KIIIA. The development of bivalent ligands combining a pore-blocker and a GMT has shown enhanced affinity compared to monovalent ligands. (Peschel et al., 2020) In the work of Agwa et al., which explored double-knottins, evidence was found to support the cooperative binding of bivalent ligands at $Na_V1.7$ (Agwa et al., 2018). However, no structural exists to confirm different toxins' simultaneous binding at Na_V-channels. Additionally, the peptide probes bound to the channel must withstand multiple steps of buffer and reagent treatment during the assay. Any reduction in binding affinity due to venom peptide modification would be detrimental to the assay’s applicability.

Nevertheless, if the modification of the PLA using venom peptide-based probes fails because simultaneous binding of venom peptides at $Na_V1.7$ does not occur, this probe design could still prove valuable. A single venom peptide-based probe that binds the channel with high affinity could substitute for the primary antibody in a classical PLA where the interaction of $Na_V1.7$ with another protein is visualized. The venom peptide-based probe would bind to NaV1.7, while a primary antibody would target the NaV1.7-interacting protein for detection. In this scenario, a fully synthetic peptide analogue could replace the need for a $Na_V1.7$ antibody. The analogue would be accessible through standard SPPS, offering complete control over structure and eliminating batch-to-batch variations in target affinity and selectivity.

5.2 Synthesis of Venom Peptide-based Probes

In This work, the synthesis and characterisation of five KIIIA- and Pn3a[D8N]-epitope-tagged probes could be realised. KIIIA was ligated to the HA epitope with two different spacer lengths. The total spacer lengths add up to the equivalent of 14 and 20 amino acids, respectively, considering the peptide bond isosteric triazole equivalent to an amino acid. Pn3a[D8N] was ligated to the FLAG epitope tag with linker lengths of 13 and 19 amino acids and to the His_6 tag with 13 amino acids spacer sequence (**Table 6**).

The overall strategy of automated MW-assisted SPPS of the modified venom peptides, thermodynamic folding, and *CuAAC* ligation produced sub-milligram amounts of final product, with total yields < 1%. The absence of yield reports in many publications of KIIIA and Pn3a syntheses complicates the comparison of the efficiency of individual synthetic steps. In the case of HA-tagged KIIIA and FLAG-tagged Pn3a[D8N], the obtained amounts of final products allowed for characterisation *via* ESI-MS, analytical RP-HPLC and electrophysiological testing at $hNa_V1.7$. In the case of His_6-tagged Pn3a[D8N], characterisation *via* HR-MS, analytical HPLC, and one Dot Blot experiment could be performed, but the absence of facilities meant no assessment of $Na_V1.7$ inhibition was possible. The HA-tagged Pn3a[D8N] could not be isolated, thus no further characterisation or testing was possible. Further testing of the compounds and potentially performing a PLA would require an upscale of probe synthesis, which is time and resource-intensive with the synthetic route followed in this work.

5.2.1 Assembly of linear modified venom peptide precursors

The yield of linear precursors synthesized during the early stages of this work at the Institute for Molecular Biosciences was noticeably higher, even though the same standard SPPS protocols for assembly were used. This may be attributed to more efficient purification achieved through preparative RP-HPLC. A higher-capacity column was employed for crude product purification, allowing for greater column loading and reducing the required preparative RP-HPLC steps. Fewer purification steps result in less material loss, as each step inevitably leads to incomplete recovery. This is particularly significant given that the correctly assembled linear precursor already constitutes a smaller fraction of the crude material obtained from SPPS, especially for Pn3a, which has a significantly longer sequence than KIIIA.

5.2.2 Thermodynamic Folding

Notably, oxidative folding and *CuAAC* ligation have significantly lowered the overall yields. For oxidative folding, an average yield of approximately 10% could be isolated from each run (**Table 6**). Even though the non-product fractions consist of misfolded venom peptides that can be subjected to refolding, repeated refolding is time-consuming, especially for Pn3a, as thermodynamic folding takes 48 hours compared to 2-4 hours for KIIIA. Additionally, refolding requires the purification of misfolded isomers from the folding buffer before the process can be repeated.

Alternatively, directed folding using different cysteine protecting groups and a stepwise cysteine pairing strategy could be considered. This approach may be more efficient at accumulating the desired isomer during consecutive disulfide bond formation compared to thermodynamic folding.

Significantly, AcG$_5$Pn3a[D8N], lacking a positively charged N-terminus, exhibited the lowest overall folding yield at just 2%, suggesting that a positive N-terminal charge may facilitate correct isomer formation of Pn3a during thermodynamic folding - a complex, multistep process driven by intramolecular interactions.

Additionally, as demonstrated by Khoo et al., the disulfide framework of KIIIA could be simplified by substituting specific cysteine residues with alanine to create µ-KIIIA[C1A,C9A]. This analogue maintained the activity and selectivity observed for native KIIIA and was synthesized through directed folding using different Cys protecting groups (Khoo et al., 2009).

5.2.3 CuAAC Ligation

Except His$_6$-tagged Pn3a, all ligations produced only single-digit yields. It was discovered that HA-tagged and His$_6$-tagged Pn3a[D8N] required additional Cu(I) equivalents for the reaction to initiate and progress. Although THPTA is a strong ligand for Cu(I) and the cysteines of Pn3a[D8N] were oxidized to form disulfides, the possibility of copper complexation by the peptide cannot be excluded. This is supported by the fact that the reaction only proceeded when more copper species and reducing agent (ascorbic acid) were added. These observations were unexpected, as *CuAAC* ligation of disulfide-rich venom peptides has been reported without noticeable interferences (Peschel et al., 2020; Tran et al., 2023b). It is hypothesized that copper species may have bound to amino acid side chains, such as methionine or histidine, hindering the initiation of the ligation until copper complexation was saturated.

In contrast to the challenges encountered during venom peptide synthesis and ligation, alkyne-functionalized epitope-tags were synthesized via manual SPPS with yields greater than 50% and high final product purity. This demonstrates that click-reactive epitope-tags for protein and peptide modification can be successfully produced using standard SPPS protocols.

5.3 Assessing Probe Affinity for hNa$_V$1.7

Venom-peptide-based probes can only replace antibodies in a PLA if they demonstrate high target selectivity and affinity. As a measure of affinity, the inhibition of hNa$_V$1.7, expressed in HEK293 cells, by HA-tagged KIIIA and FLAG-tagged Pn3a[D8N] was tested. The FLAG-tagged Pn3a[D8N]-based probes displayed significantly ($P \leq 0.0001$) lowered pIC$_{50}$ values, with a 17.7 fold decrease potency at hNa$_V$1.7 compared to Pn3a[D8N] (**Figure 37 A** and **B**). As no electrophysiological testing of G$_5$Pn3a[D8N] (no epitope-tag) could be performed, it remains unclear whether the reduction of inhibitory potential was caused by the N-terminal extension with the spacer sequence or, in particular, the FLAG tag. The FLAG-tagged Pn3a[D8N]-based probes with two different linker lengths display almost identical pIC$_{50}$ values (≈ 6.70). The longer linkers offer no advantage in maintaining native Pn3a[D8N] potency. However, the different linker lengths were also selected for assessing antibody binding efficiency, which has not yet been evaluated. It was nevertheless decided to incorporate the shorter spacer sequence into His$_6$-tagged Pn3a[D8N]-based probe for practical purposes. Due to the lack of available testing facilities, His$_6$-G$_5$-*Ta*-G$_5$-Pn3a[D8N] could not be tested at NaV1.7. However, it would be important to draw a conclusion on the influence of different epitope tags. Given the abundance of negative charge in the FLAG-tag, testing the His6-tagged probe could provide valuable insights into structure-activity relationships.

The HA-tagged KIIIA probes showed no effective inhibition at $hNa_V1.7$, with the required concentrations for proper curve fitting and IC_{50} determination out of range of the tested concentrations. For internal reference, KIIIA Isomer 1 and 2 were added.

It is assumed that the unplanned addition of one glycine in the spacer sequences for both KIIIA-based probes (HA-G_6-*Ta*-G_5KIIIA and HA-G_{11}-*Ta*-G_5KIIIA) did not mainly affect the loss of potency. As no NMR could be recorded for the purified (N_3)K-G_5KIIIA, whether the correct disulfide isomer was isolated and ligated remains to be determined. In this work, the major oxidation product was collected for ligation as previously reported in the literature (Peschel et al., 2020). However, from the data available, mass spectrometry and retention time cannot be specified for disulfide connectivity. Electrophysiological testing showed that KIIIA-based probes displayed a significantly reduced inhibition of NaV1.7, close to the behaviour observed for the inactive KIIIA isomer 2. It remains to be unambiguously determined whether modification caused the loss of activity or the isolation of the wrong isomer. As reported by Tran et al., N-terminal G_5-extension of KIIIA has not significantly influenced inhibition of $Na_V1.7$ compared to unmodified KIIIA (Tran et al., 2023b). The tolerability of N-terminal extension of KIIIA is further exemplified by bivalent $Na_V1.7$-ligands synthesized ligands by Peschel et al., consisting of a PEG-linked spider venom peptide and KIIIA. The bivalent toxins showed enhanced inhibitory potency at $Na_V1.7$ and improved dissociation rate constants (Peschel et al., 2020). With these findings, it is unlikely that the N-terminal modifications of KIIIA-based probes lead to the drop of inhibitory potential observed in this work. Most likely, an inactive disulfide isomer of KIIIA was purified, emphasizing the importance of structural determination by, e.g., NMR, to structurally characterize the product before ligation.

G_5Pn3a[D8N] and AcG_5Pn3a[D8N] could not be tested on hNaV1.7 in this work, so that no conclusions can be drawn regarding the influence of the N-terminal extension with the pentaglycine spacer or the impact of a positive N-terminal charge on Pn3a[D8N]. However, in a separate study, the addition of azidolysine ((N_3)K) to Pn3a improved the inhibitory potency compared to the wild-type Pn3a, suggesting that a positive charge at the N-terminus may be advantageous (Tran et al., 2023b).

5.4 Antibody binding of His_6-tagged Pn3a[D8N]

The preliminary Dot Blot revealed unspecific reactivity from the antibodies used in this experiment, with dots appearing in the negative control lane, which included AcG_5Pn3a[D8N], G_5Pn3a[D8N], and Pn3a[D8N]. Notably, the most intense unspecific binding was observed with the negative control AcG_5Pn3a[D8N], while positive control dots for Pra-G_5-His_6 were absent. The absence of a strong signal for the positive control could be due to incomplete transfer of the His_6-tag onto the membrane or its removal during washing steps. For His_6-tagged Pn3a[D8N], only a weak signal was observed. Due to the failure of the controls, no conclusions can be drawn regarding the efficiency of primary antibody binding. Repeating the Dot Blot with a different, ideally monoclonal, anti-His antibody is recommended.

6 Conclusion and outlook

This work proposed the use of epitope-tagged venom peptide probes, based on conotoxin KIIIA and the GMT Pn3a[D8N], in a modified PLA to selectively detect Na$_V$1.7. A modular probe design and synthesis route were presented, enabling the customisation of venom peptide probes synthesized through standard SPPS and folding protocols with different epitope tags. Given the many selective binders among venom peptides targeting Na$_V$s and other ion channels, this design and approach could lead to the development of a diverse molecular toolbox for visual detection *via* Proximity Ligation.

A route for venom peptide probe synthesis involving SPPS, thermodynamic folding, and biorthogonal *CuAAC* ligation was explored. Five out of six attempted probes were purified and characterized, four of which were tested at hNa$_V$1.7.

FLAG-tagged Pn3a inhibited hNa$_V$1.7 in the higher nanomolar range (**Table 5**), justifying further exploration of Pn3a-based probes. It was found that spacer lengths of ten and fifteen glycines had no significant impact on inhibitory activity. The HA-tagged KIIIA probes exhibited weak inhibitory activity at hNa$_V$1.7. Structural elucidation of the KIIIA-based probes or non-ligated precursors *via* NMR would be necessary to gain insights into the exact disulfide connectivity.

The Dot Blot experiment conducted in this work, aimed at evaluating the antibody binding of the His-tagged Pn3a[D8N] analogue, yielded inconclusive results. It was demonstrated that the specific polyclonal antibody used is not suitable for the intended task, and a different, validated antibody would be required. For future Dot Blots, using a 0.1 µm or 0.2 µm pore size PVDF membrane may be better suited for the low molecular weight of the peptides, especially the His$_6$-tag serving as a positive control.

Low yields of venom peptides have been a significant limitation of the chosen synthetic route. This inefficiency has slowed the production of probes, limiting the material available for characterization and testing. Therefore, the future direction of this project should involve exploring a more economical synthesis approach to improve yields, and include a structural characterisation of intermediates and products, e.g., with NMR. Further, testing all of the synthesized probes with different epitope-tags at $hNa_V1.7$ and other hNa_V isoforms would be required to complete the structure-activity profile.

For KIIIA-based probes, the use of KIIIA[C1A,C9A] and directed folding with different cysteine side-chain protecting groups could be considered. Ligation and subsequent testing at $hNa_V1.7$ should only be performed after NMR analysis and identification of the correct disulfide isomer.

Instead of SPPS, Pn3a[D8N] can be produced recombinantly. Consequently, this alternative route of recombinant expression could be explored to find a more efficient way of Pn3a production to fully exploit its potential as a selective Na_V binder and tool in chemical biology and pain research. Sharma et al. have demonstrated the expression of Pn3a in *E. coli* by a His_6-SUMO-*TEV*-Pn3a fusion construct. Final yields of 0.5 mg/L LB medium for rPn3a were achieved. The His_6-SUMO-*TEV*-Pn3a construct (*TEV*: TEV-protease recognition motif) allows purification *via* Immobilized Metal Affinity Chromatography (IMAC) with the hexahistidine tag, and increased solubility by the SUMO-tag (Sharma et al., 2020). After TEV-protease cleavage of the tags, a single glycine residue at the N-terminus of the recombinantly expressed (rPn3a) was left (Sharma et al., 2020). The linear rPn3a[G0,D8N] precursor could then be folded as described in this work. However, novel folding protocols with higher yields compared to the protocols used in this work (~10 % yield for thermodynamic folding of Pn3a[D8N] analogues) would be desirable. Thus, using the organic oxidative folding approach for rPn3a[D8N] folding could be explored as well (Kam et al., 2024; Laps and Metanis, 2024). Instead of *CuAAC*, Sortase A (SrtA) ligation could be used. The transpeptidase SrtA found in Gram-positive bacteria requires a short recognition motif (LPXTG, here: LPETGG) and a N-terminal glycine residue (Agwa et al., 2018; Mao et al., 2004; Sharma et al., 2020; Tran et al., 2021; Tran and Schroeder, 2021). The enzymatic approach maintains the modularity of the initial design. **Figure 46** presents a scheme for the proposed alternative synthesis, featuring recombinant expression of rPn3a[G0, D8N] (Sharma et al., 2020). Folded rPn3a[G0, D8N] can be ligated to epitope-tags, modified with SrtA recognition motifs (LPXTG), previously assembled *via* SPPS. These probes would need to undergo testing for target affinity and efficient antibody binding before performing a PLA.

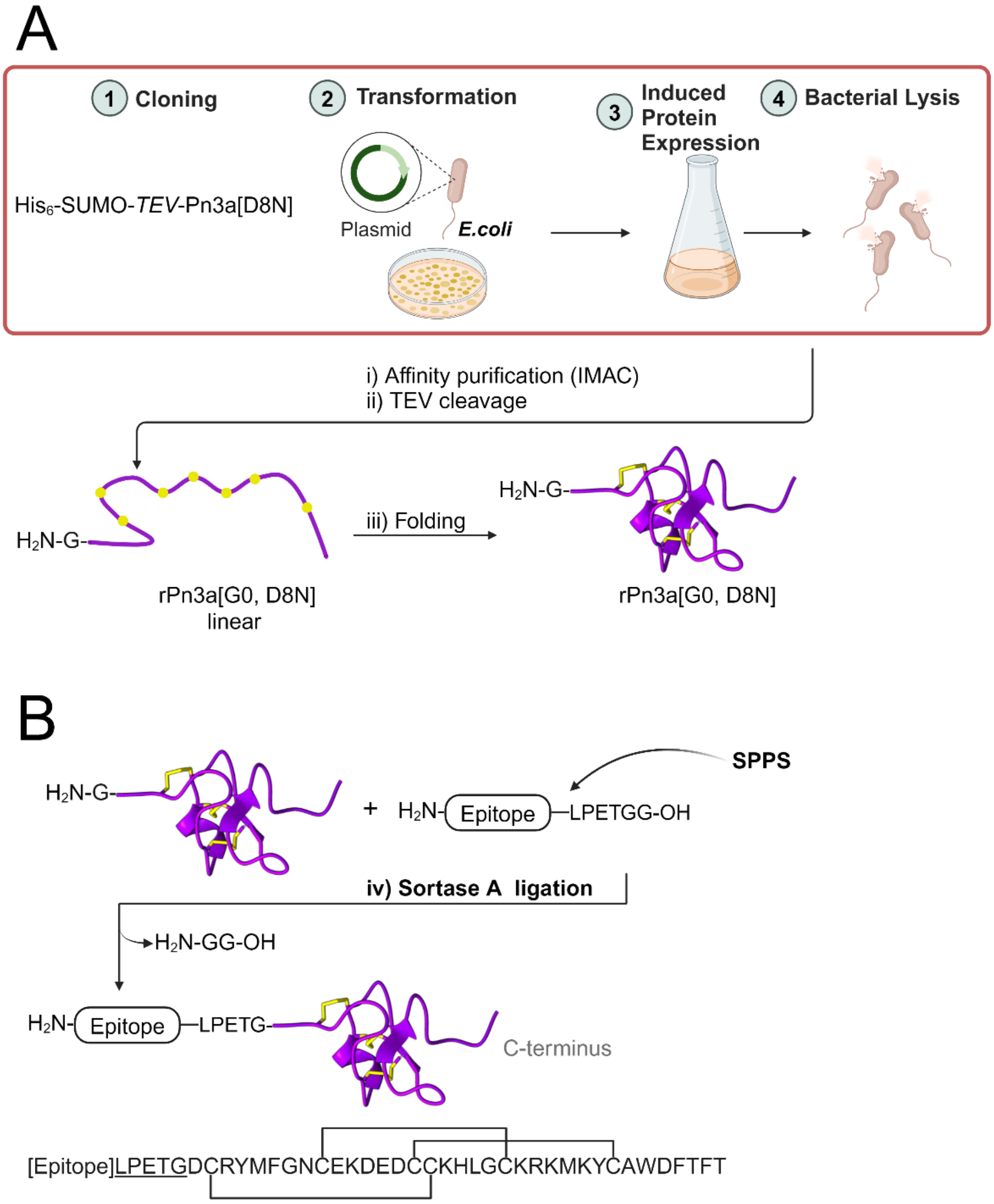

Figure 46. Recombinant expression of rPn3a[D8N] (A) and SrtA-mediated ligation with epitope-tags (B). An alternative approach for the synthesis of Pn3a[D8N] involves the recombinant expression of a His$_6$-*TEV*-SUMO-Pn3a[D8N] fusion construct in *E. coli* (**A**). Followed by affinity purification (i) using the His$_6$-tag and IMAC, the SUMO tag, which enhances solubility, is subsequently cleaved by a TEV protease (ii), leaving an N-terminal glycine residue on rPn3a[D8N]. The linear precursor is folded into the native disulfide isomer (iii).The N-terminal glycine is required for the subsequent enzymatic ligation by the transpeptidase SrtA (iv). The epitope-tag, carrying the SrtA recognition motif on its C-terminus, can be synthesized using SPPS. After ligation (**B**), the final product, [Epitope]-LPETG-Pn3a[D8N], is obtained. Idea and work-flow adapted from (Sharma et al., 2020).Figure created with BioRender.

7 Materials and Methods

This section details the materials used and the methods employed for the synthesis and characterization of peptide probes.

7.1 Materials

The chemicals and consumable labware used in this thesis were sourced from commercial suppliers.

7.1.1 Peptide Synthesis

Fmoc protected L-amino acids were purchased from Iris Biotech GmbH (Germany): Fmoc-Ala-OH, Fmoc-Arg(Pbf)-OH, Fmoc-Asn(Trt)-OH, Fmoc-Aps(OMpe)-OH, Fmoc-Cys(Trt)-OH, Fmoc-Gln(Trt)-OH, Fmoc-Glu(OtBu)-OH, Fmoc-Gly-OH and Fmoc-Gly(Tmob)-OH, Fmoc-His(Boc)-OH, Fmoc-Ile-OH, Fmoc-Leu-OH, Fmoc-Lys(Boc)-OH, Fmoc-Met-OH Fmoc-Phe-OH, Fmoc-Pro-OH, Fmoc-Ser(tBu)-OH, Fmoc-Thr(tBu)-OH, Fmoc-Trp(Boc)-OH, Fmoc-Tyr(tBu)-OH, Fmoc-Val-OH.

Additional solvents and chemicals used in this work included acetonitrile (VWR Chemicals), trifluoroacetic acid (VWR Chemicals), dichloromethane (Fisher Chemical), diethyl ether (VWR Chemicals), piperidine (Sigma-Aldrich), dimethylformamide (VWR Chemicals), HATU (Apollo Scientific), sodium ascorbate (Sigma-Aldrich), triisopropylsilane (Sigma-Aldrich), DODT (Sigma-Aldrich), diisopropylethylamine (Sigma-Aldrich), ammonium acetate (Merck), ammonium hydrogen carbonate (Merck), urea (Thermo Scientific), DIC (Merck), Oxyma Pure B (Merck), glutathione disulfide (Thermo Scientific), glutathione (FLUKA), $CuSO_4$ (Sigma-Aldrich), and THPTA (BLD Pharm).

Buffers, solvents, and mobile phases for chromatography were prepared using HPLC-grade solvents and ultrapure water from the Milli-Q® Water Purification System. Purified water from the Millipore Milli-Q® system was used as "*dd*H_2O." Solvent A consisted of *dd*H_2O with either 0.1% or 0.05% TFA by volume. Solvent B was composed of HPLC-grade acetonitrile containing either 0.08% or 0.05% TFA by volume. Additionally, a mixture of 50% acetonitrile in *dd*H_2O with 0.09% TFA by volume was used as Solvent A/B.

7.1.2 Instrumentation

During the work of this thesis, the following instruments were used: Microwave Peptide Synthesizer Liberty PRIME (CEM Corporation, Charlotte, North Carolina, USA), Nexera HPLC system for preparative HPLC, equipped with an SPD-10A detector, FCV-200AL quaternary valve, LC-20AP pump, FRC-10A fraction collector, and CBM-20A CL Communications Bus Module (Shimadzu, Kyoto, Japan), Vanquish Horizon UHPLC, equipped with a diode array detector FG, split sampler FT, and Quaternary Pump F (Thermo Fisher Scientific, Waltham, MA, USA), Lyophilizer Alpha 2-4 LDplus (Martin Christ Freeze Dryers, Osterode, Germany), Sigma 3-16PK centrifuge (Sigma Laborzentrifugen, Osterode am Harz, Germany), Nanodrop Microvolume Spectrophotometer (Thermo Fisher Scientific, Waltham, MA, USA), LC-MS system equipped with an SQ2 mass detector for Direct Injection ESI-MS and LC-MS (Waters Corporation, Milford, MA, USA)), Dionex UltiMate 3000 MSQ Plus system, equipped with an MSQ Plus mass detector, Dionex UltiMate 3000 pump, autosampler, and RS variable wavelength detector for LC-MS (Thermo Fisher Scientific, Waltham, MA, USA), maXis UHR ESI-Qq-TOF high-resolution mass spectrometer (Bruker Daltonics, Bremen, Germany) at the Mass Spectrometry Centre (University of Vienna), ChemiDoc MP Imaging System (Bio-Rad Laboratories, Inc., Hercules, California, USA), Microfiltration blotting device Bio-Dot Apparatus #1706545 (Bio-Rad Laboratories, Inc., Hercules, California, USA), QPatch Automated Patch Clamp System (Sophion Bioscience).

7.1.3 Software

Various software tools were utilized in this work. Physico-chemical properties of amino acid sequences were computed using ExPasy ProtParam, provided by the SIB Swiss Institute of Bioinformatics (https://web.expasy.org/protparam/). Chemical structures were drawn using ChemDraw, a chemical drawing software from PerkinElmer, Inc. (Waltham, Massachusetts, USA). Microsoft Office (Microsoft Corporation, Redmond, Washington, USA) was used for productivity tasks. Data visualization and analysis were performed with OriginLab, developed by OriginLab Corporation (Northampton, Massachusetts, USA). Curve fitting of electrophysiological data was performed using GraphPad Prism (GraphPad Prism version 10.0.0 for Windows, GraphPad Software, Boston, Massachusetts USA, www.graphpad.com) through nonlinear regression with a variable Hill slope for dose-response analysis and IC_{50} and pIC_{50} determination. Image analysis was conducted using ImageJ, an open-source software, available at https://imagej.net/ij/index.html [last accessed: 13.02.2024].(Schneider et al., 2012) Molecular visualization was carried out using PyMOL (The PyMOL Molecular Graphics System, Version 3.0 Schrödinger, LLC) and UCSF ChimeraX, developed by the Resource for Biocomputing, Visualization, and Informatics at the University of California, San Francisco, with support from NIH R01-GM129325 and the Office of Cyber Infrastructure and Computational Biology, National Institute of Allergy and Infectious Diseases.

7.2 Methods

7.2.1 Solid Phase Peptide Synthesis

7.2.1.1 Automated SPPS

Pn3a[D8N] derivatives, (*N_3*)K-G_5KIIIA, $G_{6/11}$-HA, and $G_{5/10}$-FLAG tags were synthesised via automated microwave-assisted solid-phase peptide synthesis (SPPS) on a Liberty PRIME synthesiser (CEM Corporation). Peptides were assembled at a 0.1 mmol scale on pre-loaded resins as follows: (*N_3*)K-G_5KIIIA on Rink Amide ProTide resin (LL) (0.19 mmol/g; CEM Corporation, Matthews, NC, USA), Pn3a[D8N] and derivatives on Fmoc-Thr(tBu) Wang Resin (LL, 0.25 mmol/g; CEM Corporation, Matthews, NC, USA), $G_{5/10}$-FLAG on Fmoc-Lys(Boc)-Wang Resin (0.64 mmol/g; aapptec, Louisville, KY, USA), and Ha-$G_{6/11}$ on Fmoc-Ala-Wang Resin (LL) (0.31 mmol/g; CEM Corporation, Matthews, NC, USA).

Amino acid chain assembly was achieved using four equivalents of side-chain protected L-amino acids for coupling. Terminal amino acid coupling for (*N_3*)K-G_5KIIIA and (*N_3*)K-G_5Pn3a[D8N] was performed with three equivalents of N-α-(Fmoc-ε-azido-L-lysine) (Iris Biotech GmbH, Marktredwitz, Germany). The respective amino acids (0.5 M) were dissolved in DMF and loaded into the reservoir. Oxyma Pure (0.25 M in DMF) and DIC (2.0 M in DMF) served as coupling reagents. The resins were swollen in DMF for 30 minutes before starting the synthesis. Fmoc deprotection was performed with a 25 vol% pyrrolidine solution in DMF, with deprotection parameters set to 4 minutes at 100°C, and coupling steps were carried out for 1 minute at 105°C.

After synthesis, the resins containing the venom-peptide derivatives were collected from the SPPS synthesiser, transferred into filter syringes with a valve, and washed manually with DMF (10 ml, 2x) to prepare for subsequent manual coupling steps.

For complete syntheses, the resins were dried by washing with DCM (10 ml, 4x) and then using N_2 gas. The resins were then placed in a desiccator for thorough drying.

7.2.1.2 Manual SPPS

Pra couplings to Ha-$G_{6/11}$ and $G_{5/10}$-FLAG (Institute for Molecular Bioscience, Brisbane), Pra-G_5-HA and Pra-G_5-His_6 syntheses as well as coupling of (N_3)K to G_5Pn3a[D8N] (Institute of Biological Chemistry, Vienna) were performed *via* manual SPPS. Peptide-resins from automated synthesis or dry preloaded resins were placed in single-use syringes with a bottom filter and flow-washed with DMF for 30 seconds. The resins were then allowed to swell in DMF for at least 2 hours or overnight. Deprotection of the N-terminal Fmoc group was achieved by adding 50% piperidine in DMF (2x for 1 minute each). The resin was then flow-washed with DMF for 1 minute.

HATU (780 µl, 0.5 M) and DIPEA (84 µl) were added to the Fmoc-L-amino acid (4 equivalents, except for 3 equivalents of Pra-Gly-OH) and the mixture was transferred to the resin. After 15 minutes of coupling, the resin was flow-washed with DMF for 1 minute. This coupling process was repeated until the desired sequence was obtained. The resin was then washed with DCM, dried under a nitrogen stream, and placed in a vacuum desiccator overnight.

For N-terminal acetylation, a stock solution was prepared by mixing acetic anhydride (435 µL) and DIPEA (235 µL) in DMF to a total volume of 7.5 ml. The acetylation of G_5Pn3a[D8N] to AcG_5Pn3a[D8N] was carried out by adding 5 ml of the acetylation solution per 0.1 mmol of peptide to the N-terminally deprotected, resin-bound, and side-chain protected G_5Pn3a[D8N]. The mixture was stirred repeatedly for 10 minutes, after which the resin was washed with DMF for 1 minute.

7.2.2 Cleavage and Global Deprotection

Each peptide was cleaved from the resin and simultaneously side-chain deprotected in a one-step reaction. The cleavage mixture was added as follows: for epitope tags, 90% TFA, 5% TIPS, and 5% H_2O; for venom peptides, 92.5% TFA, 2.5% TIPS, 2.5% H_2O, and 2.5% DODT. The reaction was carried out for 2 to 3 hours under agitation at room temperature. After the reaction, TFA was evaporated using N_2 gas. The peptides were then precipitated in cold diethyl ether (-18°C) and centrifuged (5 min, 5000 rpm, 4°C). This washing with cold diethyl ether and centrifugation was repeated. Residual ether was removed from the precipitated peptides by N_2 gas. The peptides were redissolved in a minimal amount of A/B buffer (approximately 25 ml) and subsequently lyophilized.

7.2.3 Purification via preparative RP-HPLC

Linear precursors, epitope tags, and folded peptides were purified using preparative RP-HPLC. For sample preparation, peptides were dissolved in Solvent A, filtered through a 0.45 µm pore size filter, and loaded onto the preparative or semipreparative column. The columns used included a preparative Kromasil 300 C18 (10 µm, 21.2 x 250 mm, 300 Å pore size, Nouryon, Bohus, Sweden), an Agilent ZORBAX Eclipse XDB-C18 (80 Å pore size, 7 µm particle size, 21.2 x 250 mm, Agilent Technologies, Santa Clara, CA, USA), and a semipreparative Zorbax 300SB-C18 Prep H1 (21.2 x 150 mm, 5 µm particle size).

The loaded columns were washed with Solvent A for desalting until the detector signal returned to baseline. Absorbance was measured at 214 nm and 280 nm. The gradients applied over 40 minutes of separation time varied depending on the peptide. For Pn3a[D8N] and its derivatives, a 25-45% B gradient was used. (N_3)K-G_5KIIIA was purified with a 5-35% B gradient, Pra-G_5-HA with a 10-40% B gradient, Pra-G_5-His with a 0-20% B gradient, and Pra-$_{G6/11}$-HA tags with a 10-30% B gradient. Fractions were collected and analysed; pure fractions were pooled, while impure fractions containing products were kept separately.

7.2.4 Analytical RP-HPLC

The purity of the peptides after SPPS assembly, folding, fractionation and ligation was confirmed *via* analytical HPLC. Depending on sample concentration, the injection volume varied between 2 µl and 50 µl. A Thermo Scientific Hypersil Gold C18 (100 mm x 2.1 mm) 3 µm particle size column was used with a 0 - 50% Solvent B gradient over 10 min and a flowrate of 0.5 ml per minute or a Kromasil C18 column (300-5-C18, 150 x 4.6 mm, 5 µm particle size, 300 Å pore size) with 5-65%B over 30 min. The absorbance was measured at 214 nm and 280 nm.

7.2.5 Mass Spectrometry

The masses of the reaction products were determined by direct injection ESI MS or LC-MS of a small aliquot (5-10 µL) of diluted sample in Solvent A. LC-MS was carried out of on a Kromasil C18 column (300-5-C18, 50 x 4.6 mm, 5 µm particle size, 100 Å pore size) with a gradient of solvent B (ACN +0.05 % TFA) in solvent A (ddH2O + 0.05 % TFA) over 30 min (separation time) or on a XSelect® CSH C18 reverse phase column (3 x 75 mm, particle size of 2.5 μm, 130 Å pore size) with 1-61%B over 10 min. The absorbance for LC was measured at 214 nm wavelength.

Samples for high resolution mass spectra were submitted to The Mass Spectrometry Centre at the Faculty of Chemistry, University of Vienna, and measured *via* ESI/-Qq-TOF with dual-TIMS analyser.

7.2.6 Thermodynamic Folding

7.2.6.1 (N_3)K-G_5KIIIA

Linear (N_3)K-G_5KIIIA was added to the folding buffer at a concentration of 0.3 mg/ml. The KIIIA folding buffer consisted of 0.1 M ammonium bicarbonate (NH_4HCO_3) with reduced glutathione (GSH, 100 equivalents) and oxidized glutathione (GSSG, 10 equivalents), adjusted to pH 8.0.The mixture was stirred with an open lid at room temperature. After two hours, a sample was taken for analytical RP-HPLC to monitor the progress of the reaction. The reaction was quenched by adding 10% aqueous TFA until the pH reached 5. The generated CO_2 was allowed to escape completely. The solution containing the oxidized peptide was then filtered using a 0.45 μm bottle top filter and eluted from a preparative column with a gradient of 5-35% Solvent B over 40 min. ESI mass spectrometry was used to identify the product. Fractions containing the correctly folded isomer were then loaded onto a semipreparative column and eluted using the same gradient.

7.2.6.2 Pn3a [D8N] and Derivatives

Pn3a[D8N] an all Pn3a derivatives were folded from linear precursors in the Pn3a folding buffer at a concentration of 0.3 mg/ml. The Pn3a folding buffer was composed of 2 M urea, 4.5 M ammonium acetate (NH_4OAc), GSH (100 equivalents), and GSSG (10 equivalents), also adjusted to pH 8.0. The folding was carried out for 48 hours at 4°C under stirring with an open lid. The progress of the reaction was monitored using analytical RP-HPLC. Upon completion of the reaction, the buffer was cautiously acidified by adding neat TFA until the pH reached 5. To reduce viscosity, the solution was diluted 1:1 with deionized water (*dd*H_2O) before filtration using a 0.45 μm pore size bottle top filter. The filtrate was then loaded onto a preparative column and separated over a 25-45% gradient of Solvent B for 40 min. Fractions were collected, and the product identity was confirmed *via* ESI-MS.

7.2.7 Cu(I)-Catalysed Azide–Alkyne Cycloaddition (CuAAC)

Folded and purified azido-peptides (1 eq) were coupled *via CuAAC* to the respective alkyne-epitope tags (1.5 eq). Both coupling partners were weighed into a 1.5 ml tube. A minimal amount of water was added to dissolve the peptides, and the solution was agitated for several minutes. The other reagents were then added in the following order: THPTA (6.5 eq), $CuSO_4$ (6 eq), and sodium ascorbate (10 eq) in deionized water (*dd*H_2O). The reaction was performed at room temperature. The progress of the reaction was monitored by taking small aliquots for analysis via HPLC or LC-MS, respectively. The final product was purified using semipreparative HPLC

7.2.8 Electrophysiology (QPatch)

Four different peptide-construct dilution series were prepared, using KIIIA Isomer 1 and Isomer 2 as references, along with a Pn3a[D8N] concentration-response experiment conducted under the same conditions. For the Pn3a[D8N] and Pn3a[D8N]-based probe series, an initial 1 µM solution was prepared in extracellular solution (70 mM NaCl, 70 mM choline chloride, 4 mM KCl, 2 mM $CaCl_2$, 1 mM $MgCl_2$, 10 mM HEPES, and 10 mM glucose, adjusted to pH 7.4 and 305 mOsm, with 0.1% BSA). This solution was then serially diluted (1:3) in eight steps to reach a final concentration of 457 pM. The intracellular solution contained 140 mM CsF, 1 mM EGTA, 5 mM CsOH, 10 mM HEPES, and 10 mM NaCl, adjusted to pH 7.3 using CsOH, with an osmolarity of 320 mOsm.

For KIIIA and KIIIA-based probes, an initial concentration of 10 µM was serially diluted (1:3) in eight steps to achieve a final concentration of 4.57 nM. For each condition, 450 µl of solution was prepared in a 96-well plate and loaded into a Sophion automatic QPatchII patch clamp device. HEK 293 cells, stably expressing the hNaV1.7 channel, were prepared and harvested. The cells were treated with trypsin, loaded into the QPatch automatic patch clamp device, and stirred for 30 minutes. Whole-cell concentration-response curves for voltage-dependent channel activation were recorded with a 2-minute equilibration time on single cells, followed by treatment with TTX (1 µM) and a buffer wash. Each "n" represents one recording from an individual cell. The concentration-response curves were plotted in GraphPad PRISM, and the IC_{50} and pIC_{50} (negative logarithm base 10 of the IC_{50} value) values were determined by non-linear regression.

7.2.9 Dot Blot

Vacuum transfer was performed on Bio-Rad Microfiltration blotting device (Bio-Dot Apparatus #1706545) attached to a membrane-vacuum pump. Prior to transfer, the PVDF membrane (Immobilion®-P transfer membrane, pore size 0.45 µm, Merck Millipore IPVH00010) was shortly activated in pure methanol (45 s) and washed three times with MiliQ H_2O. The membrane was placed into the Dot Blotting apparatus, attached to the pump and the wells were flushed 3 x with 200 µL of PBS. Afterwards, 20 µL of each sample (Pn3a[D8N], G_5Pn3a, AcG_5]n3a, Pra-$G_5$$His_6$, His_6-G_5-*Ta*-G_5Pn3a[D8N]) were applied to the membrane and washed again with 200 µL of PBS. Vacuum transfer was performed (10 minutes). To validate the success of the transfer, the membrane was reversibly stained (1 min) with Ponceau S solution (Sigma Aldrich, CAS: 6226-79-5, P-7170) and afterwards destained by several washing steps with PBS. After destaining, the membrane was blocked (1 h) with 5% skimmed milk solution (Skim Milk Powder, Sigma Aldrich 70166-500G) in PBS-t (0.1% Tween 80 in PBS). Afterwards, blocking solution was removed and the membrane was incubated (1 h) in primary antibody solution (His-Probe H15, Santa Cruz Biotechnology sc-803, Lot. No. H2415, dilution 1:500, rabbit polyclonal IgG). The membrane was subsequently washed (5 x for 5 min) with PBS-t solution and then incubated (1 h) with secondary antibody solution (Jackson Immunoresearch, HRP-tagged Donkey anti-Rabbit polyclonal antibody 711-035-152). The Membrane was washed with PBS-t (3 x 5 min) followed by washing with PBS (3 x 5 min). All membranes were developed with Clarity Max Western ECL Substrate (Bio-Rad, 1705062) and the ChemiDoc MP Imaging System (Bio-Rad) was used to detect chemiluminescence. The chemiluminescence of the respective spots was analyzed with ImageJ, using integrated density with background subtraction.

.

8 Appendix

Table 7. Calculated exact masses and molecular weights of the synthesized sequences and products used for product identification *via* mass spectrometry and concentration calculations.

Peptide	m_{exact} [Da]		Molecular weight [Da]	
Pra-G$_6$-HA	1538.63		1539.58	
Pra-G$_{11}$-HA	1910.77		1911.92	
Pra-G$_5$-FLAG	1392.54		1393.34	
Pra-G$_{10}$-FLAG	1764.68		1765.68	
Pra-G$_5$-HA	1481.61		1482.53	
Pra-G$_5$-His$_6$	1220.51		1221.23	
	Linear	Folded	Linear	Folded
(N_3)K-G$_5$KIIIA	2328.86	2322.81	2330.62	2324.57
(N_3)K-G$_5$Pn3a[D8N]	4712.98	4706.93	4716.40	4710.35
Pn3a[D8N]	4273.79	4267.74	4276.97	4270.92
AcG$_5$Pn3a[D8N]	4600.91	4594.86	4604.26	4598.22
G$_5$Pn3a[D8N]	4558.90	4552.85	4562.23	4556.18
HA-G$_6$-*Ta*-G$_5$KIIIA	3861.44		3864.15	
HA-G$_{11}$-*Ta*-G$_5$KIIIA	4233.58		4236.48	
FLAG-G$_5$-*Ta*-G$_5$Pn3a[D8N]	6099.48		6103.69	
FLAG-G$_{10}$-*Ta*-G$_5$Pn3a[D8N]	6471.62		6476.03	
His$_6$-G$_5$-*Ta*-G$_5$Pn3a[D8N]	5927.44		5931.58	

8.1 Chromatographic Data

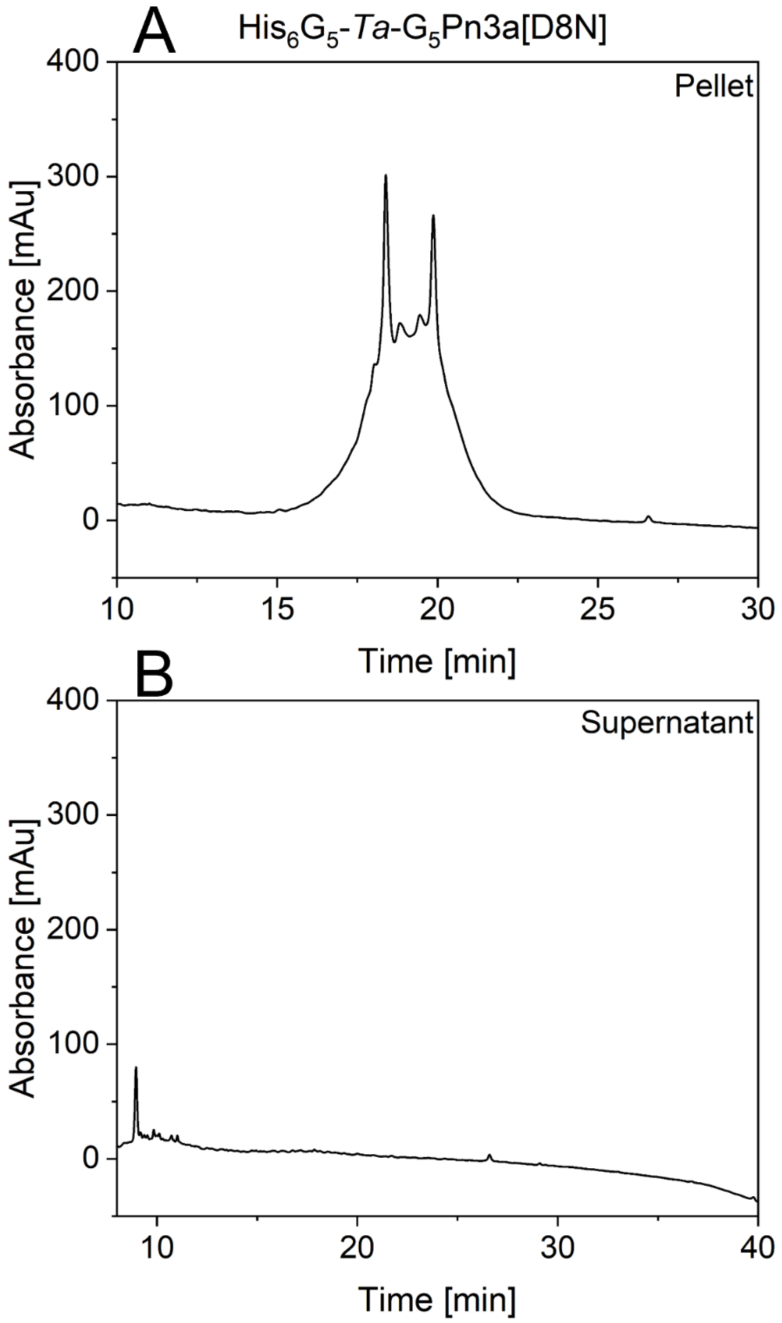

Figure 47. Analytical RP-HPLC profile of both phases (solid precipitate "pellet", and liquid supernatant) of the *CuAAC* ligation reaction after t$_5$ of His$_6$-G$_5$-*Ta*-G$_5$Pn3a[D8N]. RP-HPLC was carried out on a Kromasil C18 column (300-5-C18, 150 x 4.6 mm, 5 µm particle size, 300 Å pore size) using a Thermo Scientific UltiMate 3000 HPLC system with a 5–65 % gradient of solvent B (ACN +0.08 % TFA) in solvent A (*dd*H2O + 0.1 % TFA) over 30 min (separation time) with a flow rate of 1 mL/min. Absorbance was measured at 214 nm wavelength.

8.2 Mass spectra

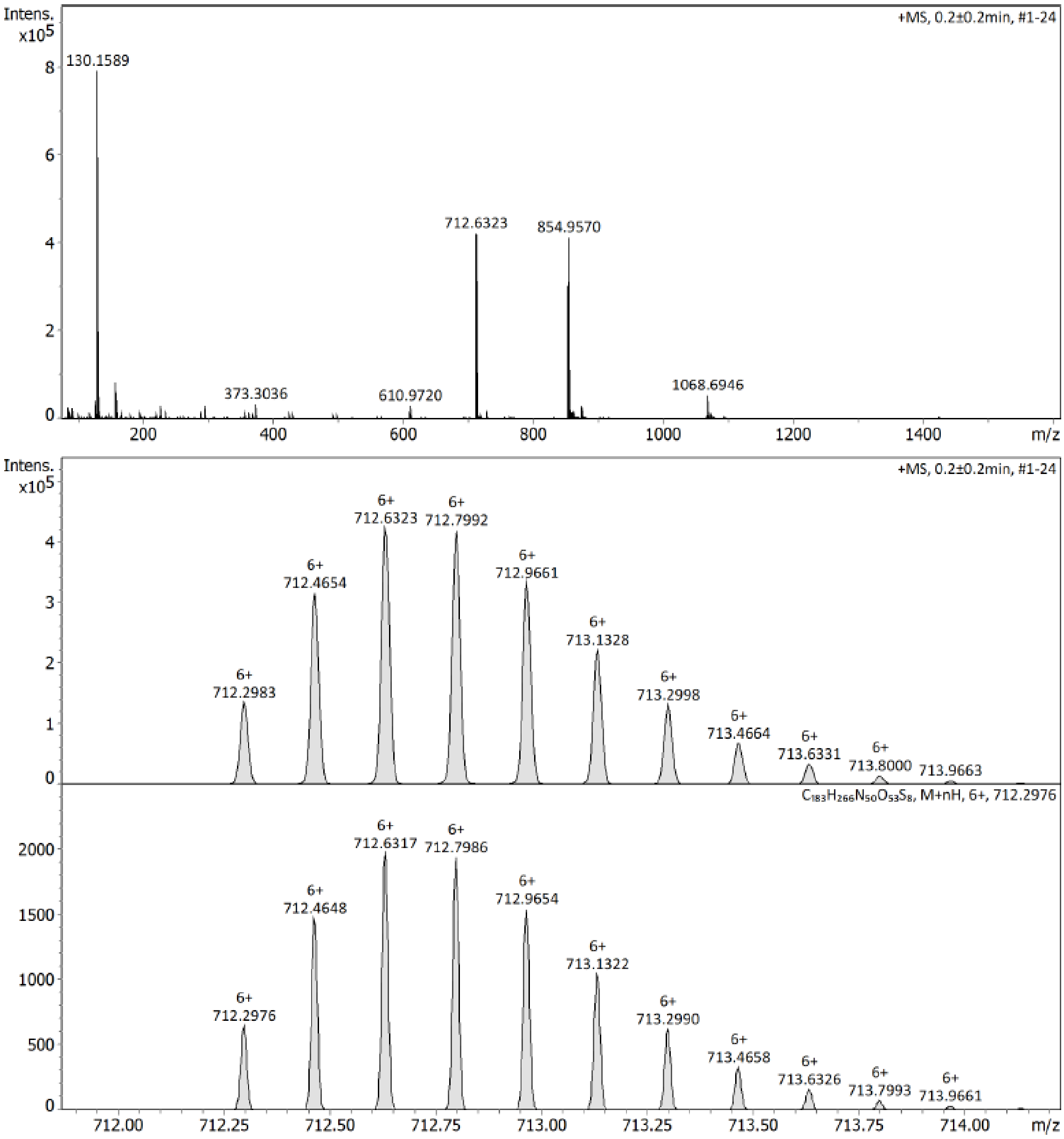

Figure 48. High resolution mass spectrum (timsTOF) of folded Pn3a[D8N].

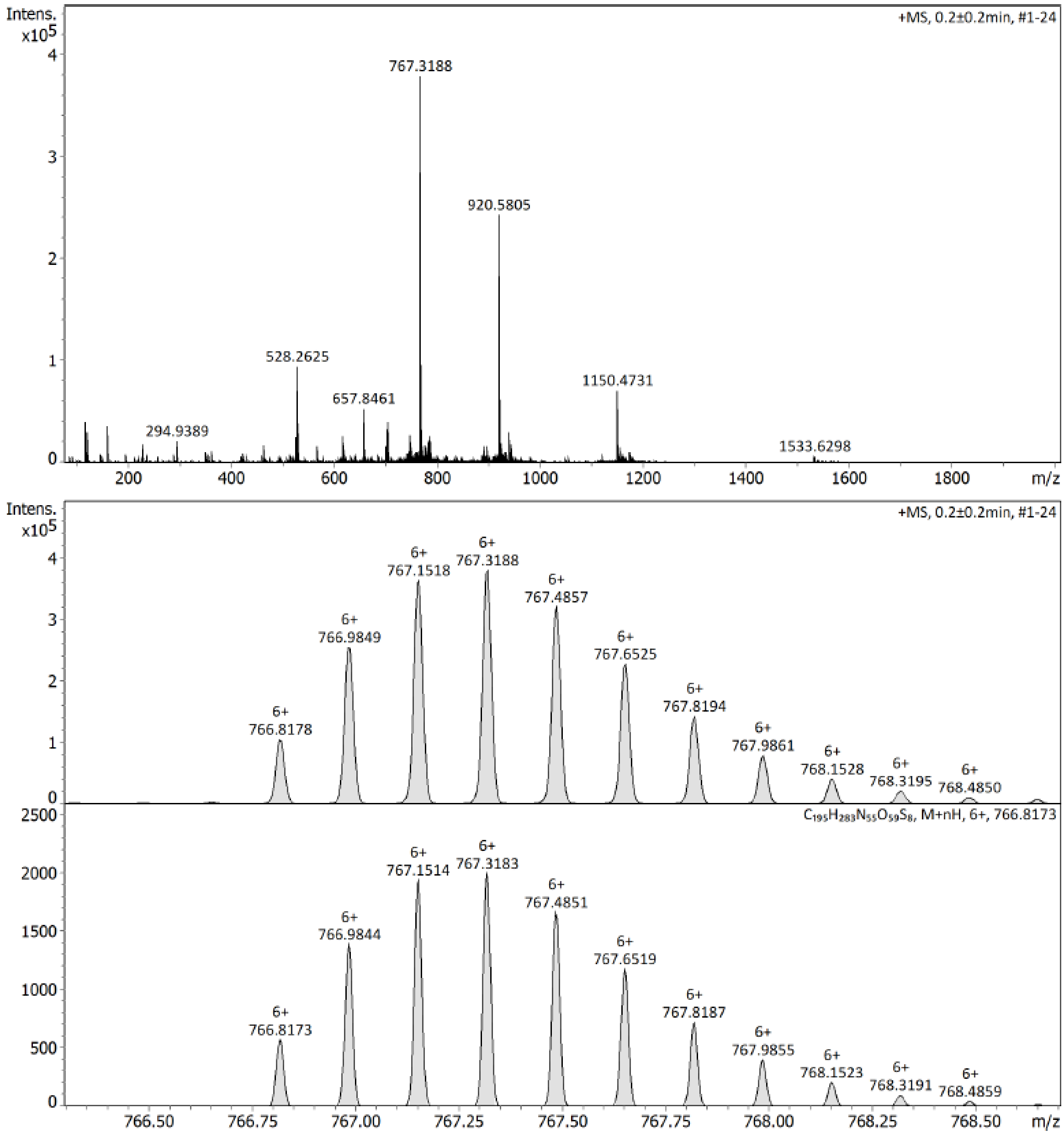

Figure 49. High resolution mass spectrum (timsTOF) of folded Ac-G5Pn3a[D8N].

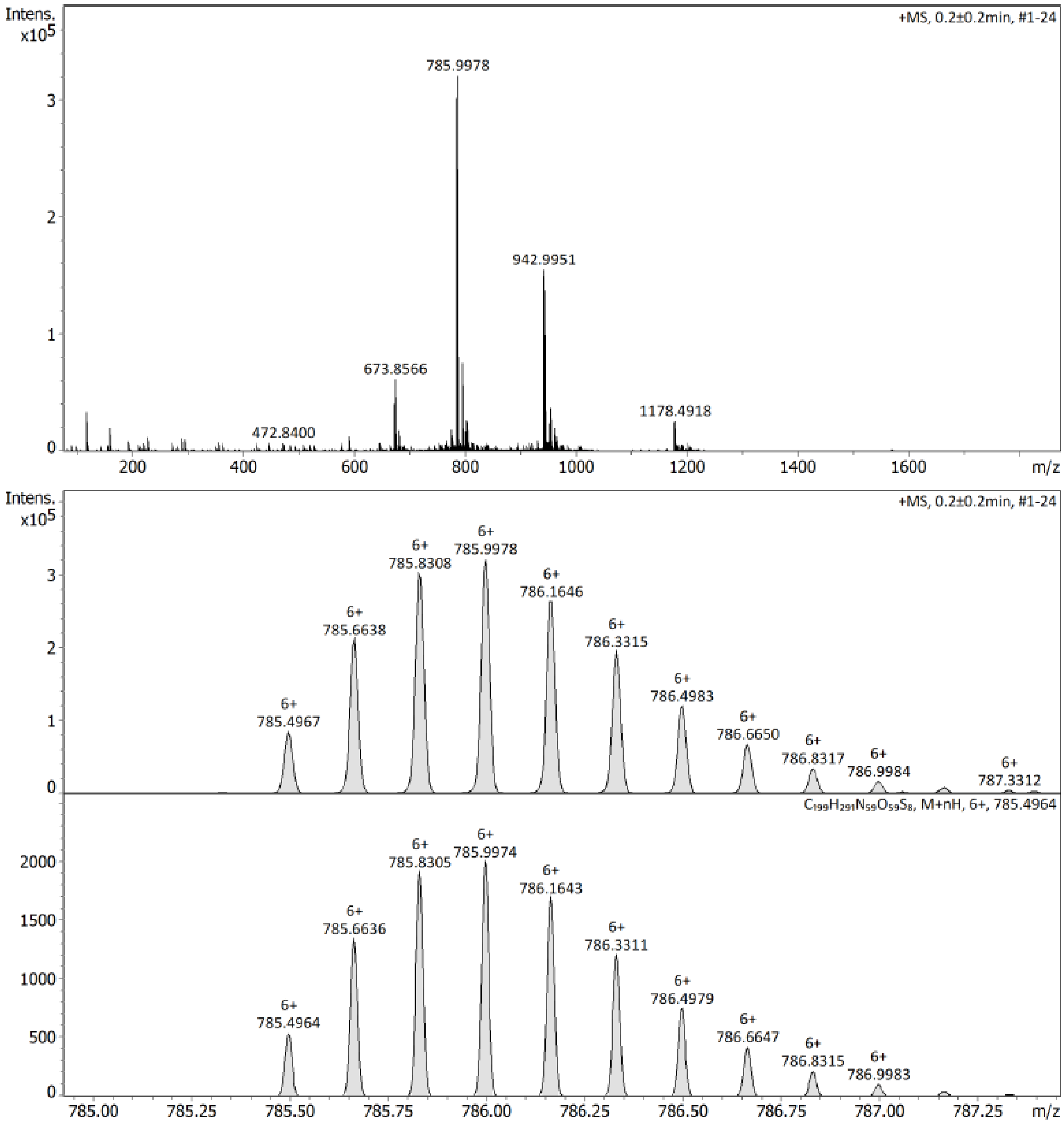

Figure 50. High resolution mass spectrum (timsTOF) of folded (*N*$_3$)K-G$_5$Pn3a[D8N].

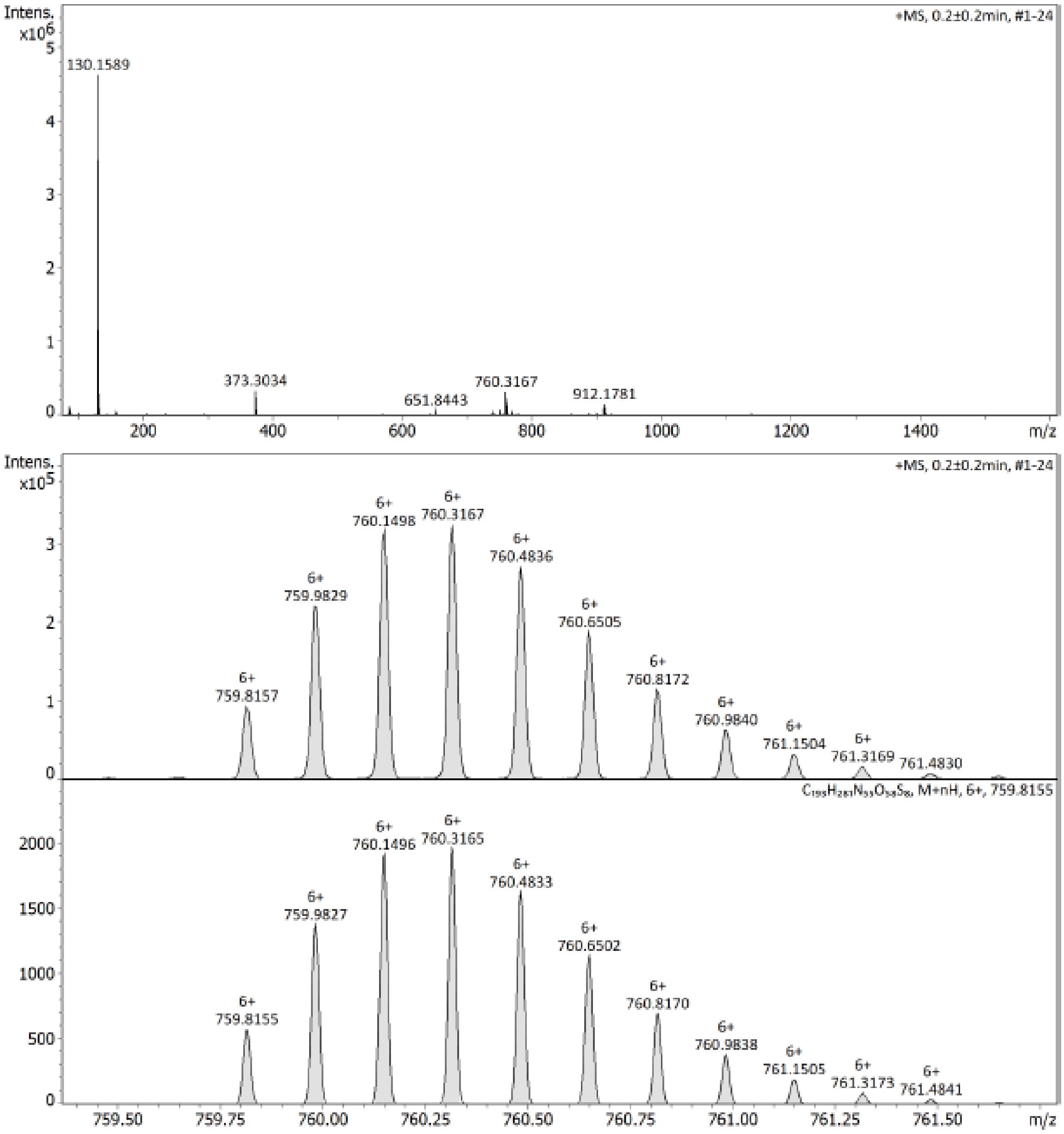

Figure 51. High resolution mass spectrum (timsTOF) of folded G₅Pn3a[D8N].

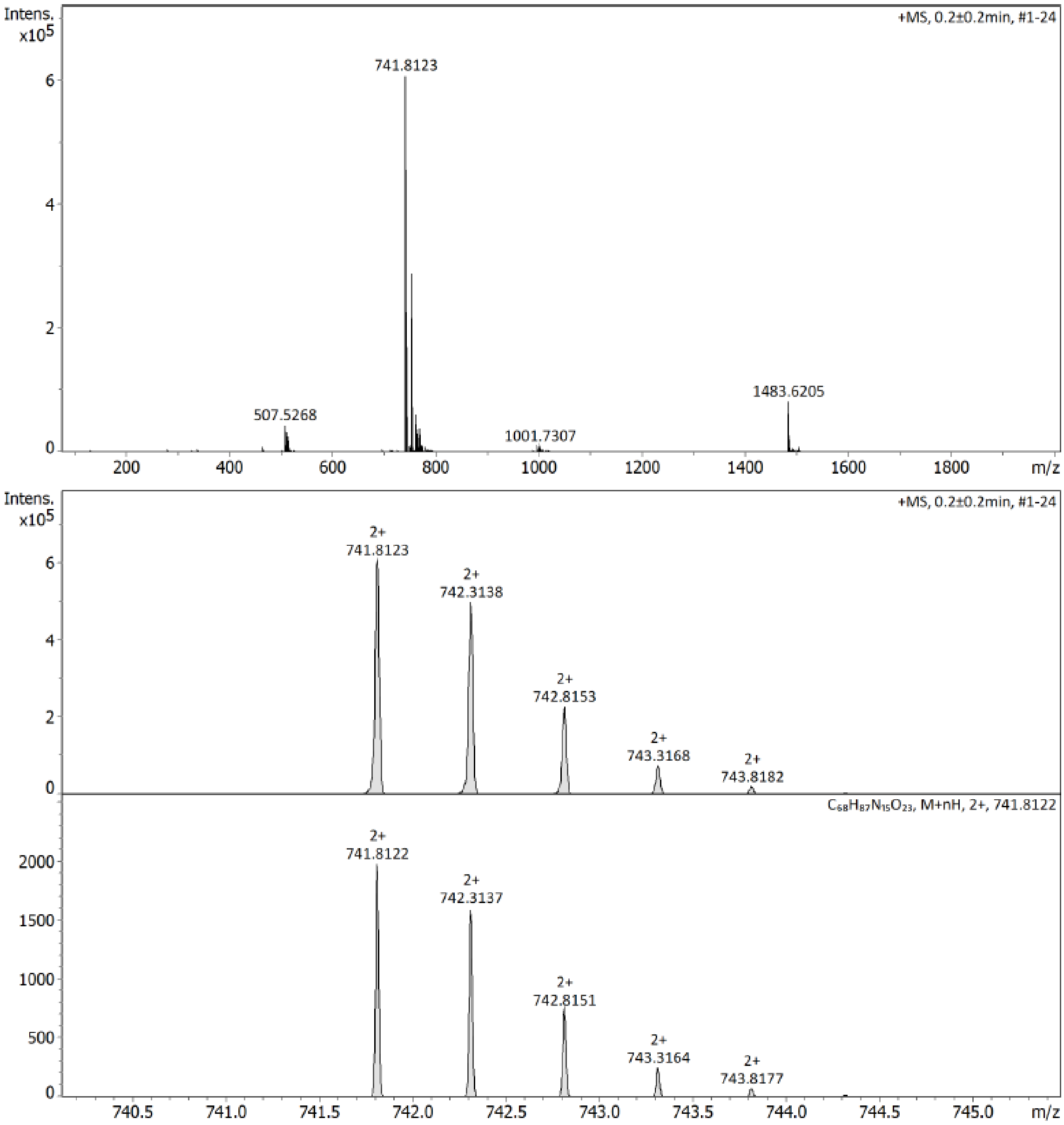

Figure 52. High resolution mass spectrum (timsTOF) of Pra-G_5HA.

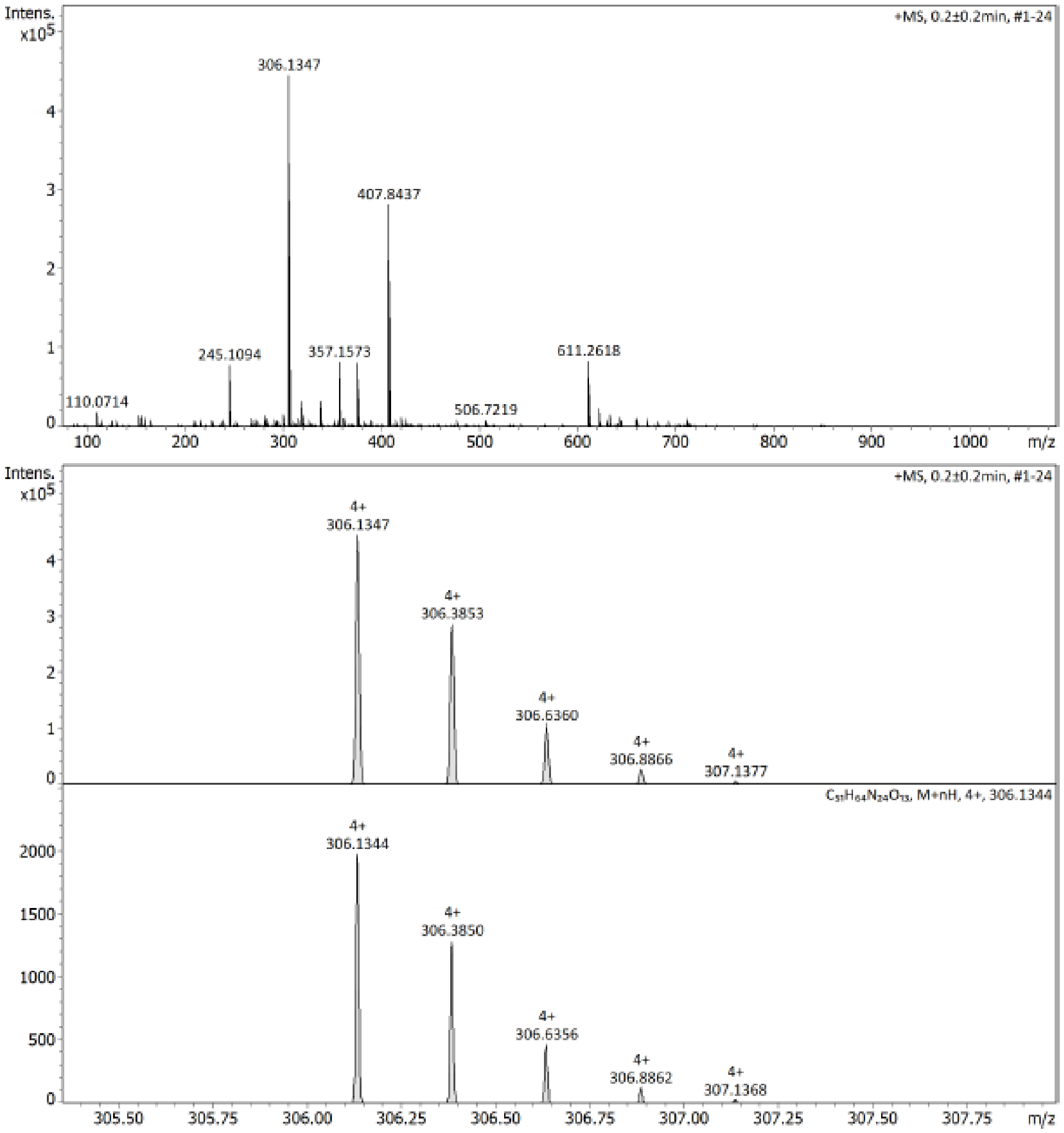

Figure 53. High resolution mass spectrum (timsTOF) of Pra-G_5His_6.

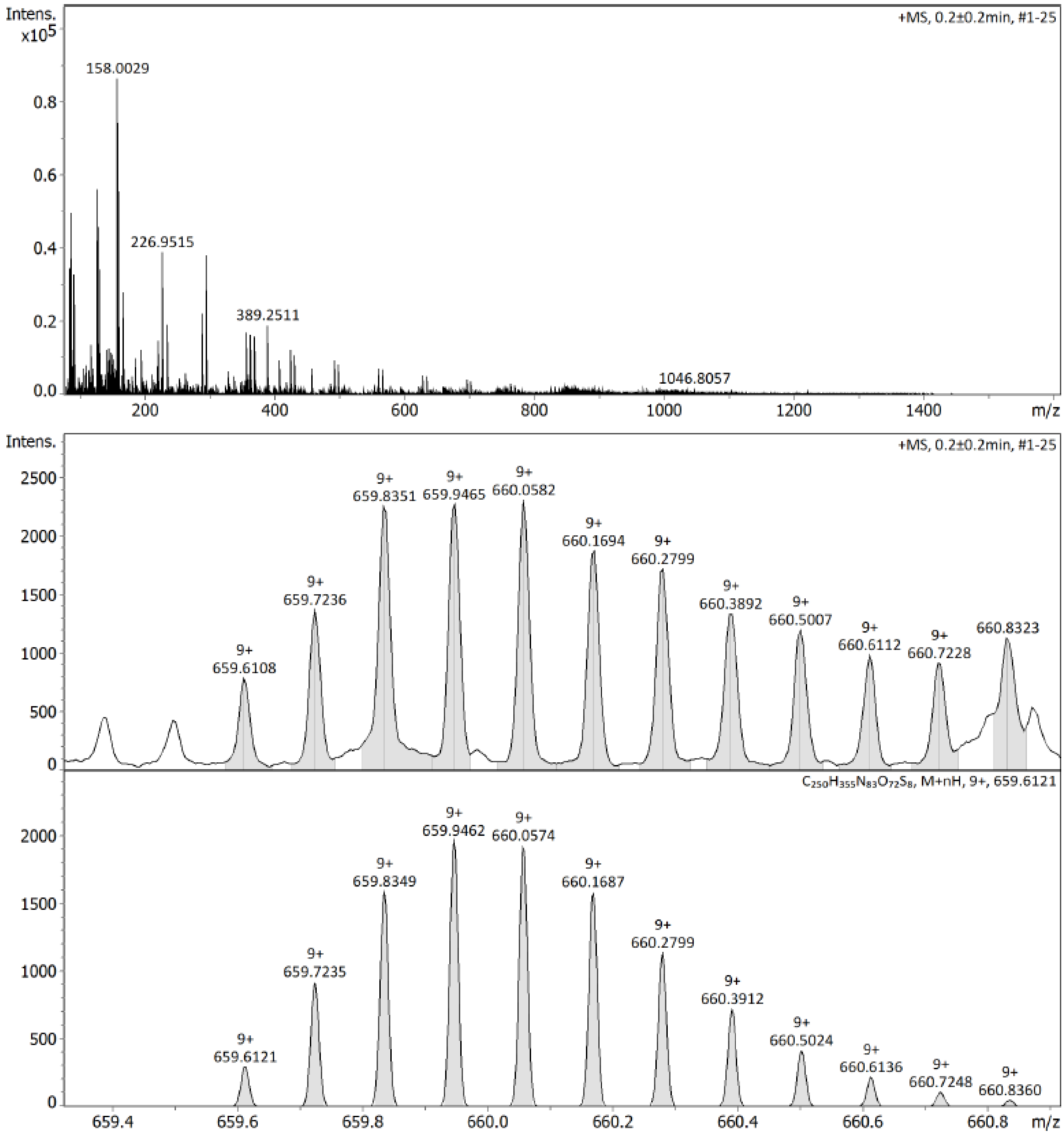

Figure 54. High resolution mass spectrum (timsTOF) of His$_6$-G$_5$-*Ta*-G$_5$Pn3a[D8N].

8.3 List of Figures

8.4 List of Tables

9 Bibliography

Agouram, N., El Hadrami, E.M., Bentama, A., 2021. 1,2,3-Triazoles as Biomimetics in Peptide Science. Molecules 26, 2937. https://doi.org/10.3390/molecules26102937

Aguilar, M.-I., 2003. HPLC of Peptides and Proteins. Humana Press, New Jersey. https://doi.org/10.1385/1592597424

Agwa, A.J., Blomster, L.V., Craik, D.J., King, G.F., Schroeder, C.I., 2018. Efficient Enzymatic Ligation of Inhibitor Cystine Knot Spider Venom Peptides: Using Sortase A To Form Double-Knottins That Probe Voltage-Gated Sodium Channel NaV1.7. Bioconjugate Chem. 29, 3309–3319. https://doi.org/10.1021/acs.bioconjchem.8b00505

Agwa, A.J., Henriques, S.T., Schroeder, C.I., 2017. Gating modifier toxin interactions with ion channels and lipid bilayers: Is the trimolecular complex real? Neuropharmacology, Venom-derived Peptides as Pharmacological Tools 127, 32–45. https://doi.org/10.1016/j.neuropharm.2017.04.004

Ahuja, S., Mukund, S., Deng, L., Khakh, K., Chang, E., Ho, H., Shriver, S., Young, C., Lin, S., Johnson, J.P., Wu, P., Li, J., Coons, M., Tam, C., Brillantes, B., Sampang, H., Mortara, K., Bowman, K.K., Clark, K.R., Estevez, A., Xie, Z., Verschoof, H., Grimwood, M., Dehnhardt, C., Andrez, J.-C., Focken, T., Sutherlin, D.P., Safina, B.S., Starovasnik, M.A., Ortwine, D.F., Franke, Y., Cohen, C.J., Hackos, D.H., Koth, C.M., Payandeh, J., 2015. Structural basis of Nav1.7 inhibition by an isoform-selective small-molecule antagonist. Science 350, aac5464. https://doi.org/10.1126/science.aac5464

Ajingi, Y.S., Rukying, N., Aroonsri, A., Jongruja, N., n.d. Recombinant Active Peptides and their Therapeutic Functions. Current Pharmaceutical Biotechnology 23, 645–663. https://doi.org/10.2174/1389201022666210702123934

Akondi, K.B., Muttenthaler, M., Dutertre, S., Kaas, Q., Craik, D.J., Lewis, R.J., Alewood, P.F., 2014. Discovery, Synthesis, and Structure–Activity

Relationships of Conotoxins. Chem. Rev. 114, 5815–5847. https://doi.org/10.1021/cr400401e

Alexander, S.P.H., Mathie, A., Peters, J.A., 2007. Guide to Receptors and Channels, 2nd edition (2007 Revision). Br J Pharmacol 150, S1. https://doi.org/10.1038/sj.bjp.0707199

Alexandrou, A.J., Brown, A.R., Chapman, M.L., Estacion, M., Turner, J., Mis, M.A., Wilbrey, A., Payne, E.C., Gutteridge, A., Cox, P.J., Doyle, R., Printzenhoff, D., Lin, Z., Marron, B.E., West, C., Swain, N.A., Storer, R.I., Stupple, P.A., Castle, N.A., Hounshell, J.A., Rivara, M., Randall, A., Dib-Hajj, S.D., Krafte, D., Waxman, S.G., Patel, M.K., Butt, R.P., Stevens, E.B., 2016. Subtype-Selective Small Molecule Inhibitors Reveal a Fundamental Role for Nav1.7 in Nociceptor Electrogenesis, Axonal Conduction and Presynaptic Release. PLOS ONE 11, e0152405. https://doi.org/10.1371/journal.pone.0152405

Armishaw, C.J., Alewood, P.F., 2005. Conotoxins as Research Tools and Drug Leads. Current Protein and Peptide Science 6, 221–240. https://doi.org/10.2174/1389203054065437

Åsberg, D., Langborg Weinmann, A., Leek, T., Lewis, R.J., Klarqvist, M., Leśko, M., Kaczmarski, K., Samuelsson, J., Fornstedt, T., 2017. The importance of ion-pairing in peptide purification by reversed-phase liquid chromatography. Journal of Chromatography A 1496, 80–91. https://doi.org/10.1016/j.chroma.2017.03.041

Avalo, Z., Barrera, M.C., Agudelo-Delgado, M., Tobón, G.J., Cañas, C.A., 2022. Biological Effects of Animal Venoms on the Human Immune System. Toxins (Basel) 14, 344. https://doi.org/10.3390/toxins14050344

Babu, V.V.S., 2001. One hundred years of peptide chemistry. Reson 6, 68–75. https://doi.org/10.1007/BF02836969

Bacsa, B., Horváti, K., Bõsze, S., Andreae, F., Kappe, C.O., 2008. Solid-Phase Synthesis of Difficult Peptide Sequences at Elevated Temperatures: A Critical Comparison of Microwave and Conventional Heating Technologies. J. Org. Chem. 73, 7532–7542. https://doi.org/10.1021/jo8013897

Bagchi, S., Fredriksson, R., Wallén-Mackenzie, Å., 2015. In Situ Proximity Ligation Assay (PLA), in: Hnasko, R. (Ed.), ELISA: Methods and Protocols. Springer, New York, NY, pp. 149–159. https://doi.org/10.1007/978-1-4939-2742-5_15

Bankar, G., Goodchild, S.J., Howard, S., Nelkenbrecher, K., Waldbrook, M., Dourado, M., Shuart, N.G., Lin, S., Young, C., Xie, Z., Khakh, K., Chang, E., Sojo, L.E., Lindgren, A., Chowdhury, S., Decker, S., Grimwood, M., Andrez, J.-C., Dehnhardt, C.M., Pang, J., Chang, J.H., Safina, B.S., Sutherlin, D.P., Johnson, J.P., Hackos, D.H., Robinette, C.L., Cohen, C.J., 2018. Selective NaV1.7 Antagonists with Long Residence Time Show Improved Efficacy against Inflammatory and Neuropathic Pain. Cell Reports 24, 3133–3145. https://doi.org/10.1016/j.celrep.2018.08.063

Barber, C.M., Madaras, F., Turnbull, R.K., Morley, T., Dunstan, N., Allen, L., Kuchel, T., Mirtschin, P., Hodgson, W.C., 2014. Comparative Studies of the Venom of a New Taipan Species, Oxyuranus temporalis, with Other Members of Its Genus. Toxins 6, 1979–1995. https://doi.org/10.3390/toxins6071979

Barlos, K., Chatzi, O., Gatos, D., Stavropoulos, G., 1991. 2-Chlorotrityl chloride resin. Int. J. Pept. Protein Res 37, 513–520.

Bennett, D.L., Clark, A.J., Huang, J., Waxman, S.G., Dib-Hajj, S.D., 2019. The Role of Voltage-Gated Sodium Channels in Pain Signaling. Physiological Reviews 99, 1079–1151. https://doi.org/10.1152/physrev.00052.2017

Bergmann, M., Zervas, L., 1932. Über ein allgemeines Verfahren der Peptid-Synthese. Berichte der deutschen chemischen Gesellschaft (A and B Series) 65, 1192–1201. https://doi.org/10.1002/cber.19320650722

Biass, D., Dutertre, S., Gerbault, A., Menou, J.-L., Offord, R., Favreau, P., Stöcklin, R., 2009. Comparative proteomic study of the venom of the piscivorous cone snail *Conus consors*. Journal of Proteomics, Venomics 72, 210–218. https://doi.org/10.1016/j.jprot.2009.01.019

Black, J.A., Frézel, N., Dib-Hajj, S.D., Waxman, S.G., 2012. Expression of Nav1.7 in DRG Neurons Extends from Peripheral Terminals in the Skin to Central Preterminal Branches and Terminals in the Dorsal Horn. Mol Pain 8, 1744-8069-8–82. https://doi.org/10.1186/1744-8069-8-82

Blackburn, C., 1998. Polymer supports for solid-phase organic synthesis. Peptide Science 47, 311–351. https://doi.org/10.1002/(SICI)1097-0282(1998)47:5<311::AID-BIP2>3.0.CO;2-V

Bonandi, E., Christodoulou, M.S., Fumagalli, G., Perdicchia, D., Rastelli, G., Passarella, D., 2017. The 1,2,3-triazole ring as a bioisostere in medicinal chemistry. Drug Discovery Today 22, 1572–1581. https://doi.org/10.1016/j.drudis.2017.05.014

Bordon, K. de C.F., Cologna, C.T., Fornari-Baldo, E.C., Pinheiro-Júnior, E.L., Cerni, F.A., Amorim, F.G., Anjolette, F.A.P., Cordeiro, F.A., Wiezel, G.A., Cardoso, I.A., Ferreira, I.G., de Oliveira, I.S., Boldrini-França, J., Pucca, M.B., Baldo, M.A., Arantes, E.C., 2020. From Animal Poisons and Venoms to Medicines: Achievements, Challenges and Perspectives in Drug Discovery. Front Pharmacol 11, 1132. https://doi.org/10.3389/fphar.2020.01132

Brik, A., Alexandratos, J., Lin, Y., Elder, J.H., Olson, A.J., Wlodawer, A., Goodsell, D.S., Wong, C., 2005. 1,2,3-Triazole as a Peptide Surrogate in the Rapid Synthesis of HIV-1 Protease Inhibitors. ChemBioChem 6, 1167–1169. https://doi.org/10.1002/cbic.200500101

Bulaj, G., West, P.J., Garrett, J.E., Watkins, M., Zhang, M.-M., Norton, R.S., Smith, B.J., Yoshikami, D., Olivera, B.M., 2005. Novel Conotoxins from Conus striatus and Conus kinoshitai Selectively Block TTX-Resistant Sodium Channels. Biochemistry 44, 7259–7265. https://doi.org/10.1021/bi0473408

Cai, S., Moutal, A., Yu, J., Chew, L.A., Isensee, J., Chawla, R., Gomez, K., Luo, S., Zhou, Y., Chefdeville, A., Madura, C., Perez-Miller, S., Bellampalli, S.S., Dorame, A., Scott, D.D., François-Moutal, L., Shan, Z., Woodward, T., Gokhale, V., Hohmann, A.G., Vanderah, T.W., Patek, M., Khanna, M., Hucho, T., Khanna, R., 2021. Selective targeting of NaV1.7 via inhibition of the CRMP2-Ubc9 interaction reduces pain in rodents. Science Translational Medicine 13, eabh1314. https://doi.org/10.1126/scitranslmed.abh1314

Cane, G., Leuchowius, K.-J., Söderberg, O., Kamali-Moghaddam, M., Jarvius, M., Helbing, I., Pardali, K., Koos, B., Ebai, T., Landegren, U., 2017. Chapter 12 - Protein Diagnostics by Proximity Ligation: Combining Multiple Recognition and DNA Amplification for Improved Protein Analyses, in: Patrinos, G.P. (Ed.), Molecular Diagnostics (Third Edition). Academic Press, pp. 219–231. https://doi.org/10.1016/B978-0-12-802971-8.00012-2

Cardoso, F.C., Lewis, R.J., 2019. Structure–Function and Therapeutic Potential of Spider Venom-Derived Cysteine Knot Peptides Targeting Sodium Channels. Front. Pharmacol. 10. https://doi.org/10.3389/fphar.2019.00366

Carpino, L.A., 1993. 1-Hydroxy-7-azabenzotriazole. An efficient peptide coupling additive. J. Am. Chem. Soc. 115, 4397–4398. https://doi.org/10.1021/ja00063a082

Carpino, L.A., Han, G.Y., 1970. 9-Fluorenylmethoxycarbonyl function, a new base-sensitive amino-protecting group. J. Am. Chem. Soc. 92, 5748–5749. https://doi.org/10.1021/ja00722a043

Casewell, N.R., Wüster, W., Vonk, F.J., Harrison, R.A., Fry, B.G., 2013. Complex cocktails: the evolutionary novelty of venoms. Trends in Ecology & Evolution 28, 219–229. https://doi.org/10.1016/j.tree.2012.10.020

Catterall, W.A., 2000. From Ionic Currents to Molecular Mechanisms: The Structure and Function of Voltage-Gated Sodium Channels. Neuron 26, 13–25. https://doi.org/10.1016/S0896-6273(00)81133-2

Catterall, W.A., Cestèle, S., Yarov-Yarovoy, V., Yu, F.H., Konoki, K., Scheuer, T., 2007. Voltage-gated ion channels and gating modifier toxins. Toxicon, Gating Modifier Peptides of Ion Channels 49, 124–141. https://doi.org/10.1016/j.toxicon.2006.09.022

Catterall, W.A., Goldin, A.L., Waxman, S.G., 2005. International Union of Pharmacology. XLVII. Nomenclature and Structure-Function Relationships of Voltage-Gated Sodium Channels. Pharmacol Rev 57, 397–409. https://doi.org/10.1124/pr.57.4.4

Cestèle, S., Catterall, W.A., 2000. Molecular mechanisms of neurotoxin action on voltage-gated sodium channels. Biochimie 82, 883–892. https://doi.org/10.1016/S0300-9084(00)01174-3

Chahine, M. (Ed.), 2018. Voltage-gated Sodium Channels: Structure, Function and Channelopathies, Handbook of Experimental Pharmacology. Springer International Publishing, Cham. https://doi.org/10.1007/978-3-319-90284-5

Chahine, M., O'Leary, M.E., 2011. Regulatory Role of Voltage-Gated Na+ Channel β Subunits in Sensory Neurons. Front. Pharmacol. 2. https://doi.org/10.3389/fphar.2011.00070

Chan, T.R., Hilgraf, R., Sharpless, K.B., Fokin, V.V., 2004. Polytriazoles as Copper(I)-Stabilizing Ligands in Catalysis. Org. Lett. 6, 2853–2855. https://doi.org/10.1021/ol0493094

Chang, W., Berta, T., Kim, Y.H., Lee, S., Lee, S.-Y., Ji, R.-R., 2018. Expression and Role of Voltage-Gated Sodium Channels in Human Dorsal Root Ganglion Neurons with Special Focus on Nav1.7, Species Differences, and Regulation by Paclitaxel. Neurosci. Bull. 34, 4–12. https://doi.org/10.1007/s12264-017-0132-3

Chattopadhyay, M., Mata, M., Fink, D.J., 2008. Continuous δ-Opioid Receptor Activation Reduces Neuronal Voltage-Gated Sodium Channel (NaV1.7) Levels through Activation of Protein Kinase C in Painful Diabetic Neuropathy. J. Neurosci. 28, 6652–6658. https://doi.org/10.1523/JNEUROSCI.5530-07.2008

Chen, F., Huang, W., Jiang, T., Yu, R., 2018. Determination of the μ-Conotoxin PIIIA Specificity Against Voltage-Gated Sodium Channels from Binding Energy Calculations. Mar Drugs 16, 153. https://doi.org/10.3390/md16050153

Chen, G., Kang, W., Li, W., Chen, S., Gao, Y., 2022. Oral delivery of protein and peptide drugs: from non-specific formulation approaches to intestinal cell targeting strategies. Theranostics 12, 1419–1439. https://doi.org/10.7150/thno.61747

Chen, J., Zhao, L., Jiang, L., Meng, E., Zhang, Y., Xiong, X., Liang, S., 2008. Transcriptome analysis revealed novel possible venom components and cellular processes of the tarantula *Chilobrachys jingzhao* venom gland. Toxicon 52, 794–806. https://doi.org/10.1016/j.toxicon.2008.08.003

Chen, X.-T., Wang, J.-Y., Ma, Y.-N., Dong, L.-Y., Jia, S.-X., Yin, H., Fu, X.-Y., Du, S.-S., Qi, Y.-K., Wang, K., 2022. DIC/Oxyma-based accelerated synthesis and oxidative folding studies of centipede toxin RhTx. Journal of Peptide Science 28, e3368. https://doi.org/10.1002/psc.3368

Church, J.E., Hodgson, W.C., 2000. Dose-dependent cardiovascular and neuromuscular effects of stonefish (*Synanceja trachynis*) venom. Toxicon 38, 391–407. https://doi.org/10.1016/S0041-0101(99)00169-5

Coelho, V.A., Cremonez, C.M., Anjolette, F.A.P., Aguiar, J.F., Varanda, W.A., Arantes, E.C., 2014. Functional and structural study comparing the C-terminal amidated β-neurotoxin Ts1 with its isoform Ts1-G isolated from *Tityus serrulatus* venom. Toxicon 83, 15–21. https://doi.org/10.1016/j.toxicon.2014.02.010

Coin, I., Beyermann, M., Bienert, M., 2007. Solid-phase peptide synthesis: from standard procedures to the synthesis of difficult sequences. Nat Protoc 2, 3247–3256. https://doi.org/10.1038/nprot.2007.454

Colgrave, M.L., Craik, D.J., 2004. Thermal, Chemical, and Enzymatic Stability of the Cyclotide Kalata B1: The Importance of the Cyclic Cystine Knot. Biochemistry 43, 5965–5975. https://doi.org/10.1021/bi049711q

Cox, J.J., Reimann, F., Nicholas, A.K., Thornton, G., Roberts, E., Springell, K., Karbani, G., Jafri, H., Mannan, J., Raashid, Y., Al-Gazali, L., Hamamy, H., Valente, E.M., Gorman, S., Williams, R., McHale, D.P., Wood, J.N., Gribble, F.M., Woods, C.G., 2006. An SCN9A channelopathy causes congenital inability to experience pain. Nature 444, 894–898. https://doi.org/10.1038/nature05413

Craik, D.J., Daly, N.L., Bond, T., Waine, C., 1999. Plant cyclotides: A unique family of cyclic and knotted proteins that defines the cyclic cystine knot structural motif1. Journal of Molecular Biology 294, 1327–1336. https://doi.org/10.1006/jmbi.1999.3383

Craik, D.J., Daly, N.L., Waine, C., 2001. The cystine knot motif in toxins and implications for drug design. Toxicon 39, 43–60. https://doi.org/10.1016/s0041-0101(00)00160-4

Cummins, T.R., Howe, J.R., Waxman, S.G., 1998. Slow Closed-State Inactivation: A Novel Mechanism Underlying Ramp Currents in Cells Expressing the hNE/PN1 Sodium Channel. J. Neurosci. 18, 9607–9619. https://doi.org/10.1523/JNEUROSCI.18-23-09607.1998

Curtius, T., 1882. Ueber einige neue der Hippursäure analog constituirte, synthetisch dargestellte Amidosäuren. Journal für Praktische Chemie 26, 145–208. https://doi.org/10.1002/prac.18820260112

Daly, N.L., Craik, D.J., 2011. Bioactive cystine knot proteins. Current Opinion in Chemical Biology, Molecular Diversity 15, 362–368. https://doi.org/10.1016/j.cbpa.2011.02.008

Davis, J., Jones, A., Lewis, R.J., 2009. Remarkable inter- and intra-species complexity of conotoxins revealed by LC/MS. Peptides 30, 1222–1227. https://doi.org/10.1016/j.peptides.2009.03.019

Davis, J.H., Bradley, E.K., Miljanich, G.P., Nadasdi, L., Ramachandran, J., Basus, V.J., 1993. Solution structure of omega-conotoxin GVIA using 2-D NMR spectroscopy and relaxation matrix analysis. Biochemistry 32, 7396–7405. https://doi.org/10.1021/bi00080a009

de Lera Ruiz, M., Kraus, R.L., 2015. Voltage-Gated Sodium Channels: Structure, Function, Pharmacology, and Clinical Indications. J. Med. Chem. 58, 7093–7118. https://doi.org/10.1021/jm501981g

Deuis, J.R., Dekan, Z., Wingerd, J.S., Smith, J.J., Munasinghe, N.R., Bhola, R.F., Imlach, W.L., Herzig, V., Armstrong, D.A., Rosengren, K.J., Bosmans, F., Waxman, S.G., Dib-Hajj, S.D., Escoubas, P., Minett, M.S., Christie, M.J., King, G.F., Alewood, P.F., Lewis, R.J., Wood, J.N., Vetter, I., 2017. Pharmacological characterisation of the highly NaV1.7 selective spider venom peptide Pn3a. Sci Rep 7, 40883. https://doi.org/10.1038/srep40883

Dib-Hajj, S.D., Cummins, T.R., Black, J.A., Waxman, S.G., 2007. From genes to pain: Nav1.7 and human pain disorders. Trends in Neurosciences 30, 555–563. https://doi.org/10.1016/j.tins.2007.08.004

Dib-Hajj, S.D., Rush, A.M., Cummins, T.R., Hisama, F.M., Novella, S., Tyrrell, L., Marshall, L., Waxman, S.G., 2005. Gain-of-function mutation in Nav1.7 in familial erythromelalgia induces bursting of sensory neurons. Brain 128, 1847–1854. https://doi.org/10.1093/brain/awh514

Dichgans, M., Freilinger, T., Eckstein, G., Babini, E., Lorenz-Depiereux, B., Biskup, S., Ferrari, M.D., Herzog, J., Maagdenberg, A.M. van den, Pusch, M., Strom, T.M., 2005. Mutation in the neuronal voltage-gated sodium channel SCN1A in familial hemiplegic migraine. The Lancet 366, 371–377. https://doi.org/10.1016/S0140-6736(05)66786-4

Dongol, Y., C. Cardoso, F., Lewis, R.J., 2019. Spider Knottin Pharmacology at Voltage-Gated Sodium Channels and Their Potential to Modulate Pain Pathways. Toxins 11, 626. https://doi.org/10.3390/toxins11110626

Donnelly, P.S., Zanatta, S.D., Zammit, S.C., White, J.M., Williams, S.J., 2008. ‘Click’ cycloaddition catalysts: copper(I) and copper(II) tris(triazolylmethyl)amine complexes. Chem. Commun. 2459–2461. https://doi.org/10.1039/B719724A

Dourtoglou, V., Ziegler, J.-C., Gross, B., 1978. L’hexafluorophosphate de O-benzotriazolyl-N,N-tetramethyluronium: Un reactif de couplage peptidique nouveau et efficace. Tetrahedron Letters 19, 1269–1272. https://doi.org/10.1016/0040-4039(78)80103-8

Dravet, C., 2011. Dravet syndrome history. Developmental Medicine & Child Neurology 53, 1–6. https://doi.org/10.1111/j.1469-8749.2011.03964.x

Dubin, A.E., Patapoutian, A., 2010. Nociceptors: the sensors of the pain pathway. J Clin Invest 120, 3760–3772. https://doi.org/10.1172/JCI42843

Dunlop, J., Bowlby, M., Peri, R., Vasilyev, D., Arias, R., 2008. High-throughput electrophysiology: an emerging paradigm for ion-channel screening and physiology. Nat Rev Drug Discov 7, 358–368. https://doi.org/10.1038/nrd2552

Dustrude, E.T., Wilson, S.M., Ju, W., Xiao, Y., Khanna, R., 2013. CRMP2 Protein SUMOylation Modulates NaV1.7 Channel Trafficking*. Journal of Biological Chemistry 288, 24316–24331. https://doi.org/10.1074/jbc.M113.474924

Dutertre, S., Jin, A.-H., Vetter, I., Hamilton, B., Sunagar, K., Lavergne, V., Dutertre, V., Fry, B.G., Antunes, A., Venter, D.J., Alewood, P.F., Lewis, R.J., 2014. Evolution of separate predation- and defence-evoked venoms in carnivorous cone snails. Nat Commun 5, 3521. https://doi.org/10.1038/ncomms4521

Dutertre, S., Lewis, R., 2011. Cone snail Biology, Bioprospecting and Conservation. pp. 85–104. https://doi.org/10.13140/2.1.3223.6489

Dutertre, S., Lewis, R.J., 2010. Use of Venom Peptides to Probe Ion Channel Structure and Function. J Biol Chem 285, 13315–13320. https://doi.org/10.1074/jbc.R109.076596

Eagles, D.A., Chow, C.Y., King, G.F., 2022. Fifteen years of NaV1.7 channels as an analgesic target: Why has excellent in vitro pharmacology not translated into in vivo analgesic efficacy? British Journal of Pharmacology 179, 3592–3611. https://doi.org/10.1111/bph.15327

Eijkelkamp, N., Linley, J.E., Baker, M.D., Minett, M.S., Cregg, R., Werdehausen, R., Rugiero, F., Wood, J.N., 2012. Neurological perspectives on voltage-gated sodium channels. Brain 135, 2585–2612. https://doi.org/10.1093/brain/aws225

El-Faham, A., Albericio, F., 2011. Peptide Coupling Reagents, More than a Letter Soup. Chem. Rev. 111, 6557–6602. https://doi.org/10.1021/cr100048w

Escoubas, P., Sollod, B., King, G.F., 2006. Venom landscapes: Mining the complexity of spider venoms via a combined cDNA and mass spectrometric approach. Toxicon, Mass Spectrometry in Toxinology 47, 650–663. https://doi.org/10.1016/j.toxicon.2006.01.018

Estacion, M., Dib-Hajj, S.D., Benke, P.J., Morsche, R.H.M. te, Eastman, E.M., Macala, L.J., Drenth, J.P.H., Waxman, S.G., 2008. NaV1.7 Gain-of-Function Mutations as a Continuum: A1632E Displays Physiological Changes Associated with Erythromelalgia and Paroxysmal Extreme Pain Disorder Mutations and Produces Symptoms of Both Disorders. J. Neurosci. 28, 11079–11088. https://doi.org/10.1523/JNEUROSCI.3443-08.2008

Fenn, J.B., Mann, M., Meng, C.K., Wong, S.F., Whitehouse, C.M., 1989. Electrospray Ionization for Mass Spectrometry of Large Biomolecules. Science 246, 64–71. https://doi.org/10.1126/science.2675315

Ferreira, S.H., 1965. A Bradykinin-Potentiating Factor (bpf) Present in the Venom of Bothrops Jararaca. British Journal of Pharmacology and Chemotherapy 24, 163–169. https://doi.org/10.1111/j.1476-5381.1965.tb02091.x

Fertleman, C.R., Baker, M.D., Parker, K.A., Moffatt, S., Elmslie, F.V., Abrahamsen, B., Ostman, J., Klugbauer, N., Wood, J.N., Gardiner, R.M., Rees, M., 2006. SCN9A Mutations in Paroxysmal Extreme Pain Disorder: Allelic Variants Underlie Distinct Channel Defects and Phenotypes. Neuron 52, 767–774. https://doi.org/10.1016/j.neuron.2006.10.006

Fischer, E., Fourneau, E., 1901. Ueber einige Derivate des Glykocolls. Berichte der deutschen chemischen Gesellschaft 34, 2868–2877. https://doi.org/10.1002/cber.190103402249

Focken, T., Liu, S., Chahal, N., Dauphinais, M., Grimwood, M.E., Chowdhury, S., Hemeon, I., Bichler, P., Bogucki, D., Waldbrook, M., Bankar, G., Sojo, L.E., Young, C., Lin, S., Shuart, N., Kwan, R., Pang, J., Chang, J.H., Safina, B.S., Sutherlin, D.P., Johnson, J.P.Jr., Dehnhardt, C.M., Mansour, T.S., Oballa, R.M., Cohen, C.J., Robinette, C.L., 2016. Discovery of Aryl

Sulfonamides as Isoform-Selective Inhibitors of NaV1.7 with Efficacy in Rodent Pain Models. ACS Med. Chem. Lett. 7, 277–282. https://doi.org/10.1021/acsmedchemlett.5b00447

Fredriksson, S., Gullberg, M., Jarvius, J., Olsson, C., Pietras, K., Gústafsdóttir, S.M., Östman, A., Landegren, U., 2002. Protein detection using proximity-dependent DNA ligation assays. Nat Biotechnol 20, 473–477. https://doi.org/10.1038/nbt0502-473

Fry, B.G., Koludarov, I., Jackson, T.N.W., Holford, M., Terrat, Y., Casewell, N.R., Undheim, E.A.B., Vetter, I., Ali, S.A., Low, D.H.W., Sunagar, K., 2015. Seeing the Woods for the Trees: Understanding Venom Evolution as a Guide for Biodiscovery. https://doi.org/10.1039/9781849737876-00001

Fry, B.G., Roelants, K., Champagne, D.E., Scheib, H., Tyndall, J.D.A., King, G.F., Nevalainen, T.J., Norman, J.A., Lewis, R.J., Norton, R.S., Renjifo, C., de la Vega, R.C.R., 2009. The Toxicogenomic Multiverse: Convergent Recruitment of Proteins Into Animal Venoms. Annual Review of Genomics and Human Genetics 10, 483–511. https://doi.org/10.1146/annurev.genom.9.081307.164356

Furman, B.L., 2012. The development of Byetta (exenatide) from the venom of the Gila monster as an anti-diabetic agent. Toxicon, From venoms to drugs 59, 464–471. https://doi.org/10.1016/j.toxicon.2010.12.016

Galochkina, T., Gelly, J.-C., 2022. Chapter 13 - Knottin peptidomimetics as therapeutics, in: Qvit, N., Rubin, S.J.S. (Eds.), Peptide and Peptidomimetic Therapeutics. Academic Press, pp. 309–319. https://doi.org/10.1016/B978-0-12-820141-1.00019-4

Gaskin, D.J., Richard, P., 2012. The Economic Costs of Pain in the United States. The Journal of Pain 13, 715–724. https://doi.org/10.1016/j.jpain.2012.03.009

Gold, M.S., Gebhart, G.F., 2010. Nociceptor sensitization in pain pathogenesis. Nat Med 16, 1248–1257. https://doi.org/10.1038/nm.2235

Goldberg, Y.P., Price, N., Namdari, R., Cohen, C.J., Lamers, M.H., Winters, C., Price, J., Young, C.E., Verschoof, H., Sherrington, R., Pimstone, S.N., Hayden, M.R., 2012. Treatment of Nav1.7-mediated pain in inherited erythromelalgia using a novel sodium channel blocker. PAIN 153, 80. https://doi.org/10.1016/j.pain.2011.09.008

Goldin, A.L., 2001. Resurgence of Sodium Channel Research. Annual Review of Physiology 63, 871–894. https://doi.org/10.1146/annurev.physiol.63.1.871

Goldin, A.L., Barchi, R.L., Caldwell, J.H., Hofmann, F., Howe, J.R., Hunter, J.C., Kallen, R.G., Mandel, G., Meisler, M.H., Netter, Y.B., Noda, M., Tamkun, M.M., Waxman, S.G., Wood, J.N., Catterall, W.A., 2000. Nomenclature of Voltage-Gated Sodium Channels. Neuron 28, 365–368. https://doi.org/10.1016/S0896-6273(00)00116-1

Goldman, A., Harper, S., Speicher, D.W., 2016. Detection of Proteins on Blot Membranes. Current Protocols in Protein Science 86, 10.8.1-10.8.11. https://doi.org/10.1002/cpps.15

Golzari, S.E., Soleimanpour, H., Mahmoodpoor, A., Safari, S., Ala, A., 2014. Lidocaine and Pain Management in the Emergency Department: A Review Article. Anesth Pain Med 4, e15444. https://doi.org/10.5812/aapm.15444

Goodman, M., Stueben, K.C., 2002. Amino Acid Active Esters. III. Base-Catalyzed Racemization of Peptide Active Esters1,2 [WWW Document]. ACS Publications. https://doi.org/10.1021/jo01057a006

Goodwin, G., McMahon, S.B., 2021. The physiological function of different voltage-gated sodium channels in pain. Nat Rev Neurosci 22, 263–274. https://doi.org/10.1038/s41583-021-00444-w

Gordon, D., Martin-Eauclaire, M.-F., Cestèle, S., Kopeyan, C., Carlier, E., Khalifa, R.B., Pelhate, M., Rochat, H., 1996. Scorpion Toxins Affecting Sodium Current Inactivation Bind to Distinct Homologous Receptor Sites on Rat Brain and Insect Sodium Channels (*). Journal of Biological Chemistry 271, 8034–8045. https://doi.org/10.1074/jbc.271.14.8034

Guo, R., Guo, G., Wang, A., Xu, G., Lai, R., Jin, H., 2024. Spider-Venom Peptides: Structure, Bioactivity, Strategy, and Research Applications. Molecules 29, 35. https://doi.org/10.3390/molecules29010035

Hakim, M.A., Yang, S., Lai, R., 2015. Centipede Venoms and Their Components: Resources for Potential Therapeutic Applications. Toxins 7, 4832–4851. https://doi.org/10.3390/toxins7114832

Haney, R.A., Ayoub, N.A., Clarke, T.H., Hayashi, C.Y., Garb, J.E., 2014. Dramatic expansion of the black widow toxin arsenal uncovered by multi-tissue transcriptomics and venom proteomics. BMC Genomics 15, 366. https://doi.org/10.1186/1471-2164-15-366

Hashimoto, K., Uchida, S., Yoshida, H., Nishiuchi, Y., Sakakibara, S., Yukari, K., 1985. Structure-activity relations of conotoxins at the neuromuscular junction. European Journal of Pharmacology 118, 351–354. https://doi.org/10.1016/0014-2999(85)90147-5

Hay, S.I., Abajobir, A.A., Abate, K.H., Abbafati, C., Abbas, K.M., Abd-Allah, F., Abdulkader, R.S., Abdulle, A.M., Abebo, T.A., Abera, S.F., Aboyans, V., Abu-Raddad, L.J., Ackerman, I.N., Adedeji, I.A., Adetokunboh, O., Afshin, A., Aggarwal, R., Agrawal, S., Agrawal, A., Ahmed, M.B., Aichour, M.T.E., Aichour, A.N., Aichour, I., Aiyar, S., Akinyemiju, T.F., Akseer, N., Lami, F.H.A., Alahdab, F., Al-Aly, Z., Alam, K., Alam, N., Alam, T., Alasfoor, D., Alene, K.A., Ali, R., Alizadeh-Navaei, R., Alkaabi, J.M., Alkerwi, A., Alla, F., Allebeck, P., Allen, C., Al-Maskari, F., AlMazroa, M.A., Al-Raddadi, R., Alsharif, U., Alsowaidi, S., Althouse, B.M., Altirkawi, K.A., Alvis-Guzman, N., Amare, A.T., Amini, E., Ammar, W., Amoako, Y.A., Ansha, M.G., Antonio, C.A.T., Anwari, P., Ärnlöv, J., Arora, M., Artaman, A., Aryal, K.K., Asgedom, S.W., Atey, T.M., Atnafu, N.T., Avila-Burgos, L., Avokpaho, E.F.G.A., Awasthi, A., Awasthi, S., Azarpazhooh, M.R., Azzopardi, P., Babalola, T.K., Bacha, U., Badawi, A., Balakrishnan, K., Bannick, M.S., Barac, A., Barker-Collo, S.L., Bärnighausen, T., Barquera, S., Barrero, L.H., Basu, S., Battista, R., Battle, K.E., Baune, B.T., Bazargan-Hejazi, S., Beardsley, J., Bedi, N., Béjot, Y., Bekele, B.B., Bell, M.L., Bennett, D.A., Bennett, J.R., Bensenor, I.M., Benson, J., Berhane, A., Berhe, D.F., Bernabé, E., Betsu, B.D., Beuran, M., Beyene, A.S., Bhansali, A., Bhatt, S., Bhutta, Z.A., Biadgilign, S., Bicer, B.K., Bienhoff, K., Bikbov, B., Birungi, C., Biryukov, S., Bisanzio, D., Bizuayehu, H.M., Blyth, F.M., Boneya, D.J., Bose, D., Bou-Orm, I.R., Bourne, R.R.A., Brainin, M., Brayne, C., Brazinova, A., Breitborde, N.J.K., Briant, P.S., Britton, G., Brugha, T.S., Buchbinder, R., Bulto, L.N.B., Bumgarner, B.R., Butt, Z.A., Cahuana-Hurtado, L., Cameron, E., Campos-Nonato, I.R., Carabin, H., Cárdenas, R., Carpenter, D.O., Carrero, J.J., Carter, A., Carvalho, F., Casey, D., Castañeda-Orjuela, C.A., Castle, C.D., Catalá-López, F., Chang, J.-C., Charlson, F.J., Chaturvedi, P., Chen, H., Chibalabala, M., Chibueze, C.E., Chisumpa, V.H., Chitheer, A.A., Chowdhury, R., Christopher, D.J., Ciobanu, L.G., Cirillo, M., Colombara, D., Cooper, L.T., Cooper, C., Cortesi, P.A., Cortinovis, M., Criqui, M.H., Cromwell, E.A., Cross, M., Crump, J.A., Dadi, A.F., Dalal, K., Damasceno, A., Dandona, L., Dandona, R., Neves, J. das, Davitoiu, D.V., Davletov, K., Courten, B. de, Leo, D.D., Steur, H.D., Defo, B.K., Degenhardt, L., Deiparine, S., Dellavalle, R.P., Deribe, K., Deribew, A., Jarlais, D.C.D., Dey, S., Dharmaratne, S.D., Dhillon, P.K., Dicker, D., Djalainia, S., Do, H.P., Dokova, K., Doku, D.T., Dorsey, E.R., Santos, K.P.B. dos, Driscoll, T.R., Dubey, M., Duncan, B.B., Ebel, B.E., Echko, M., El-Khatib, Z.Z., Enayati, A., Endries, A.Y., Ermakov, S.P., Erskine, H.E., Eshetie, S., Eshrati, B., Esteghamati, A., Estep, K., Fanuel, F.B.B., Farag, T., Farinha, C.S. e S., Faro, A., Farzadfar, F., Fazeli, M.S., Feigin, V.L., Feigl, A.B., Fereshtehnejad, S.-M., Fernandes, J.C., Ferrari, A.J., Feyissa, T.R., Filip, I., Fischer, F., Fitzmaurice, C., Flaxman, A.D., Foigt, N., Foreman, K.J., Franklin, R.C., Frostad, J.J., Fullman, N., Fürst, T., Furtado, J.M., Futran, N.D., Gakidou, E., Garcia-Basteiro, A.L., Gebre, T., Gebregergs, G.B., Gebrehiwot, T.T., Geleijnse, J.M., Geleto, A., Gemechu, B.L., Gesesew, H.A., Gething, P.W., Ghajar, A., Gibney, K.B., Gillum, R.F., Ginawi, I.A.M., Gishu, M.D., Giussani, G., Godwin, W.W., Goel, K., Goenka, S., Goldberg, E.M., Gona, P.N., Goodridge, A., Gopalani, S.V., Gosselin, R.A., Gotay, C.C., Goto, A., Goulart, A.C., Graetz, N., Gugnani, H.C., Gupta, P.C., Gupta, Rajeev, Gupta, T., Gupta, V., Gupta, Rahul, Gutiérrez, R.A., Hachinski, V., Hafezi-Nejad, N., Hailu, A.D., Hailu, G.B., Hamadeh, R.R., Hamidi, S., Hammami, M., Handal, A.J., Hankey, G.J., Hao, Y., Harb, H.L., Hareri, H.A., Haro, J.M., Harun, K.M., Harvey, J., Hassanvand, M.S., Havmoeller, R., Hay, R.J., Hedayati, M.T., Hendrie, D., Henry, N.J., Heredia-Pi, I.B., Heydarpour, P., Hoek, H.W., Hoffman, H.J., Horino, M., Horita, N., Hosgood, H.D., Hostiuc, S., Hotez, P.J., Hoy, D.G., Htet, A.S., Hu, G., Huang, J.J., Huynh, C., Iburg, K.M., Igumbor, E.U., Ikeda, C., Irvine, C.M.S., Islam, S.M.S., Jacobsen, K.H., Jahanmehr, N., Jakovljevic, M.B., James, P., Jassal, S.K., Javanbakht, M., Jayaraman, S.P., Jeemon, P., Jensen, P.N., Jha, V., Jiang, G., John, D., Johnson, C.O., Johnson, S.C., Jonas, J.B., Jürisson, M., Kabir, Z., Kadel, R., Kahsay, A., Kamal, R., Kar, C., Karam, N.E., Karch, A., Karema, C.K., Karimi, S.M., Karimkhani, C., Kasaeian, A., Kassa, G.M., Kassaw, N.A., Kassebaum, N.J., Kastor, A., Katikireddi, S.V., Kaul, A., Kawakami, N., Keiyoro, P.N., Kemmer, L., Kengne, A.P., Keren, A., Kesavachandran, C.N., Khader, Y.S., Khalil, I.A., Khan, E.A., Khang, Y.-H., Khoja, A.T., Khosravi, A., Khubchandani, J., Kiadaliri, A.A., Kieling, C., Kim, Y.J., Kim, D., Kimokoti, R.W., Kinfu, Y., Kisa, A., Kissimova-Skarbek, K.A., Kissoon, N., Kivimaki, M., Knudsen, A.K., Kokubo, Y., Kolte, D., Kopec, J.A., Kosen, S., Kotsakis, G.A., Koul, P.A., Koyanagi, A., Kravchenko, M., Krohn, K.J., Kumar, G.A., Kumar, P., Kyu, H.H., Lager, A.C.J., Lal, D.K., Lalloo, R., Lallukka, T., Lambert, N., Lan, Q., Lansingh, V.C., Larsson, A., Leasher, J.L., Lee, P.H., Leigh, J., Leshargie, C.T., Leung, J., Leung, R., Levi, M., Li, Yichong, Li, Yongmei, Liang, X., Liben, M.L., Lim, S.S., Linn, S., Liu, P.Y., Liu, A., Liu, S., Liu, Y., Lodha, R., Logroscino, G., Looker, K.J., Lopez, A.D., Lorkowski, S., Lotufo, P.A., Lozano, R., Lucas, T.C.D., Lunevicius, R., Lyons, R.A., Macarayan, E.R.K., Maddison, E.R., Razek, H.M.A.M.A.E., Razek, M.M.A.E., Magis-Rodriguez, C., Mahdavi, M., Majdan, M., Majdzadeh, R., Majeed, A., Malekzadeh, R., Malhotra, R., Malta, D.C., Mamun, A.A., Manguerra, H., Manhertz, T., Mantovani, L.G., Mapoma, C.C., March, L.M., Marczak, L.B., Martinez-Raga, J., Martins, P.H.V., Martins-Melo, F.R., Martopullo, I., März, W., Mathur, M.R., Mazidi, M., McAlinden, C., McGaughey, M., McGrath, J.J., McKee, M., Mehata, S., Meier, T., Meles, K.G., Memiah, P., Memish, Z.A., Mendoza, W., Mengesha, M.M., Mengistie, M.A., Mengistu, D.T., Mensah, G.A., Meretoja, T.J., Meretoja, A., Mezgebe, H.B., Micha, R., Millear, A., Miller, T.R., Minnig, S., Mirarefin, M., Mirrakhimov, E.M., Misganaw, A., Mishra, S.R., Mitchell, P.B., Mohammad, K.A., Mohammadi, A., Mohammed, M.S.K., Mohammed, K.E., Mohammed, S., Mohan, M.B.V., Mokdad, A.H., Mollenkopf, S.K., Monasta, L., Hernandez, J.C.M., Montico, M., Moradi-Lakeh, M., Moraga, P., Morawska, L., Mori, R., Morrison, S.D., Moses, M., Mountjoy-Venning, C., Mruts, K.B., Mueller, U.O., Muller, K., Murdoch, M.E., Murthy, G.V.S., Murthy, S., Musa, K.I., Nachega, J.B., Nagel, G., Naghavi, M., Naheed, A., Naidoo, K.S., Nangia, V., Nasher, J.T., Natarajan, G., Negasa, D.E., Negoi, R.I., Negoi, I., Newton, C.R., Ngunjiri, J.W., Nguyen, C.T., Nguyen, Q.L., Nguyen, T.H., Nguyen, G., Nguyen, M., Nichols, E., Ningrum, D.N.A., Nong, V.M., Norheim, O.F., Norrving, B., Noubiap, J.J.N., Nyandwi, A., Obermeyer, C.M., O'Donnell, M.J., Ogbo, F.A., Oh, I.-H., Okoro, A., Oladimeji, O., Olagunju, A.T., Olagunju, T.O., Olsen, H.E., Olusanya, B.O., Olusanya, J.O., Ong, K., Opio, J.N., Oren, E., Ortiz, A., Osborne, R.H., Osgood-Zimmerman, A., Osman, M., Ota, E., Owolabi, M.O., Pa, M., Pacella, R.E., Panda, B.K., Pandian, J.D., Papachristou, C., Park, E.-K., Parry, C.D., Parsaeian, M., Patil, S.T., Patten, S.B., Patton, G.C., Paudel, D., Paulson, K., Pearce, N., Pereira, D.M., Perez, K.M., Perico, N., Pesudovs, K., Peterson, C.B., Petri, W.A., Petzold, M., Phillips, M.R., Phipps, G., Pigott, D.M., Pillay, J.D., Pinho, C., Piradov, M.A., Plass, D., Pletcher, M.A., Popova, S., Poulton, R.G., Pourmalek, F., Prabhakaran, D., Prasad, N., Purcell, C., Purwar, M., Qorbani, M., Quintanilla, B.P.A., Rabiee, R.H.S., Radfar, A., Rafay, A., Rahimi, K., Rahimi-Movaghar, A., Rahimi-Movaghar, V., Rahman, M.H.U., Rahman, M.A., Rahman, M., Rai, R.K., Rajsic, S., Ram, U., Ranabhat, C.L., Rangaswamy, T., Rankin, Z., Rao, P.V., Rao, P.C., Rawaf, S., Ray, S.E., Reiner, R.C., Reinig, N., Reitsma, M., Remuzzi, G., Renzaho, A.M.N., Resnikoff, S., Rezaei, S., Ribeiro, A.L., Rivas, J.C., Roba, H.S., Robinson, S.R., Rojas-Rueda, D., Rokni, M.B., Ronfani, L., Roshandel, G., Roth, G.A., Rothenbacher, D., Roy, A., Rubagotti, E., Ruhago, G.M., Saadat, S., Safdarian, M., Safiri, S., Sagar, R., Sahathevan, R., Sahraian, M.A., Salama, J., Saleh, M.M., Salomon, J.A., Salvi, S.S., Samy, A.M., Sanabria, J.R., Sanchez-Niño, M.D., Santomauro, D., Santos, J.V., Santos, I.S., Milicevic, M.M.S., Sartorius, B., Satpathy, M., Sawhney, M., Saxena, S., Schelonka, K., Schmidt, M.I., Schneider, I.J.C., Schöttker, B., Schutte, A.E., Schwebel, D.C., Schwendicke, F., Seedat, S., Sepanlou, S.G., Servan-Mori, E.E., Shaheen, A., Shaikh, M.A., Shamsipour, M., Sharma, R., Sharma, J., She, J., Shi, P., Shibuya, K., Shields, C., Shifa, G.T., Shiferaw, M.S., Shigematsu, M., Shiri, R., Shirkoohi, R., Shirude, S., Shishani, K., Shoman, H., Siabani, S., Sibai, A.M., Sigfusdottir, I.D., Silberberg, D.H., Silva, D.A.S., Silva, J.P., Silveira, D.G.A., Singh, J.A., Singh, O.P., Singh, N.P., Singh, V., Sinha, D.N., Skiadaresi, E., Slepak, E.L., Smith, D.L., Smith, M., Sobaih, B.H.A., Sobngwi, E., Soljak, M., Sorensen, R.J.D., Sousa, T.C.M., Sposato, L.A., Sreeramareddy, C.T., Srinivasan, V., Stanaway, J.D., Stathopoulou, V., Steel, N., Stein, D.J., Steiner, C., Steinke, S., Stokes, M.A., Stovner, L.J., Strub, B., Subart, M., Sufiyan, M.B., Sunguya, B.F., Sur, P.J., Swaminathan, S., Sykes, B.L., Sylte, D., Szoeke, C.E.I., Tabarés-Seisdedos, R., Tadakamadla, S.K., Taffere, G.R., Takala, J.S., Tandon, N., Tanne, D., Tarekegn, Y.L., Tavakkoli, M., Taveira, N., Taylor, H.R., Tegegne, T.K., Tehrani-Banihashemi, A., Tekelab, T., Terkawi, A.S., Tesfaye, D.J., Tesssema, B., Thakur, J.S., Thamsuwan, O., Theadom, A.M., Theis, A.M., Thomas, K.E., Thomas, N., Thompson, R., Thrift, A.G., Tobe-Gai, R., Tobollik, M., Tonelli, M., Topor-Madry, R., Tortajada, M., Touvier, M., Traebert, J., Tran, B.X., Troeger, C., Truelsen, T., Tsoi, D., Tuzcu, E.M., Tymeson, H., Tyrovolas, S., Ukwaja, K.N., Undurraga, E.A., Uneke, C.J., Updike, R., Uthman, O.A., Uzochukwu, B.S.C., Boven, J.F.M. van, Varughese, S., Vasankari, T., Veerman, L.J., Venkatesh, S., Venketasubramanian, N., Vidavalur, R., Vijayakumar, L., Violante, F.S., Vishnu, A., Vladimirov, S.K., Vlassov, V.V., Vollset, S.E., Vos, T., Wadilo, F., Wakayo, T., Wallin, M.T., Wang, Y.-P., Weichenthal, S., Weiderpass, E., Weintraub, R.G., Weiss, D.J., Werdecker, A., Westerman, R., Whiteford, H.A., Wijeratne, T., Williams, H.C., Wiysonge, C.S., Woldeyes, B.G., Wolfe, C.D.A., Woodbrook, R., Woolf, A.D., Workicho, A., Xavier, D., Xu, G., Yadgir, S., Yaghoubi, M., Yakob, B., Yan, L.L., Yano, Y., Ye, P., Yihdego, M.G., Yimam, H.H., Yip, P., Yonemoto, N., Yoon, S.-J., Yotebieng, M., Younis, M.Z., Yu, C., Zaidi, Z., Zaki, M.E.S., Zegeye, E.A., Zenebe, Z.M., Zhang, X., Zheng, Y., Zhou, M., Zipkin, B., Zodpey, S., Zoeckler, L., Zuhlke, L.J., Murray, C.J.L., 2017. Global, regional, and national disability-adjusted life-years (DALYs) for 333 diseases and injuries and healthy life expectancy (HALE) for 195 countries and territories, 1990–2016: a systematic analysis for the Global Burden of Disease Study 2016. The Lancet 390, 1260–1344. https://doi.org/10.1016/S0140-6736(17)32130-X

Heinicke, E., Kumar, U., Munoz, D.G., 1992. Quantitative dot-blot assay for proteins using enhanced chemiluminescence. Journal of Immunological Methods 152, 227–236. https://doi.org/10.1016/0022-1759(92)90144-I

Henriques, S.T., Deplazes, E., Lawrence, N., Cheneval, O., Chaousis, S., Inserra, M., Thongyoo, P., King, G.F., Mark, A.E., Vetter, I., Craik, D.J., Schroeder, C.I., 2016. Interaction of Tarantula Venom Peptide ProTx-II with Lipid Membranes Is a Prerequisite for Its Inhibition of Human Voltage-gated Sodium Channel NaV1.7 *. Journal of Biological Chemistry 291, 17049–17065. https://doi.org/10.1074/jbc.M116.729095

Héron, J., Balcells, D., 2022. Concerted Cycloaddition Mechanism in the CuAAC Reaction Catalyzed by 1,8-Naphthyridine Dicopper Complexes. ACS Catal. 12, 4744–4753. https://doi.org/10.1021/acscatal.2c00723

Herzig, V., 2019. Arthropod assassins: Crawling biochemists with diverse toxin pharmacopeias. Toxicon 158, 33–37. https://doi.org/10.1016/j.toxicon.2018.11.312

Hill, C.L., Stephens, G.J., 2021. An Introduction to Patch Clamp Recording, in: Dallas, M., Bell, D. (Eds.), Patch Clamp Electrophysiology: Methods and Protocols. Springer US, New York, NY, pp. 1–19. https://doi.org/10.1007/978-1-0716-0818-0_1

Hill, J.M., Alewood, P.F., Craik, D.J., 1997. Solution structure of the sodium channel antagonist conotoxin GS: a new molecular caliper for probing sodium channel geometry. Structure 5, 571–583. https://doi.org/10.1016/S0969-2126(97)00212-8

Hill, R., 2000. NK1 (substance P) receptor antagonists – why are they not analgesic in humans? Trends in Pharmacological Sciences 21, 244–246. https://doi.org/10.1016/S0165-6147(00)01502-9

Hodgkin, A.L., Huxley, A.F., 1952. Currents carried by sodium and potassium ions through the membrane of the giant axon of Loligo. J Physiol 116, 449–472.

Holmes, A., Christelis, N., Arnold, C., 2013. Depression and chronic pain. Med J Aust 199, S17–S20. https://doi.org/10.5694/mja12.10589

Hudson, D., 1999. Matrix Assisted Synthetic Transformations: A Mosaic of Diverse Contributions. I. The Pattern Emerges. J. Comb. Chem. 1, 333–360. https://doi.org/10.1021/cc990022l

Hui, K., Lipkind, G., Fozzard, H.A., French, R.J., 2002. Electrostatic and Steric Contributions to Block of the Skeletal Muscle Sodium Channel by μ-Conotoxin. Journal of General Physiology 119, 45–54. https://doi.org/10.1085/jgp.119.1.45

Isidro-Llobet, A., Álvarez, M., Albericio, F., 2009. Amino Acid-Protecting Groups. Chem. Rev. 109, 2455–2504. https://doi.org/10.1021/cr800323s

Isom, L.L., 2002. The role of sodium channels in cell adhesion. FBL 7, 12–23. https://doi.org/10.2741/isom

Isom, L.L., 2000. I. Cellular and molecular biology of sodium channel β-subunits: therapeutic implications for pain? American Journal of Physiology-Gastrointestinal and Liver Physiology 278, G349–G353. https://doi.org/10.1152/ajpgi.2000.278.3.G349

Israel, M.R., Tay, B., Deuis, J.R., Vetter, I., 2017. Chapter Three - Sodium Channels and Venom Peptide Pharmacology, in: Geraghty, D.P., Rash, L.D. (Eds.), Advances in Pharmacology, Ion Channels DownUnder. Academic Press, pp. 67–116. https://doi.org/10.1016/bs.apha.2017.01.004

Jackson, H., Parks, T.N., 1989. Spider toxins: recent applications in neurobiology.

Jaradat, D.M.M., 2018. Thirteen decades of peptide synthesis: key developments in solid phase peptide synthesis and amide bond formation utilized in peptide ligation. Amino Acids 50, 39–68. https://doi.org/10.1007/s00726-017-2516-0

Jian, X., Wu, Y., Mei, Z., Zhu, X., Zhangsun, D., Luo, S., 2023. Synthesis of the Most Potent Isomer of μ-Conotoxin KIIIA Using Different Strategies. Molecules 28, 3377. https://doi.org/10.3390/molecules28083377

Jiang, D., Tonggu, L., Gamal El-Din, T.M., Banh, R., Pomès, R., Zheng, N., Catterall, W.A., 2021. Structural basis for voltage-sensor trapping of the cardiac sodium channel by a deathstalker scorpion toxin. Nat Commun 12, 128. https://doi.org/10.1038/s41467-020-20078-3

Jin, A.-H., Muttenthaler, M., Dutertre, S., Himaya, S.W.A., Kaas, Q., Craik, D.J., Lewis, R.J., Alewood, P.F., 2019. Conotoxins: Chemistry and Biology. Chem. Rev. 119, 11510–11549. https://doi.org/10.1021/acs.chemrev.9b00207

Johnson, T., Quibell, M., Owen, D., Sheppard, R.C., 1993. A reversible protecting group for the amide bond in peptides. Use in the synthesis of 'difficult sequences.' J. Chem. Soc., Chem. Commun. 369–372. https://doi.org/10.1039/C39930000369

Johnson, T., Quibell, M., Sheppard, R.C., 1995. N,O-bisFmoc derivatives of N-(2-hydroxy-4-methoxybenzyl)-amino acids: Useful intermediates in peptide synthesis. Journal of Peptide Science 1, 11–25. https://doi.org/10.1002/psc.310010104

Jonathan, M., Collins, M.J., Collins, R.C., 2003. Novel Method for Solid Phase Peptide Synthesis Using Microwave Energy. CEM Publishing, Matthews, North Carolina.

Jung, H.H., Jung, H.J., Milescu, M., Lee, C.W., Lee, S., Lee, J.Y., Eu, Y.-J., Kim, H.H., Swartz, K.J., Kim, J.I., 2010. Structure and Orientation of a Voltage-Sensor Toxin in Lipid Membranes. Biophysical Journal 99, 638–646. https://doi.org/10.1016/j.bpj.2010.04.061

Kaas, Q., Westermann, J.-C., Craik, D.J., 2010. Conopeptide characterization and classifications: an analysis using ConoServer. Toxicon 55, 1491–1509. https://doi.org/10.1016/j.toxicon.2010.03.002

Kalia, J., Milescu, M., Salvatierra, J., Wagner, J., Klint, J.K., King, G.F., Olivera, B.M., Bosmans, F., 2015. From Foe to Friend: Using Animal Toxins to Investigate Ion Channel Function. Journal of Molecular Biology, Understanding Functions and Mechanisms of Ion Channels 427, 158–175. https://doi.org/10.1016/j.jmb.2014.07.027

Kam, A., Loo, S., Qiu, Y., Liu, C.-F., Tam, J.P., 2024. Ultrafast Biomimetic Oxidative Folding of Cysteine-rich Peptides and Microproteins in Organic Solvents. Angewandte Chemie International Edition 63, e202317789. https://doi.org/10.1002/anie.202317789

Karlström, A., Undén, A., 1996. A new protecting group for aspartic acid that minimizes piperidine-catalyzed aspartimide formation in Fmoc solid phase peptide synthesis. Tetrahedron Letters 37, 4243–4246. https://doi.org/10.1016/0040-4039(96)00807-6

Kauzmann, W., 1959. II. 2 - RELATIVE PROBABILITIES OF ISOMERS IN CYSTINE-CONTAINING RANDOMLY COILED POLYPEPTIDES, in: Benesch, R., Benesch, R.E., Boyer, P.D., Klotz, I.M., Middlebrook, W.R., Szent-györgyi, A.G., Schwarz, D.R. (Eds.), Sulfur in Proteins. Academic Press, pp. 93–108. https://doi.org/10.1016/B978-0-12-395705-4.50013-2

Kent, S.B.H., 1988. CHEMICAL SYNTHESIS OF PEPTIDES AND PROTEINS. Annual Review of Biochemistry 57, 957–989. https://doi.org/10.1146/annurev.bi.57.070188.004521

Khoo, K.K., Feng, Z.-P., Smith, B.J., Zhang, M.-M., Yoshikami, D., Olivera, B.M., Bulaj, G., Norton, R.S., 2009. Structure of the Analgesic μ-Conotoxin KIIIA and Effects on the Structure and Function of Disulfide Deletion. Biochemistry 48, 1210–1219. https://doi.org/10.1021/bi801998a

Khoo, K.K., Gupta, K., Green, B.R., Zhang, M.-M., Watkins, M., Olivera, B.M., Balaram, P., Yoshikami, D., Bulaj, G., Norton, R.S., 2012. Distinct Disulfide Isomers of μ-Conotoxins KIIIA and KIIIB Block Voltage-Gated Sodium Channels. Biochemistry 51, 9826–9835. https://doi.org/10.1021/bi301256s

King, G.F. (Ed.), 2015. Venoms to Drugs: Venom as a Source for the Development of Human Therapeutics, Drug Discovery. Royal Society of Chemistry, Cambridge. https://doi.org/10.1039/9781849737876

King, G.F., 2011. Venoms as a platform for human drugs: translating toxins into therapeutics. Expert Opin Biol Ther 11, 1469–1484. https://doi.org/10.1517/14712598.2011.621940

King, G.F., Escoubas, P., Nicholson, G.M., 2008a. Peptide toxins that selectively target insect NaV and CaV channels. Channels 2, 100–116. https://doi.org/10.4161/chan.2.2.6022

King, G.F., Gentz, M.C., Escoubas, P., Nicholson, G.M., 2008b. A rational nomenclature for naming peptide toxins from spiders and other venomous animals. Toxicon 52, 264–276. https://doi.org/10.1016/j.toxicon.2008.05.020

King, G.F., Hardy, M.C., 2013. Spider-Venom Peptides: Structure, Pharmacology, and Potential for Control of Insect Pests. Annual Review of Entomology 58, 475–496. https://doi.org/10.1146/annurev-ento-120811-153650

Klint, J.K., Senff, S., Rupasinghe, D.B., Er, S.Y., Herzig, V., Nicholson, G.M., King, G.F., 2012. Spider-venom peptides that target voltage-gated sodium channels: Pharmacological tools and potential therapeutic leads. Toxicon, Advancing in Basic and Translational Venomics 60, 478–491. https://doi.org/10.1016/j.toxicon.2012.04.337

Kolb, H.C., Finn, M.G., Sharpless, K.B., 2001. Click Chemistry: Diverse Chemical Function from a Few Good Reactions. Angewandte Chemie International Edition 40, 2004–2021. https://doi.org/10.1002/1521-3773(20010601)40:11<2004::AID-ANIE2004>3.0.CO;2-5

Kolb, H.C., Sharpless, K.B., 2003. The growing impact of click chemistry on drug discovery. Drug Discov Today 8, 1128–1137. https://doi.org/10.1016/s1359-6446(03)02933-7

Kolmar, H., 2008. Alternative binding proteins: Biological activity and therapeutic potential of cystine-knot miniproteins. The FEBS Journal 275, 2684–2690. https://doi.org/10.1111/j.1742-4658.2008.06440.x

König, W., Geiger, R., 1970. Eine neue Methode zur Synthese von Peptiden: Aktivierung der Carboxylgruppe mit Dicyclohexylcarbodiimid unter Zusatz von 1-Hydroxy-benzotriazolen. Chemische Berichte 103, 788–798. https://doi.org/10.1002/cber.19701030319

Kotecha, M., Cheshire, W.P., Finnigan, H., Giblin, K., Naik, H., Palmer, J., Tate, S., Zakrzewska, J.M., 2020. Design of Phase 3 Studies Evaluating Vixotrigine for Treatment of Trigeminal Neuralgia. Journal of Pain Research 13, 1601–1609. https://doi.org/10.2147/JPR.S247182

Kozlov, S., 2018. Animal toxins for channelopathy treatment. Neuropharmacology, Channelopathies 132, 83–97. https://doi.org/10.1016/j.neuropharm.2017.10.031

Kremsmayr, T., Muttenthaler, M., 2022. Fmoc Solid Phase Peptide Synthesis of Oxytocin and Analogues. Methods Mol Biol 2384, 175–199. https://doi.org/10.1007/978-1-0716-1759-5_11

Kuhn-Nentwig, L., Stöcklin, R., Nentwig, W., 2011. Venom Composition and Strategies in Spiders: Is Everything Possible?☆☆Dedicated to Prof. Dr. Lev G. Magazanik, Sechenov Institute of Evolutionary Physiology and Biochemistry, RAS, St. Petersburg, Russia, at the occasion of his 80th anniversary., in: Casas, J. (Ed.), Advances in Insect Physiology, Spider Physiology and Behaviour. Academic Press, pp. 1–86. https://doi.org/10.1016/B978-0-12-387668-3.00001-5

Kumari, S., Carmona, A.V., Tiwari, A.K., Trippier, P.C., 2020. Amide Bond Bioisosteres: Strategies, Synthesis, and Successes. J. Med. Chem. 63, 12290–12358. https://doi.org/10.1021/acs.jmedchem.0c00530

Kurreck, J., Engels, J.W., Lottspeich, F. (Eds.), 2022. Bioanalytik. Springer, Berlin, Heidelberg. https://doi.org/10.1007/978-3-662-61707-6

Langenegger, N., Nentwig, W., Kuhn-Nentwig, L., 2019. Spider Venom: Components, Modes of Action, and Novel Strategies in Transcriptomic and Proteomic Analyses. Toxins 11, 611. https://doi.org/10.3390/toxins11100611

Laps, S., Metanis, N., 2024. Organic solvent enhances oxidative folding of disulfide-rich proteins. Nat. Chem. 16, 680–681. https://doi.org/10.1038/s41557-024-01518-9

Lau, C.H.Y., King, G.F., Mobli, M., 2016. Molecular basis of the interaction between gating modifier spider toxins and the voltage sensor of voltage-gated ion channels. Sci Rep 6, 34333. https://doi.org/10.1038/srep34333

Lavergne, V., Alewood, P.F., Mobli, M., King, G.F., 2015. CHAPTER 2. The Structural Universe of Disulfide-Rich Venom Peptides, in: King, G.F. (Ed.), Drug Discovery. Royal Society of Chemistry, Cambridge, pp. 37–79. https://doi.org/10.1039/9781849737876-00037

Li, X., 2011. Click to Join Peptides/Proteins Together. Chemistry – An Asian Journal 6, 2606–2616. https://doi.org/10.1002/asia.201100329

Liu, Y., Wu, Z., Tang, D., Xun, X., Liu, L., Li, X., Nie, D., Xiang, Y., Yi, Jianming, Yi, Jizu, 2014. Analgesic effects of Huwentoxin-IV on animal models of inflammatory and neuropathic pain. Protein Pept Lett 21, 153–158. https://doi.org/10.2174/09298665113206660119

Loughney, K., Kreber, R., Ganetzky, B., 1989. Molecular analysis of the para locus, a sodium channel gene in Drosophila. Cell 58, 1143–1154. https://doi.org/10.1016/0092-8674(89)90512-6

Loya-López, S.I., Duran, P., Ran, D., Calderon-Rivera, A., Gomez, K., Moutal, A., Khanna, R., 2022. Cell specific regulation of NaV1.7 activity and trafficking in rat nodose ganglia neurons. Neurobiology of Pain 12, 100109. https://doi.org/10.1016/j.ynpai.2022.100109

Lüddecke, T., Herzig, V., von Reumont, B.M., Vilcinskas, A., 2022. The biology and evolution of spider venoms. Biological Reviews 97, 163–178. https://doi.org/10.1111/brv.12793

MacKinnon, R., Miller, C., 1988. Mechanism of charybdotoxin block of the high-conductance, Ca2+-activated K+ channel. J Gen Physiol 91, 335–349. https://doi.org/10.1085/jgp.91.3.335

Manchikanti, L., Helm, S., Fellows, B., Janata, J.W., Pampati, V., Grider, J.S., Boswell, M.V., 2012. Opioid epidemic in the United States. Pain Physician 15, ES9-38.

Manne, S.R., Sharma, A., Sazonovas, A., El-Faham, A., de la Torre, B.G., Albericio, F., 2022. Understanding OxymaPure as a Peptide Coupling Additive: A Guide to New Oxyma Derivatives. ACS Omega 7, 6007–6023. https://doi.org/10.1021/acsomega.1c06342

Mant, C.T., Hodges, R.S. (Eds.), 2019. High-Performance Liquid Chromatography of Peptides and Proteins: Separation, Analysis, and Conformation. CRC Press, Boca Raton. https://doi.org/10.1201/9780203751947

Mantegazza, M., Curia, G., Biagini, G., Ragsdale, D.S., Avoli, M., 2010. Voltage-gated sodium channels as therapeutic targets in epilepsy and other neurological disorders. The Lancet Neurology 9, 413–424. https://doi.org/10.1016/S1474-4422(10)70059-4

Mao, H., Hart, S.A., Schink, A., Pollok, B.A., 2004. Sortase-Mediated Protein Ligation: A New Method for Protein Engineering. J. Am. Chem. Soc. 126, 2670–2671. https://doi.org/10.1021/ja039915e

Marder, O., Shvo, Y., Albericio, F., 2003. HCTU and TCTU: New Coupling Reagents — Development and Industrial Aspects. ChemInform 34. https://doi.org/10.1002/chin.200332258

Marglin, B., Merrifield, R.B., 1966. The Synthesis of Bovine Insulin by the Solid Phase Method1. J. Am. Chem. Soc. 88, 5051–5052. https://doi.org/10.1021/ja00973a068

Masoodi, K.Z., Lone, S.M., Rasool, R.S., 2021. Chapter 21 - Dot blot analysis, in: Masoodi, K.Z., Lone, S.M., Rasool, R.S. (Eds.), Advanced Methods in Molecular Biology and Biotechnology. Academic Press, pp. 123–125. https://doi.org/10.1016/B978-0-12-824449-4.00021-9

Mathes, C., 2006. QPatch: the past, present and future of automated patch clamp. Expert Opinion on Therapeutic Targets 10, 319–327. https://doi.org/10.1517/14728222.10.2.319

McCullagh, J., Oldham, N., 2019. Mass Spectrometry (Oxford Chemistry Primers). Oxford University Press.

McDonnell, A., Collins, S., Ali, Z., Iavarone, L., Surujbally, R., Kirby, S., Butt, R.P., 2018. Efficacy of the Nav1.7 blocker PF-05089771 in a randomised, placebo-controlled, double-blind clinical study in subjects with painful diabetic peripheral neuropathy. PAIN 159, 1465. https://doi.org/10.1097/j.pain.0000000000001227

McKay, F.C., Albertson, N.F., 1957. New Amine-masking Groups for Peptide Synthesis. J. Am. Chem. Soc. 79, 4686–4690. https://doi.org/10.1021/ja01574a029

Merrifield, R.B., 1965. Automated Synthesis of Peptides. Science 150, 178–185. https://doi.org/10.1126/science.150.3693.178

Merrifield, R.B., 1963. Solid Phase Peptide Synthesis. I. The Synthesis of a Tetrapeptide. J. Am. Chem. Soc. 85, 2149–2154. https://doi.org/10.1021/ja00897a025

Milescu, M., Vobecky, J., Roh, S.H., Kim, S.H., Jung, H.J., Kim, J.I., Swartz, K.J., 2007. Tarantula Toxins Interact with Voltage Sensors within Lipid Membranes. J Gen Physiol 130, 497–511. https://doi.org/10.1085/jgp.200709869

Minassian, N.A., Gibbs, A., Shih, A.Y., Liu, Y., Neff, R.A., Sutton, S.W., Mirzadegan, T., Connor, J., Fellows, R., Husovsky, M., Nelson, S., Hunter, M.J., Flinspach, M., Wickenden, A.D., 2013. Analysis of the Structural and Molecular Basis of Voltage-sensitive Sodium Channel Inhibition by the Spider Toxin Huwentoxin-IV (μ-TRTX-Hh2a). Journal of Biological Chemistry 288, 22707–22720. https://doi.org/10.1074/jbc.M113.461392

Mirza, U.A., Chait, B.T., 1994. Effects of Anions on the Positive Ion Electrospray Ionization Mass Spectra of Peptides and Proteins. Anal. Chem. 66, 2898–2904. https://doi.org/10.1021/ac00090a017

Mishra, V., 2022. Dot-blotting: A quick method for expression analysis of recombinant proteins. Curr Protoc 2, e546. https://doi.org/10.1002/cpz1.546

Mogil, J.S., 2009. Animal models of pain: progress and challenges. Nat Rev Neurosci 10, 283–294. https://doi.org/10.1038/nrn2606

Molleman, A., 2003. Patch Clamping: An Introductory Guide to Patch Clamp Electrophysiology. John Wiley & Sons.

Morgenstern, D., King, G.F., 2013. The venom optimization hypothesis revisited. Toxicon 63, 120–128. https://doi.org/10.1016/j.toxicon.2012.11.022

Moutal, A., Cai, S., Yu, J., Stratton, H.J., Chefdeville, A., Gomez, K., Ran, D., Madura, C.L., Boinon, L., Soto, M., Zhou, Y., Shan, Z., Chew, L.A., Rodgers, K.E., Khanna, R., 2020. Studies on CRMP2 SUMOylation–deficient transgenic mice identify sex-specific Nav1.7 regulation in the pathogenesis of chronic neuropathic pain. PAIN 161, 2629. https://doi.org/10.1097/j.pain.0000000000001951

Mueller, A., 2020. Engineering an optimized analgesic from the NaV1.7 selective spider venom peptide Pn3a (PhD Thesis). The University of Queensland. https://doi.org/10.14264/da5597e

Mueller, A., Dekan, Z., Kaas, Q., Agwa, A.J., Starobova, H., Alewood, P.F., Schroeder, C.I., Mobli, M., Deuis, J.R., Vetter, I., 2020. Mapping the Molecular Surface of the Analgesic NaV1.7-Selective Peptide Pn3a Reveals Residues Essential for Membrane and Channel Interactions. ACS Pharmacol. Transl. Sci. 3, 535–546. https://doi.org/10.1021/acsptsci.0c00002

Mueller, A., Starobova, H., Morgan, M., Dekan, Z., Cheneval, O., Schroeder, C.I., Alewood, P.F., Deuis, J.R., Vetter, I., 2019. Antiallodynic effects of the selective NaV1.7 inhibitor Pn3a in a mouse model of acute postsurgical pain: evidence for analgesic synergy with opioids and baclofen. Pain 160, 1766–1780. https://doi.org/10.1097/j.pain.0000000000001567

Mulcahy, J.V., Pajouhesh, H., Beckley, J.T., Delwig, A., Du Bois, J., Hunter, J.C., 2019. Challenges and Opportunities for Therapeutics Targeting the Voltage-Gated Sodium Channel Isoform NaV1.7. J. Med. Chem. 62, 8695–8710. https://doi.org/10.1021/acs.jmedchem.8b01906

Munson, M.C., Garcia-Echeverria, C., Albericio, F., Barany, G., 1992. S-2,4,6-trimethoxybenzyl (Tmob): a novel cysteine protecting group for the N.alpha.-(9-fluorenylmethoxycarbonyl) (Fmoc) strategy of peptide synthesis. J. Org. Chem. 57, 3013–3018. https://doi.org/10.1021/jo00037a013

Murray, J.K., Aral, J., Miranda, L.P., 2011. Solid-Phase Peptide Synthesis Using Microwave Irradiation, in: Satyanarayanajois, S.D. (Ed.), Drug Design and Discovery, Methods in Molecular Biology. Humana Press, Totowa, NJ, pp. 73–88. https://doi.org/10.1007/978-1-61779-012-6_5

Muttenthaler, M., King, G.F., Adams, D.J., Alewood, P.F., 2021. Trends in peptide drug discovery. Nat Rev Drug Discov 20, 309–325. https://doi.org/10.1038/s41573-020-00135-8

Narahashi, T., 1974. Chemicals as tools in the study of excitable membranes. Physiological Reviews 54, 813–889. https://doi.org/10.1152/physrev.1974.54.4.813

Neff, R.A., Wickenden, A.D., 2021. Selective Targeting of Nav1.7 with Engineered Spider Venom-Based Peptides. Channels 15, 193–207. https://doi.org/10.1080/19336950.2020.1860382

Neher, E., Sakmann, B., 1976. Noise analysis of drug induced voltage clamp currents in denervated frog muscle fibres. J Physiol 258, 705–729. https://doi.org/10.1113/jphysiol.1976.sp011442

Neher, E., Sakmann, B., Steinbach, J.H., 1978. The extracellular patch clamp: a method for resolving currents through individual open channels in biological membranes. Pflugers Arch 375, 219–228. https://doi.org/10.1007/BF00584247

Nelsen, D.R., Nisani, Z., Cooper, A.M., Fox, G.A., Gren, E.C.K., Corbit, A.G., Hayes, W.K., 2014. Poisons, toxungens, and venoms: redefining and classifying toxic biological secretions and the organisms that employ them. Biological Reviews 89, 450–465. https://doi.org/10.1111/brv.12062

NMBE - World Spider Catalog [WWW Document], 2024. URL https://wsc.nmbe.ch/statistics/ (accessed 7.18.24).

Noda, M., Ikeda, T., Suzuki, H., Takeshima, H., Takahashi, T., Kuno, M., Numa, S., 1986. Expression of functional sodium channels from cloned cDNA. Nature 322, 826–828. https://doi.org/10.1038/322826a0

Norton, R.S., 2010. μ-Conotoxins as Leads in the Development of New Analgesics. Molecules 15, 2825–2844. https://doi.org/10.3390/molecules15042825

Nugrahadi, P.P., Hinrichs, W.L.J., Frijlink, H.W., Schöneich, C., Avanti, C., 2023. Designing Formulation Strategies for Enhanced Stability of Therapeutic Peptides in Aqueous Solutions: A Review. Pharmaceutics 15, 935. https://doi.org/10.3390/pharmaceutics15030935

Nyffeler, M., 1999. Prey Selection of Spiders in the Field. The Journal of Arachnology 27, 317–324.

Nyffeler, M., Birkhofer, K., 2017. An estimated 400–800 million tons of prey are annually killed by the global spider community. Sci Nat 104, 30. https://doi.org/10.1007/s00114-017-1440-1

Obergrussberger, A., Friis, S., Brüggemann, A., Fertig, N., 2021. Automated patch clamp in drug discovery: major breakthroughs and innovation in the last decade. Expert Opinion on Drug Discovery 16, 1–5. https://doi.org/10.1080/17460441.2020.1791079

O’Ferrall, R.A.M., Slae, S., 1970. β-Elimination of 9-fluorenylmethanol in aqueous solution: an E1cB mechanism. J. Chem. Soc. B 260–268. https://doi.org/10.1039/J29700000260

Ohnishi, S., Kamikubo, H., Onitsuka, M., Kataoka, M., Shortle, D., 2006. Conformational Preference of Polyglycine in Solution to Elongated Structure. J. Am. Chem. Soc. 128, 16338–16344. https://doi.org/10.1021/ja066008b

Okumura, M., Saiki, M., Yamaguchi, H., Hidaka, Y., 2011. Acceleration of disulfide-coupled protein folding using glutathione derivatives. The FEBS Journal 278, 1137–1144. https://doi.org/10.1111/j.1742-4658.2011.08039.x

Olivera, B.M., McIntosh, J.M., Cruz, L.J., Luque, F.A., Gray, W.R., 1984. Purification and sequence of a presynaptic peptide toxin from Conus geographus venom. Biochemistry 23, 5087–5090. https://doi.org/10.1021/bi00317a001

Osteen, J.D., Herzig, V., Gilchrist, J., Emrick, J.J., Zhang, C., Wang, X., Castro, J., Garcia-Caraballo, S., Grundy, L., Rychkov, G.Y., Weyer, A.D., Dekan, Z., Undheim, E.A.B., Alewood, P., Stucky, C.L., Brierley, S.M., Basbaum, A.I., Bosmans, F., King, G.F., Julius, D., 2016. Selective spider toxins reveal a role for the Nav1.1 channel in mechanical pain. Nature 534, 494–499. https://doi.org/10.1038/nature17976

Pallaghy, P.K., Norton, R.S., Nielsen, K.J., Craik, D.J., 1994. A common structural motif incorporating a cystine knot and a triple-stranded β-sheet in toxic and inhibitory polypeptides. Protein Science 3, 1833–1839. https://doi.org/10.1002/pro.5560031022

Pan, X., Li, Z., Huang, X., Huang, G., Gao, S., Shen, H., Liu, L., Lei, J., Yan, N., 2019. Molecular basis for pore blockade of human Na+ channel Nav1.2 by the μ-conotoxin KIIIA. Science 363, 1309–1313. https://doi.org/10.1126/science.aaw2999

Park, J.H., Carlin, K.P., Wu, G., Ilyin, V.I., Musza, L.L., Blake, P.R., Kyle, D.J., 2014. Studies Examining the Relationship between the Chemical Structure of Protoxin II and Its Activity on Voltage Gated Sodium Channels. J. Med. Chem. 57, 6623–6631. https://doi.org/10.1021/jm500687u

Paulozzi, L.J., Weisler, R.H., Patkar, A.A., 2011. A National Epidemic of Unintentional Prescription Opioid Overdose Deaths: How Physicians Can Help Control It: (Commentary). J. Clin. Psychiatry 72, 589–592. https://doi.org/10.4088/JCP.10com06560

Pearson, D.A., Blanchette, M., Baker, M.L., Guindon, C.A., 1989. Trialkylsilanes as scavengers for the trifluoroacetic acid deblocking of protecting groups in peptide synthesis. Tetrahedron Letters 30, 2739–2742. https://doi.org/10.1016/S0040-4039(00)99113-5

Peigneur, S., Tytgat, J., 2018. Toxins in Drug Discovery and Pharmacology. Toxins 10, 126. https://doi.org/10.3390/toxins10030126

Peng, K., Shu, Q., Liu, Z., Liang, S., 2002. Function and Solution Structure of Huwentoxin-IV, a Potent Neuronal Tetrodotoxin (TTX)-sensitive Sodium Channel Antagonist from Chinese Bird Spider Selenocosmia huwena *. Journal of Biological Chemistry 277, 47564–47571. https://doi.org/10.1074/jbc.M204063200

Peschel, A., Cardoso, F.C., Walker, A.A., Durek, T., Stone, M.R.L., Braga Emidio, N., Dawson, P.E., Muttenthaler, M., King, G.F., 2020. Two for the Price of One: Heterobivalent Ligand Design Targeting Two Binding Sites on Voltage-Gated Sodium Channels Slows Ligand Dissociation and Enhances Potency. J. Med. Chem. 63, 12773–12785. https://doi.org/10.1021/acs.jmedchem.0c01107

Pineda, S.S., Chin, Y.K.-Y., Undheim, E.A.B., Senff, S., Mobli, M., Dauly, C., Escoubas, P., Nicholson, G.M., Kaas, Q., Guo, S., Herzig, V., Mattick, J.S., King, G.F., 2020. Structural venomics reveals evolution of a complex venom by duplication and diversification of an ancient peptide-encoding gene. Proceedings of the National Academy of Sciences 117, 11399–11408. https://doi.org/10.1073/pnas.1914536117

Possani, L.D., Becerril, B., Delepierre, M., Tytgat, J., 1999. Scorpion toxins specific for Na+-channels. European Journal of Biochemistry 264, 287–300. https://doi.org/10.1046/j.1432-1327.1999.00625.x

Postic, G., Gracy, J., Périn, C., Chiche, L., Gelly, J.-C., 2018. KNOTTIN: the database of inhibitor cystine knot scaffold after 10 years, toward a systematic structure modeling. Nucleic Acids Res 46, D454–D458. https://doi.org/10.1093/nar/gkx1084

Postma, T.M., Albericio, F., 2014. Disulfide Formation Strategies in Peptide Synthesis. European Journal of Organic Chemistry 2014, 3519–3530. https://doi.org/10.1002/ejoc.201402149

Price, N., Namdari, R., Neville, J., Proctor, K.J.W., Kaber, S., Vest, J., Fetell, M., Malamut, R., Sherrington, R.P., Pimstone, S.N., Goldberg, Y.P., 2017. Safety and Efficacy of a Topical Sodium Channel Inhibitor (TV-45070) in

Patients With Postherpetic Neuralgia (PHN): A Randomized, Controlled, Proof-of-Concept, Crossover Study, With a Subgroup Analysis of the Nav1.7 R1150W Genotype. The Clinical Journal of Pain 33, 310. https://doi.org/10.1097/AJP.0000000000000408

Price-Carter, M., Hull, M.S., Goldenberg, D.P., 1998. Roles of Individual Disulfide Bonds in the Stability and Folding of an ω-Conotoxin. Biochemistry 37, 9851–9861. https://doi.org/10.1021/bi9803978

Puillandre, N., Duda, T.F., Meyer, C., Olivera, B.M., Bouchet, P., 2015. One, four or 100 genera? A new classification of the cone snails. Journal of Molluscan Studies 81, 1–23. https://doi.org/10.1093/mollus/eyu055

Py, C., Martina, M., Diaz-Quijada, G.A., Luk, C.C., Martinez, D., Denhoff, M.W., Charrier, A., Comas, T., Monette, R., Krantis, A., Syed, N.I., Mealing, G.A., 2011. From Understanding Cellular Function to Novel Drug Discovery: The Role of Planar Patch-Clamp Array Chip Technology. Front. Pharmacol. 2. https://doi.org/10.3389/fphar.2011.00051

Qi, X., Zhang, Yunyun, Zhang, Yuan, Ni, T., Zhang, W., Yang, C., Mi, J., Zhang, J., Tian, G., 2018. High Throughput, Absolute Determination of the Content of a Selected Protein at Tissue Levels Using Quantitative Dot Blot Analysis (QDB). JoVE (Journal of Visualized Experiments) e56885. https://doi.org/10.3791/56885

Rahnama, S., Deuis, J.R., Cardoso, F.C., Ramanujam, V., Lewis, R.J., Rash, L.D., King, G.F., Vetter, I., Mobli, M., 2017. The structure, dynamics and selectivity profile of a NaV1.7 potency-optimised huwentoxin-IV variant. PLOS ONE 12, e0173551. https://doi.org/10.1371/journal.pone.0173551

Raja, S.N., Carr, D.B., Cohen, M., Finnerup, N.B., Flor, H., Gibson, S., Keefe, F., Mogil, J.S., Ringkamp, M., Sluka, K.A., Song, X.-J., Stevens, B., Sullivan, M., Tutelman, P., Ushida, T., Vader, K., 2020. The Revised IASP definition of pain: concepts, challenges, and compromises. Pain 161, 1976–1982. https://doi.org/10.1097/j.pain.0000000000001939

Rash, L.D., Hodgson, W.C., 2002. Pharmacology and biochemistry of spider venoms. Toxicon 40, 225–254. https://doi.org/10.1016/S0041-0101(01)00199-4

Rauch, A., Wieczorek, D., Graf, E., Wieland, T., Endele, S., Schwarzmayr, T., Albrecht, B., Bartholdi, D., Beygo, J., Donato, N.D., Dufke, A., Cremer, K., Hempel, M., Horn, D., Hoyer, J., Joset, P., Röpke, A., Moog, U., Riess, A., Thiel, C.T., Tzschach, A., Wiesener, A., Wohlleber, E., Zweier, C., Ekici, A.B., Zink, A.M., Rump, A., Meisinger, C., Grallert, H., Sticht, H., Schenck, A., Engels, H., Rappold, G., Schröck, E., Wieacker, P., Riess, O., Meitinger, T., Reis, A., Strom, T.M., 2012. Range of genetic mutations associated with severe non-syndromic sporadic intellectual disability: an exome sequencing study. The Lancet 380, 1674–1682. https://doi.org/10.1016/S0140-6736(12)61480-9

Recio, C., Maione, F., Iqbal, A.J., Mascolo, N., De Feo, V., 2017. The Potential Therapeutic Application of Peptides and Peptidomimetics in Cardiovascular Disease. Front Pharmacol 7, 526. https://doi.org/10.3389/fphar.2016.00526

Rees, D.C., Lipscomb, W.N., 1980. Structure of the potato inhibitor complex of carboxypeptidase A at 2.5-A resolution. Proceedings of the National Academy of Sciences 77, 4633–4637. https://doi.org/10.1073/pnas.77.8.4633

Rink, H., 1987. Solid-phase synthesis of protected peptide fragments using a trialkoxy-diphenyl-methylester resin. Tetrahedron Letters 28, 3787–3790. https://doi.org/10.1016/S0040-4039(00)96384-6

Robinson, S.D., Deuis, J.R., Niu, P., Touchard, A., Mueller, A., Schendel, V., Brinkwirth, N., King, G.F., Vetter, I., Schmidt, J.O., 2024. Peptide toxins that target vertebrate voltage-gated sodium channels underly the painful stings of harvester ants. Journal of Biological Chemistry 300. https://doi.org/10.1016/j.jbc.2023.105577

Röckel, D., Korn, W., Kohn, A.J., 1995. Manual of the living Conidae. (No Title).

Roesler, K.R., Rao, A.G., 2000. A single disulfide bond restores thermodynamic and proteolytic stability to an extensively mutated protein. Protein Science 9, 1642–1650. https://doi.org/10.1110/ps.9.9.1642

Rostovtsev, V.V., Green, L.G., Fokin, V.V., Sharpless, K.B., 2002. A Stepwise Huisgen Cycloaddition Process: Copper(I)-Catalyzed Regioselective “Ligation” of Azides and Terminal Alkynes. Angewandte Chemie International Edition 41, 2596–2599. https://doi.org/10.1002/1521-3773(20020715)41:14<2596::AID-ANIE2596>3.0.CO;2-4

Rupprecht, K.R., Nair, R.K., Harwick, L.C., Grote, J., Beligere, G.S., Rege, S.D., Chen, Y.-Y., Lin, Z., Fishpaugh, J.R., 2010. Development of a dot-blot assay for screening monoclonal antibodies to low-molecular-mass drugs. Analytical Biochemistry 407, 160–164. https://doi.org/10.1016/j.ab.2010.08.003

Rush, A.M., Cummins, T.R., Waxman, S.G., 2007. Multiple sodium channels and their roles in electrogenesis within dorsal root ganglion neurons. The Journal of Physiology 579, 1–14. https://doi.org/10.1113/jphysiol.2006.121483

Saez, N.J., Senff, S., Jensen, J.E., Er, S.Y., Herzig, V., Rash, L.D., King, G.F., 2010. Spider-Venom Peptides as Therapeutics. Toxins 2, 2851–2871. https://doi.org/10.3390/toxins2122851

Safavi-Hemami, H., Brogan, S.E., Olivera, B.M., 2019. Pain therapeutics from cone snail venoms: From Ziconotide to novel non-opioid pathways. Journal of Proteomics, Proteomics in chronic pain; investigating mechanistic markers of pain 190, 12–20. https://doi.org/10.1016/j.jprot.2018.05.009

Sanders, S.J., Campbell, A.J., Cottrell, J.R., Moller, R.S., Wagner, F.F., Auldridge, A.L., Bernier, R.A., Catterall, W.A., Chung, W.K., Empfield, J.R., George, A.L., Hipp, J.F., Khwaja, O., Kiskinis, E., Lal, D., Malhotra, D., Millichap, J.J., Otis, T.S., Petrou, S., Pitt, G., Schust, L.F., Taylor, C.M., Tjernagel, J., Spiro, J.E., Bender, K.J., 2018. Progress in Understanding and Treating SCN2A-Mediated Disorders. Trends in Neurosciences 41, 442–456. https://doi.org/10.1016/j.tins.2018.03.011

Schendel, V., Rash, L.D., Jenner, R.A., Undheim, E.A.B., 2019. The Diversity of Venom: The Importance of Behavior and Venom System Morphology in Understanding Its Ecology and Evolution. Toxins (Basel) 11, 666. https://doi.org/10.3390/toxins11110666

Schmalhofer, W.A., Calhoun, J., Burrows, R., Bailey, T., Kohler, M.G., Weinglass, A.B., Kaczorowski, G.J., Garcia, M.L., Koltzenburg, M., Priest, B.T., 2008. ProTx-II, a Selective Inhibitor of NaV1.7 Sodium Channels, Blocks Action Potential Propagation in Nociceptors. Mol Pharmacol 74, 1476–1484. https://doi.org/10.1124/mol.108.047670

Schmidt, M., Toplak, A., Quaedflieg, P.J., Nuijens, T., 2017. Enzyme-mediated ligation technologies for peptides and proteins. Current Opinion in Chemical Biology, Next Generation Therapeutics 38, 1–7. https://doi.org/10.1016/j.cbpa.2017.01.017

Schneider, C.A., Rasband, W.S., Eliceiri, K.W., 2012. NIH Image to ImageJ: 25 years of image analysis. Nat Methods 9, 671–675. https://doi.org/10.1038/nmeth.2089

Senji Laxme, R.R., Suranse, V., Sunagar, K., 2019. Arthropod venoms: Biochemistry, ecology and evolution. Toxicon 158, 84–103. https://doi.org/10.1016/j.toxicon.2018.11.433

Shaikh, N.Y., Sunagar, K., 2023. The deep-rooted origin of disulfide-rich spider venom toxins. eLife 12, e83761. https://doi.org/10.7554/eLife.83761

Sharma, G., Deuis, J.R., Jia, X., Mueller, A., Vetter, I., Mobli, M., 2020. Recombinant production, bioconjugation and membrane binding studies of Pn3a, a selective NaV1.7 inhibitor. Biochemical Pharmacology, Pharmacology and Therapeutic Potential of Venom Peptides 181, 114148. https://doi.org/10.1016/j.bcp.2020.114148

Sheehan, J., Cruickshank, P., Boshart, G., 1961. Notes- A Convenient Synthesis of Water-Soluble Carbodiimides. J. Org. Chem. 26, 2525–2528. https://doi.org/10.1021/jo01351a600

Sheehan, J.C., Hess, G.P., 1955. A New Method of Forming Peptide Bonds. J. Am. Chem. Soc. 77, 1067–1068. https://doi.org/10.1021/ja01609a099

Shen, H., Li, Z., Jiang, Y., Pan, X., Wu, J., Cristofori-Armstrong, B., Smith, J.J., Chin, Y.K.Y., Lei, J., Zhou, Q., King, G.F., Yan, N., 2018. Structural basis for the modulation of voltage-gated sodium channels by animal toxins. Science 362, eaau2596. https://doi.org/10.1126/science.aau2596

Shen, H., Liu, D., Wu, K., Lei, J., Yan, N., 2019. Structures of human Nav1.7 channel in complex with auxiliary subunits and animal toxins. Science 363, 1303–1308. https://doi.org/10.1126/science.aaw2493

Sieber, P., 1987. A new acid-labile anchor group for the solid-phase synthesis of C-terminal peptide amides by the Fmoc method. Tetrahedron Letters 28, 2107–2110. https://doi.org/10.1016/S0040-4039(00)96055-6

Smith, H.S., Deer, T.R., 2009. Safety and efficacy of intrathecal ziconotide in the management of severe chronic pain. Ther Clin Risk Manag 5, 521–534.

Society, T.E.P., 1998. Peptides 1996: Proceedings of the Twenty-fourth European Peptide Symposium. Mayflower Scientific Limited.

Söderberg, O., Gullberg, M., Jarvius, M., Ridderstråle, K., Leuchowius, K.-J., Jarvius, J., Wester, K., Hydbring, P., Bahram, F., Larsson, L.-G., Landegren, U., 2006. Direct observation of individual endogenous protein complexes in situ by proximity ligation. Nat Methods 3, 995–1000. https://doi.org/10.1038/nmeth947

Spears, R.J., McMahon, C., Chudasama, V., 2021. Cysteine protecting groups: applications in peptide and protein science. Chem. Soc. Rev. 50, 11098–11155. https://doi.org/10.1039/D1CS00271F

Stevens, M., Peigneur, S., Tytgat, J., 2011. Neurotoxins and Their Binding Areas on Voltage-Gated Sodium Channels. Front. Pharmacol. 2. https://doi.org/10.3389/fphar.2011.00071

Stott, D.I., 1989. Immunoblotting and dot blotting. Journal of Immunological Methods 119, 153–187. https://doi.org/10.1016/0022-1759(89)90394-3

Subirós-Funosas, R., Prohens, R., Barbas, R., El-Faham, A., Albericio, F., 2009. Oxyma: An Efficient Additive for Peptide Synthesis to Replace the Benzotriazole-Based HOBt and HOAt with a Lower Risk of Explosion[1]. Chemistry – A European Journal 15, 9394–9403. https://doi.org/10.1002/chem.200900614

Sun, S., J Cohen, C., M Dehnhardt, C., 2014. Inhibitors of voltage-gated Sodium Channel Nav1.7: Patent Applications Since 2010. Pharmaceutical Patent Analyst 3, 509–521. https://doi.org/10.4155/ppa.14.39

Teixeira, A., Benckhuijsen, W., De Koning, P., Valentijn, A., Drijfhout, J., 2002. The use of Dodt as a Non-Malodorous Scavenger in Fmoc-Based Peptide Synthesis. PPL 9, 379–385. https://doi.org/10.2174/0929866023408481

Terlau, H., Olivera, B.M., 2004. Conus Venoms: A Rich Source of Novel Ion Channel-Targeted Peptides. Physiological Reviews 84, 41–68. https://doi.org/10.1152/physrev.00020.2003

Terlau, H., Shon, K.-J., Grilley, M., Stocker, M., Stühmer, W., Olivera, B.M., 1996. Strategy for rapid immobilization of prey by a fish-hunting marine snail. Nature 381, 148–151. https://doi.org/10.1038/381148a0

Thakur, R., Suri, C.R., Kaur, I.P., Rishi, P., 2022. Peptides as Diagnostic, Therapeutic, and Theranostic Tools: Progress and Future Challenges. Crit Rev Ther Drug Carrier Syst 40, 49–100. https://doi.org/10.1615/CritRevTherDrugCarrierSyst.2022040322

The Nobel Prize in Chemistry 1955 [WWW Document], 2024. . NobelPrize.org. URL https://www.nobelprize.org/prizes/chemistry/1955/summary/ (accessed 7.1.24).

The Nobel Prize in Chemistry 1984 [WWW Document], 2024. . NobelPrize.org. URL https://www.nobelprize.org/prizes/chemistry/1984/summary/ (accessed 7.2.24).

The Nobel Prize in Chemistry 2022 [WWW Document], 2024. . NobelPrize.org. URL https://www.nobelprize.org/prizes/chemistry/2022/summary/ (accessed 6.3.24).

The Nobel Prize in Physiology or Medicine 1991 [WWW Document], 2024. . NobelPrize.org. URL https://www.nobelprize.org/prizes/medicine/1991/summary/ (accessed 6.6.24).

The UniProt Consortium, 2023. UniProt: the Universal Protein Knowledgebase in 2023. Nucleic Acids Research 51, D523–D531. https://doi.org/10.1093/nar/gkac1052

Tilley, D.C., Eum, K.S., Fletcher-Taylor, S., Austin, D.C., Dupré, C., Patrón, L.A., Garcia, R.L., Lam, K., Yarov-Yarovoy, V., Cohen, B.E., Sack, J.T., 2014. Chemoselective tarantula toxins report voltage activation of wild-type ion channels in live cells. Proceedings of the National Academy of Sciences 111, E4789–E4796. https://doi.org/10.1073/pnas.1406876111

Toledo-Aral, J.J., Moss, B.L., He, Z.-J., Koszowski, A.G., Whisenand, T., Levinson, S.R., Wolf, J.J., Silos-Santiago, I., Halegoua, S., Mandel, G., 1997. Identification of PN1, a predominant voltage-dependent sodium channel expressed principally in peripheral neurons. Proceedings of the National Academy of Sciences of the United States of America 94, 1527–1532. https://doi.org/10.1073/pnas.94.4.1527

Toniolo, C., Bonora, G.M., Mutter, M., Pillai, V.N.R., 1981. Linear oligopeptides, 78. The effect of the insertion of the proline residue on the solution conformation of host peptides. Die Makromolekulare Chemie 182, 2007–2014. https://doi.org/10.1002/macp.1981.021820713

Tornøe, C.W., Christensen, C., Meldal, M., 2002. Peptidotriazoles on Solid Phase: [1,2,3]-Triazoles by Regiospecific Copper(I)-Catalyzed 1,3-Dipolar Cycloadditions of Terminal Alkynes to Azides. J. Org. Chem. 67, 3057–3064. https://doi.org/10.1021/jo011148j

Tran, H.N.T., McMahon, K.L., Deuis, J.R., Vetter, I., Schroeder, C.I., 2022. Structural and functional insights into the inhibition of human voltage-gated sodium channels by μ-conotoxin KIIIA disulfide isomers. Journal of Biological Chemistry 298. https://doi.org/10.1016/j.jbc.2022.101728

Tran, H.N.T., Tran, P., Deuis, J.R., Agwa, A.J., Zhang, A.H., Vetter, I., Schroeder, C.I., 2020. Enzymatic Ligation of a Pore Blocker Toxin and a Gating Modifier Toxin: Creating Double-Knotted Peptides with Improved Sodium Channel NaV1.7 Inhibition. Bioconjugate Chem. 31, 64–73. https://doi.org/10.1021/acs.bioconjchem.9b00744

Tran, H.N.T., Tran, P., Deuis, J.R., McMahon, K.L., Yap, K., Craik, D.J., Vetter, I., Schroeder, C.I., 2021. Evaluation of Efficient Non-reducing Enzymatic and Chemical Ligation Strategies for Complex Disulfide-Rich Peptides. Bioconjugate Chem. 32, 2407–2419. https://doi.org/10.1021/acs.bioconjchem.1c00452

Tran, P., Crawford, T., Ragnarsson, L., Deuis, J.R., Mobli, M., Sharpe, S.J., Schroeder, C.I., Vetter, I., 2023a. Structural Conformation and Activity of Spider-Derived Inhibitory Cystine Knot Peptide Pn3a Are Modulated by pH. ACS Omega 8, 26276–26286. https://doi.org/10.1021/acsomega.3c02664

Tran, P., Schroeder, C.I., 2021. Enzymatic Ligation of Disulfide-Rich Animal Venom Peptides: Using Sortase A to Form Double-Knotted Peptides. Methods Mol Biol 2355, 83–92. https://doi.org/10.1007/978-1-0716-1617-8_8

Tran, P., Tran, H.N.T., McMahon, K.L., Deuis, J.R., Ragnarsson, L., Norman, A., Sharpe, S.J., Payne, R.J., Vetter, I., Schroeder, C.I., 2023b. Changes in Potency and Subtype Selectivity of Bivalent NaV Toxins are Knot-Specific. Bioconjugate Chem. 34, 1072–1083. https://doi.org/10.1021/acs.bioconjchem.3c00135

Tulla-Puche, J., El-Faham, A., Galanis, A.S., de Oliveira, E., Zompra, A.A., Albericio, F., 2015. Methods for the Peptide Synthesis and Analysis, in: Peptide Chemistry and Drug Design. John Wiley & Sons, Ltd, pp. 11–73. https://doi.org/10.1002/9781118995303.ch2

Undheim, E.A.B., Mobli, M., King, G.F., 2016. Toxin structures as evolutionary tools: Using conserved 3D folds to study the evolution of rapidly evolving peptides. BioEssays 38, 539–548. https://doi.org/10.1002/bies.201500165

Vanier, G.S., 2013. Microwave-Assisted Solid-Phase Peptide Synthesis Based on the Fmoc Protecting Group Strategy (CEM), in: Jensen, K.J., Tofteng Shelton, P., Pedersen, S.L. (Eds.), Peptide Synthesis and Applications. Humana Press, Totowa, NJ, pp. 235–249. https://doi.org/10.1007/978-1-62703-544-6_17

Vetter, I., Deuis, J.R., Mueller, A., Israel, M.R., Starobova, H., Zhang, A., Rash, L.D., Mobli, M., 2017. NaV1.7 as a pain target – From gene to pharmacology. Pharmacology & Therapeutics 172, 73–100. https://doi.org/10.1016/j.pharmthera.2016.11.015

Vetter, I., Lewis, R.J., 2012. Therapeutic potential of cone snail venom peptides (conopeptides). Curr Top Med Chem 12, 1546–1552. https://doi.org/10.2174/156802612802652457

Vigneaud, V. du, Ressler, C., Swan, C.J.M., Roberts, C.W., Katsoyannis, P.G., Gordon, S., 1953. THE SYNTHESIS OF AN OCTAPEPTIDE AMIDE WITH THE HORMONAL ACTIVITY OF OXYTOCIN. J. Am. Chem. Soc. 75, 4879–4880. https://doi.org/10.1021/ja01115a553

Wang, B., Dunlop, J.A., Selden, P.A., Garwood, R.J., Shear, W.A., Müller, P., Lei, X., 2018. Cretaceous arachnid Chimerarachne yingi gen. et sp. nov. illuminates spider origins. Nat Ecol Evol 2, 614–622. https://doi.org/10.1038/s41559-017-0449-3

Wang, L., Wang, N., Zhang, W., Cheng, X., Yan, Z., Shao, G., Wang, X., Wang, R., Fu, C., 2022. Therapeutic peptides: current applications and future directions. Sig Transduct Target Ther 7, 1–27. https://doi.org/10.1038/s41392-022-00904-4

Wang, S.-Sun., 1973. p-Alkoxybenzyl Alcohol Resin and p-Alkoxybenzyloxycarbonylhydrazide Resin for Solid Phase Synthesis of Protected Peptide Fragments. J. Am. Chem. Soc. 95, 1328–1333. https://doi.org/10.1021/ja00785a602

Waxman, S.G., Dib-Hajj, S., Cummins, T.R., Black, J.A., 1999. Sodium channels and pain. Proceedings of the National Academy of Sciences 96, 7635–7639. https://doi.org/10.1073/pnas.96.14.7635

Weiss, J., Pyrski, M., Jacobi, E., Bufe, B., Willnecker, V., Schick, B., Zizzari, P., Gossage, S.J., Greer, C.A., Leinders-Zufall, T., Woods, C.G., Wood, J.N., Zufall, F., 2011. Loss-of-function mutations in sodium channel Nav1.7 cause anosmia. Nature 472, 186–190. https://doi.org/10.1038/nature09975

Wilson, M.J., Yoshikami, D., Azam, L., Gajewiak, J., Olivera, B.M., Bulaj, G., Zhang, M.-M., 2011. μ-Conotoxins that differentially block sodium channels NaV1.1 through 1.8 identify those responsible for action potentials in sciatic nerve. Proceedings of the National Academy of Sciences 108, 10302–10307. https://doi.org/10.1073/pnas.1107027108

Wong, C.T.T., Taichi, M., Nishio, H., Nishiuchi, Y., Tam, J.P., 2011. Optimal Oxidative Folding of the Novel Antimicrobial Cyclotide from Hedyotis biflora Requires High Alcohol Concentrations. Biochemistry 50, 7275–7283. https://doi.org/10.1021/bi2007004

Worrell, B.T., Malik, J.A., Fokin, V.V., 2013. Direct Evidence of a Dinuclear Copper Intermediate in Cu(I)-Catalyzed Azide-Alkyne Cycloadditions. Science 340, 457–460. https://doi.org/10.1126/science.1229506

Wu, X., Wu, Y., Zhu, F., Yang, Q., Wu, Q., Zhangsun, D., Luo, S., 2013. Optimal Cleavage and Oxidative Folding of α-Conotoxin TxIB as a Therapeutic Candidate Peptide. Mar Drugs 11, 3537–3553. https://doi.org/10.3390/md11093537

Xiao, Y., Bingham, J.-P., Zhu, W., Moczydlowski, E., Liang, S., Cummins, T.R., 2008. Tarantula Huwentoxin-IV Inhibits Neuronal Sodium Channels by Binding to Receptor Site 4 and Trapping the Domain II Voltage Sensor in the Closed Configuration*. Journal of Biological Chemistry 283, 27300–27313. https://doi.org/10.1074/jbc.M708447200

Xiao, Y., Blumenthal, K., Jackson, J.O., Liang, S., Cummins, T.R., 2010. The Tarantula Toxins ProTx-II and Huwentoxin-IV Differentially Interact with Human Nav1.7 Voltage Sensors to Inhibit Channel Activation and

Inactivation. Mol Pharmacol 78, 1124–1134. https://doi.org/10.1124/mol.110.066332

Xu, H., Li, T., Rohou, A., Arthur, C.P., Tzakoniati, F., Wong, E., Estevez, A., Kugel, C., Franke, Y., Chen, J., Ciferri, C., Hackos, D.H., Koth, C.M., Payandeh, J., 2019. Structural Basis of Nav1.7 Inhibition by a Gating-Modifier Spider Toxin. Cell 176, 1238–1239. https://doi.org/10.1016/j.cell.2019.01.047

Xu, Y., Chen, J., Zhang, Y., Zhang, P., 2024. Recent Progress in Peptide-Based Molecular Probes for Disease Bioimaging. Biomacromolecules 25, 2222–2242. https://doi.org/10.1021/acs.biomac.3c01413

Yam, M.F., Loh, Y.C., Tan, C.S., Khadijah Adam, S., Abdul Manan, N., Basir, R., 2018. General Pathways of Pain Sensation and the Major Neurotransmitters Involved in Pain Regulation. International Journal of Molecular Sciences 19, 2164. https://doi.org/10.3390/ijms19082164

Yang, Y., Mis, M.A., Estacion, M., Dib-Hajj, S.D., Waxman, S.G., 2018. NaV1.7 as a Pharmacogenomic Target for Pain: Moving Toward Precision Medicine. Trends in Pharmacological Sciences 39, 258–275. https://doi.org/10.1016/j.tips.2017.11.010

Yu, H.M., Chen, S.T., Wang, K.T., 1992. Enhanced coupling efficiency in solid-phase peptide synthesis by microwave irradiation. J. Org. Chem. 57, 4781–4784. https://doi.org/10.1021/jo00044a001

Zakrzewska, J.M., Palmer, J., Morisset, V., Giblin, G.M., Obermann, M., Ettlin, D.A., Cruccu, G., Bendtsen, L., Estacion, M., Derjean, D., Waxman, S.G., Layton, G., Gunn, K., Tate, S., 2017. Safety and efficacy of a Nav1.7 selective sodium channel blocker in patients with trigeminal neuralgia: a double-blind, placebo-controlled, randomised withdrawal phase 2a trial. The Lancet Neurology 16, 291–300. https://doi.org/10.1016/S1474-4422(17)30005-4

Zhang, G., Annan, R.S., Carr, S.A., Neubert, T.A., 2014. Overview of Peptide and Protein Analysis by Mass Spectrometry. CP Molecular Biology 108. https://doi.org/10.1002/0471142727.mb1021s108

Zhang, M.-M., Green, B.R., Catlin, P., Fiedler, B., Azam, L., Chadwick, A., Terlau, H., McArthur, J.R., French, R.J., Gulyas, J., Rivier, J.E., Smith, B.J., Norton, R.S., Olivera, B.M., Yoshikami, D., Bulaj, G., 2007. Structure/Function Characterization of µ-Conotoxin KIIIA, an Analgesic, Nearly Irreversible Blocker of Mammalian Neuronal Sodium Channels *. Journal of Biological Chemistry 282, 30699–30706. https://doi.org/10.1074/jbc.M704616200

Zhao, Z., Pan, T., Chen, S., Harvey, P.J., Zhang, J., Li, X., Yang, M., Huang, L., Wang, S., Craik, D.J., Jiang, T., Yu, R., 2023. Design, synthesis, and mechanism of action of novel µ-conotoxin KIIIA analogues for inhibition of the voltage-gated sodium channel Nav1.7. Journal of Biological Chemistry 299. https://doi.org/10.1016/j.jbc.2023.103068

Zhou, X., Ma, T., Yang, L., Peng, S., Li, L., Wang, Z., Xiao, Z., Zhang, Q., Wang, L., Huang, Y., Chen, M., Liang, S., Zhang, X., Liu, J.Y., Liu, Z., 2020. Spider venom-derived peptide induces hyperalgesia in Nav1.7 knockout mice by activating Nav1.9 channels. Nat Commun 11, 2293. https://doi.org/10.1038/s41467-020-16210-y

Zhu, S., Darbon, H., Dyason, K., Verdonck, F., Tytgat, J., 2003. Evolutionary origin of inhibitor cystine knot peptides. The FASEB Journal 17, 1765–1767. https://doi.org/10.1096/fj.02-1044fje

Zoukimian, C., Béroud, R., Boturyn, D., 2022. 2-Hydroxy-4-methoxybenzyl as a Thiol-Protecting Group for Directed-Disulfide Bond Formation. Org. Lett. 24, 3407–3410. https://doi.org/10.1021/acs.orglett.2c01190